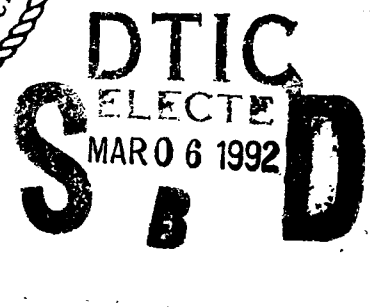


NAVAL POSTGRADUATE SCHOOL

Monterey, California

AD-A246 992



THESIS

SEASONAL WIND AND OCEAN THERMAL FORCING
INFLUENCES ON THE GENERATION OF THE
LEEUVIN CURRENT AND ITS EDDIES

by

LCDR Eric Judson Bayler, USN

September, 1991

Thesis Advisor:

M.L. Batteen

Approved for public release; distribution is unlimited

Prepared for:
Office of Naval Research
800 N. Quincy Street
Arlington, VA 22217-5000

92 0 03 211

92-05805



NAVAL POSTGRADUATE SCHOOL
Monterey, CA 93943

Rear Admiral Ralph W. West, Jr.
Superintendent

Harrison Shull
Provost


This project was funded by the National Science Foundation,
1800 G Street N. W., Washington, DC 20550.

Reproduction of all or part of this report is authorized.

Principal author for this report was


E. J. Bayler, LCDR, USN

Approved by:


C. A. Collins, Chairman
Department of Oceanography

Released by:


P. J. Marto, Dean of Research

UNCLASSIFIED

SECURITY CLASSIFICATION OF THIS PAGE

REPORT DOCUMENTATION PAGE				
1a REPORT SECURITY CLASSIFICATION UNCLASSIFIED			1b RESTRICTIVE MARKINGS	
2a SECURITY CLASSIFICATION AUTHORITY			3. DISTRIBUTION/AVAILABILITY OF REPORT Approved for public release; distribution is unlimited.	
2b DECLASSIFICATION/DOWNGRADING SCHEDULE				
4. PERFORMING ORGANIZATION REPORT NUMBER(S) NPS OC-91-003			5. MONITORING ORGANIZATION REPORT NUMBER(S)	
6a NAME OF PERFORMING ORGANIZATION Naval Postgraduate School		6b OFFICE SYMBOL (If applicable) OC		7a. NAME OF MONITORING ORGANIZATION Office of Naval Research
6c. ADDRESS (City, State, and ZIP Code) Monterey, CA 93943-5000			7b. ADDRESS (City, State, and ZIP Code) 800 N. Quincy Street Arlington, VA 2217-5000	
8a NAME OF FUNDING/SPONSORING ORGANIZATION National Science Foundation		8b OFFICE SYMBOL (If applicable)		9. PROCUREMENT INSTRUMENT IDENTIFICATION NUMBER NSF Grant No. OCE-8809465
8c. ADDRESS (City, State, and ZIP Code) 1800 G Street N. W. Washington, DC 20550			10. SOURCE OF FUNDING NUMBERS	
			Program Element No	Project No
			Task No	Work Unit Accession Number
11 TITLE (Include Security Classification) SEASONAL WIND AND OCEAN THERMAL INFLUENCES ON THE GENERATION OF THE LEEUWIN CURRENT AND ITS EDDIES				
12 PERSONAL AUTHOR(S) Bayler, Eric Judson, in conjunction with Mary L. Batteen				
13a TYPE OF REPORT Master's Thesis		13b. TIME COVERED From To		14. DATE OF REPORT (year, month, day) September 1991
15 PAGE COUNT 209				
16 SUPPLEMENTARY NOTATION The views expressed in this thesis are those of the author and do not reflect the official policy or position of the Department of Defense or the U.S. Government.				
17 COSATI CODES			18 SUBJECT TERMS (continue on reverse if necessary and identify by block number)	
FIELD	GROUP	SUBGROUP		
			Coastal Numerical Ocean Modeling, Leeuwin Current, Western Australia, Eddy-Resolving, Seasonal Wind Forcing, Seasonal Ocean Thermal Forcing, Annual Mean Wind Forcing, Annual Mean Ocean Thermal Forcing, North West Shelf Waters	
19 ABSTRACT (continue on reverse if necessary and identify by block number)				
<p>A high-resolution, multi-level, primitive equation ocean model is used to examine the response of an idealized, flat bottomed, eastern boundary oceanic regime on a beta-plane to constant ocean thermal and wind forcing by annual mean and seasonal mean climatologies. The focus of the study is the Leeuwin Current along the coastal region, from 20 degrees S to 35 degrees S, off Western Australia.</p> <p>The annual mean ocean thermal forcing is sufficient to produce a poleward surface coastal current and an equatorward undercurrent. Seasonal variation of the ocean thermal forcing provides little enhancement of the current structure, although the seasonal variation does enhance eddy generation during the periods of stronger thermal gradient. Wind forcing by annual mean climatology significantly inhibits the poleward coastal flow, but does not eliminate it. Seasonal wind forcing generates a strong seasonal signal in the poleward coastal flow, but never dominates over the pressure gradient forcing.</p> <p>The combination of wind and thermal cycles allows the formation of the North West Shelf waters and, subsequently, triggers the release of poleward flowing North West Shelf waters. This additional forcing produces a strong surge in poleward flow during the austral autumn. A nonlinear feedback mechanism acts to extend the duration of this flow through the austral winter.</p>				
20 DISTRIBUTION/AVAILABILITY OF ABSTRACT			21 ABSTRACT SECURITY CLASSIFICATION	
<input checked="" type="checkbox"/> UNCLASSIFIED-UNLIMITED <input type="checkbox"/> SAME AS REPORT <input type="checkbox"/> DTIC USERS			Unclassified	
22a NAME OF RESPONSIBLE INDIVIDUAL Mary L. Batteen			22b TELEPHONE (Include Area code) (408) 646-3265	
			22c OFFICE SYMBOL OC/Bv	

DD FORM 1473, 84 MAR

83 APR edition may be used until exhausted
All other editions are obsoleteSECURITY CLASSIFICATION OF THIS PAGE
UNCLASSIFIED

Approved for public release; distribution is unlimited.

Seasonal Wind and Ocean Thermal Forcing Influences
on the Generation of the
Leeuwin Current and its Eddies

by

Eric J. Bayler
Lieutenant Commander, United States Navy
B.S., United States Naval Academy, 1980


Submitted in partial fulfillment
of the requirements for the degrees of

MASTER OF SCIENCE IN PHYSICAL OCEANOGRAPHY
and
MASTER OF SCIENCE IN METEOROLOGY

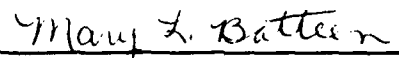
from the

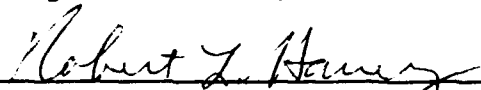
NAVAL POSTGRADUATE SCHOOL
September 1991


Author:


Eric J. Bayler

Approved by:


Mary L. Batteen, Thesis Advisor


Robert L. Haney, Second Reader
Chairman, Department of Meteorology


Curtis A. Collins, Chairman,
Department of Oceanography

ABSTRACT

A high-resolution, multi-level, primitive equation ocean model is used to examine the response of an idealized, flat-bottomed, eastern boundary oceanic regime on a beta-plane to constant ocean thermal and wind forcing by annual mean and seasonal mean climatologies. The focus of the study is the Leeuwin Current along the coastal region, from 20° S to 35° S, off Western Australia.

The annual mean ocean thermal forcing is sufficient to produce a poleward surface coastal current and an equatorward undercurrent. Seasonal variation of the ocean thermal forcing provides little enhancement to the current structure, although the seasonal variation does enhance eddy generation during the periods of stronger thermal gradient. Wind forcing by annual mean climatology significantly inhibits the poleward coastal flow, but does not eliminate it. Seasonal wind forcing generates a strong seasonal signal in the poleward coastal flow, but never dominates over the pressure gradient forcing.

The combination of wind and thermal cycles allows the formation of the North West Shelf waters and, subsequently, triggers the release of poleward flowing North West Shelf waters. This additional forcing produces a strong surge in poleward flow during the austral autumn. A nonlinear feedback mechanism acts to extend the duration of this flow through the austral winter.



Accession For	
NTIS GRA&I	<input checked="" type="checkbox"/>
DTIC TAB	<input type="checkbox"/>
Unannounced	<input type="checkbox"/>
Justification	
By	
Distribution/	
Availability Codes	
Dist	Avail and/or Special
A-1	

TABLE OF CONTENTS

I.	INTRODUCTION	1
II.	BACKGROUND	4
	A. DESCRIPTION OF THE LEEUWIN CURRENT	4
	B. PREVIOUS STUDIES	5
III.	MODEL DESCRIPTION	13
	A. DOMAIN SIZE AND RESOLUTION	13
	B. MODEL EQUATIONS	13
	C. BOUNDARY CONDITIONS	15
	D. FINITE DIFFERENCING	18
	E. HEAT AND MOMENTUM DIFFUSION	18
	F. SURFACE THERMAL FORCING	19
	G. MODEL INITIALIZATION	21
	H. OCEAN THERMAL FORCING	21
	I. WIND FORCING	24
	J. EXPERIMENT DESIGN	25
IV.	ANALYSIS TECHNIQUES	32
	A. ENERGY ANALYSIS	32
	1. Kinetic Energy	32
	2. Available Potential Energy	33
	3. Energy Transfers	33
	B. SPECTRAL ANALYSIS	34
	C. STABILITY ANALYSIS	35
	D. GEOSTROPHIC VERSUS EKMAN FORCING	36
V.	RESULTS AND DISCUSSION	42
	A. SEASONAL AND ANNUAL MEAN THERMAL FORCING	42
	B. SEASONAL AND ANNUAL MEAN WIND FORCING	43
	C. SEASONAL THERMAL FORCING INFLUENCES	45
	1. Time Sequence Analysis	45
	2. Energy Analysis	51
	3. Spectral Analysis	52
	4. Instability Analysis	52

D.	SEASONAL WIND FIELD INFLUENCES	54
1.	Time Sequence Analysis	54
2.	Energy Analysis	59
3.	Spectral Analysis	60
4.	Stability Analysis	60
E.	COMBINED WIND AND THERMAL FORCING INFLUENCE	61
F.	NORTH WEST SHELF WATER INFLUENCE	63
G.	COMPARISONS WITH PREVIOUS STUDIES	66
H.	LEEUVIN CURRENT INTERDISCIPLINARY EXPERIMENT DATA	72
VI.	SUMMARY AND RECOMMENDATIONS	186
A.	SUMMARY	186
B.	RECOMMENDATIONS	188
	LIST OF REFERENCES	189
	INITIAL DISTRIBUTION LIST	193

LIST OF TABLES

Table 3.1	MODEL SYMBOL DEFINITIONS	15
Table 3.2	VALUES OF CONSTANTS USED IN THE MODEL	16
Table 3.3	TEMPERATURE PROFILE: NORTH WEST SHELF WATERS	23

LIST OF FIGURES

Figure 1.1 Model Domain	3
Figure 2.1 The Leeuwin Current and ocean circulation off Western Australia	11
Figure 2.2 Ocean basin sea surface slopes	12
Figure 3.1 Annual mean temperature gradient	27
Figure 3.2 Seasonal mean temperature gradients	28
Figure 3.3 Model boundary and forcing diagram	29
Figure 3.4 Imposed seasonal meridional temperature difference versus time for model domain (20° S to 35° S)	30
Figure 3.5 Annual cycle of net forcing for the Leeuwin Current . .	31
Figure 4.1 Coherency of meridional spatial series versus spatial frequency	39
Figure 4.2 Integrated geopotential anomaly versus depth (LUCIE) .	40
Figure 4.3 Representative 300 dbar pressure surface	41
Figure 5.1 Observed seasonal dynamic height fields off Western Australia	76
Figure 5.2 Annual mean wind vector field with magnitude contours for model domain	77
Figure 5.3 Seasonal mean wind vector fields and meridional component contour plots for model domain	78
Figure 5.4 Initial condition for surface temperature field	81
Figure 5.5 Case 1 surface fields, day 40	82
Figure 5.6 Case 2 surface fields, day 40	83
Figure 5.7 Case 1 surface fields, day 80	84
Figure 5.8 Case 1 surface fields, day 120	85
Figure 5.9 Case 2 surface fields, day 80	86
Figure 5.10 Case 2 surface fields, day 120	87

Figure 5.11	Case 1 30-day time-averaged meridional velocity cross-sections centered on day 60	88
Figure 5.12	Case 2 30-day time-averaged meridional velocity cross-sections centered on day 60	89
Figure 5.13	Case 1 30-day time-averaged meridional velocity cross-sections centered on day 120	90
Figure 5.14	Case 2 30-day time-averaged meridional velocity cross-sections centered on day 120	91
Figure 5.15	Case 2, Case 1 surface pressure, meridional velocity, current vector fields, day 180	92
Figure 5.16	Case 2 30-day time-averaged meridional velocity cross-sections centered on day 180	93
Figure 5.17	Case 1 30-day time-averaged meridional velocity cross-sections centered on day 180	94
Figure 5.18	Case 1, Case 2 pressure, meridional velocity, current velocity vector fields for the surface, day 240	95
Figure 5.19	Case 2 30-day time-averaged meridional velocity cross-sections centered on day 240	96
Figure 5.20	Case 1 30-day time-averaged meridional velocity cross-sections centered on day 240	97
Figure 5.21	Case 2 pressure, meridional velocity fields for the surface at days 250, 280	98
Figure 5.22	Case 1 pressure, meridional velocity fields for the surface at days 250, 280	99
Figure 5.23	Case 1 30-day time-averaged meridional velocity cross-sections centered on day 300	100
Figure 5.24	Case 2 30-day time-averaged meridional velocity cross-sections centered on day 300	101
Figure 5.25	Case 1, Case 2 meridional velocity, pressure fields for the surface, day 360	102

Figure 5.26	Case 1 instantaneous and 30-day time-averaged surface meridional velocity fields	103
Figure 5.27	Case 2 instantaneous and 30-day time-averaged meridional velocity fields	105
Figure 5.28	Kinetic energy time-series	107
Figure 5.29	Case 1 spectral density, day 60 and day 100	108
Figure 5.30	Case 2 spectral density at day 60 and day 90	109
Figure 5.31	Case 1 instability, days 60 - 90	110
Figure 5.32	Case 2 instability, days 60 - 80	111
Figure 5.33	Case 1 instability, days 230 - 260	112
Figure 5.34	Case 2 instability, days 220 - 240	113
Figure 5.35	Meridional surface thermal advection	114
Figure 5.36	Case 3 pressure, meridional velocity, and current vector fields for the surface, day 40	115
Figure 5.37	Case 3 surface pressure fields, day 80 and day 120	116
Figure 5.38	Case 4 pressure, meridional velocity, and current vector velocity fields for the surface, day 40	117
Figure 5.39	Case 3 30-day time-averaged meridional velocity cross-sections centered on day 60	118
Figure 5.40	Case 4 30-day time-averaged meridional velocity cross-sections centered on day 60	119
Figure 5.41	Case 4 surface pressure fields, days 80 and 120	120
Figure 5.42	Case 3, Case 4 current vector velocity fields for the surface, day 80 and day 120	121
Figure 5.43	Case 3, Case 4 pressure and meridional velocity fields for the surface, day 180	122
Figure 5.44	Case 3, Case 4 surface current velocity vector fields, day 180	123
Figure 5.45	Case 3 30-day time-averaged meridional velocity cross-sections centered on day 180	124

Figure 5.46	Case 4 30-day time-averaged meridional velocity cross-	
	sections centered on day 180	125
Figure 5.47	Case 3 pressure, meridional velocity, and current vector	
	fields at the surface, day 240	126
Figure 5.48	Case 3 30-day time-averaged meridional velocity cross-	
	sections centered on day 240	127
Figure 5.49	Case 4 30-day time-averaged meridional velocity cross-	
	sections centered on day 240	128
Figure 5.50	Case 4 pressure, meridional velocity, and current	
	velocity vector fields for the surface, day 240	129
Figure 5.51	Case 4 pressure, meridional velocity, and current	
	velocity vector fields for the surface, day 300	130
Figure 5.52	Case 3 30-day time-averaged meridional velocity cross-	
	sections centered on day 300	131
Figure 5.53	Case 3 pressure, meridional velocity, and current	
	velocity vector fields for the surface, day 300	132
Figure 5.54	Case 4 30-day time-averaged meridional velocity cross-	
	sections centered on day 300	133
Figure 5.55	Case 3 pressure, meridional velocity, and current	
	velocity vector fields for the surface, Day 360	134
Figure 5.56	Case 4 pressure, meridional velocity, and current	
	velocity vector fields for the surface, day 360	135
Figure 5.57	Case 3 instantaneous and 30-day time-averaged meridional	
	surface velocity fields	136
Figure 5.58	Case 4 instantaneous and 30-day time-averaged meridional	
	surface velocity fields	138
Figure 5.59	Case 3, Case 4 time series of kinetic energy	140
Figure 5.60	Case 3 spectral density, day 80 and day 110	141
Figure 5.61	Case 4 spectral density, day 70 and day 100	143
Figure 5.62	Case 3 spectral density, day 170 and day 210	144
Figure 5.63	Case 4 spectral density, day 200 and day 230	145

Figure 5.64	Case 3 energy transfer fields, days 80 - 110	146
Figure 5.65	Case 4 energy transfer fields, days 70 - 90	147
Figure 5.66	Case 3 energy transfer fields, days 170 - 200	148
Figure 5.67	Case 4 energy transfer fields, days 200 - 220	149
Figure 5.68	Climatological forcing cycles	150
Figure 5.69	Geostrophic versus surface Ekman forcing	151
Figure 5.70	Case 2, Case 4 pressure, meridional velocity, current velocity vector fields at the surface, day 90	154
Figure 5.71	Case 1, Case 3 pressure, meridional velocity, current velocity vector fields at the surface, day 90	155
Figure 5.72	Case 2, Case 4 pressure, meridional velocity, current velocity vector fields at the surface, day 180	156
Figure 5.73	Case 1, Case 3 pressure, meridional velocity, current velocity vector fields at the surface, day 180	157
Figure 5.74	Case 2, Case 4 pressure, meridional velocity, current velocity vector fields at the surface, day 270	158
Figure 5.75	Case 1, Case 3 pressure, meridional velocity, current velocity vector fields at the surface, day 270	159
Figure 5.76	Case 2, Case 4 pressure, meridional velocity, current velocity vector fields at the surface, day 360	160
Figure 5.77	Case 1, Case 3 pressure, meridional velocity, current velocity vector fields at the surface, day 360	161
Figure 5.78	Case 1, Case 5 pressure, meridional velocity, current velocity vector fields at the surface, day 210	162
Figure 5.79	Case 1, Case 5 pressure, meridional velocity, current velocity vector fields at the surface, day 240	163
Figure 5.80	Case 1, Case 5 meridional surface velocity, days 300, 330, 360	164
Figure 5.81	Case 2, Case 6 pressure, meridional velocity, current velocity vector fields at the surface, day 210	165

Figure 5.82	Case 2, Case 6 pressure, meridional velocity, current velocity vector fields at the surface, day 240	166
Figure 5.83	Case 2, Case 6 meridional surface velocity, days 300, 330, 360	167
Figure 5.84	Case 3, Case 7 pressure, meridional velocity, current velocity vector fields at the surface, day 210	168
Figure 5.85	Case 3, Case 7 pressure, meridional velocity, current velocity vector fields at the surface, day 240	169
Figure 5.86	Case 3, Case 7 meridional surface velocity, days 300, 330, 360	170
Figure 5.87	Case 4, Case 8 pressure, meridional velocity, current velocity vector fields at the surface, day 210	171
Figure 5.88	Case 4, Case 8 pressure, meridional velocity, current velocity vector fields at the surface, day 240	172
Figure 5.89	Case 4, Case 8 meridional surface velocity, days 300, 330, 360	173
Figure 5.90	Time series of kinetic energy for North West Shelf forcing cases	174
Figure 5.91	Case 5 20-day time-averaged meridional velocity cross-sections centered on day 200	175
Figure 5.92	Case 5 20-day time-averaged meridional velocity cross-sections centered on day 240	176
Figure 5.93	LUCIE cross-sections of mean meridional velocity . . .	177
Figure 5.94	Case 8 annual average meridional velocity cross-section	178
Figure 5.95	Case 4 annual average meridional velocity cross-section	179
Figure 5.96	Case 8 100-day time-averaged meridional velocity cross-sections centered on day 90	180
Figure 5.97	Case 8 100-day time-averaged meridional velocity cross-sections centered on day 215	181

Figure 5.98 Case 8 100-day time-averaged meridional velocity cross-	
sections centered on day 295	182
Figure 5.99 Case 8 30-day time-averaged surface velocity vector and	
meridional velocity fields	183
Figure 5.100 Time series of coastal surface flow	185

ACKNOWLEDGMENTS

The author wishes to thank Dr. Mary Batteen for her guidance and patience. Her expertise and enthusiasm has made this learning experience most enjoyable and rewarding. Thanks also to Dr. Robert L. Haney and Dr. Curtis A. Collins for their assistance in finalizing this report. Special thanks to Pedro Tsai and Arlene Guest for their efforts and assistance with my many computer programming projects and problems. Finally, thanks to Gail, my wife, for her many contributions to this project and for all the help that has allowed me to focus on completing this goal.

I. INTRODUCTION

The Leeuwin Current off Western Australia provides a unique opportunity to examine the roles of wind and ocean thermal forcing on the generation and maintenance of an eastern boundary current and its eddies. Studying the Leeuwin Current, an anomalous poleward eastern boundary flow, will help reveal the governing dynamics of eastern boundary currents by contrasting the Leeuwin Current conditions and ocean response with the more typical equatorward flows found at other eastern ocean boundaries.

The Office of Naval Research identified eastern boundary currents and their eddy generation as the subject of interest for an accelerated research initiative. Specifically, the goal is to understand the physical dynamics of mesoscale interactions in weakly nonlinear flow regimes in eastern boundary currents. Some of the key issues concern the causes and characteristics of eastern boundary jets and associated undercurrents; the exchanges and transport of energy and momentum between and by the eddies and jets which dominate the mesoscale; the cause of the eddies and their role in maintaining or dissipating the flow in the eastern boundary regime; and the importance of local forcing, such as wind and heating, on the mesoscale ocean structure.

This study explores the response of eastern boundary flow to anomalous conditions, and examines and models the interrelation of the forcing mechanisms. The numerical model used for this study was developed by Haney (1985), and adapted for eastern boundary current regions by Batteen (1989). Although previous simulations of the Leeuwin Current have used a high-resolution, multi-level, primitive equation model, this study extends prior efforts through the addition of continuous, seasonally-varying, climatological ocean thermal forcing. The addition of seasonally-varying wind forcing from the annual cycle of climatological winds further improves the representativeness of the results.

The objective of this study is to examine the role of seasonal ocean thermal forcing and the role of seasonal wind forcing in the observed seasonal structure of the Leeuwin Current flow in the region shown in Figure 1.1. The additional seasonally varying ocean thermal forcing from the warm waters of the North West Shelf region is also addressed.

The organization of this study is as follows: Chapter II provides background on the Leeuwin Current system and previous studies; Chapter III describes the numerical model used, including the ocean thermal forcing, the wind forcing, assumptions, and approximations; Chapter IV presents the analysis techniques used; Chapter V provides results and a discussion of their significance; and, Chapter VI includes a summary of the results and their significance.

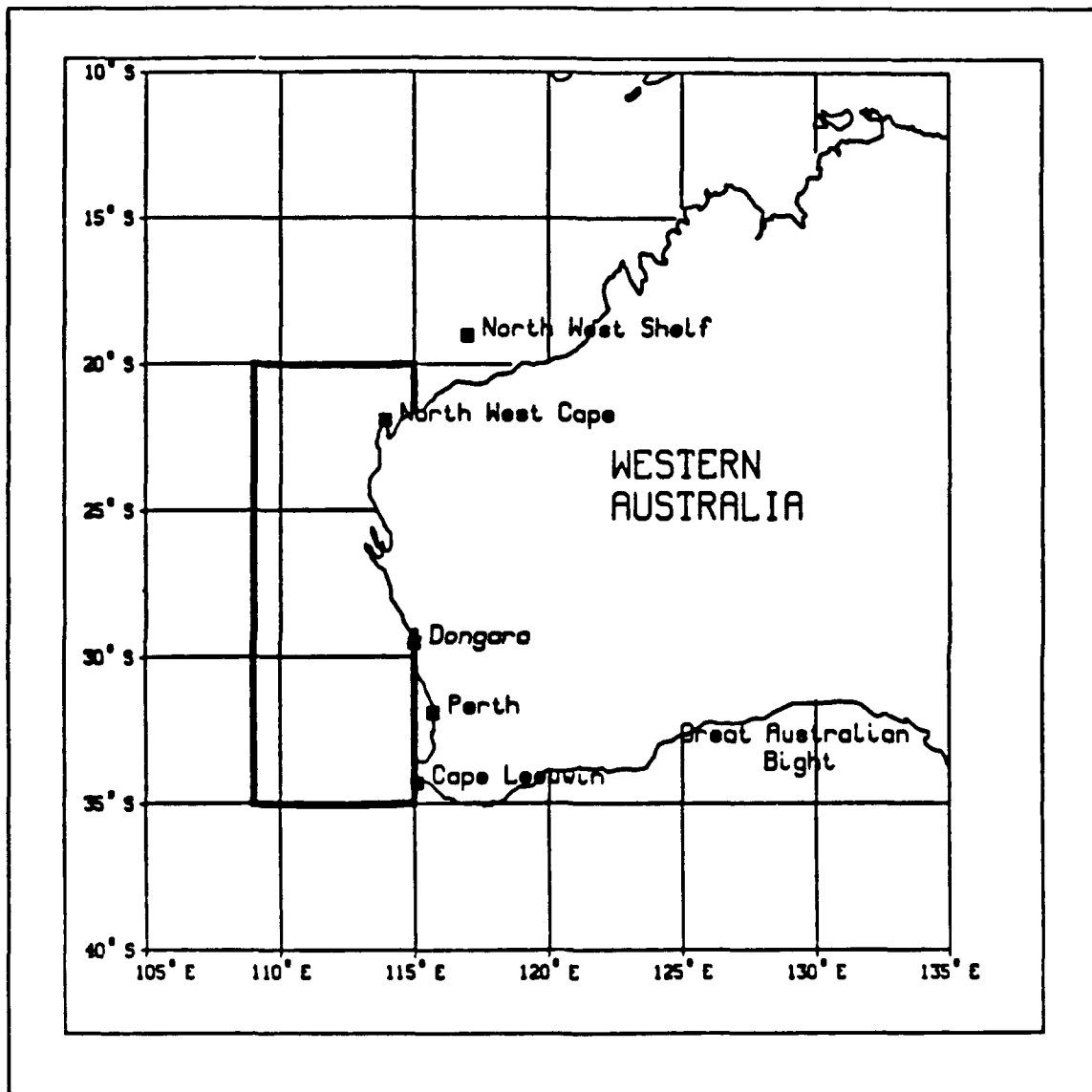


Figure 1.1 Model Domain: Area of study is a 576 km by 1600 km box off the west coast of Australia.

II. BACKGROUND

A. DESCRIPTION OF THE LEEUWIN CURRENT

The Leeuwin Current can be characterized as a surface stream of warm, low-salinity tropical water flowing southward from northwestern Australia to Cape Leeuwin in southwest Australia and then eastward to and across the Great Australian Bight (Cresswell and Golding, 1980) (Figure 2.1). Church et al. (1989) further describe the Leeuwin Current as flowing principally, but not exclusively, in the austral autumn and austral winter. Smith et al. (1991) report that the surface poleward current is weakest and shallowest between November and January, followed by the period of most intense and deepest flow between March and May. During the austral winter (May through July) Smith et al. (1991) note that flow remains poleward but it is weaker, broader, shallower, and no longer confined to the upper slope. At the equatorward end of the Leeuwin Current domain, the flow is broad and shallow (200 km wide by about 50 m deep), tapering and deepening with poleward alongshore distance to become a narrow (less than 100 km wide) flow extending vertically to about 200 m depth. Maximum speeds of near 1.8 m s^{-1} have been recorded. Church et al. (1989) also note that the principal flow is centered at the shelf edge. With this anomalous poleward flow, there is an equally anomalous, significant equatorward undercurrent centered near 350 m depth that can attain speeds comparable to the surface flow, exceeding, on the average, 10 cm s^{-1} (Smith et al., 1991).

The unusual nature of the Leeuwin Current is highlighted by the fact that, despite strong equatorward wind stress, there is no steady equatorward flow and, consequently, there is no upwelling typical of other eastern boundary currents. Godfrey and Ridgway (1985) argue that the very strong meridional pressure gradient of the eastern Indian Ocean drives onshore flow that turns poleward at the coast, forming the Leeuwin Current. They note that the meridional pressure gradient off Western Australia is comparable to the pressure gradient driving the strong western boundary currents in most of the other ocean basins (Figure 2.2). Godfrey and Ridgway (1985) discuss the relative strengths of the pressure gradient forcing and the opposing wind forcing, pointing out that the individual seasonal cycle of one forcing mechanism reinforces seasonal trends of the other, creating a strong seasonal signal in the flow of the Leeuwin Current.

Added to the general seasonal cycles of forcing by the pressure gradient and the wind is an observed surge of warm, less saline water flowing poleward out of the North West Shelf region (Figure 2.1) during the austral autumn (March through May) (Smith et al., 1991). Gentilli (1972) proposed that shallow through-flow from the Pacific Ocean to the Indian Ocean in the austral autumn and winter is isolated by a reversal of the flow in the spring. The water then achieves thermal homogeneity over the summer to become a "raft" of warm water that flows poleward during the following autumn and winter. While an actual reversal of flow has not been supported by data (Smith et al., 1991), the flow during the austral spring and summer is greatly diminished by climatologically stronger winds and a climatologically weaker pressure gradient, effectively yielding the same result.

B. PREVIOUS STUDIES

The Leeuwin Current, as an anomalous eastern boundary current, presents a distinct challenge in coastal modeling. The underlying dynamical processes of the current are not well understood and modelers are confounded by a general lack of detailed data. With the recent completion of the Leeuwin Current Interdisciplinary Experiment (LUCIE), modelers will have better data for examining the inter-dependencies of various forcing mechanisms.

Recent modeling efforts have focused on process-oriented studies to better describe the contributing forcing mechanisms and their relative importance. There is general agreement that the principal driving force is Indian Ocean geostrophic inflow, created by the significant north-south density gradient prevalent offshore. Thompson (1987) presents a linear analytical model which accounts for a significant portion of the observed phenomena. He proposes that, assuming seasonal time scales and continental length scales, the geostrophic inflow from the west due to the alongshore density gradient is balanced by return flux in the frictional (Ekman) bottom layer over the shelf, producing a near bottom poleward longshore current. This onshore flux creates a cross-shelf pressure gradient to push the flux back out via the bottom Ekman layer, which, in turn, creates a poleward geostrophic current at the surface in addition to the poleward flow generated by the bottom friction layer.

Without focusing on the causes of onshore flow or the observed deep mixed layer, Thompson (1987) uses climatological values for the mixed layer depth and the wind stress to show that nowhere is the wind stress term dominant over the pressure and Coriolis terms. Consequently, downwelling results, causing baroclinic shear that enhances the poleward

current. Because the climatological winds are upwelling favorable, recognition that the pressure gradient force dominates over the wind stress provides enlightenment on the relative contributions of these forces. Thompson (1987) notes that the choice of alongshore pressure gradients, with respect to cross-shore location on the shelf, results in either a strong seasonal signal (near-zero flow in spring and early summer and poleward in the fall and winter) or continuous poleward flow throughout the year. These differing results are due to the relative strength of the pressure gradient force versus the climatological wind stress during the various seasons.

Even though Thompson (1987) assumes that the advection and local terms are small over seasonal time scales, he acknowledges the importance of advection in the Leeuwin Current system. He points out that the flow exhibits nonlinearity in that it has self-perpetuating baroclinicity; i.e., tropical water is transported poleward along the coast and mid-latitude water is moved north offshore. The significant nonlinear baroclinic instability that would result from this situation is, therefore, not adequately addressed. Thompson's (1987) theory does, however, explain the flow into the wind, the equatorward undercurrent, and the existence of sharp fronts.

Weaver and Middleton (1989, 1990), using a different linear analytical model, assume a steady state, a continental shelf and forcing by an unchanging alongshore density gradient. By coupling the analytical model to a two-layer ocean model, they are able to produce a geostrophically-balanced onshore flow that turns south at the coast, intensifying the southward flow with poleward alongshore distance. Peak velocities are near the shelf break and are comparable to observations and results from numerical models, but the model is unable to predict the weak subsurface equatorward flow. The notable aspect of this model is that it produces the poleward current without the employment of wind stress or cross-shelf bottom stress, leading Weaver and Middleton (1989, 1990), after an examination of limiting cases, to conclude that the shelf is important to the Leeuwin Current dynamics.

Using longitudinally-independent thermohaline forcing in cases with steady density forcing, seasonal density forcing, and seasonal wind-band forcing superimposed on the steady density forcing, McCreary et al. (1986) demonstrate that, for their linear, viscid, continuously-stratified numerical model, the eastward geostrophic current from the ocean's interior forces downwelling at the eastern boundary, creating a poleward surface current with an associated equatorward undercurrent. McCreary et al. (1986) simplify their analysis by assuming a geostrophically balanced

alongshore current. This current results from mass convergence at the coast, and is fed by geostrophic onshore flow due to the alongshore density gradient. McCreary et al. (1986) rejected other choices of possible primary forcing mechanisms. Local wind curl is almost always positive and would drive an equatorward surface current. Remote forcing, such as the North West Shelf (NWS) waters or Indonesian flow-through (Kundu and McCreary, 1986), should weaken away from the forcing region, contrary to the observed poleward intensification of the Leeuwin Current. A uniformly deep ocean was used, eliminating shelf processes as a contributing factor in both the results of McCreary et al. (1986) and Kundu and McCreary (1986).

McCreary et al. (1986) note that vertical mixing is crucial to their model because, as vertical mixing approaches zero, the coastal circulation weakens due to the beta-effect, allowing coastal circulation in an inviscid model to leak completely offshore via the radiation of Rossby waves. Vertical mixing inhibits this process by damping the Rossby waves, associated with the higher order baroclinic modes, preventing the Rossby waves from propagating very far offshore. Vertical mixing also directly affects the mixed layer thickness and, consequently, the alongshore density gradient of the region above the thermocline. The density gradient of this portion of the water column has been identified as the forcing mechanism for the geostrophic onshore flow that drives the Leeuwin Current.

Recognizing limitations with their linear model, as evidenced by weak current and undercurrent mean speeds, McCreary et al. (1986) concluded that the Leeuwin Current is significantly forced by a steady sea surface density field and seasonally varying wind stress. They also note that, based on observations and their model's limitations, nonlinear remote forcing and other nonlinear enhancements could play a significant role in Leeuwin Current dynamics.

Weaver and Middleton (1989) extend the numerical modeling of the Leeuwin Current by developing a nonlinear model that allows for the advection of temperature and salinity. The model is a closed basin with boundaries remote from the area of interest. An initial north-south density gradient is imposed in the top 500 m of the entire model ocean. The model ocean then geostrophically adjusts over time in the absence of any additional external forcing. The imposed initial density gradient is based only on annual mean data from Levitus (1982) and Rochford (1962, 1969). However, in light of the marked seasonality of the Leeuwin Current signal, the annual variation of the density gradient may be a significant factor in the driving mechanism for the Leeuwin Current. Weaver and

Middleton (1989) also do not address the influence of the highly seasonal wind regimes. The model includes bottom friction, a sloping shelf, and vertical mixing, each of which has been shown capable of independently generating an alongshore current under given circumstances in a linear environment. Forcing by the North West Shelf (NWS) waters is simulated as a "dam-breaking," as proposed by Gentilli (1972), and is initiated at the commencement of the model run.

In addition to the strongly nonlinear remote forcing from the NWS waters, Weaver and Middleton (1989) observe other nonlinear effects. Because the alongshore barotropic flow on the shelf remains large during the transient stages of the model spin-up, poleward temperature and salinity advection continues and strong offshore temperature and salinity gradients are created. These gradients generate thermal winds that significantly enhance the poleward flow seaward of the barotropic, shelf-water-velocity maximum. In a linear case without a continental shelf, the Weaver and Middleton (1989) model produced an initially strong eastern boundary current that dissipated through westward migration, eliminating poleward surface flow at the coast. After 55 days of model time, a feedback mechanism asserted itself. The strong offshore fronts, caused by the initial southward advection, generated thermal winds that provided feedback to enhance the poleward surface flow. Because the alongshore barotropic flow on the shelf was always present, net advection was larger. The resulting thermal winds were stronger and, therefore, the resulting southward flow was also stronger. This strongly nonlinear effect may significantly contribute to the poleward intensification of the Leeuwin Current and the persistence of the current over time. After analysis of the cases in their study, Weaver and Middleton (1989) rule out the NWS waters as a primary driving mechanism for the Leeuwin Current and conclude that the NWS waters only provide a significant enhancement to the flow.

Weaver and Middleton (1989) note that their model is somewhat unsatisfactory due to its inability to maintain the intensity of the modeled Leeuwin Current for a long period of time. They attribute this deficiency to the shortness of the model run (only 80 model days) and to the energy loss within the model as time progresses. The model evolves from initial conditions without any further forcing so that energy continues to dissipate through friction.

Batteen and Rutherford (1990) advanced the Leeuwin Current modeling efforts by simulating the generation of realistic mesoscale (eddy) features in addition to a poleward surface current and equatorward undercurrent. Their nonlinear primitive equation model employs open boundary conditions and a constant depth ocean. Similar to Weaver and

Middleton (1989), Batteen and Rutherford (1990) force their model only through the initial conditions based on annual mean temperature climatology from Levitus (1982). Also similar to Weaver and Middleton (1989), Batteen and Rutherford (1990) simulate the forcing by the NWS waters as a dam-breaking that initiates with the commencement of the model run. Batteen and Rutherford (1990) extend the duration of their model run beyond the 80 days of Weaver and Middleton (1989) to 160 model days to simulate the season of strongest flow for the Leeuwin Current.

The focus of the Batteen and Rutherford (1990) model was the generation and stability of the Leeuwin Current and its eddies. Their study identified that the Indian Ocean temperature structure was sufficient to drive an unstable poleward surface flow and an equatorward undercurrent. With and without NWS forcing, their model produced a surface current that, after reaching its largest velocity, subsequently broadened and drifted westward through baroclinic Rossby wave propagation. Additionally, their model experienced the nonlinear feedback described by Weaver and Middleton (1989). For the current driven by the Indian Ocean temperature gradient only, barotropic instability developed as the dominant instability mechanism in the poleward end of the domain. The addition of NWS waters created a far more energetic and unstable current, adding to the baroclinicity of the flow, as well as the barotropy.

Batteen and Rutherford (1990) concluded that, consistent with Weaver and Middleton (1989), a shelf is not required to produce and maintain the Leeuwin Current. The scales of their model-generated current and mesoscale features, missing from previous modeling studies, are comparable with available observations.

Batteen et al. (1991) add idealized wind forcing, representative of the period of maximum Leeuwin Current flow (austral autumn / austral winter), to the Batteen and Rutherford (1990) model. Cases with and without NWS forcing are simulated and run for 160 model days. Unstable flow is generated in both cases. Batteen et al. (1991) note that wind forcing effects are only discernible at the equatorward end of their model domain. The density-driven flow dominates at the poleward end, despite stronger winds. At the equatorward end of the domain, the effects of the NWS waters completely dominate the flows driven by the Indian Ocean and the wind stress. The effects of the NWS waters weaken away from the source region, but they continue to augment the Indian Ocean forcing, resulting in a stronger flow along the entire coastal boundary. Again, barotropic (horizontal shear) instability dominates over baroclinic (vertical shear) instability in the regions of eddy development. The NWS waters add baroclinicity to the Leeuwin Current, as well as barotropy.

instability in the vicinity of the NWS source region. The baroclinicity weakens poleward.

The objective of this study is to extend the above studies by adding continuously-forced ocean thermal forcing and wind forcing to eliminate the loss of energy experienced by initial-condition-forced models as model time progresses. This model capability allows seasonal variation of both the ocean thermal forcing and the wind forcing, permitting a significantly more representative forcing of the highly seasonal Leeuwin Current system. The progression from one season to the next can be examined without the undue influence of adjustment to initial conditions. The longer model runs, to day 360, also should provide better insight into longer term processes versus transient phenomena. The model can also generate a signal without relying on initial conditions to produce a seasonal surge, which should lead to more realistic model simulations.

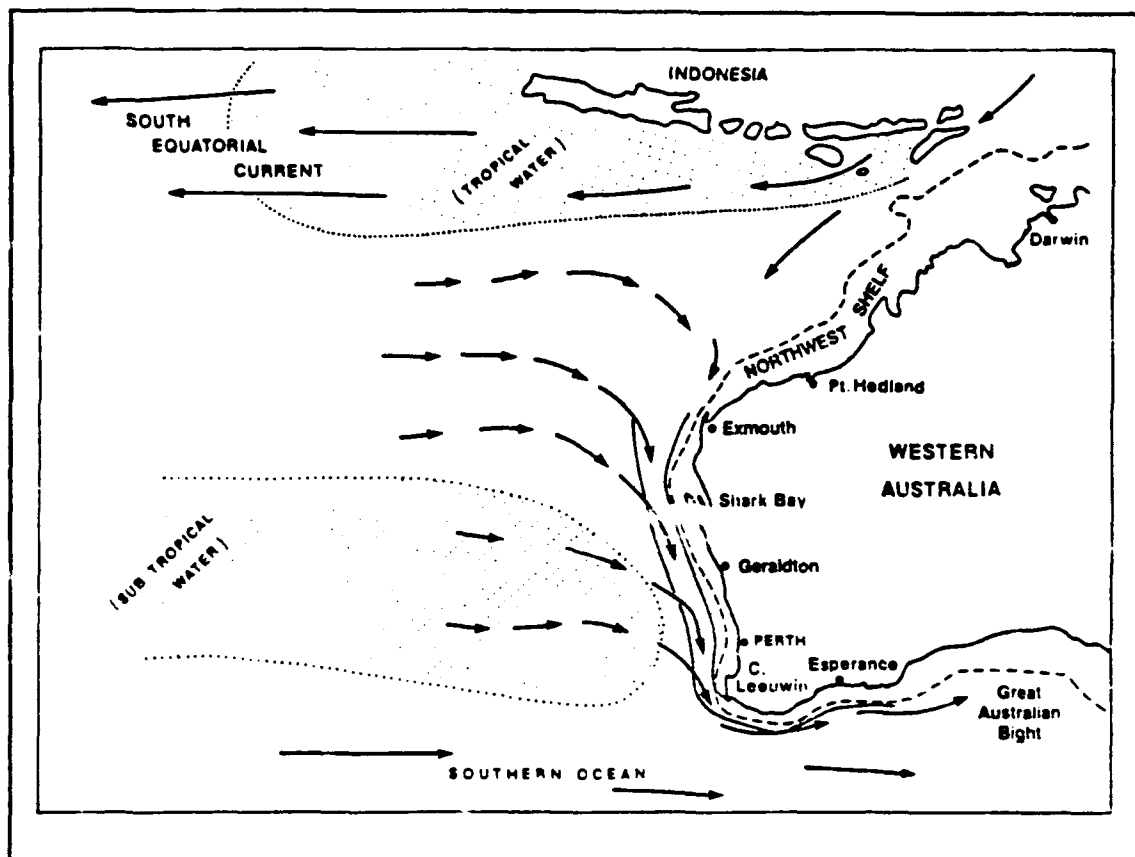


Figure 2.1 The Leeuwin Current and ocean circulation off Western Australia (from Pearce and Cresswell, 1985).

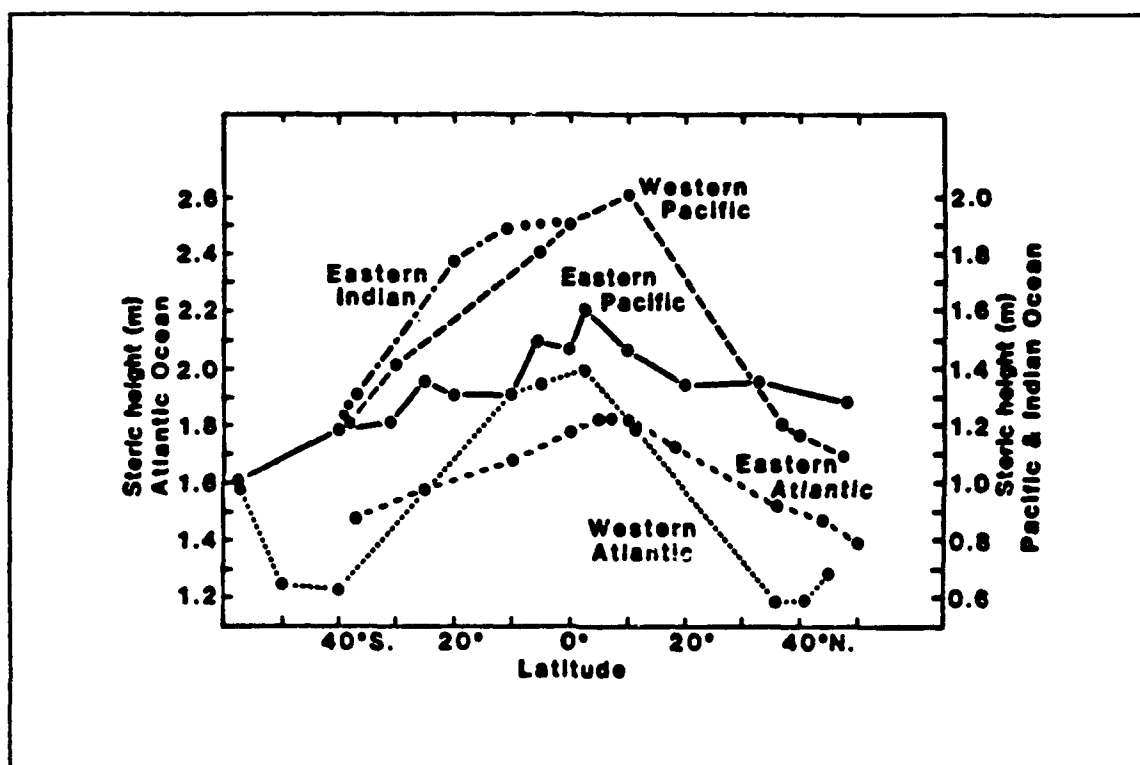


Figure 2.2 Ocean basin sea surface slopes (from Godfrey and Ridgway, 1985).

III. MODEL DESCRIPTION

A. DOMAIN SIZE AND RESOLUTION

The modeled area (Figure 1.1) employs a meridional straight-line approximation for the continental shelf off the west coast of Australia, extending for 1600 km between latitudes 20° S and 35° S. The rectangular domain has a cross-shore dimension of 576 km oriented east-west, ranging from 109° E to 115° E. Batteen and Rutherford (1990) note that comparisons with higher resolution numerical simulations, 10 km by 9 km, showed no significant degradation in the resolution of mesoscale features when using a coarser grid in the alongshore direction of the model. As a result, horizontal resolution is 25 km in the alongshore direction and 9 km in the cross-shore direction. The vertical resolution, following Haney (1974), concentrates more layers in the dynamically active region of the upper ocean above the thermocline and is defined by the following ten constant depth levels: 13, 46, 98, 182, 316, 529, 870, 1416, 2283 and 3656 m.

B. MODEL EQUATIONS

Developed by Haney (1974, 1985) and then adapted by Batteen (1989) and Batteen et al. (1989), the primitive equation (PE) model applies to baroclinic, limited area, eastern boundary current regions with open north, west, and south borders. It has been successfully used to study the Leeuwin Current region off Western Australia by Batteen and Rutherford (1990) and Batteen et al. (1991). This full primitive equation (PE) model, integrates in time from a specified initial condition and incorporates the full non-adiabatic physics of both dynamic and thermodynamic processes. The hydrostatic and traditional assumptions characteristic of PE models (Phillips, 1966) are invoked. The Boussinesq approximation, which assumes that the ocean is incompressible and that density variations are important only when involving buoyancy force calculations (Phillips, 1969), is applied. There are no major salinity sources or sinks in the model domain, so temperature is the dominant factor in density variations and static stability. Following Batteen and Rutherford (1990), the salinity values from Levitus (1982) have a range of only 35.6 ± 0.2 psu over most of the domain in the upper five layers; therefore, density is allowed to vary only as a function of temperature. The model is capable of either f -plane or β -plane dynamics. To allow for the propagation of Rossby waves in this study, the β -plane approximation is made for all cases. Friction forces and surface thermal forcing are

assumed to be either known functions or expressible in terms of the other variables. The governing equations are:

Equations of Motion:

$$\frac{du}{dt} = \frac{-1}{\rho_0} \frac{\partial p'}{\partial x} + f v - A_H \nabla^2 u + K_H \frac{\partial^2 u}{\partial z^2} + \delta_d(u) \quad [3.1]$$

$$\frac{dv}{dt} = \frac{-1}{\rho_0} \frac{\partial p'}{\partial y} - f u - A_H \nabla^2 v + K_H \frac{\partial^2 v}{\partial z^2} + \delta_d(v) \quad [3.2]$$

$$w = - \int_{-H}^z \left(\frac{\partial u}{\partial x} + \frac{\partial v}{\partial y} \right) dz \quad [3.3]$$

Hydrostatic Equation:

$$p' = \int_z^0 \rho g dz - \frac{1}{H} \int_{-H}^0 \left(\int_z^0 \rho g dz \right) dz \quad [3.4]$$

Equation of State:

$$\rho = \rho_0 (1 - \alpha (T - T_0)) \quad [3.5]$$

First Law of Thermodynamics:

$$\frac{dT}{dt} = -A_H \nabla^2 T + K_H \frac{\partial^2 T}{\partial z^2} + Q_S + \delta_d(T) \quad [3.6]$$

In the above equations, (x, y, z) is a right-handed coordinate system (x positive eastward, y positive northward, and z positive upward) with corresponding velocity components (u, v, w) . The other variables are denoted as time (t) , temperature (T) , density (ρ) , and the departure from the vertically averaged pressure (p') . The depth-averaged pressure is assumed to be zero, i.e., the barotropic mode is ignored. In equations [3.1] and [3.2], f is the Coriolis parameter and, in equations [3.3] and [3.4], z is a dummy variable of integration. Table 3.1 provides a list of pertinent symbol definitions and Table 3.2 identifies constants and their assigned values. The governing equations above comprise a system of six

scalar equations and six unknowns (u, v, w, ρ, p, T). The prognostic variables are u, v, T and the diagnostic variables are p, w, ρ .

C. BOUNDARY CONDITIONS

The eastern boundary of the model domain represents a coastal boundary which the model simulates as a straight, vertical wall. On this boundary,

Table 3.1 MODEL SYMBOL DEFINITIONS

	Value	Description
K	Equation 4.1	Kinetic energy
P	Equation 4.4	Potential energy
p	Equation 4.15	pressure, with respect to a designated reference level
Q_B	Equation 3.9, 3.22	Net upward longwave radiation
Q_S	Equation 3.21	Sensible heat flux
Q_E	Equation 3.21	Latent heat flux
S_0	Equation 3.19	Solar radiation at sea surface
S_0^*	Equation 3.19	Downward flux of solar radiation
S_A^*	Equation 3.20	Flux of solar radiation at top of atmosphere
$ V $	Equation 3.23	Wind speed
\mathbf{v}	Equation 4.9	Horizontal velocity vector
$\overline{w'T'}$	Equation 3.21	Surface generated heat flux
γ	Equation 3.13	Geostrophic inflow angle
δ	Equation 3.1	Dynamic adjustment term
ζ	Equation 4.12	Relative vorticity
τ	Equation 3.7	Wind stress
ϕ	Equation 4.14	Geopotential anomaly

a closed boundary for all fluxes consequently results, consistent with the kinematic boundary condition of no flow through the boundary (imposed on cross-shore velocity). A no-slip boundary condition applies to velocity in the alongshore direction.

The north, west, and south open boundaries employ modified radiation boundary conditions based on Camerlengo and O'Brien (1980). Inflow/outflow for a prognostic variable at a boundary gridpoint is determined by the sign of a dynamically computed effective group velocity. An inflow value at a boundary gridpoint stays the same as the value in the

Table 3.2 VALUES OF CONSTANTS USED IN THE MODEL

	Value	Name
A_H, A_M	$2.0 \times 10^{17} \text{ cm}^4 \text{ s}^{-1}$	Biharmonic heat, momentum diffusion coefficients
C	$0.958 \text{ cal gm}^{-1} \text{ }^\circ\text{K}^{-1}$	Specific heat of sea water
C_D	1.22×10^{-3}	Bottom drag coefficient
C_d	1.3×10^{-3}	Atmospheric drag coefficient
C_H	1.757×10^{-3}	Heat exchange coefficient
C_p	$0.24 \text{ cal g}^{-1} \text{ }^\circ\text{C}^{-1}$	Specific heat of dry air
$D \text{ or } H$	$4.5 \times 10^5 \text{ cm}$	Total ocean depth
e_s	20.8 mb	Saturation vapor pressure (T_s)
e_a	16.49 mb	Atmospheric vapor pressure
g	980 cm s^{-2}	Acceleration of gravity
K_H, K_M	0.5 cm s^{-1}	Vertical eddy conductivity, viscosity
L	595 cal gm^{-1}	Latent heat of sea water
n	0.65	Fractional cloud cover
	5%	Reflectivity of sea surface
	26%	Reduction of insolation by atmospheric absorption
P_A	1013.25	Sea level atmospheric pressure

previous time step, while an outflow value for the same gridpoint is set to the value at the nearest interior gridpoint.

Vertical boundary conditions invoked include a rigid-lid approximation to filter out external gravity waves, permitting a longer time step ($\Delta t = 800 \text{ s}$), and the assumption of a flat constant-depth bottom. The surface

Table 3.2 continued.

	Value	Name
T_0	278.2° K	Constant reference temperature
T_a	298.0° K	Ambient air temperature
T_s	21.5° C	Sea surface temperature
α	$2.01 \times 10^{-4} \text{ } ^\circ\text{K}^{-1}$	Thermal expansion coefficient
Δt	800 s	Time step
Δx	$9.0 \times 10^5 \text{ cm}$	Zonal grid spacing
Δy	$25.0 \times 10^5 \text{ cm}$	Meridional grid spacing
ρ_a	$1.23 \times 10^{-3} \text{ gm cm}^{-3}$	Density of air at sea level
ρ_0	$1.0276 \text{ gm cm}^{-3}$	Density of sea water at T_0
σ	1.35×10^{-12}	Stefan-Boltzmann constant

($z = 0$) boundary conditions are represented by:

$$K_H \frac{\partial u}{\partial z} = \frac{\tau_x}{\rho_0} \quad [3.7]$$

$$K_H \frac{\partial v}{\partial z} = \frac{\tau_y}{\rho_0} \quad [3.8]$$

$$K_H \frac{\partial T}{\partial z} = -Q_B \quad [3.9]$$

$$w = 0 \quad [3.10]$$

The tau (τ) components are surface wind stress components. The Q_B term represents the net upward flux of longwave radiation, sensible and latent heat across the sea surface.

The bottom ($z = -H$) boundary conditions are represented by:

$$K_H \frac{\partial T}{\partial z} = 0 \quad [3.11]$$

$$K_B \frac{\partial u}{\partial z} = C_D (u^2 + v^2)^{1/2} (u \cos \gamma - v \sin \gamma) \quad [3.12]$$

$$K_B \frac{\partial v}{\partial z} = C_D (u^2 + v^2)^{1/2} (v \cos \gamma + u \sin \gamma) \quad [3.13]$$

$$w = 0. \quad [3.14]$$

These conditions specify zero vertical velocity, zero vertical heat flux, a flat bottom and a bottom drag coefficient in conjunction with a geostrophic inflow angle (γ) for a simple parameterization of a bottom Ekman layer (Weatherly, 1972). The imposition of a flat bottom boundary condition, while not particularly realistic, permits, in this process-oriented study, the isolation of wind forcing effects, and eliminates topographic wave effects and the joint effects of baroclinicity and bottom relief (JEBAR). Although Weaver and Middleton (1988, 1989) needed the presence of a sloping shelf to trap a linear eastern boundary current, Weaver and Middleton (1989) also demonstrated that topography was not necessary for trapping the eastern boundary current in a nonlinear model. The inclusion of coastline features and bottom topography, and an examination of their influence on the Leeuwin Current and its eddies, is considered a separate study.

D. FINITE DIFFERENCING

Following Arakawa and Lamb (1977) and Batteen and Han (1981), this model uses a B-scheme space staggered grid, with (u, v) and (T, w, p, ρ) variable groupings offset in the model's grid. The eastern boundary of the grid lies on temperature points which avoids possible lateral momentum leaks (Haney, 1974; Semtner and Mintz, 1977). The model is vertically staggered: (u, v, T, ρ) are at each of the ten prescribed levels, while (w, p) are located between these levels, with $(w = 0)$ at the ocean surface ($z = 0$) and at the bottom ($z = -H$).

E. HEAT AND MOMENTUM DIFFUSION

One of the objectives of this study is to investigate the development of mesoscale eddies. This can influence the choice of diffusion mechanisms. Laplacian lateral heat diffusion suppresses mesoscale eddy formation by diminishing the baroclinic signal at the eddy scale and,

consequently, any baroclinic instability dominance over diffusive damping (Holland and Batteen, 1986). The biharmonic diffusion of both heat and momentum used in this model allows for the formation of mesoscale instabilities by applying damping only at scales smaller than the eddies (Holland, 1978). Weak vertical eddy viscosities and vertical eddy conductivities are also employed (see Table 3.1), where the choices for the coefficients are the same as in Batteen et al. (1989) and Batteen and Rutherford (1990). Vertical turbulent mixing of heat and zonal and meridional momentum due to surface layer processes is represented in equations [3.1], [3.2], and [3.6] with a dynamic adjustment mechanism (δ), based on a generalization of the convective adjustment mechanism. The underlying assumption employs a critical Richardson number for the maintenance of water column dynamic stability (Adamec et al., 1981).

F. SURFACE THERMAL FORCING

Simplifying the surface thermal forcing allows the study to focus on wind and oceanic forcing mechanisms. By choosing an air temperature that forces the total heat flux, $S_0 - Q_E$, across the sea surface to equal zero at the initial time, any fluctuations in Q_E can be attributed to wind/oceanic-forced perturbations in the sea surface temperature (Haney et al., 1978; Batteen et al., 1989). Consistent with Batteen and Rutherford (1990), the air temperature required and used for a zero initial heat flux in all experiments is 298° K.

The surface heating due to solar radiation, Q_s in equation [3.6], is a function of depth,

$$Q_s = \frac{1}{\rho_0 C} \frac{\partial S}{\partial z} \quad [3.15]$$

with

$$S = S_0 (R e^{-\frac{z}{z_1}} + (1-R) e^{-\frac{z}{z_2}}) \quad [3.16]$$

The downward flux of solar radiation at the surface (S_0) is attenuated over depth following Paulson and Simpson (1977), where $R = 0.62$ is the fraction of solar radiation absorbed through depth $z_1 = 1.5$ m. The remainder, $(1 - R) = 0.38$, penetrates deeper and is absorbed by depth $z_2 = 20.0$ m. Following Haney et al. (1978),

$$S_0 - (\overline{w'T'}) = 0 , \quad [3.17]$$

where:

$$S_0 = \frac{S_0^*}{\rho_0 C} \quad [3.18]$$

$$S_0^* = 0.95 (0.74 - 0.6n) S_A^* \quad [3.19]$$

$$S_A^* = 3.642 \times 10^{-3} \quad [3.20]$$

and

$$(\overline{w'T'})_0 = \frac{(Q_B + Q_S + Q_E)}{\rho_0 C} \quad [3.21]$$

$$Q_B = 0.985 \sigma (T_g)^4 \times (0.39 - 5.0 (e_g)^{\frac{1}{2}}) (1 - 0.6n^2) \quad [3.22]$$

$$Q_S = \rho_a C_H C_p |V| (T_g - T_a) \quad [3.23]$$

$$Q_E = \rho_a C_H L |V| \left(\frac{0.622}{p_a} \right) (e_g - e_a) . \quad [3.24]$$

The variables in the above equations are identified in Table 3.1. Input values for T_g , n , p_a , e_g , specific humidity and relative humidity (for computing e_a) are taken from USSR Ministry of Defense (1979). Solar insolation values are from List (1951). Steady solar insolation ($595.5 \text{ cal cm}^{-2} \text{ day}^{-1}$) is applied in this process oriented study to more clearly isolate the effects of seasonal wind and ocean thermal forcing.

G. MODEL INITIALIZATION

The thermal profile differences between the two sets of experiments, annual average forcing versus seasonally varying forcing, dictated two choices for initialization to avoid an unrealistic "shock start" to the numerical model, as explained below. When conducting experiments involving annual average oceanic thermal forcing, the annual average temperature climatology from Levitus (1982) provided initialization values. However, when examining the seasonal cycle, it was necessary to choose one of the seasonal climatologies as the starting point. Levitus (1982) provided quarterly temperature climatologies to describe the upper 250 m of the model ocean and annual average climatology for filling the model levels below this depth. The September climatology was chosen for the initialization of seasonal experiments. The rationale for starting the model after the primary surge of the seasonal Leeuwin Current, February through August (Church *et al.*, 1989; Weaver and Middleton, 1989), was to allow the model to geostrophically adjust prior to the period of interest, i.e., the austral summer transition to austral autumn when the Leeuwin Current begins its surge.

A linear spatial interpolation was applied to the Levitus (1982) data. Zonally averaged values were computed for the north and south grid boundaries for each model level, linearly interpolating vertically to extract model level values from the data levels. To fill the interior grid values, the north-south thermal gradient was approximated with a meridional linear interpolation for each model level. These conditions simulate the general eastern Indian Ocean environment. Data immediately adjacent to the coast was not incorporated into the initialization because these values reflect advection by the Leeuwin Current and they distort the representation of open ocean geostrophic inflow forcing. Rather, the model is allowed to evolve the eastern boundary thermal characteristics since these are a focus of this study. Figures 3.1 and 3.2.a provide the annual mean and the August-September-October seasonal temperature profiles used as the initial conditions for the annual mean and seasonal cases, respectively.

H. OCEAN THERMAL FORCING

Previous efforts at numerically modeling the Leeuwin Current have started with an imposed initial condition, and have then allowed the model to evolve in the absence of external thermal forcing, with and without wind forcing (Weaver and Middleton, 1989; Batteen and Rutherford, 1990; Batteen *et al.*, 1991). These studies focused on the existing thermohaline structure of the eastern Indian Ocean and its ability to create a Leeuwin

Current type of flow. Weaver and Middleton (1989) examined the response of a linear and nonlinear closed-basin models, while Batteen and Rutherford (1990) studied a nonlinear, open-boundary system. The model in this study follows Batteen and Rutherford (1990), but differs by applying a steady rather than initialized thermal forcing, simulating the persistent equator-to-pole thermal gradient found in the open eastern Indian Ocean.

Forcing is applied by continuously specifying the north and south boundary temperatures only along the open ocean segment of these two grid boundaries while leaving a segment of normal open boundary conditions nearest the coast (Figure 3.3). Because, in the mid-latitudes, density is principally determined by temperature (McCreary et al., 1986), no attempt is made to compensate for meridional variations in salinity (Batteen and Rutherford, 1990). The interior is allowed to adjust in response to the boundary conditions. A linear interpolation smoothes the transition between the forced and unforced segments. This forcing method allows thermal advection by the Leeuwin Current to smoothly exit the domain instead of pooling at the poleward coastal corner (inhibited outflow caused by a mismatch between the poleward advected isotherms and any specified temperature boundary conditions). The purpose of the continuous thermal forcing is to more realistically represent the continuous forcing of the Leeuwin Current due to geostrophic inflow. Previous studies without continuous forcing observed only the initial geostrophic adjustment of the model used. The equator-to-pole thermal gradient eventually diminishes with increasing simulated time. Since one of the objectives of this study is to examine the cycle of the Leeuwin Current over a typical year, it is necessary to apply the continuous thermal forcing.

For the cases forced with the annual average temperature profile, the forced segments of the north and south boundaries are not permitted to change with time. When conducting the seasonally-changing experiments, the north and south boundary values were linearly interpolated in time from one season to the next, with the seasonal magnitude achieved at the midpoint of each season. The linear interpolation approach was chosen for simplicity because the seasonal cycle of thermal variation is not symmetrical and the cycle of each level at each boundary is different. The boundary forcing values for the upper four model layers increment each model day while the lower six layers are held constant.

Time-varying only the upper layers is consistent with other studies (e.g., Hamon, 1965; McCreary et al., 1986; Smith et al., 1991). The north-south pressure gradient forcing for the Indian Ocean geostrophic

inflow, the principle forcing mechanism for the Leeuwin Current (Weaver and Middleton, 1989), is contained in the thin layer above the thermocline, as in McCreary et al. (1986) and Thompson (1987). The Leeuwin Current, strongest at the surface, diminishes to near zero at only 150 m, which closely correlates with the thermocline (Thompson, 1987). Leeuwin Current Interdisciplinary Experiment (LUCIE) data indicate near zero flow at approximately 200 to 250 m (Smith et al., 1991). Below this depth, the pressure gradient reverses. This shallow character of the Leeuwin Current flow permits forcing of the model with time-varying temperatures in only the upper four model layers (the fourth layer being at 182 m depth). Figures 3.1 and 3.2.a - 3.2.d provide the meridional temperature profiles for the annual mean and the four seasons, respectively, while Figure 3.4 shows the north-south temperature difference versus time for each of the ten model levels.

The North West Shelf (NWS) waters provide a significant influx of warm tropical water to the Leeuwin Current. Weaver and Middleton (1989), Batteen and Rutherford (1990), and Batteen et al. (1991) model the NWS water as a horizontally homogeneous raft of warm water that is allowed to interact with the rest of the domain starting at the initial time ($t = 0$). This study employs the same choice as Batteen and Rutherford (1990) for the NWS temperature profile (Table 3.3), which incorporates an equivalent temperature to compensate for variations in density due to significant NWS

Table 3.3 TEMPERATURE PROFILE: NORTH WEST SHELF WATERS

Layer	Temperature (°C)
1	29.5
2	28.5
3	26.0
4	20.5
5	15.7

deviations from a mean salinity of 35.6 psu. This modeling approach simulates a "dam breaking" and it follows from the hypothesis of flow reversals isolating water on the NWS, then releasing it to flow poleward as presented by Gentilli (1972) and supported by Church et al. (1989).

The dam breaks are believed to be a function of switching between monsoonal wind regimes combined with a sudden large change in the north-

south thermal gradient. The timing of the dam break can be inferred from the onset of the Leeuwin Current surge in the austral autumn. Figure 3.5, from Godfrey and Ridgway (1985), illustrates the seasonal cycle of the net pressure gradient and wind stress forcing, and suggests that the dam break could be initiated when the net forcing becomes poleward, which is usually in mid-March. This study simulates the dam break by inserting the NWS profile only once on a chosen day, and then letting the model evolve through geostrophic adjustment. When adding the NWS waters to the model, the velocity fields are not specified. All adjustments to the existing velocity fields are made by the model in response to the inserted thermal forcing. This method closely follows the approach of Weaver and Middleton (1989), Batteen and Rutherford (1990), and Batteen et al. (1991). The major difference introduced by this study is that the NWS water is now merging with an already-complex ocean environment. The influence of the added flow can be more clearly isolated, in contrast to earlier stages where the large initial adjustment of the previous studies could obscure the NWS-induced features.

I. WIND FORCING

The shallow nature of the Leeuwin Current and the NWS waters support the hypothesis that the flow fluctuations can be significantly driven by the wind forcing; as such, wind forcing could play an important role. The wind forcing for this study was extracted from the mean annual cycle in surface wind stress over the global oceans derived from the European Centre for Medium Range Weather Forecasts (ECMWF) surface wind analyses, covering seven years (1980-86) (Trenberth et al., 1990). This 80-month climatology data set provides both climate annual mean and climate monthly means for zonal and meridional winds, mean stress in the x and y directions, the mean of the wind stress curl, and the annual mean and monthly mean standard deviations for each of these parameters. The data sets have been computed on a $2.5^\circ \times 2.5^\circ$ grid, based upon twice-daily 1000 mb wind analyses from the ECMWF (Trenberth et al. 1990). The extracted data require no smoothing or conversion to the wind speed input used by the model. The wind velocity component data for the model domain were linearly interpolated onto the 65×65 model grid.

In these experiments, the annual mean wind forcing was superimposed on the annual mean ocean thermal forcing; likewise, the monthly-mean wind cycle forcing was superimposed on the seasonally-varying ocean thermal forcing which is applied at the boundaries. A constant wind forcing of the ocean surface with annual mean wind values provides a basis for comparison with the monthly-varying wind forcing case. For the

experiments conducted with the monthly mean climatologies, the model incremented the wind values each model day along a temporal linear interpolation from one monthly mean to the next. The daily increments do not imply daily climatologies, but rather are strictly linear interpolations for a smooth model transition between the monthly mean climatologies. At model initiation ($t = 0$), the monthly-mean wind cycle is set to begin in mid-September, coordinating with the arbitrarily chosen beginning of the ocean thermal cycle, which is the middle of the Levitus (1982) August-September-October quarter. Trenberth et al. (1989a) provides appropriate values for the drag coefficient (C_d) over the world's oceans. For the various seasons, the value of C_d in the model's domain remains close to 1.3×10^{-3} , which matches the choice used by Batteen and Rutherford (1990) and Batteen et al. (1991).

Unlike McCreary et al. (1986) and Batteen et al. (1991), wind-band forcing is not used; instead wind forcing is applied at all surface grid points and at all time steps. The wind data represents a realistic wind field rather than an idealized wind forcing regime. (Recommended by McCreary (1981) and used by McCreary et al. (1987), Batteen et al. (1989), and Batteen et al. (1991) to produce a realistic undercurrent rather than a surface current that simply deepens with time, the artifice of alongshore wind band forcing is not necessary due to both spatial and temporal variability of the applied wind forcing. This artifice allows for the propagation of coastal Kelvin waves which, thereby establish the alongshore pressure gradient field, with the result that a surface-trapped coastal jet and a relatively realistic undercurrent are generated (McCreary, 1981; McCreary et al., 1987; Batteen et al., 1989).

J. EXPERIMENT DESIGN

Four principle cases are examined to isolate the seasonal influences. Case 1 provides a reference for the subsequent cases through consideration of only the effects of continuous forcing by the annual-mean, ocean thermal climatology. Wind forcing is ignored. This case is most similar to previous experiments (Weaver and Middleton, 1989; Batteen and Rutherford, 1990; etc.), but now the model is continuously forced and the model run extends out for a model year.

Case 2 is designed to reveal the nature of the influence from a seasonally-varying ocean thermal structure. This case idealistically models the Leeuwin Current region for a model year by using linearly-interpolated time variations of the ocean thermal structure, derived from Levitus' (1982) seasonal climatologies, to continuously force north and south grid boundary segments in the upper four model layers. The initial

condition for this case was set to match the climatological values for the August-September-October season (Levitus, 1982), with mid-September designated as the starting date. There is no wind forcing in this case. The lower six model layers are continuously forced with annual-mean climatology along the same north/south grid boundary segments.

Case 3 uses the same ocean thermal forcing design as Case 1, but now the model is additionally forced with the regional annual-mean winds derived from Trenberth et al. (1990). Through a comparison with Case 1, this case should illustrate the effects of annual-mean wind forcing, highlighting the net effect of wind versus thermal forcing.

Case 4 adds linearly time-interpolated, monthly wind climatologies from Trenberth et al. (1990) to the seasonal thermal forcing regime described in Case 2. The initial wind conditions match the September monthly climatology, and mid-September is used for the starting date to correlate with the ocean thermal forcing. This case should best describe the complex interaction of seasonal influences.

Additional cases explore the added influence of the North West Shelf (NWS) waters. These cases, Cases 5 through 8, simply superimpose the NWS "dam-breaking" analogy on each of the first four cases, respectively. The release of NWS water is set for the model's mid-March time frame. The NWS forcing consists of a one-time initialization of a "raft" of NWS water (Table 3.3) in the coastal equatorward corner of the model domain. The model is then permitted to evolve without any further manipulation of the NWS water mass or the resulting flow regime. The purpose of these cases is to examine the net effects of synchronizing the NWS forcing with the seasonal ocean thermal and wind forcing.

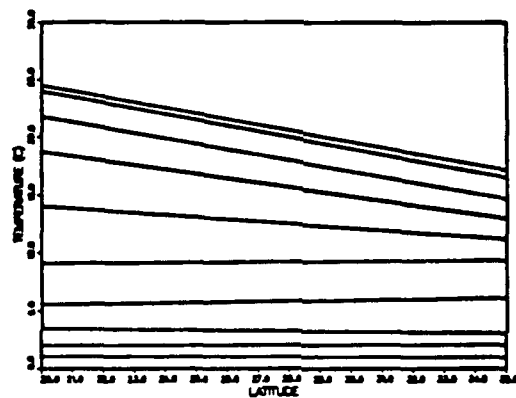


Figure 3.1 Annual mean temperature gradient: Initial meridional temperature ($^{\circ}\text{C}$) structure and continuously-forced annual mean temperature gradient. Isolines represent model levels. Each level is initially zonally homogeneous.

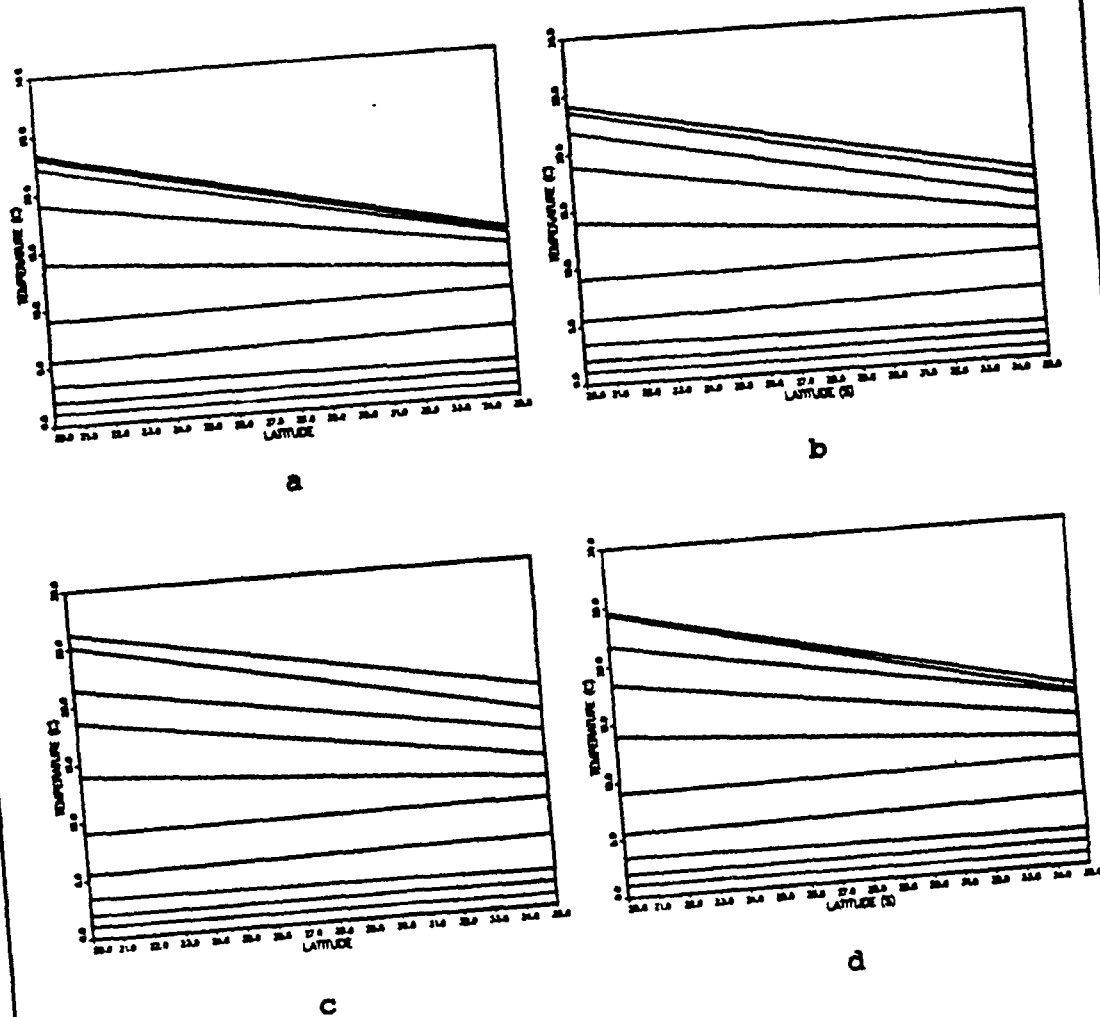


Figure 3.2 Seasonal mean temperature gradients: (a) Initial seasonal zonally-homogeneous meridional thermal structure (isolines represent model levels). Seasonal thermal forcing gradients (a) Aug-Sep-Oct, (b) Nov-Dec-Jan, (c) Feb-Mar-Apr, (d) May-Jun-Jul.

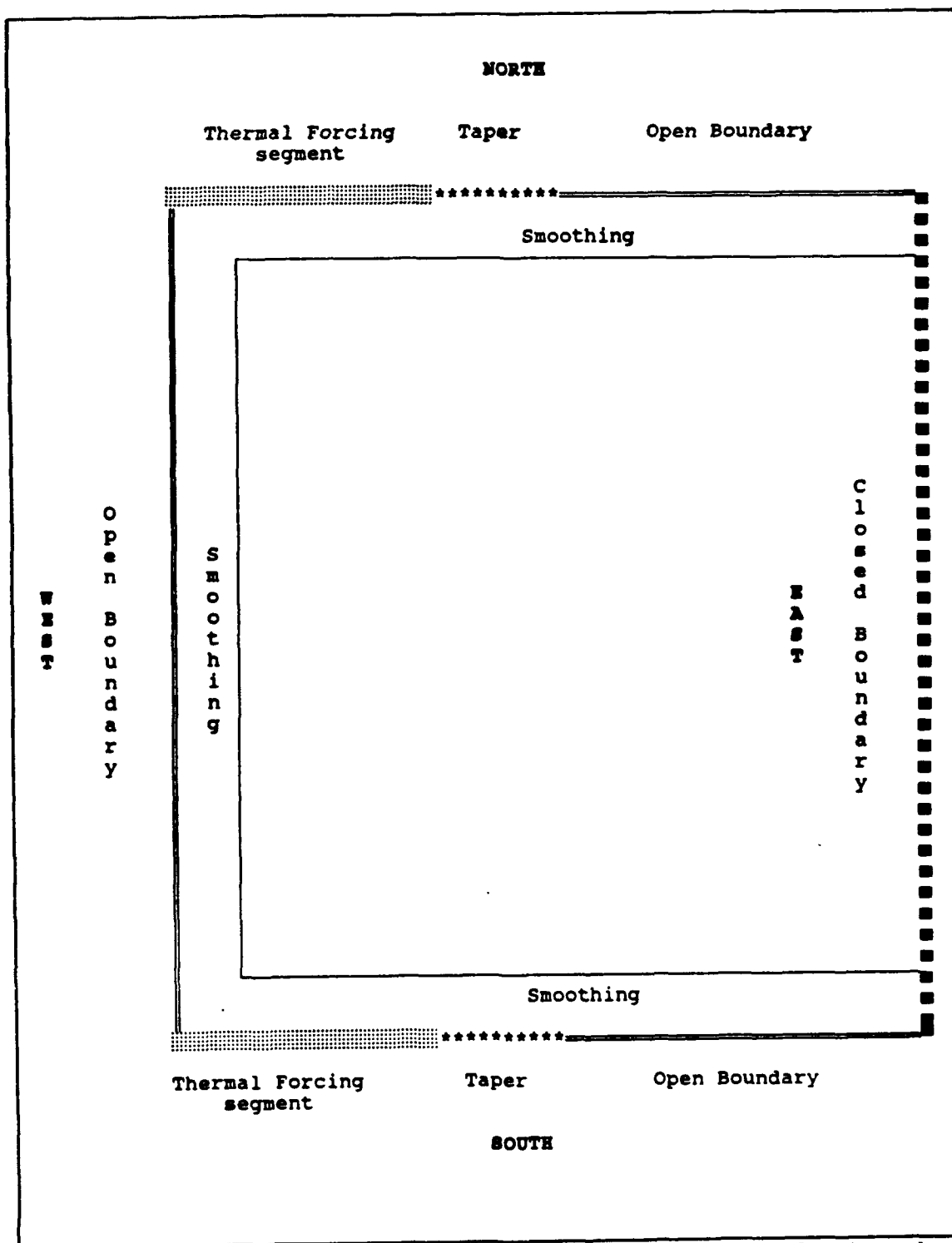


Figure 3.3 Model boundary and forcing diagram: Thermal forcing along indicated segments of northern and southern model boundaries. Linear taper scheme used to merge with unforced segments.

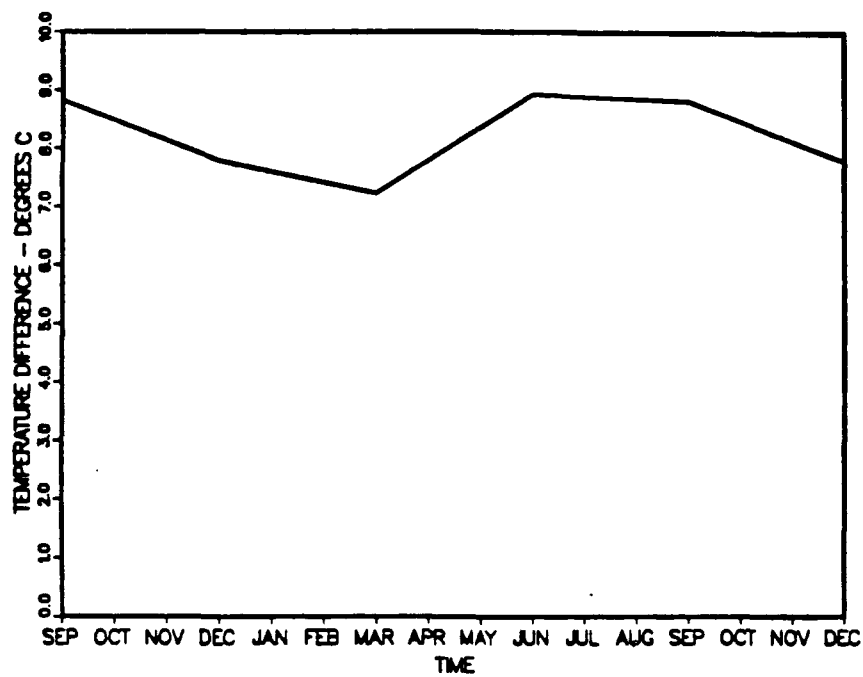


Figure 3.4 Imposed seasonal meridional temperature difference versus time for model domain (20° S to 35° S).

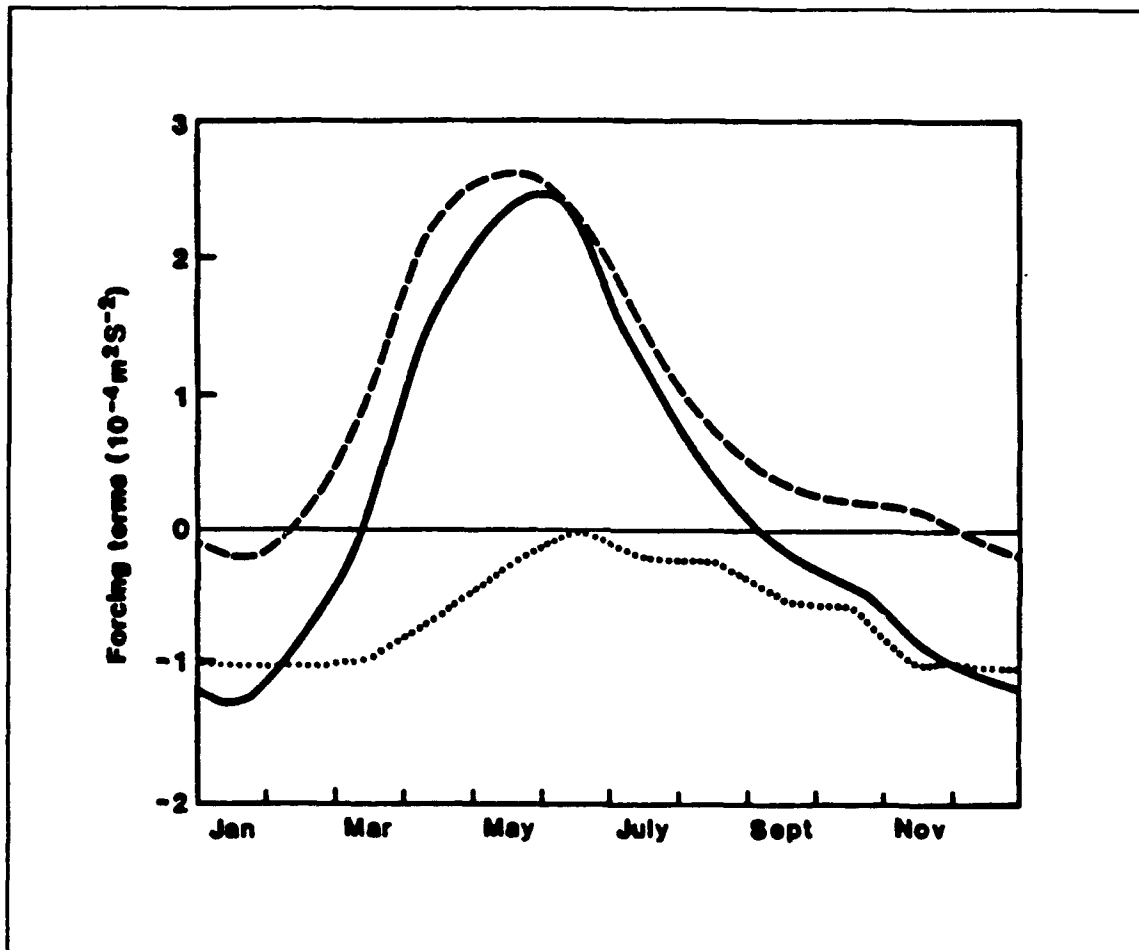


Figure 3.5 Annual cycle of net forcing for the Leeuwin Current: Dashed line, observed pressure gradient forcing; dotted line, wind stress; solid line, net forcing (from Godfrey and Ridgway, 1985).

IV. ANALYSIS TECHNIQUES

The principal relationships, assumptions, and procedures highlighted below follow the techniques for energy distribution and transfer analysis, spectral analysis, and stability analysis presented by Batteen and Rutherford (1990). Following this, a method for comparing the relative strengths of geostrophic versus surface Ekman flow is described.

A. ENERGY ANALYSIS

The approach, used by Batteen and Rutherford (1990), of separating time-mean and transient motions, has proven useful for understanding energy interactions between the time-averaged flow and mesoscale eddies. Available potential energy is addressed rather than total potential energy. Time-mean and transient equations for available potential energy and kinetic energy are formed for each layer. Both baroclinic (vertical shear) and barotropic (horizontal shear) instabilities can form. Baroclinic instability, measured locally as a positive correlation between w' and T' , describes the transformation of eddy available potential energy into eddy kinetic energy (Equation 4.7). Barotropic instability is measured as a positive transformation of mean kinetic energy into eddy kinetic energy (Equation 4.9).

Han (1975) and Semtner and Mintz (1977) provide a foundation for understanding the energy transfers in an unstable flow. This study uses the Semtner and Mintz (1977) notation:

$\overline{(\quad)}$ time average,

$(\quad)'$ time deviation,

$\overline{(\quad)}$ horizontal space average, and

$(\quad)^*$ horizontal space deviation.

1. Kinetic Energy

Kinetic energy (K) is calculated by:

$$K = \frac{u^2 + v^2}{2} . \quad [4.1]$$

The kinetic energy is plotted in a time series to determine when a quasi-steady state, as defined by a nearly constant value of kinetic energy, is reached. The temporal-mean kinetic energy may then be calculated by:

$$\bar{K} = \frac{(\bar{u})^2 + (\bar{v})^2}{2} . \quad [4.2]$$

The temporal-eddy kinetic energy may be calculated by:

$$K' = \frac{\overline{u'^2} + \overline{v'^2}}{2} . \quad [4.3]$$

2. Available Potential Energy

Available potential energy (P) is calculated by:

$$P = \alpha g \left[\frac{1}{2} (\overline{T'})^2 \left(\frac{\partial \bar{T}}{\partial z} \right)^{-1} \right] \quad [4.4]$$

and, similar to the kinetic energy analysis, plotted in a time series to determine when a quasi-steady state is reached. The time-mean and time-eddy available potential energies may then be calculated by:

$$\bar{P} = \alpha g \left[\frac{1}{2} (\overline{T'})^2 \left(\frac{\partial \bar{T}}{\partial z} \right)^{-1} \right] \quad [4.5]$$

$$P' = \alpha g \left[\frac{1}{2} \overline{(T')^2} \left(\frac{\partial \bar{T}}{\partial z} \right)^{-1} \right] . \quad [4.6]$$

3. Energy Transfers

Following the notation of Semtner and Mintz (1977), as did Batteen and Rutherford (1990), the transfers between energy types are defined as below:

$$\{\bar{K} - \bar{P}\} = -\alpha g [\bar{T} \bar{w}] \quad [4.7]$$

$$\{P'-K'\} = \alpha g [\overline{T'w}] \quad [4.8]$$

$$\{\overline{K}-K'\} = \overline{v} \cdot \left(\nabla \cdot \overline{v'v'} + \frac{\partial}{\partial z} \overline{w'v'} \right) \quad [4.9]$$

$$\{\overline{P}-P'\} = \alpha g \left[\overline{T'} \nabla \cdot \overline{v'T'} \left(\frac{\partial \overline{T'}}{\partial z} \right)^{-1} \right]. \quad [4.10]$$

The stored model output consists of only horizontal velocity components and temperature. Consequently, the calculation procedures for energy transfers, which require both vertical velocity and numerous advection terms, must recompute the appropriate values from the stored values of u , v , and T . By using the same procedures as in the original model calculations, the recomputed energy values are consistent with the values initially obtained during the model run.

For those periods in which the total kinetic and available potential energies are nearly constant, energy transfer diagrams can be constructed by combining the calculated energy transfers with the temporal-mean and eddy values for both kinetic and available potential energy. Following the Semtner and Mintz (1977) energy transfer analysis for currents that had become unstable, generated eddies, and then reached a quasi-steady state, Batteen and Rutherford (1990) examined the steady energetic state prior to eddy generation. Using energy transfer plots and diagrams, Batteen and Rutherford (1990) argue for the instability mechanism, i.e., baroclinic or barotropic instability, that led to the initial eddy generation in each case.

B. SPECTRAL ANALYSIS

The applied spectral analysis technique focuses on the dominant wavelengths of eddy growth. Instantaneous spectral density plots during periods of interest show the dominant wavelengths. Three-dimensional time series plots of spectral density versus alongshore wavenumber reveal growth trends. As in Batteen and Rutherford (1990), the alongshore wavenumber is selected based on an assumption of a meridional anisotropic preference for the eddy development. Discrete Fourier transforms are perfectly suited for the model's entire domain, a 64×64 grid of velocity data. A Hanning window reduces the leakage due to finite series length. Appropriate scaling of the calculated one-sided spectral density, by a

factor of 2.0 (Lopes da Costa, 1989), compensates for the loss of variance due to the windowing. This technique favors the determination of the wavenumber with the maximum energy.

As a foundation for the spectral analysis, an examination was made of the longitudinal separation necessary for independent spectral estimates. The procedure that was used to test the independence of estimates compared the coherency of meridional spatial series versus longitudinal separation from an arbitrarily chosen reference meridional series. The reference series was chosen from the general region of the Leeuwin Current, yet separated from the coastal boundary to help reduce any boundary influence. Incrementing by longitudinal grid spacing intervals, the coherency of the test series with the reference series was computed using 256 model days to provide independent estimates of the coherency, resulting in 512 degrees of freedom. The spatial separation necessary to minimize the coherency, yet still provide a reasonable number of spectral estimates for computing instantaneous spectral densities, was five grid points, which equates to a 45 km longitudinal separation between independent spectral estimates. For the 45 km spatial separation, the resolvable spatial frequency spectrum, determined by the dimensions of the model grid, had a maximum coherency (Figure 4.1) of 0.3 with a 95% confidence interval of ± 0.1 (Bendat and Piersol, 1986). The 0.3 value is smaller than $(1/e)$ times 1.0 (perfect coherency), and is accepted as representing independence. The most dynamic case, seasonal thermal forcing only, was used in the determination of this correlation.

Accepting the above level of coherency between independent spectral estimates spaced every fifth gridpoint gives the instantaneous spectral density plot, computed from the entire domain, 26 degrees of freedom; two degrees of freedom for each spectral estimate included in the average. Confidence intervals are then computed, maintaining a five gridpoint separation for independent spectral estimates, based on the width of the subregion being examined.

C. STABILITY ANALYSIS

Batteen et al. (1989) investigated the dynamics of eddy generation, as observed in a PE model, providing the basis for the stability analysis in this study. Potential vorticity (q) of the flow and its cross-shore derivative ($\partial q / \partial x$) determine the potential for instability. The potential vorticity is calculated by:

$$q = (f + \zeta) \frac{\partial T}{\partial z} - \frac{\partial T}{\partial x} \frac{\partial v}{\partial z} , \quad [4.11]$$

where

$$\zeta = \frac{\partial v}{\partial x} - \frac{\partial u}{\partial y} . \quad [4.12]$$

For a flow with a slowly changing basic state, spatial and temporal, Kamenkovich et al. (1986) identify the necessary conditions for baroclinic instability: $\partial q / \partial x$ must change sign, and $\bar{v} \partial q / \partial x$ must be positive somewhere in the flow.

The sufficient condition for baroclinic instability given by Kamenkovich et al. (1986) of a minimum vertical shear is not required for this study because Olivier (1987) showed that, for meridional flow on a β -plane, energy can be released in a meridional flow without being acted upon by β . Therefore, since the mean flow of the model, and of the Leeuwin current, is strongly meridional, any vertical shear which is greater than the dissipation level in the model may produce instability.

For baroclinic instability, the source of energy is the vertical shear in the mean flow ($\partial \bar{v} / \partial z$). The scale of the generated disturbances is of the order of the Rossby radius of deformation. Horizontal shear in the mean flow ($\partial \bar{v} / \partial x$) provides the energy source for barotropic instability. These disturbances grow at a scale less than the Rossby radius.

In summary, using the analysis tools described in the previous sections, the energy transfer analysis locates and identifies the magnitude of baroclinic and barotropic transfers. The spectral analysis verifies the existence of the resulting unstable waves, particularly the fastest growing waves, and identifies their wavelengths.

D. GEOSTROPHIC VERSUS EKMAN FORCING

Examining the relative magnitudes of the geostrophic flow component versus the surface Ekman flow component provides relevant insight into the driving mechanisms for the Leeuwin current and the current's fluctuations. Following Smith et al. (1991), the balance of forces in the x-direction is scrutinized for dominance at the surface by either the wind stress or the pressure gradient force. If the relative acceleration (du/dt) is negligible (i.e. small Rossby number) and since the depth averaged flow in this model is zero, the pertinent equation is:

$$\int_B^0 f u dz = 0 = - \int_B^0 \frac{1}{\rho} \left(\frac{\partial p}{\partial y} \right) dz + \frac{\tau_{wy}}{\rho} - \frac{\tau_{by}}{\rho} , \quad [4.13]$$

which can then be written as

$$0 = \int_B^0 \left(\frac{\partial \phi}{\partial y} \right) dz - \tau_{wy} + C_D |\mathbf{v}| \mathbf{v}, \quad [4.14]$$

where ϕ is the geopotential anomaly (dynamic height), B is the bottom depth, τ_{wy} is the alongshore wind stress, τ_{By} is the bottom stress, C_D is a dimensionless bottom drag coefficient, and \mathbf{v} is the velocity above the bottom boundary layer. The first term on the right-hand side of Equation [4.13] represents the vertically integrated onshore geostrophic transport, while the second term represents the vertically integrated surface Ekman flow. The relative magnitudes of these two terms are compared to identify the dominant surface forcing mechanism. The focus is on near-surface processes because of the shallow nature of the Leeuwin Current. Smith et al. (1991) estimate the geostrophic transport term as:

$$\int_z^0 \left(\frac{\partial \phi}{\partial y} \right) dz = \frac{\partial}{\partial y} \left(\int_z^0 \phi dz \right) = \frac{\partial p}{\partial y}, \quad [4.15]$$

where z represents some depth, preferably a nearly level pressure surface.

McCreary et al. (1986) noted that when the surface density field oscillated at the annual cycle, the density field in the interior ocean is affected only in a thin boundary layer near the surface. Consequently, the resulting pressure gradient field and corresponding geostrophic zonal currents are surface trapped. Hamon (1965), noting the importance of the upper 300m in determining the surface dynamic topography, provides evidence, further supported by Hamon (1972) and Godfrey and Ridgway (1985), that the slope of the 300 dbar surface is minimal. Smith et al. (1991), using data from the Leeuwin Current Interdisciplinary Experiment (LUCIE), also show an essentially level pressure surface at 300 dbar, with the poleward Leeuwin Current in the layer above and an equatorward undercurrent below. Figure 4.2, taken from Smith et al. (1991), shows that the vertically-integrated geopotential anomaly stops increasing at approximately 250 m depth, indicating that a near-level surface exists in this region. By using the 300 dbar pressure surface as a reference level for studying the surface region, a slightly conservative estimate of geostrophic flow will result because the slight decrease in the vertically-integrated geopotential anomaly at that level implies a small reversal of the pressure surface slope. For these reasons, the 300 dbar pressure surface was chosen for the reference level when analyzing the competing influences of geostrophic flow and surface Ekman flow. Figure

4.3 depicts a representative example of the model's 300 dbar pressure surface during both the large, initial adjustment period (day 10) and during the nonlinear feedback period (day 80).

The pressure gradient in Equation [4.13] is simply computed as follows. First, the dynamic height is vertically integrated (referenced to 300 dbar) at each gridpoint from the surface down to the desired level for comparison. Second, the height is converted to a pressure value. Next, the alongshore gradient is computed. Finally, a comparison is made with the climatological monthly mean wind stress.

The surface Ekman flow component of Equation [4.13] was directly extracted from the global wind data set provided by Trenberth et al. (1990). These $2.5^\circ \times 2.5^\circ$ wind stress values were linearly interpolated to the model grid using the same procedures as for the wind velocity data. Because the wind stress values were provided as monthly climatologies, the alongshore pressure gradient values were time-averaged over 30 model days to provide a better basis for comparison. A single alongshore line of the applied, time-varying, pressure gradient forcing and the applied wind stress values is taken for comparison. The wind points are located 162 km from the eastern model boundary, while the pressure gradient is taken in a location representative of the open ocean forcing region. These locations were chosen to more clearly examine the relationship between the open ocean geostrophic flow and the surface Ekman flow, while remaining in essentially the same wind forcing regime present over the Leeuwin Current.

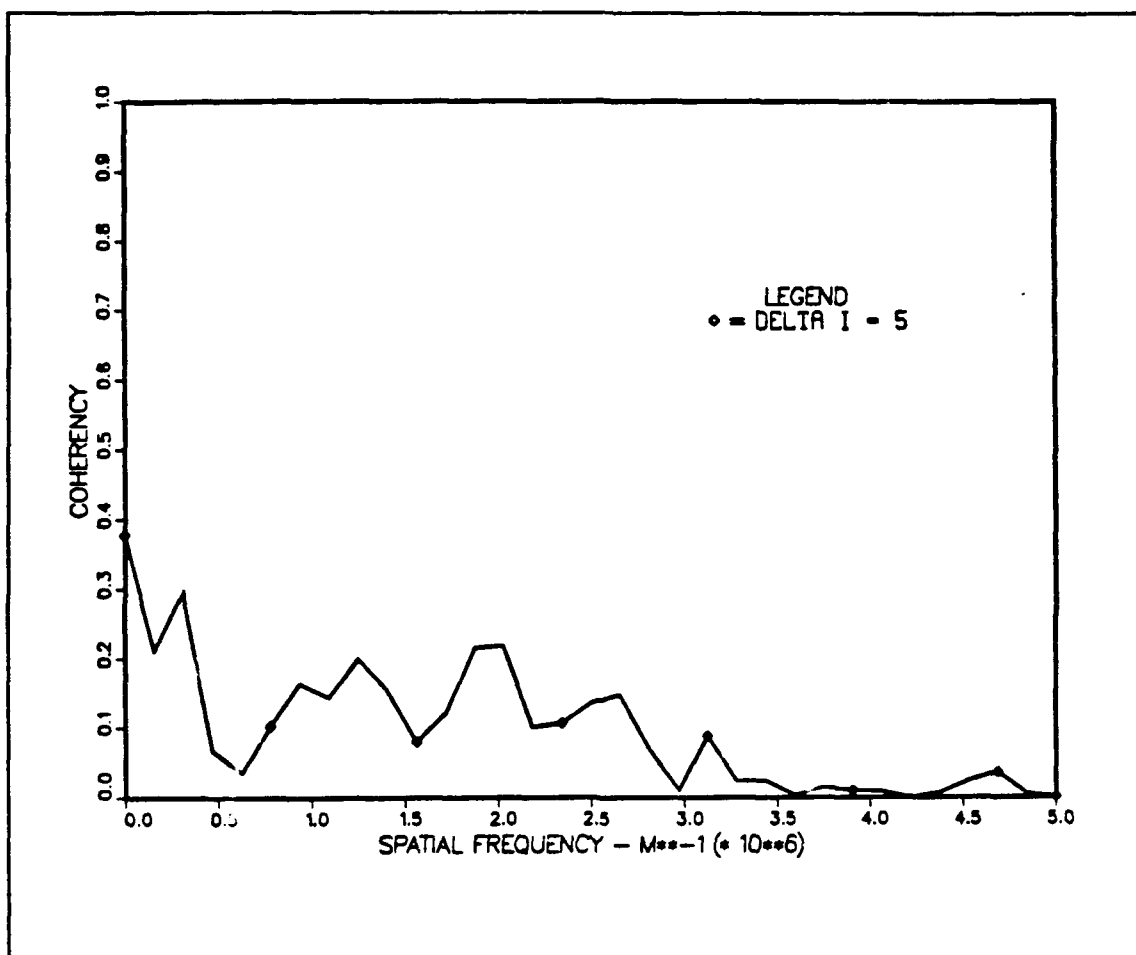


Figure 4.1 Coherency of meridional spatial series versus spatial frequency: The coherency of meridional flow fluctuations is for two meridional series with longitudinal separation of five grid intervals (45 km).

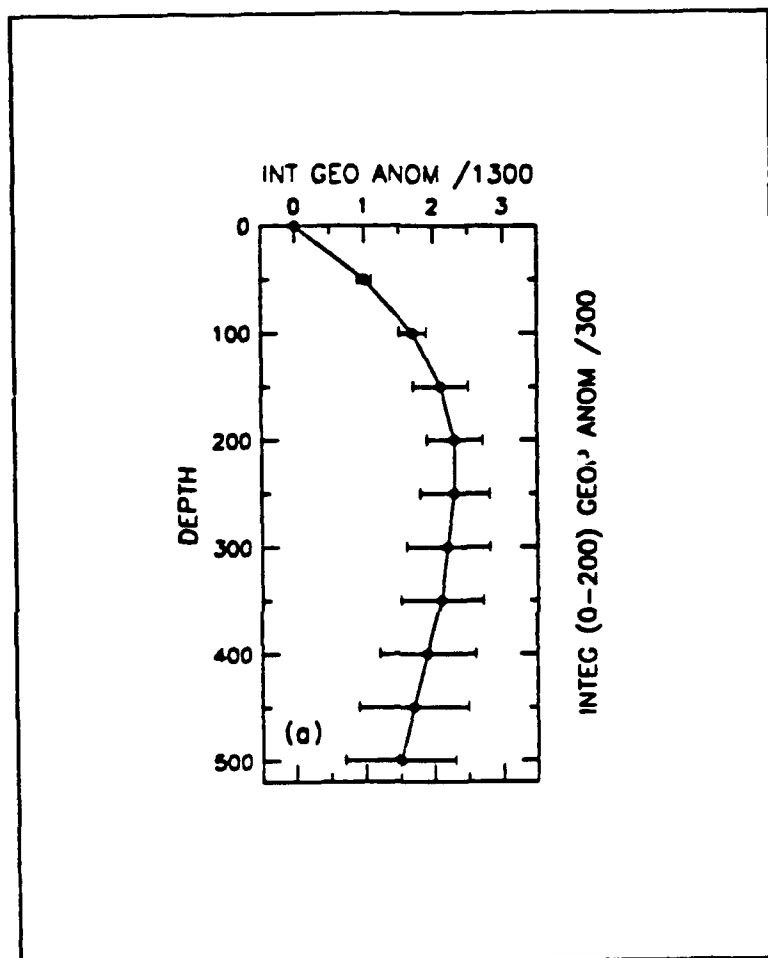


Figure 4.2 Integrated geopotential anomaly versus depth (LUCIE): $\partial p(z)/\partial y$ ($\times 10^{-4} \text{ m}^2 \text{ s}^{-2}$) integrated to depth z with confidence intervals (from Smith et al., 1991).

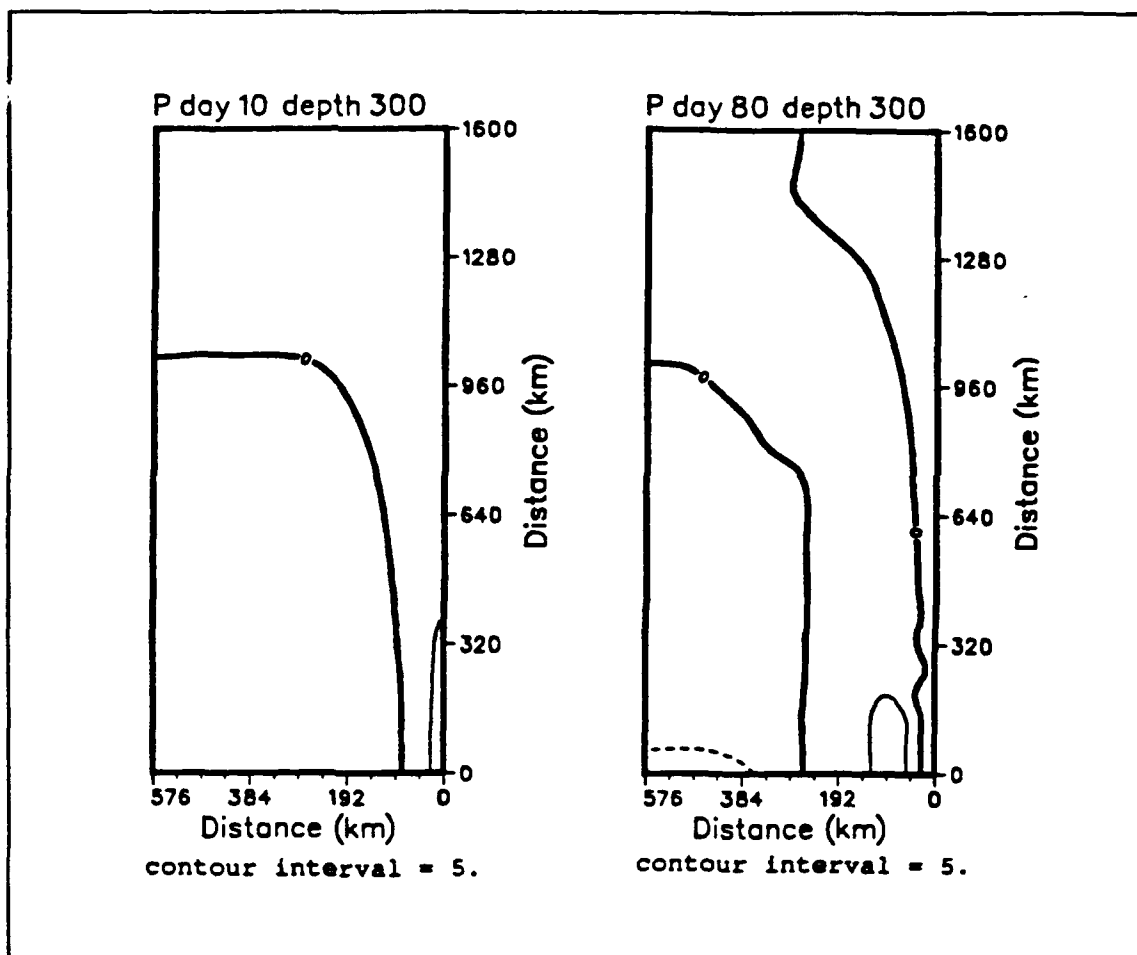


Figure 4.3 Representative 300 dbar pressure surface: Approximate level of no motion (Case 4). Dynamic height anomaly (cm) relative to a reference level of 2000 m depth. Contour interval is 5 cm (negative values are dashed).

V. RESULTS AND DISCUSSION

A. SEASONAL AND ANNUAL MEAN THERMAL FORCING

Examining the magnitudes of the meridional surface temperature gradient across the domain provides insight as to why the annual mean ocean temperature climatology is not particularly representative of the thermal forcing regime off of Western Australia. The annual mean north-south surface temperature difference for the modeled region is 7.36°C while the maximum (minimum) seasonal climatological surface temperature difference is 8.92°C (7.23°C) (Figure 3.4).

An unusual feature of this region is that the seasonal cycle of temperature variation is not symmetrical with respect to the seasons. The minimum and maximum temperature difference seasons (Figure 3.4), February-March-April and May-June-July, are immediately adjacent in time. The maximum temperature difference closely follows the minimum temperature difference, effectively leading to a sudden surge of thermal forcing and a very steep sea-surface slope. The already steep, shelf-edge, sea-surface slope (Figure 2.2) is doubled between January and May (Godfrey and Ridgway, 1985).

The Leeuwin Current, described as being significantly forced by the alongshore pressure gradient with annual variability attributed to wind forcing (McCreary et al., 1986), has previously been modeled only with annual mean gradients (Weaver and Middleton, 1989; Batteen and Rutherford, 1990; etc.) or with an idealized gradient and time cycle (McCreary et al., 1986). McCreary et al. (1986) conclude that Leeuwin Current variability cannot be related to offshore variations in sea level by pointing out that the sea-surface slope 1000 km offshore is practically constant throughout the year (Figure 5.1). Yet, this observation appears to ignore the sharply changing gradient closer to shore or the possibility that the thermal forcing mechanism may originate in the Indonesian Archipelago region, not extending westward to the central Indian Ocean (Godfrey and Ridgway, 1985). Regardless of the ultimate cause of the large change in the alongshore temperature gradient (almost a 25 percent increase from the minimum gradient), the result will still be a significantly changing geostrophic influx of water from the Indian Ocean. From continuity considerations, this variable influx must significantly modify the Leeuwin Current flow, especially in light of the relatively weak magnitude of opposing wind forcing (discussed below). Weaver and Middleton (1989) present a similar observation in discussing the weakness of forcing with

annual mean data. McCreary et al. (1986), however, believe that the fluctuation in the net strength of the Leeuwin Current is principally a function of variations in the opposing wind strength.

A proposed hypothesis for seasonal thermal gradient influences on the Leeuwin Current flow is that the sudden sharp change in sea-surface slope, closely synchronized with the climatological wind shift, acts as a triggering mechanism for the poleward flow of NWS waters. Once released, the NWS waters add seasonal barotropic and baroclinic influences to augment what normally is a geostrophically-driven current. Included in this hypothesis is that the weakest thermal gradient, coinciding during the austral summer with the strongest opposing climatological winds, facilitates the formation of the NWS waters by allowing the wind to more effectively inhibit down-gradient flow. This superposition of seasonal cycles traps the NWS waters in a shallow warm region where the water can effectively absorb heat for later transport poleward. Godfrey and Ridgway (1985) present supporting evidence for this concept of separate wind and pressure gradient forcing cycles synchronized to produce reinforcing effects (Figure 3.5).

B. SEASONAL AND ANNUAL MEAN WIND FORCING

The wind forcing climatology off western Australia has a distinct annual cycle, which is quite monsoonal in nature. The significance of this for modeling efforts is the inability of the annual mean wind field to adequately represent a realistic forcing function for extended model runs.

The annual mean wind forcing field (Figure 5.2) shows a predominately equatorward wind with a slight offshore component. At the poleward end of the domain the wind is strongest and oriented equatorward with a slight offshore component; at the equatorward end the winds are weaker and have a relatively greater offshore component. The offshore poleward region has the strongest magnitudes, approximately 650 cm s^{-1} , while the equatorward coastal region has the weakest, approximately 300 cm s^{-1} . As an annual mean, the wind forcing supports both equatorward and offshore flow. The vertically integrated Ekman transport, however, shows a small poleward component in addition to the larger offshore component. The annual mean wind field most closely matches the April mean wind field (Figure 5.3.g).

The seasonal cycle of the climatological wind forcing field, Figure 5.3 (a through l), has a magnitude maximum in February (Figure 5.3 e), approximately 1025 cm s^{-1} , and a magnitude minimum near June (Figure 5.3.i) and September (not shown), approximately 600 cm s^{-1} . The contour plots of the alongshore wind component magnitudes (Figure 5.3) depict the

climatological variation in the strength of the force, which opposes the pressure gradient force. The seasonal cycle also includes a significant switch in magnitude of the cross-shore component, leading to a sharp change in wind direction. From January through March (seen in the February wind field, Figure 5.3.e), the flow has a strong equatorward component at all locations. The poleward region has a moderate westward cross-shore component, while the equatorward region has a strong eastward cross-shore component. Magnitudes increase in the equatorward offshore corner through April (Figure 5.3.g), while the magnitude minima remains in the equatorward coastal region at about the same strength. By April, the equatorward end has shifted to a westward cross-shore component, while the poleward end retains a moderate westward component. By June (Figure 5.3.i), the flow at the equatorward end is nearly completely westward, while the poleward end weakens, but remains mostly equatorward. From April through June, the region of maximum velocities, approximately 650 cm s^{-1} , migrates equatorward to dominate the equatorward end of the domain, with the weakest magnitudes, approximately 100 cm s^{-1} , now located in the poleward coastal region. The winds in the poleward area develop a slight eastward component in July (not shown) that remains through September (seen in the plot for August, Figure 5.3.k). By August (Figure 5.3.k), the winds at the low latitudes begin slowly rotating equatorward, becoming northward by December (Figure 5.3.c). In conjunction with this wind shift, the region of the maximum magnitude slowly returns to the higher latitudes, to reach its maximum poleward migration by February (Figure 5.3.e).

In summary, the two principal features of the seasonal wind cycle are the equatorward and poleward migration of the wind maxima, with the maximum reaching the equatorward limit of excursion in February and the poleward limit in July, and the swinging of the cross-shore component from an eastward maximum in December to a westward maximum in July. The eastward component maximum in December would produce a maximum equatorward, vertically-integrated transport, countering a significant portion of the weakened geostrophic forcing. The cross-shore component shifts from eastward to westward between March and April, changing the meridional component of the vertically-integrated transport from equatorward to poleward. Despite the equatorward component of surface stress, the change in transport component direction diminishes the role of the wind forcing as a countering influence to the poleward Leeuwin Current flow.

The climatological wind pattern appears to be a separate cycle from the ocean thermal forcing. The wind pattern is more driven by the

Southern Indian Ocean, anticyclonic, atmospheric gyre and the general monsoonal atmospheric circulation over the rest of the Indian Ocean basin than by local considerations (Trenberth et al., 1989b). The juxtaposition of the wind shift with the maximum ocean thermal gradient contributes to the strongly seasonal nature of the Leeuwin Current. The superposition in time and direction of major changes in both forcing mechanisms lends support to the "dam-breaking" hypothesis and modeling approach for the forcing by the North West Shelf waters.

C. SEASONAL THERMAL FORCING INFLUENCES

To highlight the effects of seasonally-varying thermal forcing, Case 2 (seasonally-varying thermal forcing) will be compared with Case 1 (annual mean thermal forcing). The tools used for comparison will be a time-sequence analysis, derived from instantaneous plots of u , v , T , and p and time-averaged meridional cross-sections, an energy analysis, a spectral analysis, and an instability analysis.

1. Time Sequence Analysis

The geostrophic adjustment of the model to the initial conditions (Figure 5.4) during the first 15 days is the same for both Case 1 and Case 2. The geostrophic adjustment of the initial conditions almost immediately creates a poleward Eastern Boundary Current (EBC). The initially very strong EBC, approximately 70 cm s^{-1} at the core, flows along the entire coastal boundary, diminishing to about 50 cm s^{-1} by day 40 as the high velocity core steadily advects poleward (Figures 5.5 and 5.6). The coastal equatorward region of the model domain becomes almost quiescent. The u -field indicates that the strongest Indian Ocean geostrophic inflow is found in the equatorward half of the domain. Greater inflow is observed, as is expected, in Case 2 because of the steeper alongshore temperature gradient. As model time progresses, the poleward bending of the onshore flow extends seaward due to advection from the previously established Leeuwin Current flow (Figures 5.7 and 5.8). The progression of the flow transformation, a gradual tapering from a zonal flow to a meridional flow, is clearly seen in the time sequence of the temperature and pressure fields.

The more dynamic nature of the seasonal forcing becomes evident as eddy generation begins. The seasonally-forced Case 2 exhibits eddy generation by day 60 (not shown); whereas, Case 1 does not show eddy formation until around day 80. In both cases the initial eddy forms in about the same vicinity, along the coast at about 300 km from the poleward end of the domain. The Case 1 eddy (Figure 5.7) originates slightly offshore as a large pinched off meander, quickly transforming into an eddy

pair (Figure 5.8) with a broad weak cyclonic eddy equatorward and a more intense and smaller anticyclonic eddy poleward. A second small, but more intense, cyclonic eddy soon forms poleward of the anticyclonic eddy. The two cyclonic eddies pinch the anticyclonic eddy off from the coast at about day 120 (Figure 5.8), after which the anticyclonic eddy drifts westward while dissipating. The Case 2 eddy generation is somewhat different, but has similar results. An anticyclonic eddy forms first at the coast (Figure 5.9), moving slowly offshore with time. Once the anticyclonic eddy has separated from the coast, day 90, two cyclonic eddies form at the coast, with the poleward eddy being smaller and more intense (Figure 5.10). From generation through dissipation, the anticyclonic eddy, present in both Cases 1 and 2, drifts westward and equatorward. The slight difference in the generation pattern between the two cases is attributed to the stronger pressure gradient present in Case 2 limiting the instability mechanisms to a smaller radius of curvature.

During this initial eddy generation period, by day 70 for both cases, the coastal equatorward region develops a narrow, weak, equatorward flow. The no-slip boundary condition creates curl, driving a weak equatorward flow in the region where the accumulated geostrophic inflow is small. Just offshore of the poleward EBC flow, the open ocean flow becomes increasingly equatorward, setting up an apparent anticyclonic gyre in the equatorward end of the domain (Figures 5.7.e and 5.9.e). This phenomenon is an interesting feature to follow, because this gyre, evident in all cases, oscillates between cyclonic and anticyclonic rotation at a fairly predictable rate of about 70 days per complete cycle, with a standard deviation of about 25 days. It is speculated that the cyclical nature of this feature is a function of the baroclinic Rossby wave propagation described by Weaver and Middleton (1989) and seen in the model results of Batteen and Rutherford (1990). Flow at the western boundary remains a geostrophic inflow.

For both cases, the coherent flow of the poleward EBC diminishes to an intensity minimum by about day 50, with the minimum alongshore extent of the poleward flow core occurring near day 70. This result is consistent with a nonlinear feedback mechanism described by Weaver and Middleton (1989), where, after about 55 days, the strong offshore fronts, caused by the initial southward advection, generate thermal winds that feed back to enhance the poleward flow at the surface. However, unlike the linear model presented by Weaver and Middleton (1988), the EBC in this nonlinear model does not dissipate westward and the surface current at the coast does not diminish to zero. As the feedback mechanism intensifies the poleward coastal surface flow through day 120, the coherent poleward

EBC flow expands to include the entire length of the coastal region (Figures 5.8 and 5.10).

The equatorward undercurrent associated with the Leeuwin Current is well established for both cases by day 60, with maximum intensities associated with the maximum surface velocities at the poleward end and much weaker intensities at the equatorward end of the domain. The 30-day average meridional velocities for Case 2, centered in time about day 60, are minimally greater in magnitude than and in about the same location as those for Case 1, approximately 32 km offshore at a depth of about 500 m (Figures 5.11 and 5.12). The undercurrent velocity core is more intense, slightly closer to the coast, and slightly deeper at the poleward end (Figures 5.11.c and 5.12.c) than the flow at the equatorward end (Figures 5.11.a and 5.12.a) of the domain. This undercurrent structure is consistent with the findings of Batteen and Rutherford (1990).

During the next development stage, days 60 through 120 (Figures 5.13 and 5.14), which equates to the austral spring and early summer, the undercurrent mimics the seasonal response of the surface current. The Case 2 (Figure 5.14) undercurrent continues to be generally stronger than that seen in Case 1 (Figure 5.13). For both cases, the undercurrent stays near the 500 m depth and just offshore of the core of the surface current, reflecting the relative strength of the surface current at that location (Figure 5.13 and 5.14). The weaker surface current and undercurrent magnitudes seen in the mid-domain cross-section (Figure 5.14.b) are due to time-averaging across the more-developed eddy field of Case 2.

Days 120 through 180 correlate with the remainder of the austral summer. The general pattern of greater dynamic activity for Case 2 (Figure 5.15.a-c) continues, with more eddies and eddies of greater intensity than Case 1 (Figure 5.15.d-f). For both cases, the equatorward end of the domain has a broad poleward-component flow that narrows as it flows poleward through the mid-domain eddy field. The broadening, then weakening, of the poleward flow is consistent with the baroclinic Rossby wave propagation described by Weaver and Middleton (1989). The flow at the equatorward end of the domain now follows a cyclonic gyre (Figures 5.15.c and 5.15.f), having switched directions at about day 140. This cyclonic flow augments the coastal current, strongly contributing to the distinctly poleward flow along the coast.

By day 150 (not shown), the poleward cyclonic eddy in Case 2 develops a filament-type structure around the eddy's poleward limit. The filament continues to extend itself farther offshore through day 170 (not shown). By day 180, the filament has pinched off to form an anticyclonic eddy offshore of the parent cyclonic eddy (Figure 5.15.a). This

anticyclonic eddy disappears by day 210 (not shown). Case 1 generates a comparable feature, but is much slower in doing so, developing the filament feature about 150 km further equatorward by day 170 (not shown) and loses its signature by day 240 (not shown). The filament in this case is significantly more extensive, spanning the entire width of the domain.

Despite the weakening surface current, Case 2 (Figure 5.16) retains its undercurrent. Poleward, the undercurrent is submerged to its usual depth of 500 m and is positioned on the coast. There is a suggestion of a secondary core on the offshore side of the EBC at about 500 m depth. Mid-domain, the surface current is broad and offshore which correlates to a meander around an anticyclonic eddy. Equatorward flow at the coast in this alongshore location broadens below the surface and the undercurrent is closer to the surface on the coastal side of the EBC and of the eddy. At the equatorward end, the undercurrent core is in its usual place of offshore at 500 m depth and is very weak. The undercurrent for Case 1 (Figure 5.17) is more similar to the pattern seen at day 120 with the velocity core rising and decreasing in magnitude with equatorward displacement (Figure 5.17). The most poleward cross-section (Figure 5.17.c) displays a stronger surface EBC than Case 2 and a minimal undercurrent at the coast. This situation is attributed to the direction of the flow, in Case 2, around the existing eddy, temporarily causing u-component flow to dominate the EBC. The signature of the flow is thereby reduced in the meridional cross-section. Additionally, the Case 2 seasonal cycle of the alongshore temperature gradient is at a minimum, minimizing the geostrophic inflow forcing of the Leeuwin Current.

From days 180 through 240 the domain becomes dominated by a high pressure gyre at the equatorward end. This anticyclonic gyre causes the coastal flow of both Case 1 and Case 2 to become strongly equatorward in the equatorward-half of the domain. Both cases continue to evolve their filament-like features, eventually shedding them as anticyclonic eddies. These filament-spawned anticyclonic eddies soon drift west out of the domain. Both cases also form a strong anticyclonic eddy along the poleward coastal boundary. The eddy in Case 2 forms about 20 days sooner, but Case 1 consolidates somewhat quicker. As result, by day 240, the two cases exhibit similar flow patterns (Figure 5.18).

The vertical structure of the flow during days 180 through 240 (Figures 5.19 and 5.20) becomes less consistent, partially due to the strong influence of the eddy field in the poleward region. In this region, Case 2 exhibits a strong equatorward undercurrent with a negligible poleward surface current. At mid-domain (Figure 5.19.b) the poleward surface current has strengthened while the equatorward

undercurrent has significantly diminished in extent and in intensity. The coastal flow in the equatorward region (Figure 5.19.a) is, as expected from the anticyclonic gyre, strictly an equatorward surface flow (Figure 5.19). The flow in Case 1 is similar, with the equatorward undercurrent resembling a deep offshore surface flow, and the small poleward coastal current weakening with equatorward alongshore distance (Figure 5.20).

Westward propagation of baroclinic Rossby waves characterizes the next period (days 240 through 300) for both cases. The offshore migration of the dominant high pressure region leads to a resurgence of poleward coastal flow, consolidating first at the poleward end of the domain by day 250 (Figures 5.21.a,b and 5.22.a,b) for both cases and then extending to the equatorward boundary by day 270 (day 280 shown for comparison with Case 1) for Case 2 and day 280 for Case 1 (Figure 5.21 and 5.22, respectively). The regeneration of the poleward coastal current re-establishes the equatorward undercurrent (Figures 5.23 and 5.24). At day 300, the surface current at the poleward end in Case 2 is more intense than Case 1 and, correspondingly, so is the undercurrent. The undercurrent is positioned adjacent to the coast in both the poleward and mid-regions for both cases, but is not discernible in the equatorward region.

Days 210 through 300 equate to the austral autumn time period, April through July. The Leeuwin Current flow is at a maximum during this period. Cases 1 and 2 do not seem to reflect a seasonal increase during this interval (Figures 5.23 and 5.24). For these cases during this time period, the flow variations appear to be a stronger function of the timing of the baroclinic Rossby wave propagation cycle than of the seasonal variation of the thermal forcing. This seasonal period should be increasingly thermally dynamic due to the rapid increase from a minimum to a maximum thermal gradient. A time lag may exist between the seasonal increase in the meridional thermal gradient of the model and the geostrophic inflow response, as well as an additional time lag before the forcing is manifested as a stronger Leeuwin Current flow. The EBC poleward velocities generated by Case 1 during this period reach a maximum of about 60 cm s^{-1} , while the velocities generated by Case 2 reach a maximum of about 80 cm s^{-1} .

For both cases, the evolution of the poleward EBC during the final 60 days of the simulated annual cycle, days 300 through 360, shows a significant strengthening and coherence of flow (Figure 5.25). The flow patterns are quite similar between the two cases, implying that the resurgence of the poleward EBC is less a function of the periodic thermal forcing than of the phase of the baroclinic Rossby wave propagation

(Figure 5.25). Additional specific experiments are necessary to assess the role of seasonal thermal forcing in the phasing of the baroclinic Rossby wave propagation. The correlation initially appears weak.

One possible source for baroclinic Rossby waves may be the initialization of the model. The sudden onshore geostrophic flow interacting with the coastal boundary prior to forming the coastal poleward flow, may generate transient features that require long duration (multi-year) model runs to filter out. Each case appears to experience a similar Rossby wave response. Despite any transient features, the differences between the cases yield information on the response of the modeled Leeuwin Current to seasonal forcing.

The influence of the seasonal cycle of the ocean thermal forcing is best seen in 30-day time averages of the meridional velocity component, centered at days 90, 180, 270, and 360 to represent spring, summer, autumn, and winter, respectively (Figures 5.26 and 5.27). Representative instantaneous plots of the meridional velocity component are also provided for reference. From the time plot of meridional temperature differences (Figure 5.3.5), the largest meridional thermal gradient is observed in the austral winter (May, June, and July), closely matched by the austral spring (August, September, and October). The weakest thermal gradients are in the austral summer (November, December, and January) and the austral autumn (February, March, and April). These variations about the mean are reflected in the comparison of the time-averaged meridional velocity fields of Case 2 versus Case 1 (Figure 5.26 and 5.27).

At day 90, representative of the austral summer, Case 2 (Figure 5.27.a) exhibits instantaneous poleward EBC flow that has greater coastal extent and greater core velocities than that developed by Case 1 (Figure 5.26.a), but the time-averaged flows are nearly the same, as expected from the decreasing seasonal gradient (Figures 5.26.b and 5.27.b). The initially strong austral spring thermal gradient, weakening with the onset of summer, coupled with an inherent time lag for the ocean response, contributes to the greater poleward velocities found in Case 2 during the austral summer.

The weakest seasonal gradient, occurring in the austral autumn (February, March, April), results in broad, generally weak, poleward flow. Coherent poleward flow is interrupted by the eddy field in the poleward end of the domain and no consistent core of higher poleward velocities is evident in Case 2 (Figure 5.27.c), except in the time-averaged flow (Figure 5.27.d). Because the annual mean thermal forcing magnitude exceeds the seasonal magnitude during this period, the results from Case 1 show a stronger, coherent core of instantaneous poleward velocities at

the coast (Figure 5.26.c). The Case 1 time-averaged flow shows the same trend (Figure 5.26.d). The velocity field at day 270 depicts the resurgence of the poleward EBC in Case 2 (Figure 5.27.e and f), with core velocities exceeding 60 cm s^{-1} . The maximum strength of the meridional thermal gradient provides impetus to the poleward flow that is greater than when the model is forced only by the annual mean thermal gradient (Figure 5.26.e and f). The generally strong poleward flow in Case 2 is maintained through to the austral spring by the continuing strength of the thermal gradient (Figure 5.27.g and h). Case 1 reflects the same trend of poleward velocities, but at reduced magnitudes, consistent with the weaker annual mean thermal gradient (Figure 5.26.g and h).

2. Energy Analysis

The time series of kinetic energy within the region of interest and for all model layers, is used in conjunction with a similar time series of available potential energy to identify periods of near-constant total energy. Regions of large energy transfer are identified for these periods, along with the dominant type of energy transfer. These observations assist in the classification of principle instability mechanisms.

The time series of available potential energy for Cases 1 and 2 (not shown) show a large initial loss of available potential energy during the first 80 model days as the model adjusts to the initial conditions. Thereafter, the magnitude of available potential energy varies about the adjusted level of available potential energy due to eddy generation and baroclinic Rossby wave propagation. Although the magnitudes for the seasonal case are larger than the annual mean case, correlation of the variations in the available potential energy with the seasons appears slight.

The kinetic energy plots for Cases 1 and 2 reveal very similar profiles through about day 240 (Figures 5.28.a and 5.28.b). Thereafter, Case 2 significantly increases in kinetic energy. This increase correlates in time with May and the rapid change to the strongest meridional temperature gradient. Observations report that the most intense Leeuwin Current flow occurs at this time of the year. The other contribution to the total kinetic energy is due to the more active eddy field evident in Case 2.

Two periods of quasi-steady kinetic energy in Case 1 can be identified: days 60 through 80 and days 230 through 260. Two such periods are also noted for Case 2: days 60 through 80 and days 220 through

240. In the following sections, these periods are examined for dominant energy wavelengths and insights into the driving instability mechanisms.

3. Spectral Analysis

Using comparisons of spectral density plots of u , v , and T before and after the identified periods of energy transfer, the wavelengths of growth can be identified. By analyzing a reduced region in the vicinity of the Leeuwin Current, both boundary noise and the muting effect of averaging in spectra from quiescent open ocean areas can be reduced. The reduced region still permits 16 degrees of freedom for computing confidence intervals.

The first period of energy transfer in Case 1 has notable growth of energy at a wavelength near 160 km (wavenumber $\approx 0.0063 \text{ km}^{-1}$). The u -field at days 60 (Figure 5.29.a) and 100 (Figure 5.29.b) highlights this growth (the growth is also evident in the spectra of v and t (not shown)). The first period for Case 2 produces notable growth at wavelengths near 220 km (wavenumber $\approx 0.0046 \text{ km}^{-1}$) and 85 km (wavenumber $\approx 0.012 \text{ km}^{-1}$) for the same three variables. The v -field at days 60 (Figure 5.30.a) and 90 (Figure 5.30.b) best depicts this concentration of energy. Following the second period of energy transfer, the differences between the spectra for Cases 1 and 2 are negligible. The insights to be gained by these results are that the seasonal variation of the thermal forcing modifies the wavelengths at which energy growth occurs, and that the growth at these wavelengths is seasonally dependent.

4. Instability Analysis

Plots of barotropic and baroclinic energy transfer highlight regions of eddy generation. The u -velocity field, being of smaller magnitudes and less complexity, provides a fairly clear indication of the locations of eddy generation, while the pressure field best depicts the extent and intensity of eddies.

In Case 1, the barotropic and baroclinic energy transfer plots for days 60 through 90 (Figure 5.31), show significant energy transfer at the same location along the coast at the poleward end. For the comparable period in Case 2, the energy transfers are much larger, approximately 2.5 times greater for both barotropic and baroclinic transfers, highlighting the greater development and dynamic nature of Case 2 versus Case 1 (Figure 5.32). In both cases, the barotropic energy transfers had maximum values almost twice the maximum baroclinic transfer value. The greater transfer values for Case 2 can be attributed to the greater temperature gradient in Case 2 inducing greater geostrophic flow and, consequently, greater

thermal advection during the adjustment phase. The relative magnitudes of the barotropic versus the baroclinic transfers provides evidence that, at least for this phase, the barotropic influences dominate the flow regime at the poleward end of the domain. This result is consistent with the mass continuity argument describing the Leeuwin Current as principally a response to geostrophic inflow from the Indian Ocean.

The second quasi-steady kinetic energy period, days 230 through 260 for Case 1 and days 220 through 240 for Case 2, depicts a change in the relative contributions of barotropic energy transfer versus baroclinic transfer. The energy transfers from these two mechanisms are comparable in magnitude (Figure 5.33 and 5.34). The barotropic transfers are primarily located in the poleward interior, while the baroclinic transfers appear to be associated with the flow in the poleward coastal region. For each case, both types of energy transfer increase significantly in magnitude versus the earlier analysis period. The barotropic energy transfer in Case 1 appears to be associated with the spawning of cyclonic eddies near the coast and the spawning of a secondary anticyclonic center in the offshore anticyclonic eddy. The negative regions indicate barotropic transfer of energy back from the eddy to the mean flow. The local meridional velocity maxima (Figure 5.21.b) in those regions supports this conclusion. During its comparable period, the barotropic energy transfer for Case 2 appears to be associated with cyclonic eddy generation near the coast and with intensification of the offshore cyclonic eddy. The second energy transfer period equates to the end of the austral autumn when the thermal gradient forcing is increasing to a maximum. An increase in kinetic energy for Case 2 is expected as the available potential energy is converted to kinetic energy through down-gradient flow.

The thermal gradient governs the zonal mass influx from the Indian Ocean. This increasing net contribution with poleward alongshore distance supports the intensification of the Leeuwin Current in the poleward direction and the current's subsequent tendency toward barotropic instability. Baroclinic instability is expected as the alongshore thermal gradient approaches its maximum and the cross-shore temperature differences increase following significant poleward advection of warm tropical water along the coast. However, following the adjustment to the initial conditions in Case 2 and prior to the middle of the austral winter (see day 270 versus day 90, 5.35), little variation occurs in the position of the isotherms, suggesting that the baroclinic instability, seen especially in the austral autumn, has a source that does not originate with the waters flowing into the current from the west. The anticipated source of the warm water is from the North West Shelf region, and this

development is seen in Cases 5 and 6. Consequently, for Case 2, barotropic instability is expected to dominate over baroclinic instability during the above period.

D. SEASONAL WIND FIELD INFLUENCES

To highlight the seasonal aspects of the ocean's response to wind forcing in the Leeuwin Current region, the case of annual mean wind forcing superimposed on the annual mean ocean thermal forcing (Case 3), will be compared with the case of seasonal wind forcing superimposed on the seasonal ocean thermal forcing (Case 4). These two cases show the significant role of wind forcing in the determining the strength and variability of Leeuwin Current flow.

1. Time Sequence Analysis

Case 3, in general, was found to be the least dynamic of all the cases. The model's geostrophic adjustment (Figure 5.36) to the initial conditions produce a poleward velocity core of near 45 cm s^{-1} (Figure 5.36.b), closely matching the responses seen in Cases 1 and 2. Following this initial adjustment, the EBC continues to lose intensity until, by day 80 (not shown), it is about one-half the magnitude of that in Case 1 (not shown), approximately 20 cm s^{-1} versus about 40 cm s^{-1} . The development of eddies is very slow and weak. Illustrating this characteristic is that, although, like Case 1, eddy generation begins at around day 80 (Figure 5.37.a), subsequent growth and intensification do not create a closed-contour eddy until about day 120 (Figure 5.37.b). In contrast, well-developed eddies occurred by day 100 for Case 1.

The annual mean wind field used to force Case 3 is very similar to the September and October wind climatology, so initial differences between Cases 3 and 4 should be minor. Because the differences due to the thermal forcing variation have been shown to be relatively small in comparing Cases 1 and 2 (especially when compared to the seasonal variation of the observations discussed in Section H), the differences between Cases 3 and 4 should arise from the time varying nature of the wind field in Case 4. The EBC response after the initial 40-day adjustment period is very similar to Case 3, but the EBC core velocities in Case 4 are slightly weaker and the velocity core has advected slightly further poleward (Figure 5.38). An examination of the velocity vectors (Figure 5.38.c) reveals that Case 4 develops a stronger anticyclonic gyre at the equatorward end of the domain by day 40, whereas Case 3 does not show comparable flow until at this time (Figure 5.36.c). The initiation of the gyre formation at the equatorward end of the domain is significant because the timing of flow reversals about this gyre significantly

modifies the strength, direction, and coherency of the coastal flow. Time-averaged cross-sections of the meridional velocities (Figures 5.39 and 5.40) show the development of a poleward surface current at the coast and a corresponding equatorward undercurrent. Both the surface current and the undercurrent have their greatest intensities at the poleward end (Figure 5.39.c and 5.40.c). Neither case at this time exhibits significant currents at the equatorward end (Figures 5.39.a and 5.40.a). The weaker currents seen in Case 4 (Figure 5.40) can be attributed to the greater development of anticyclonic flow and its countering effect on poleward flow in the equatorward part of the domain.

Eddy generation occurs sooner in Case 4 than in Case 3, developing an eddy by day 80 (Figure 5.41), but, similar to Case 3, development through day 120 is slow and weak. As in Case 3 (Figure 5.37.b), the first eddy to form is cyclonic and, unlike Batteen and Rutherford (1990) a predominance of anticyclonic eddies is not evident in either case. Differing from Case 3, this eddy develops further poleward. By day 120, the Case 4 eddies have intensified markedly more than those in Case 3 (Figure 5.41). A portion of the greater intensification may be attributed to boundary interaction at the poleward boundary. The features are valid features, having been generated in the interior of the domain. Expanding until interaction begins with the boundary, the features then artificially intensify.

The general flow between days 40 and 120 is dominated by poleward flow in the offshore region. During this period, a strong, narrow equatorward flow develops and broadens immediately offshore of the coastal flow. An anticyclonic gyre governs flow in the equatorward half of the domain. A poleward EBC is evident in the poleward half of the domain, while equatorward flow of comparable magnitude is observed along the equatorward coast. Case 4, due to its earlier generation of the equatorward gyre, continues to lead Case 3 in the evolution of this feature. The baroclinic Rossby wave propagation, once initiated, appears to be independent of the forcing mechanism. Consequently, by day 120, Case 4 exhibits an established cyclonic gyre (Figure 5.42.d), while Case 3 is in mid-transition to cyclonic flow (Figure 5.42.b). The time-averaged meridional velocity cross-section (not shown) for day 120 depicts comparable surface currents and undercurrents for both Cases 3 and 4, although Case 3 develops a slightly stronger undercurrent.

Days 120 through 180 (Figure 5.43), for both cases, are characterized by the slow generation of an anticyclonic eddy along the coast at the poleward end of the domain (compare Figures 5.37.b and 5.41.b at day 120 with Figure 5.43 at day 180). The flow in Case 3 remains weak

and the offshore anticyclonic eddy dissipates by day 190 (not shown), while the cyclonic eddy gradually intensifies and expands. The dominating eddy pair in Case 4 intensifies through day 150 (not shown), after which it separates from the poleward boundary influence and drifts westward, eventually exiting the domain. An anticyclonic eddy generates along the poleward coast at about the same time and location as the anticyclonic eddy generated in Case 3. The Case 4 eddy is smaller and arrested in development and life span, consistent with the strongest wind opposition to the pressure gradient forcing and weakest thermal gradient.

The general flow field for days 120 through 180 becomes increasingly poleward, starting at the coast, except along the equatorward coastal boundary where equatorward flow is maintained (Figure 5.44). The equatorward flow in this region is consistent with the small accumulated geostrophic inflow, curl generated by the frictional boundary condition, and the strongest equatorward wind forcing. The poleward flow is amplified by the cyclonic gyre dominating the overall flow field. Additionally, in Case 4 near the equatorward boundary, a small anticyclonic gyre develops by day 150, expanding to fill the equatorward-third of the domain by day 180 as the baroclinic Rossby wave propagates westward and the model transitions from a cyclonic to an anticyclonic flow regime. Case 3 develops the anticyclonic gyre by day 160 but its development is very much slower than in Case 4 (Figure 5.44). Poleward velocities are between 20 and 30 cm s^{-1} for both cases, although the EBC flow is somewhat obscured by the dominating eddies in Case 4. For Case 4, model day 180 equates to the mid-March forcing regime. The time-averaged meridional velocity cross-sections near the poleward end for both cases (Figures 5.45.c and 5.46.c) show a broad poleward flow offshore with a higher-velocity core and equatorward undercurrent near the coast. The mid-domain flow of Case 3 (Figure 5.45.b) features a weak poleward surface flow and an undercurrent, while Case 4 (Figure 5.46.b) shows negligible flow. The equatorward end of the domain, for both cases (Figures 5.45.a and 5.46.a), has equatorward flow at the coast but no undercurrent.

For Case 3, days 180 through 240 feature the slow growth and slight intensification of the existing cyclonic eddy and the westward drift of the eddy pair (Figure 5.47). Equatorward flow at the coast expands from the equatorward half of the domain, causing all coastal flow to become equatorward by day 210. Coherent poleward flow is pushed offshore as the band of equatorward flow expands westward in response to baroclinic Rossby wave propagation. By day 240 (Figure 5.47.c), the flow in the equatorward half of the domain describes an anticyclonic gyre, with significant equatorward flow at the coast. The core velocity of the

coastal equatorward flow exceeds 20 cm s^{-1} . The time-averaged meridional velocity cross-sections confirm the above observations (Figure 5.48). Case 4 core velocities are greater than those of Case 3 at each of the cross-section latitudes (Figure 5.49).

The trends evident in Case 4 for the same time period include westward migration of existing features and the spawning of a new cyclonic eddy from the existing cyclonic eddy (Figure 5.50). This new eddy forms somewhat offshore at the poleward end of the domain. This eddy quickly intensifies, partly due to boundary interaction. This feature is considered a real feature because a comparable, but weaker, feature develops in Case 3 following a previously identified time lag. The general flow field depicts equatorward flow of greater extent and magnitude than Case 3 (Figure 5.50). The equatorward coastal flow has core velocities comparable to Case 3, but extending farther in the alongshore direction.

Westward baroclinic Rossby wave propagation characterizes the next 60 model days, days 240 through 300. By day 280, Case 3 generates a couple of moderately weak cyclonic eddies near the coast in the poleward half of the domain. By day 300 these eddies have not significantly grown nor moved (Figure 5.51). Also by day 280, the general flow field at the equatorward end begins to transition to cyclonic flow. A ribbon of poleward flow develops by day 280, at the coast in the poleward end of the domain, shifting slightly to be offshore of the coastal equatorward flow at the equatorward end (Figure 5.51). The time-averaged meridional velocity cross-section (Figure 5.52) highlights these same features.

For this same period, Case 4 exhibits the same westward propagation trend. Cyclonic gyre formation is evident by day 290 and a resulting increase in the coherency of the poleward flow becomes observable (Figure 5.53). Due to the more vigorous nature of the flow in Case 4, eddy generation during the comparable period produces both cyclonic and anticyclonic eddies of greater intensity than Case 3. The location for the cyclonic eddies is nearly the same as in Case 3. Again, after forming and while developing, the poleward-most eddies interact with the poleward boundary, artificially amplifying their pressure signature. However, the eddies removed from the undue influence of the boundary are also larger and more intense in Case 4 than in Case 3 (Figure 5.53). The time-averaged meridional velocity cross-sections confirm the poleward coastal flow and the associated equatorward undercurrent at the poleward end of the domain. At the equatorward end of the domain the flow is equatorward with evidence of a poleward undercurrent (Figure 5.54).

The final 60 days for Case 3, days 300 through 360, are also highlighted by westward propagation of baroclinic Rossby waves, but there are very few additional distinguishing developments (Figure 5.55). Only two small anticyclonic eddies appear at the poleward coast by day 360. The band of poleward flow widens, while a narrow wedge of equatorward flow remains at the equatorward end of the domain.

During this same time period, Case 4 (Figure 5.56) marks a departure from the pattern of baroclinic Rossby wave propagation. Until about day 270, Case 4 leads Case 3 in phase for Rossby wave propagation. At around day 270, Case 4 retards until it is in phase with Case 3 and then, subsequently, lags Case 3. It appears that the flow is responding to the model's minimum in equatorward wind stress corresponding to the June and July climatological minimum. The relative increase in the influence of the ocean thermal forcing allows for greater poleward advection of warmer waters, building the coastal pressure gradient and amplifying the poleward flow both linearly and nonlinearly. Poleward velocities exceed 40 cm s^{-1} versus only 20 cm s^{-1} for Case 3.

The seasonal cycle of the wind forcing strongly affects the strength of the surface flow. The annual mean wind forcing alone is sufficient to significantly weaken the Leeuwin Current signature. In the mean, the wind flows equatorward (Figure 5.2) which tries to force the surface-most water equatorward against the general flow of the Leeuwin Current. Additionally, the net Ekman flow resulting from wind forcing is offshore, countering some of the geostrophic inflow due to the ocean thermal forcing. By day 90, representing the austral summer, the seasonal wind is building to an equatorward maximum velocity (Figure 5.3.c and d). Consequently, the poleward EBC velocities in Case 4 are markedly weaker than those in Case 3 (Figure 5.57.b and 5.58.b). The seasonal climatological winds for March, day 180, (Figure 5.3.e and g) are still significantly stronger than the annual mean winds, especially at the poleward end of the domain where the Leeuwin Current is typically strongest. The EBC flow in Case 3 remains stronger than the EBC flow in Case 4 due to the continuing maximum of opposing equatorward winds as compared to the weaker opposing annual mean winds.

During the austral autumn, the seasonal winds diminish in strength to a minimum and rotate offshore, with the extrema of both magnitude and rotation occurring in June (Figure 5.3.i). Following the minimum in equatorward wind forcing around day 270 (Figure 5.3.i) and coinciding with the maximum in ocean thermal forcing, the EBC builds at the coast (Figure 5.58.e and f). There is an apparent phase problem because the maximum flow of the Leeuwin Current is observed in the May

time frame, not in July or August as indicated by the model. Additionally, it was expected that the poleward EBC would build more substantially as the winds diminished. The North West Shelf (NWS) waters, which contribute to the Leeuwin Current flow during this period and are not included in these two simulations, may be the missing factor.

The winds in September, day 360 (similar to August winds, Figure 5.3.k), are still near a minimum in magnitude but they have begun to rotate back to an equatorward direction. The EBC in Case 4 (Figure 5.58 g and h) has regained its strength and it is notably stronger and more coherent than the EBC in Case 3 (Figure 5.57.g and h). Again, these results were anticipated to occur approximately 90 days sooner.

2. Energy Analysis

A comparison of the kinetic energy time series for Case 3 with Case 4 (Figures 5.59.a and b), and with Cases 1 and 2 (Figure 5.28.a and b) reveals that Case 3 is the least dynamic of the cases. This result is not unexpected because Case 3 has the weakest ocean thermal gradient coupled with a steadily-strong opposing wind field. The seasonal cycles of wind and ocean thermal forcing in Case 4, however, are phased such that changes in the opposing forces have complementary effects. In the austral summer the thermal gradient is the weakest and the wind forcing is the strongest; therefore, a minimum in kinetic energy is expected. The maximum of wind forcing does not induce much additional kinetic energy because, as discussed later, the magnitude of the pressure gradient force always significantly exceeds the magnitude of the wind forcing, leaving the wind forcing in the role of a countering effect rather than a primary driving mechanism. The anticipated relative minimum in kinetic energy can be observed near day 180 (March) (Figure 5.59.b). The rise in kinetic energy during the period preceding day 180 is attributed to the nonlinear feedback described by Weaver and Middleton (1989). The following decline in equatorward wind through day 270 (June) is matched by a corresponding increase in kinetic energy. This large increase in kinetic energy can be attributed, at least in part, to the magnitude and duration of the "relaxation event." The winds begin to reassert their influence about day 330 (August) and a decrease in kinetic energy is observed. In summary, the variable wind forcing serves to create fluctuations superimposed on the primary Leeuwin Current signal generated by ocean thermal forcing.

The time series of available potential energy (not shown) show that the superimposition of wind forcing on the ocean thermal forcing inhibits the variations in available potential energy. This damping effect is consistent with reduced dynamic activity in response to the opposing wind

forcing. Consistent with Cases 1 and 2, there is a large initial decrease in available potential energy during the adjustment period (days 1 through 80). For Case 3, the general trend of decreasing available potential energy continues through day 270. Thereafter, the available potential energy becomes steadier. For Case 4, following the initial adjustment period, the time series (not shown) of available potential energy is dominated by fluctuations resulting from mesoscale features. The general trend of these fluctuations is nearly level and the correlation with seasonal variations is weak. These results are consistent with a general barotropic flow, resulting primarily from a geostrophic forcing mechanism.

3. Spectral Analysis

The spectral density plots, highlighting the wavelengths experiencing energy growth during the first energy transfer period (days 80 through 110), depict energy growth for Case 3 at wavelengths essentially the same as those in Cases 1 and 2. The v-field spectral density plots for Case 3 (Figure 5.60.a and b) highlight the significance of the 85 km and the 220 km wavelengths (wavenumbers $\approx 0.012 \text{ km}^{-1}$ and 0.0046 km^{-1} , respectively), while the u-field (Figure 5.60.c and d) and T-field (not shown) spectral density plots depict the growth at the 160 km wavelength (wavenumber $\approx 0.0063 \text{ km}^{-1}$). The influence of the seasonal winds in Case 4, however, leads to growth at slightly different wavelengths. The change in the u-field spectral density plots (Figure 5.61) over the span of the energy transfer period depicts energy growth at wavelengths of 90 km and 130 km (wavenumbers $\approx 0.011 \text{ km}^{-1}$ and 0.0078 km^{-1} , respectively).

The growth in the second energy transfer period (days 170 through 200) for Case 3 is principally seen in the T-field spectral density plot (Figure 5.62). The wavelength with noticeable growth is the 220 km wave (wavenumber $\approx 0.0046 \text{ km}^{-1}$). For Case 4, the energy growth appears in the v-field spectral density plot (Figure 5.63) at a wavelength near 120 km (wavenumber $\approx 0.0085 \text{ km}^{-1}$).

4. Stability Analysis

The kinetic energy time series plots for both Cases 3 and 4 are virtually identical through day 90. Not surprisingly, the barotropic energy transfers and the baroclinic energy transfers at that time are quite similar in magnitude and location (Figures 5.64 and 5.65). Similar to Cases 1 and 2, the barotropic energy transfer is about twice the magnitude of the baroclinic energy transfer. The similarity between Cases 3 and 4 during this period is due to the time required for the

initial adjustment of the model and the mid-range values for both wind and thermal forcing during the instability growth period.

The period between days 170 and 200 in Case 3 illustrates the continuing dominance of barotropic instability in eddy generation, despite the weakness of the kinetic energy (Figure 5.66). The comparable period for Case 4 (days 200 through 220) (Figure 5.67) depicts energy transfer in the vicinity of an intensifying eddy. The barotropic energy transfer is approximately three times the magnitude of the baroclinic energy transfer. The continuing dominance of barotropic instability intimates that the constant geostrophic influx of water from the Indian Ocean is the underlying force driving the Leeuwin Current rather than the seasonal thermal or wind forcing signals.

E. COMBINED WIND AND THERMAL FORCING INFLUENCE

The Leeuwin Current flow is controlled by the resultant of two opposing forces: the dominant poleward pressure gradient force versus the weaker equatorward wind stress. One measure of the relative strengths of these two forcing mechanisms is a comparison of the meridional pressure gradient force with the meridional wind stress component. The climatological meridional pressure gradient force [Equation 4.15] is positive everywhere throughout the year (Figure 5.2), creating an onshore geostrophic flow component. The meridional wind stress component is also essentially positive everywhere in the domain at all times; however this wind stress imparts an offshore Ekman component to the surface flow. These two mechanisms are always in opposition. Variations in the Leeuwin Current flow result from fluctuations in the relative strengths of the two components. Godfrey and Ridgway (1985) (Figure 3.5) present their analysis of the cycles of each forcing component and of the net effect. The seasonal forcing cycles (Figure 5.68) for this model closely match those of Godfrey and Ridgway (1985). Representative seasonal meridional profiles of the pressure gradient force versus the wind stress (Figure 5.69) show that the magnitude of the pressure gradient force for every month far exceeds (by at least a factor of three) the magnitude of the opposing wind stress. Notice that, in February (Figure 5.68 and 5.69.c), the near-maximum wind stress coincides with the minimum pressure gradient force, creating the conditions for the minimum Leeuwin Current forcing. These conditions are consistent with Smith et al. (1991). By June (Figure 5.68 and 5.69.e), in the season that immediately follows, the opposing meridional wind stress sharply shifts to a minimum, coinciding with the significantly increasing pressure gradient force, and setting up the conditions for maximum Leeuwin Current forcing. The asymmetry of the

Leeuwin Current forcing provides an explanation for the pulsating character of the Leeuwin Current flow.

Through a comparison of Cases 2 and 4, the relative influences of the two principal forcing mechanisms are examined. A comparison of Cases 1 and 3 provides a reference for evaluating the magnitudes involved in the other two cases. At day 90, Case 4 (Figure 5.70.d-f) exhibits inhibited eddy development, with respect to Case 2 (Figure 5.70.a-c), and the eddy development that occurs is located further poleward. It is hypothesized that the eddies form further poleward in Case 4 because a greater accumulation of Indian Ocean inflow is necessary, in the face of the opposing equatorward wind stress, to be sufficient to trigger barotropic instability. Greater accumulated inflow is achieved with poleward alongshore displacement. The wind forcing in Case 4 assists the weak equatorward flow along the coast at the equatorward end. Cases 1 (Figure 5.71.a-c) and 3 (Figure 5.71.d-f) display a similar relationship, but with reduced magnitudes.

At day 180, when the poleward forcing of the Leeuwin Current is near its minimum (Figure 5.68), Case 4 (Figure 5.72.d-f) represents a "wind-retarded" version of Case 2 (Figure 5.72.a-c), as evidenced by fewer and smaller eddies along the coast. These results are consistent with the minimum of flow expected and observed during this period. At this time, note that the influence of the wind turns the weak flow along the coast at the equatorward end towards the equator. Again, Cases 1 (Figure 5.73.a-c) and 3 (Figure 5.73.d-f) closely resemble each other, but with weaker magnitudes in Case 3. Day 270, for Case 2 (Figure 5.74.a,c), displays the regeneration of the Leeuwin Current along the coast, yet Case 4 (Figure 5.74.d-f) still has significant equatorward flow at the coast. Case 1 (Figure 5.75.a through c) shows a narrow sporadic poleward flow due to the complex eddy field along the coast at the poleward end. Case 3 (Figure 5.75.d through f) displays no consistent eastern boundary flow at day 270.

The maximum net poleward forcing occurs in September, day 360 (Figure 5.68). For Case 2, strong poleward flow spans the entire length of the domain, meandering as coherent flow through the eddy field at the poleward end. The influence of wind in Case 4 is seen in the weaker cross-shore pressure gradient along the coast (Figure 5.76). The net result of the weaker pressure gradient is lower poleward flow velocities. Cases 1 and 3 both have coherent poleward flow slightly offshore. The flow in Case 1 is in a fairly similar pattern to Case 3 and is, again, very much stronger due to the lack of an opposing wind (Figure 5.77).

The comparisons of seasonal forcings with annual mean forcings emphasize the inadequacies of modeling the Leeuwin Current using annual

mean forcing. The highly seasonal nature of the Leeuwin Current can be attributed to the large range of greater than 1 dyne cm^{-2} in net forcing magnitude. The particular synchronization of the ocean thermal forcing cycle and the wind forcing cycle contributes heavily to the surging nature of the Leeuwin Current.

F. NORTH WEST SHELF WATER INFLUENCE

So far, little has been mentioned about the influence of the North West Shelf (NWS) waters. The NWS waters provide a significant baroclinic and barotropic influence on the poleward eastern boundary current (EBC) flow; however, this forcing, as of yet, has not been included in the model. It is hypothesized that, while the NWS waters are not a major forcing mechanism for the Leeuwin Current, their release resulting in poleward flow, when the climatological winds relax in the austral autumn, significantly affects the timing of flow patterns at the coast. The quick release of NWS waters adds to the surging nature of the Leeuwin Current. Observations, including satellite imagery, confirm the existence of the warm water mass over the North West Shelf during the austral summer (Church *et al.*, 1989).

This study does not attempt to explain the formation of the NWS waters, but rather their influence on the Leeuwin Current flow. This model initiates the onset of the NWS water's added influence at model time equivalent to the middle of March. The forcing from NWS waters (described in Section 3.H) was added to each of the previous cases, Cases 1 through 4, and the new cases are designated as Cases 5 through 8 respectively. Points to be noted are the effects on the direction and coherency of coastal flow and the interaction of the surge with the existing eddy field.

Case 5, annual mean ocean thermal forcing plus NWS forcing with no wind forcing, shows the increased pressure gradient at the coast caused by the poleward advection of the warm NWS waters. The Coriolis force keeps the poleward flow close to the coast. Developing eddies grow quicker and more intense than those found in Case 1 (Figure 5.78). Weak equatorward flow along the coast at the equatorward end of the domain in Case 1 converts to strong poleward flow. By day 240, a narrow band of coherent poleward flow exists all along the coast, with maximum core velocities exceeding 60 cm s^{-1} (Figure 5.79). The strong influence of the NWS waters on current direction and magnitude continues to be seen through day 300 (mid-July) (Figure 5.80). After this time, the band of poleward flow widens due to baroclinic Rossby wave propagation. The poleward flow generated by Case 5 diminishes, approaching the slow state created by the

annual mean thermal gradient in Case 1, and leaving several active mesoscale features (Figure 5.80). As the seasonal pulse of the NWS waters is advected poleward and weakened through diffusion and mixing, the Leeuwin Current flow regime returns to a flow pattern more typical of the geostrophic/Ekman forcing balance previously seen. Note that the inclusion of the NWS forcing has transformed the previously weak poleward flow of the austral autumn to a significant flow of magnitudes comparable with observations.

Case 6, seasonal ocean thermal forcing plus NWS forcing with no wind forcing, exhibits a tighter pressure gradient at the equatorward coast that has eliminated the development of the large anticyclonic eddy present in that part of the domain in Case 1 (Figure 5.81). The meridional velocity field (Figure 5.81) response closely mirrors Case 5. The weaker poleward response at the coast for Case 6 can be attributed to the time lag between the seasonal thermal forcing change and the open ocean and Leeuwin Current responses. Again, the addition of NWS forcing has transformed weakly poleward flow at the coast to a more coherent poleward current (Figure 5.82). The poleward EBC continues to intensify through day 300, with maximum core velocities again slightly greater than 60 cm s^{-1} (Figure 5.83). The high velocities in the equatorward corner are believed to be due to the nonlinear feedback mechanism (Weaver and Middleton, 1989), in response to the initial NWS forcing profile. These high velocities are believed to be symbolic of the oceanic response off Western Australia.

Case 7, annual mean wind and ocean thermal forcing plus NWS forcing, again demonstrates that the NWS waters build the pressure along the coast, creating poleward geostrophic flow. The enhanced poleward flow at the coast exceeds the minimum criteria necessary for eddy generation, thereby forming numerous eddies at the coastal boundary. Significant coherent poleward flow quickly develops and then diminishes, with maximum core velocities diminishing from near 80 cm s^{-1} at day 190 to near 40 cm s^{-1} by day 210 (Figure 5.84). For the comparable period in Case 3, the flow at the coast is entirely equatorward. By day 240, the influence of the NWS forcing has apparently vanished and the coastal flow, as a result, is rather nebulous and only weakly poleward versus the weak equatorward flow of Case 3 (Figure 5.85). Interpreted as resulting from nonlinear feedback as described by Weaver and Middleton (1989), a strong poleward EBC re-emerges along the entire coast by day 250. Maximum core velocities approach 80 cm s^{-1} , diminishing to near 60 cm s^{-1} by day 300 (Figure 5.86). Following its revitalization, the EBC flow continues to broaden in cross-shore extent through day 360 (Figure 5.86) in response to baroclinic

Rossby wave propagation. While the timing of the poleward rush still appears slightly out of phase, strong poleward flow is now seen in the austral autumn. This strong poleward flow appears in two phases, an initial surge following the release of the NWS waters and a resurgence, which is apparently associated with a nonlinear ocean feedback mechanism. Beginning in the model period equating with late May, during which observations report the strongest flow (Godfrey and Ridgway, 1985), the second phase provides a strong EBC.

Case 8, seasonal wind and ocean thermal forcing plus NWS forcing, produces similar initial results to Case 7, with an early formation of the EBC and with initial maximum core velocities near 80 cm s^{-1} , which diminish to around 50 cm s^{-1} by day 210 (Figure 5.87). No significant poleward coastal flow is evident for the comparable time in Case 4. By day 240, numerous cyclonic eddies have formed along the coast (Figure 5.88). Case 4 never develops comparable features. The coastal flow in Case 4 at day 240 is notably equatorward; however, the influence of the NWS forcing in Case 8 causes the coastal regime to become a narrow band of poleward flow with velocities still exceeding 40 cm s^{-1} (Figure 5.88). While the poleward flow diminishes in strength to its weakest magnitude near day 240, the poleward flow remains substantial along the entire extent of the coast. Following day 240, the current rebuilds and widens through day 360, eventually achieving poleward velocities in excess of 60 cm s^{-1} (Figure 5.89). These velocity magnitudes far exceed those produced by Case 4. Clearly, the NWS waters significantly modify the Leeuwin Current response to the combined open ocean pressure gradient forcing and climatological wind forcing.

The role of the NWS waters appears to be that of an initial baroclinic/barotropic influence followed by a nonlinear baroclinic feedback mechanism. In both parts, the Leeuwin Current flow responds through acceleration to achieve geostrophic balance. The effect of the NWS forcing is moderated by opposing wind stress in Cases 7 and 8, but the flow is so strong that the net result is only a small reduction of the maximum core velocities. It should be remembered that, during this period of NWS-augmented flow, the wind forcing is near its climatological minimum (Figure 5.68).

The relative importance of the NWS waters to the Leeuwin Current energetics can be visualized by comparing the time series of kinetic energy for Cases 5, 6, 7, and 8 (Figure 5.90.a through d) with the total kinetic energy time series previously shown for Cases 1 through 4 (5.28.a, 5.28.b, 5.59.a, and 5.59.b respectively).

The kinetic energy time series for Case 5 (Figure 5.90.a) depicts a small jump in kinetic energy near day 180 when the NWS forcing was initiated. The kinetic energy for the period following the input of the NWS waters more than doubles, continuing to increase through the end of the experiment. The general increase in kinetic energy for this period is also seen for Case 1 (Figure 5.28.a), but it is much smaller.

The trend seen in Case 6 (Figure 5.90.b) shows a slow increase in kinetic energy for the first 80 days (days 180 through 260) following the input of NWS forcing, followed by a sharp growth between days 260 and 300. This growth then slows for the remainder of the experiment. This surge in kinetic energy is consistent with the seasonal surge of the Leeuwin Current.

Case 7 (Figure 5.90.c) shows the same trends in its time series of kinetic energy as Case 6 (Figure 5.90.b). Again, there is a slow growth period of about 80 days following the initiation of NWS forcing. The trend in this period is interpreted as the initial pulse of NWS waters flowing poleward. The large growth in kinetic energy starting near day 260 is attributed to a nonlinear feedback mechanism. The Case 8 (Figure 5.90.d) results depict the same trends as Case 7 (Figure 5.90.c), but are superimposed on the seasonal results of Case 4 (Figure 5.59.b).

G. COMPARISONS WITH PREVIOUS STUDIES

Previous numerical modeling studies of the Leeuwin Current system available for comparison with the results of this study include McCreary et al. (1986), Weaver and Middleton (1989), Batteen and Rutherford (1990), and Batteen et al. (1991). The linear model of McCreary et al. (1986) examined both steady and periodic density-driven flow. Additionally, the influence of a patch of idealized wind forcing was investigated. McCreary et al. (1986) invoke a vertical mixing term to produce and maintain their steady poleward eastern boundary flow. With steady forcing from an assumed mid-latitude temperature gradient of 15°C per 20° of latitude, their model generated a poleward surface flow of approximately 45 cm s^{-1} and an equatorward undercurrent of approximately 10 cm s^{-1} . Results from Case 1, using the spatially-averaged, Levitus (1984) climatological annual mean temperature gradient of only about 7.5°C per 15° of latitude (Weaver and Middleton, 1989; Batteen and Rutherford, 1990; Batteen et al., 1991), show similar surface current velocities but greater undercurrent velocities. The current system achieves a 30-day time-averaged surface current velocity of near 40 cm s^{-1} (Figure 5.13.c) and a 30-day time-averaged undercurrent velocity of near 20 cm s^{-1} (Figures 5.11.c and 5.13.b).

McCreary et al. (1986), employing a simplistic sinusoidal time variation of density, found that periodic density forcing produced a current that was weaker and more surface-trapped than that generated by steady density forcing. Surface current velocities were near 40 cm s^{-1} and undercurrent velocities were near 10 cm s^{-1} . As mentioned in Section 3.H and shown in Figure 3.4, sinusoidal variation of the forcing inadequately describes the forcing in the Leeuwin Current system. Case 2, with comparable forcing conditions, produced surface current velocities near 95 cm s^{-1} (Figure 5.24.c) and undercurrent velocities exceeding 25 cm s^{-1} (Figure 5.12.c).

When superimposing a sinusoidal-time-varying, 1 dyne cm^{-2} , patch of wind forcing, equivalent to a wind velocity of approximately 800 cm s^{-1} , upon their steady thermohaline forcing, McCreary et al. (1986) found that their model produced a response typical of upwelling regions, an equatorward surface flow and a poleward undercurrent (although the response was weak). For the comparable time period and alongshore position, Case 4 shows a similar result (Figure 5.40.a), but, because of the current's poleward intensification due to the accumulation of geostrophic inflow, the equatorward region of the domain examined by McCreary et al. (1986) is the least representative of the Leeuwin Current, as seen by the time-averaged cross-section of the poleward region of the domain for the same time period (Figure 5.40.c). Consequently, the wind forcing will have a greater relative influence on the flow in the equatorward region.

The McCreary et al. (1986) model also suffers from the limitation of being a linear model of a flow regime that has been shown by Weaver and Middleton (1989) to be a highly nonlinear system. As such and as seen, the cases from this seasonal nonlinear study that parallel those of McCreary et al. (1986) produce results more representative of the Leeuwin Current system.

Weaver and Middleton (1989) work with an unforced closed basin nonlinear model. Initial conditions are specified and the model is allowed to evolve from there. The problem with this type of model is that the total energy of the system diminishes with time. Weaver and Middleton (1989) examine the role of shelf topography in trapping the current at the coast. Additionally, they analyze the influence of forcing by the North West Shelf (NWS) waters, employing the same dam-breaking analogy in their model. Their Experiment 1 includes idealized bottom topography and is forced only by annual mean density data. Experiment 3 of Weaver and Middleton (1989) adds the NWS waters as an initial condition, timing the dam-break to coincide with the start of the model run. Both experiments

simulate flow during the first 80 model days. Comparisons will be made here between the Experiments 1 and 3 of Weaver and Middleton (1989) and the comparable cases of this study, Cases 1 and 5. (Their Experiment 2, as a variation of the first and third experiments, provides little additional material for comparison.)

Experiment 1 reveals the inability of the Weaver and Middleton (1989) model to maintain the intensity of the Leeuwin Current for a long period of time; however, the modeled current's resurgence by day 80 illustrates an important nonlinear feedback mechanism that develops. Following the geostrophic adjustment to the initial conditions, Case 1 of this study experiences a similar sequence of events. The isotherm pattern leading to the feedback mechanism is similar between this study and the Weaver and Middleton (1989) results. Due to the inclusion of topography in their model (and consistent with Thompson, 1981), the isotherms in Weaver and Middleton (1989) display an equatorward bent over the shelf near the coast. During the initial surge to geostrophically adjust to the initial conditions, the Weaver and Middleton (1989) model achieves poleward velocities of the order of 30 cm s^{-1} , diminishing to around 20 cm s^{-1} by day 40 and subsequently intensifying to around 40 cm s^{-1} at the poleward end (20 cm s^{-1} at the equatorward end) by day 80. The associated undercurrent reaches speeds of the order of 15 cm s^{-1} , with the strongest intensities at the equatorward end. In contrast, Case 1 achieves an initial adjustment poleward velocity of near 80 cm s^{-1} , a day 40 maximum poleward velocity near 50 cm s^{-1} (Figure 5.5), and a day 80 maximum poleward velocity of 40 cm s^{-1} (Figure 5.7). The 30-day time-averaged undercurrent developed by Case 1 at day 60 exceeds 20 cm s^{-1} and is centered near 500 m depth at the poleward end, rising and weakening significantly with equatorward alongshore distance (Figure 5.11). There is no apparent eddy generation in Weaver and Middleton (1989); in contrast, Case 1 shows a distinct indication of eddy generation during the same model period (Figure 5.7.a and d). This difference is likely due to this study's use of biharmonic damping versus the Laplacian damping used by Weaver and Middleton (1989).

Experiment 3, from Weaver and Middleton (1989), includes the NWS waters. The eastern boundary current's (EBC) poleward velocities, measured at day 30, are a maximum of 23 cm s^{-1} at the equatorward end of the Leeuwin Current domain and a maximum of 29 cm s^{-1} at the poleward end. The equatorward value increases to 30 cm s^{-1} and the poleward value decreases to about 25 cm s^{-1} respectively by day 40. The negligible change at the poleward end, with respect to Experiment 1, is attributed to insufficient model time to allow advection of the NWS waters to that

region. Additionally, as expected from an advected quantity, there is a diminishing influence from the NWS waters with increasing distance from the source. After the nonlinear feedback mechanism has reinvigorated the poleward flow, poleward surface velocities at the equatorward of the Leeuwin Current domain are around 28 cm s^{-1} and at the poleward end are over 50 cm s^{-1} . The undercurrent, typically between 5 and 10 cm s^{-1} , in contrast with Experiment 1, now rises and weakens with equatorward alongshore distance.

Case 5, 30 days after initiation of NWS forcing (Figure 5.78), exhibits significant increases in poleward velocities of the EBC. Note that maximum core velocities exceed 40 cm s^{-1} and that eddies are more intense. (Because this study initiated the NWS forcing in the middle of the model run (day 181), the notation for the number of days following the initiation of the NWS forcing will be a primed value, e.g. day 30'). The intensification continues through day 40', with maximum velocities exceeding 60 cm s^{-1} adjacent to the NWS initialization region and also in the vicinity of eddies. By day 80' (day 260), the poleward EBC velocities were greater than 40 cm s^{-1} , exceeding 60 cm s^{-1} in several isolated spots. The cross-section of the 20-day time-averaged flow at day 20' depicts a 50 cm s^{-1} poleward surface current and a 5 cm s^{-1} equatorward undercurrent at the poleward end and a 20 cm s^{-1} poleward surface current with a 5 cm s^{-1} equatorward undercurrent at the equatorward end (Figure 5.91). The 20-day time-average at day 60' shows a 40 cm s^{-1} surface current over a 50 cm s^{-1} undercurrent (Figure 5.92). Both the surface current and the undercurrent have been transformed into much stronger and tighter cores of flow. Comparisons with Figure 5.26 show the significant enhancement that the NWS waters provide to the poleward surface flow and the equatorward undercurrent.

Weaver and Middleton (1989) acknowledge that the short periods of the experiments in their paper may be inadequate to resolve the dynamics of the Leeuwin Current and that, during the period of their model runs, their model is still subject to important influences from transient responses related to the initialization of the model. Decaying transient features of the adjustment process are still evident at day 80. The results of this study are consistent with the 80 days required for model adjustment seen by Weaver and Middleton (1989). The kinetic energy plots of Cases 1 through 3 are virtually identical through day 80. The kinetic energy plot for the first 80 days of Case 4 depicts the same energy trend as the other three cases with only slightly smaller magnitudes. This result provides evidence for the conclusion that the adjustment process to the initial conditions is still significantly affecting the flow regime through day

80. Consequently, the method for initiating the NWS forcing used by this study provides a better representation of the influence of the NWS waters on the Leeuwin Current flow. Additionally, with the method in this study, the interactions of the NWS waters with an existing flow field can be examined. Comparisons of the appropriate cases of this study with Batteen and Rutherford (1990) reveal the differences attributed to the application of continuous ocean thermal forcing. The use of the same model design and physics allows for a close comparison of results. Case 1 of this study correlates with Case 1 of Batteen and Rutherford (the Cases in Batteen and Rutherford will be referred to as Experiments from here on to eliminate confusion).

Experiment 1 (Batteen and Rutherford, 1990) produces initial (day 10) poleward velocities of near 70 cm s^{-1} , day 40 velocities near 30 cm s^{-1} , day 80 velocities near 20 cm s^{-1} , day 120 velocities near 40 cm s^{-1} , and day 160 velocities near 50 cm s^{-1} . Case 1 results show corresponding velocities for day 10 near 80 cm s^{-1} , day 40 near 50 cm s^{-1} , day 80 near 40 cm s^{-1} , day 120 near 60 cm s^{-1} , and day 160 near 60 cm s^{-1} (Figures 5.5, 5.7, and 5.10). A comparable time-averaged cross-section, a 30-day average centered on day 60 (Figure 5.11.c), shows a surface current of 30 cm s^{-1} and an undercurrent of slightly more than 20 cm s^{-1} versus 18 cm s^{-1} for the surface current and 14 cm s^{-1} for the undercurrent in Batteen and Rutherford (1990). These higher magnitudes are more consistent with the data obtained during the Leeuwin Current Interdisciplinary Experiment (LUCIE). A comparison of model data from this study with LUCIE data is included in the following section.

Experiment 2 from Batteen and Rutherford (1990) examines the additional influence of the NWS forcing. Their poleward EBC begins with an initial surge (day 10) of about 120 cm s^{-1} , weakening by day 40 to about 40 cm s^{-1} , and then rebuilding and leveling off near 80 cm s^{-1} for days 80 through 160. Comparable periods in experiment 5 (annotated as before with primed days for days after initiation of NWS forcing at day 181) show a somewhat different evolution. Day 10' depicts a poleward current velocity maximum of near 60 cm s^{-1} , staying at that level through day 80', and then building to near 80 cm s^{-1} by day 120', leveling off there through day 160' (Figures 5.78, 5.79, and 5.80). The very large poleward velocity achieved by Batteen and Rutherford appears to be due to rapid geostrophic adjustment in response to initial conditions. Their experiment design allows the NWS waters to amplify the initial adjustment response. The better measure of the NWS water influence is in the magnitude of the current's resurgence in response to the nonlinear feedback mechanism, because that is a function of the baroclinic conditions created by

poleward advection of the NWS waters. Note that the ultimate response to the imposition of the same NWS forcing as in Batteen and Rutherford (1990), but with the remainder of the domain already geostrophically adjusted and an existing eddy field in place, yields similar magnitudes, despite the convoluted flow pattern. The time-averaged meridional cross-section presented in Batteen and Rutherford shows a surface current of near 45 cm s^{-1} and an undercurrent near 30 cm s^{-1} . The corresponding time-averaged cross-section for Case 5 (Figure 5.92.b) depicts a surface current near 45 cm s^{-1} and an undercurrent near 50 cm s^{-1} , comparable to Batteen and Rutherford and consistent with LUCIE (Boland et al., 1988).

Batteen et al. (1991) apply an idealized wind, representing the climatological winds for the austral autumn, to the same thermal forcing cases as in Batteen and Rutherford (1990). Their two experiments correspond with Cases 3 and 7 of this study. The results of Case 3 are very similar to Batteen et al. (1991). Principal differences appear to be a greater strength and development of eddies in Case 3. This difference is consistent with the difference between continuous thermal forcing versus evolution from only an initial condition. The poleward velocities produced in Experiment 1 show significant differences only in the initial adjustment period (day 10) and at day 160. In both instances, the velocities in Case 3 are about 15 cm s^{-1} greater than those in Experiment 1. The EBC maximum velocities in Case 3 are about 70 cm s^{-1} at day 10, 40 cm s^{-1} at day 40, 20 cm s^{-1} at day 80, 20 cm s^{-1} at day 120, and 40 cm s^{-1} at day 160 (Figures 5.36 and 5.39).

Experiment 2 from Batteen et al. (1991) adds the NWS forcing to the annual mean thermal forcing and the idealized wind forcing. Again there are velocity differences resulting from the initial adjustment stage, with Experiment having velocities near 100 cm s^{-1} at day 10 versus Case 7 having velocities near 80 cm s^{-1} at day 10'. Both Experiment 2 and Case 7 had velocities near 40 cm s^{-1} at day 40 (40'), 60 cm s^{-1} at day 80 (80'), and 60 cm s^{-1} at day 120 (120') (Figures 5.84, 5.85, and 5.86). By day 100', Case 7 flow had intensified to near 100 cm s^{-1} (Figure 5.86), while Experiment 2 remained near 60 cm s^{-1} . The consistency between results from this study's method for adding the NWS forcing and Batteen et al. (1991), following the first 40 model days indicates that the initial high velocities in Batteen et al. (1991) are principally due to model adjustment to the initial conditions and that the results, starting at about day 60, are more representative of the Leeuwin Current system.

H. LEEUWIN CURRENT INTERDISCIPLINARY EXPERIMENT DATA

The Leeuwin Current Interdisciplinary Experiment (LUCIE), conducted from September 1986 to August 1987, provided the first comprehensive data on the Leeuwin Current. The model results from this study will be compared with the findings presented in Smith et al. (1991) to demonstrate the validity of this modeling effort. It should be noted at the outset that Smith et al. (1991) recognize several limitations in the design of the LUCIE data collection, including the observation that the eddies and the undercurrent associated with the Leeuwin Current were not adequately defined by the current meter arrays.

The results from Case 8 will be used for comparison with the LUCIE data because they are considered the most representative of the Leeuwin Current System. Smith et al. (1991) report 325-day-mean poleward surface velocities of near 30 cm s^{-1} (near 50 cm s^{-1} for some shorter periods at some locations on the upper slope) and equatorward undercurrent velocities near 10 cm s^{-1} (Figure 5.93). The 360-day time-averaged flow produced by Case 8 just exceeded 30 cm s^{-1} for the poleward surface current and was near 10 cm s^{-1} for the equatorward undercurrent (Figure 5.94). Case 4, the same as Case 8 but without the NWS forcing, produced a 15 cm s^{-1} poleward surface current and an equatorward undercurrent exceeding 5 cm s^{-1} (Figure 5.95).

A better measure of model performance is the examination of seasonal averages versus observations. Smith et al. (1991) describe the Leeuwin Current seasonal cycle as being weakest and shallowest from November through January, as strongest from March through May, and as becoming broader, somewhat weaker, and shallower between May and July. The strongest poleward flow is noted in March, with the velocity maximum advecting poleward with time and remaining very strong through August, exceeding 100 cm s^{-1} offshore of LUCIE current meter arrays during June. LUCIE measured a large alongshore transport in March at the North West Cape, suggesting the augmentation of the Leeuwin Current by flow from the North West Shelf at this time. The undercurrent was strongest near the shelf edge in the late austral summer and early austral autumn (March through May). The undercurrent migrated seaward in the austral winter (June through August), becoming weaker and closer to the shelf edge in the austral spring (September through December), and then almost vanishing in early summer (January). (Smith et al, 1991)

Smith et al. (1991) provide four seasonally-averaged meridional velocity cross-sections (Figure 5.93). Model results for the same periods (Figures 5.96, 5.97, and 5.98) show a close resemblance to the LUCIE observations. For the first period, November through mid-January, LUCIE

data depict a poleward surface current near 20 cm s^{-1} and an equatorward undercurrent near 10 cm s^{-1} (Figure 5.93). The model also produced a poleward surface current near 20 cm s^{-1} and an equatorward undercurrent near 10 cm s^{-1} (Figure 5.96).

During the second period, March through mid-May, the Leeuwin current is the strongest, with observations recording a poleward surface current near 55 cm s^{-1} and an equatorward undercurrent near 5 cm s^{-1} (Figure 5.93). For the same period, the model develops a poleward surface current of over 35 cm s^{-1} and an equatorward undercurrent of near 30 cm s^{-1} (Figure 5.97). The large difference between the model's results and observed values of the undercurrent is attributed to modeling simplifications, in particular the dam breaking analogy versus a somewhat smoother, more gradual release of the NWS waters in nature, and the poor resolution of the LUCIE undercurrent measurements. Additionally, this averaging period brackets the model's initiation of the NWS waters, so there is some initial adjustment noise and weaker pre-initiation flow included in the period's average flow velocity. The data indicate that strong poleward flow near the North West Cape already exists by mid-March (Smith et al. 1991), suggesting that the model's dam break of NWS waters should perhaps be initiated earlier, e.g., in mid-February or early March.

The observations from the third period, mid-May through the end of July, shows a diminishing and broadening of the Leeuwin Current, with peak poleward core velocities near 30 cm s^{-1} and equatorward undercurrent velocities near 5 cm s^{-1} (Figure 5.93). The model produced a peak poleward surface velocity of near 50 cm s^{-1} and an equatorward undercurrent velocity near 5 cm s^{-1} (Figure 5.98). The broadening nature of the flow is also followed by the model (Figure 5.99). The higher model surface velocity could be attributed to the insufficient offshore extent of the LUCIE current meter arrays, as noted by Smith et al. (1991). Current velocities in excess of 100 cm s^{-1} were observed offshore during this period. Also the nonlinear feedback mechanism (Weaver and Middleton, 1989) responds to the NWS water pulse and becomes significant during this time period. Because this nonlinear feedback mechanism is a function of baroclinicity, the effects of choices made for the NWS water climatology are amplified. As seen in the above comparisons, the model demonstrates a strong resemblance to the LUCIE observations and serves as notable evidence in support of the modeling techniques and choices used in this study. Seasonal 30-day time-average plots of u , v , and T (Figure 5.99) highlight representative flow patterns and depict the seasonal nature of the Leeuwin Current.

A time series of daily, spatially-averaged, meridional velocity values (Figure 5.100), for a coastal strip (of approximately 45 km) extending the length of the domain, provides an interesting comparison of the flow produced by Case 8 versus the current meter records from LUCIE (Smith et al., 1991). Features seen in the time series of model output include: the initial model adjustment (days 0 to 80); the nonlinear feedback to the initial conditions (days 80 to 120); the austral summer weakening of the Leeuwin Current flow (days 120 to 180); the NWS dam-break (days 180 to 200); the poleward advection and reduction of the NWS signal (days 200 to 220); the nonlinear response to the NWS pulse (days 220 to 260); baroclinic Rossby wave propagation (days 260 to 300); and the strong mid-winter flow (days 300 to 360). Note the strong similarities of the Case 8 time series with the LUCIE data for a comparable span of time (Figure 5.100).

The LUCIE observations (Smith et al., 1991) also confirm that there is greater flow variability with increasing poleward alongshore distance, specifically at 34°S versus 29.5°S. Consistent with this observation, the model has a much greater tendency for eddy generation at the poleward end of the domain. The compounding geostrophic inflow with poleward alongshore distance contributes to a greater tendency for barotropic instability. Also, the poleward advection of warm equatorial waters increases the likelihood, with increasing poleward alongshore distance, of baroclinic instability at the current's seaward front.

Smith et al. (1991) observe that the LUCIE data reveal no significant seasonal variation of the alongshore gradient of the vertical integral of geopotential anomaly. However, these observations may not extend sufficiently far offshore to capture the seasonal signal. Variations in the alongshore pressure gradient, the principal forcing mechanism for the Leeuwin Current, may be masked by the alongshore advection of equatorial waters, which force isotherms more parallel to the shore. Also noted was that surface Ekman transport is negligible with respect to the geostrophic transport even if the wind stress was underestimated by a factor of two. These two forcing mechanisms have similar relative strengths in the forcing of this model (Figure 5.69). Smith et al. (1991) suggest that the wind drag coefficient (C_D) should be greater than 1.5×10^{-3} during the austral winter (June, August, and September) to be consistent with the observed wave climate. This model uses a constant C_D equal to 1.3×10^{-3} . While the wave climate may merit a larger wind drag coefficient, it is noted that the winds during this period are the weakest of the annual cycle and that the winds are oriented in their most cross-shore direction,

minimizing the effect of a smaller drag coefficient on the modeled Leeuwin Current flow.

In summary, the model in Case 8 is able to closely follow the seasonal variations in the strength and character of the Leeuwin Current. The associated undercurrent and flow variability (eddies) are also reproduced with close resemblance to observations. Possible refinements to the model include better choices on when to initiate the NWS forcing into the model, to better represent the thermodynamic characteristics of the NWS water mass.

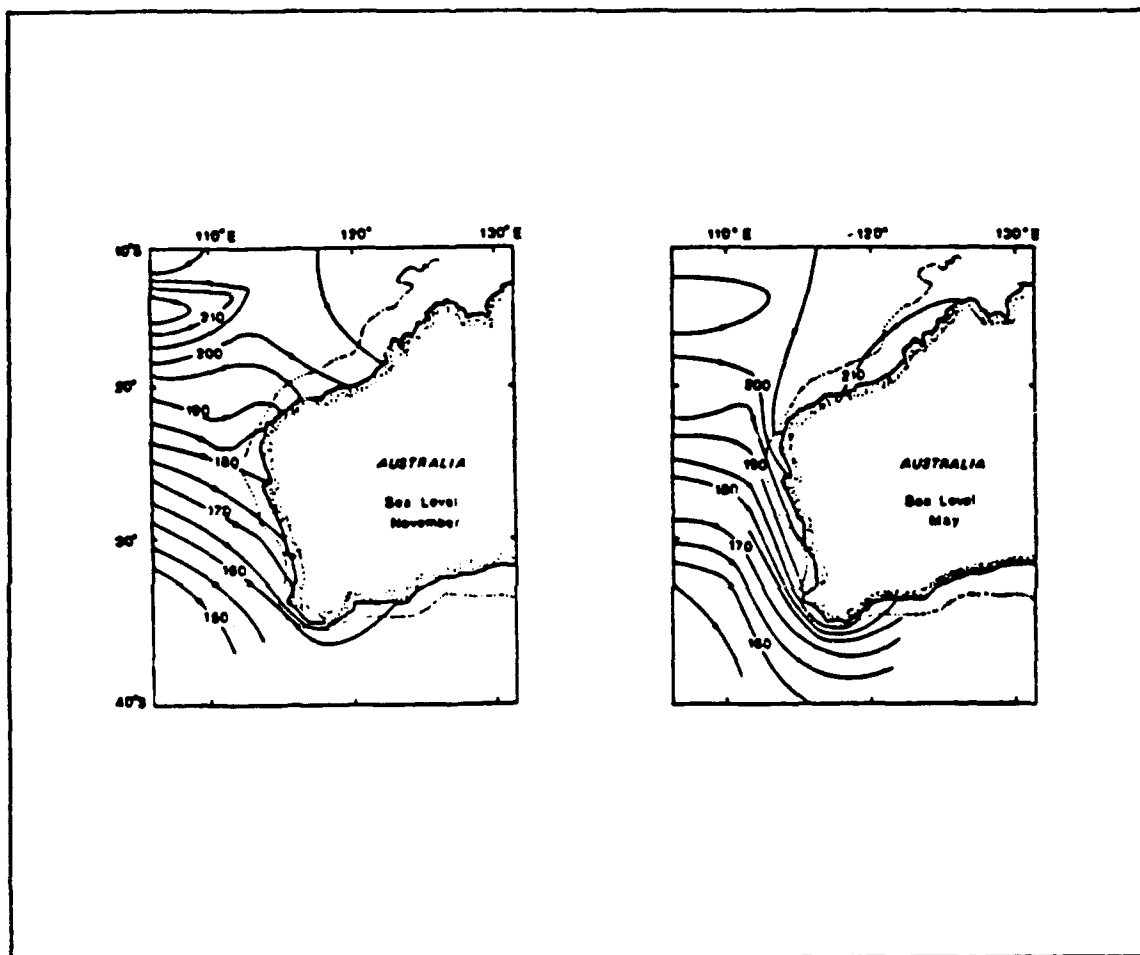


Figure 5.1 Observed seasonal dynamic height fields off Western Australia: Observations (m) relative to 1300 dbar (from McCreary et al., 1986; after Godfrey and Ridgway, 1985).

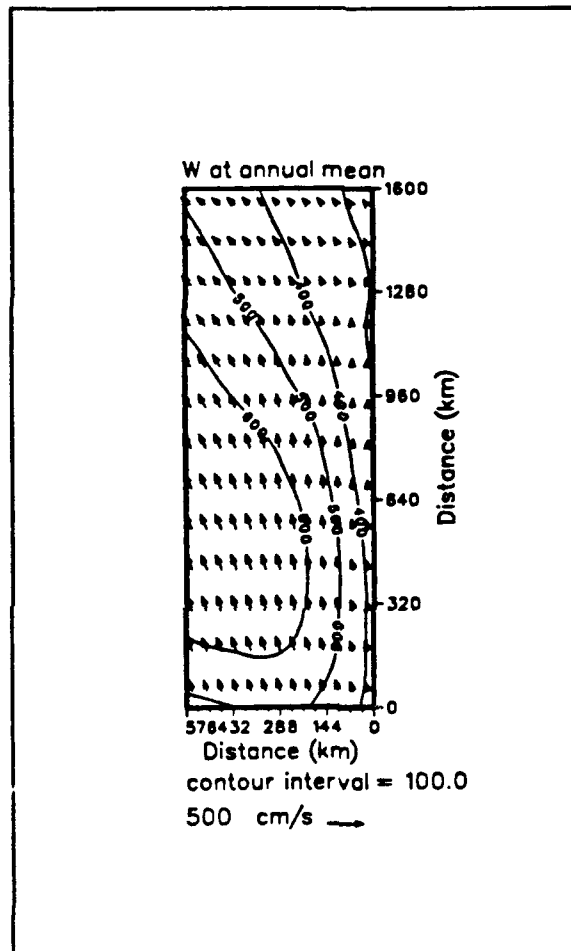
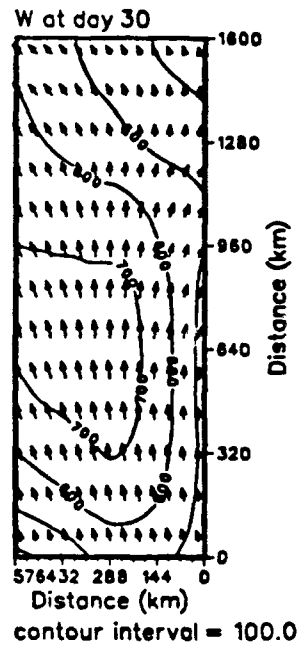
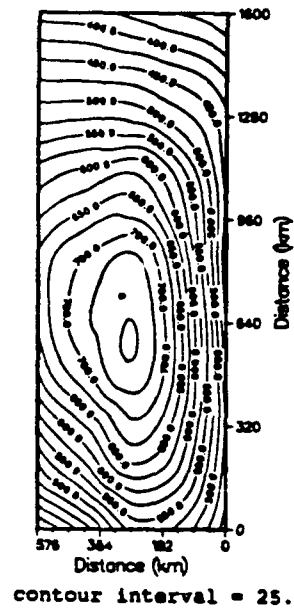


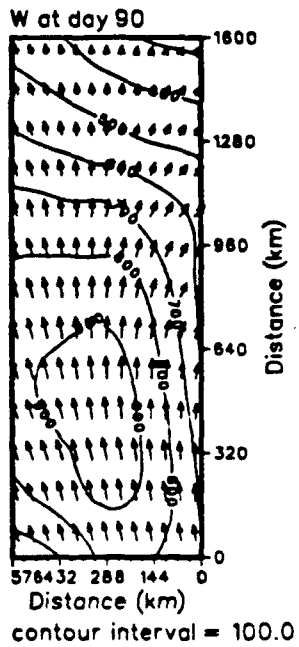
Figure 5.2 Annual mean wind vector field with magnitude contours for model domain: Contour interval (100 cm/s).



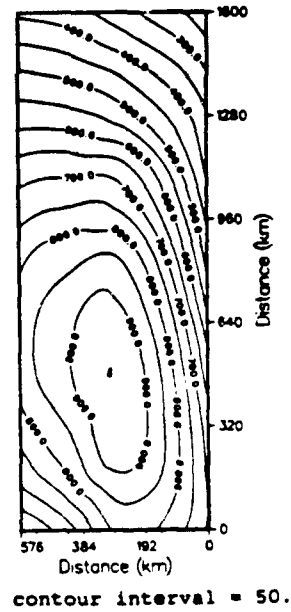
a



b



c



d

Figure 5.3 Seasonal mean wind vector fields and meridional component contour plots for model domain: (a, b) October, (c, d) December.

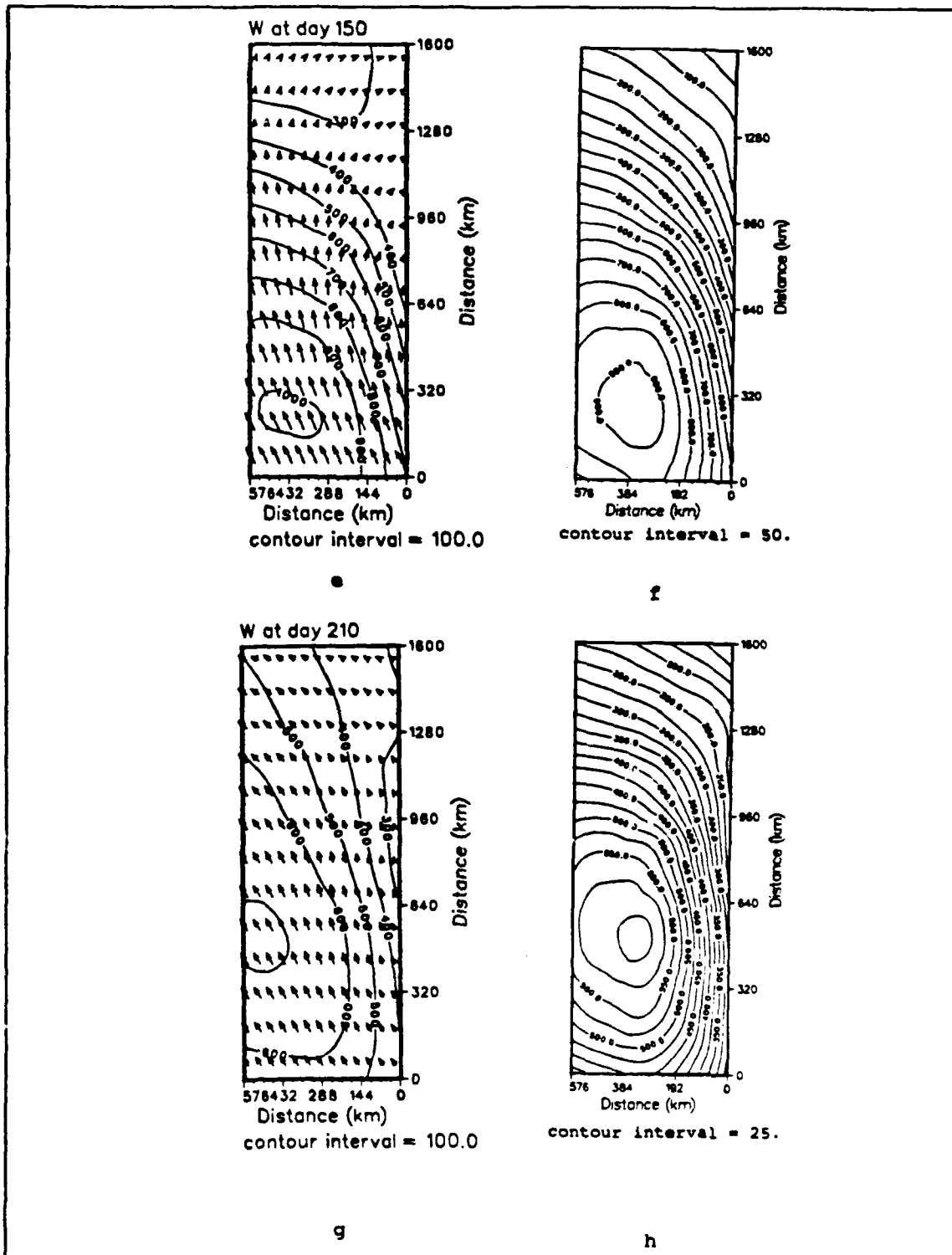


Figure 5.3 cont. Seasonal mean wind vector fields and meridional component contour plots for model domain. (e, f) February, (g, h) April.

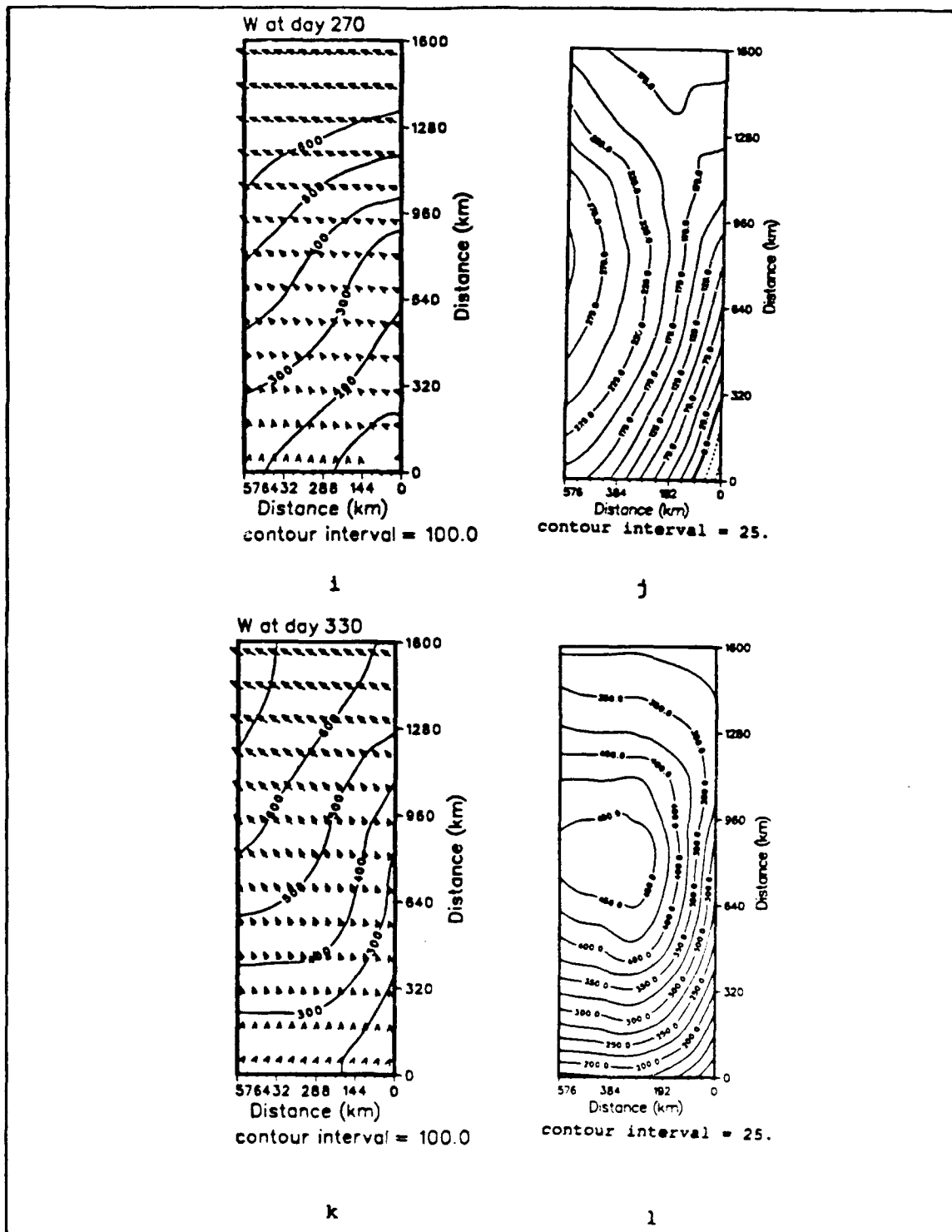


Figure 5.3 cont. Seasonal mean wind vector fields and meridional component contour plots for model domain: (i, j) June, (k, l) August; dashed contours denote negative (poleward) values.

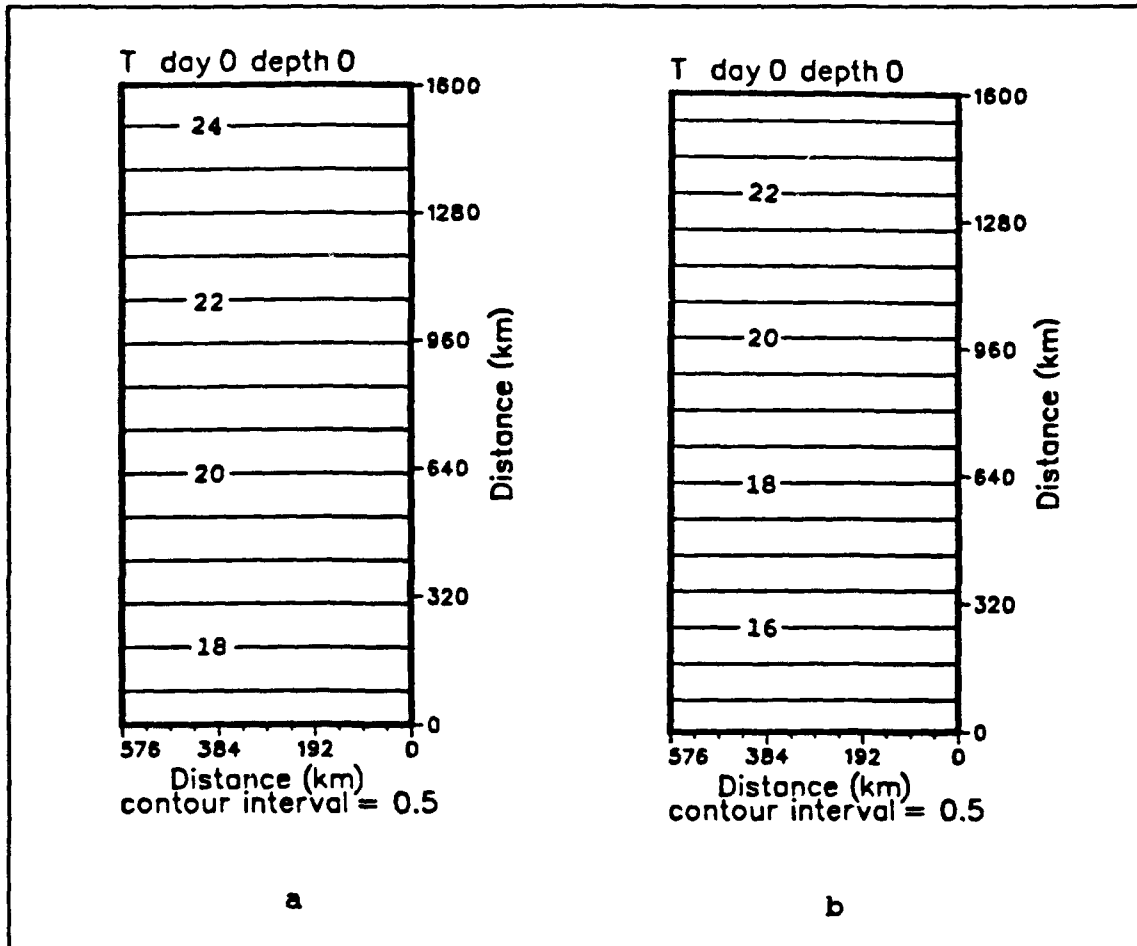


Figure 5.4 Initial condition for surface temperature field: (a) Annual mean climatology forcing; (b) seasonal climatology forcing for mid-September (nominally 15 Sep.); contour interval (0.5 °C).

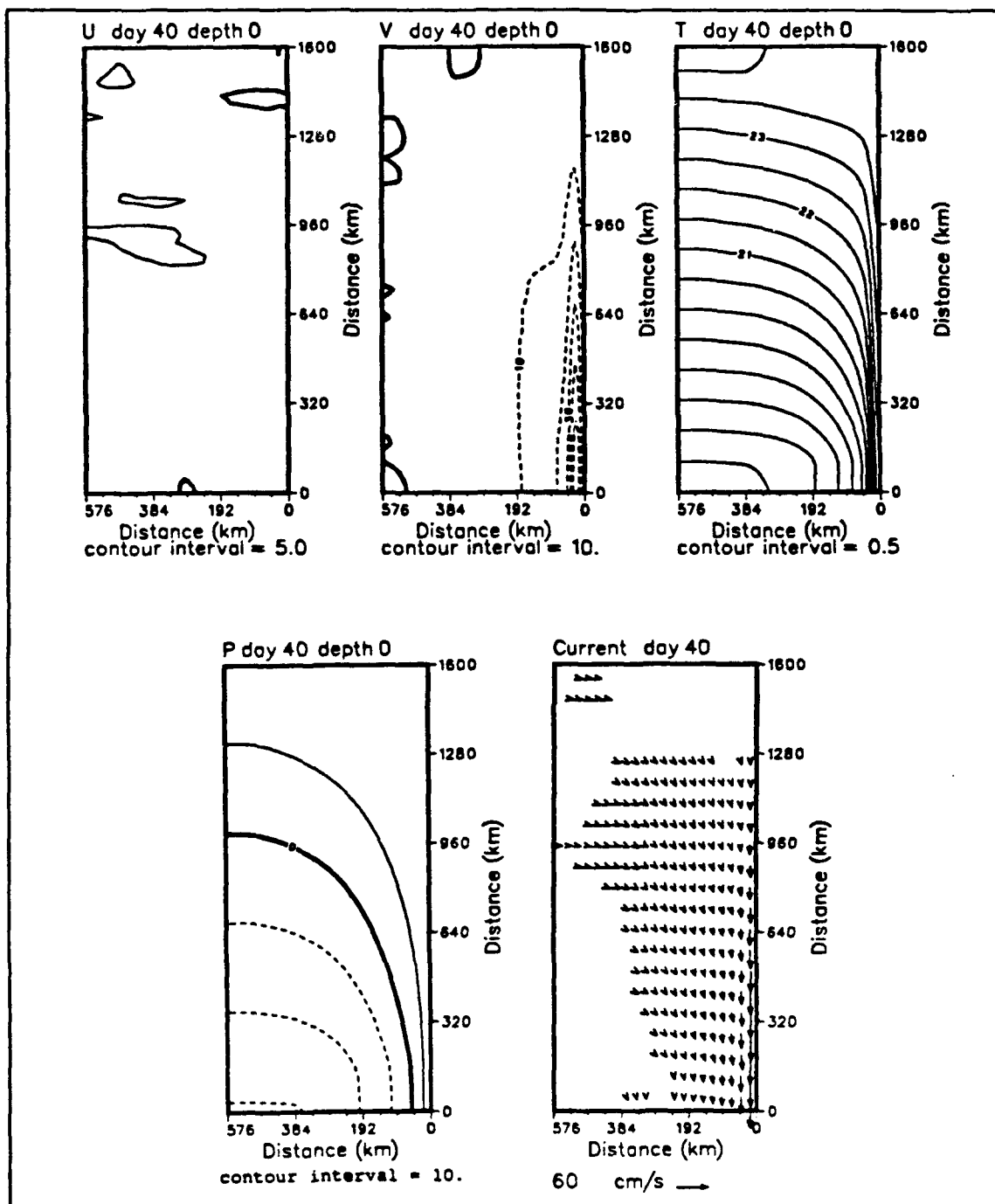


Figure 5.5 Case 1 surface fields, day 40: Dashes denote negative values; velocity (cross-shore, alongshore) (cm/s), temperature (°C), pressure (dynamic height anomaly (cm), ref. 2000 m), current velocity vectors. To avoid clutter, velocity vectors for all following vector plots are plotted at every fifth gridpoint in both the cross-shore and alongshore directions, and velocities less than 5 cm/s are not plotted.

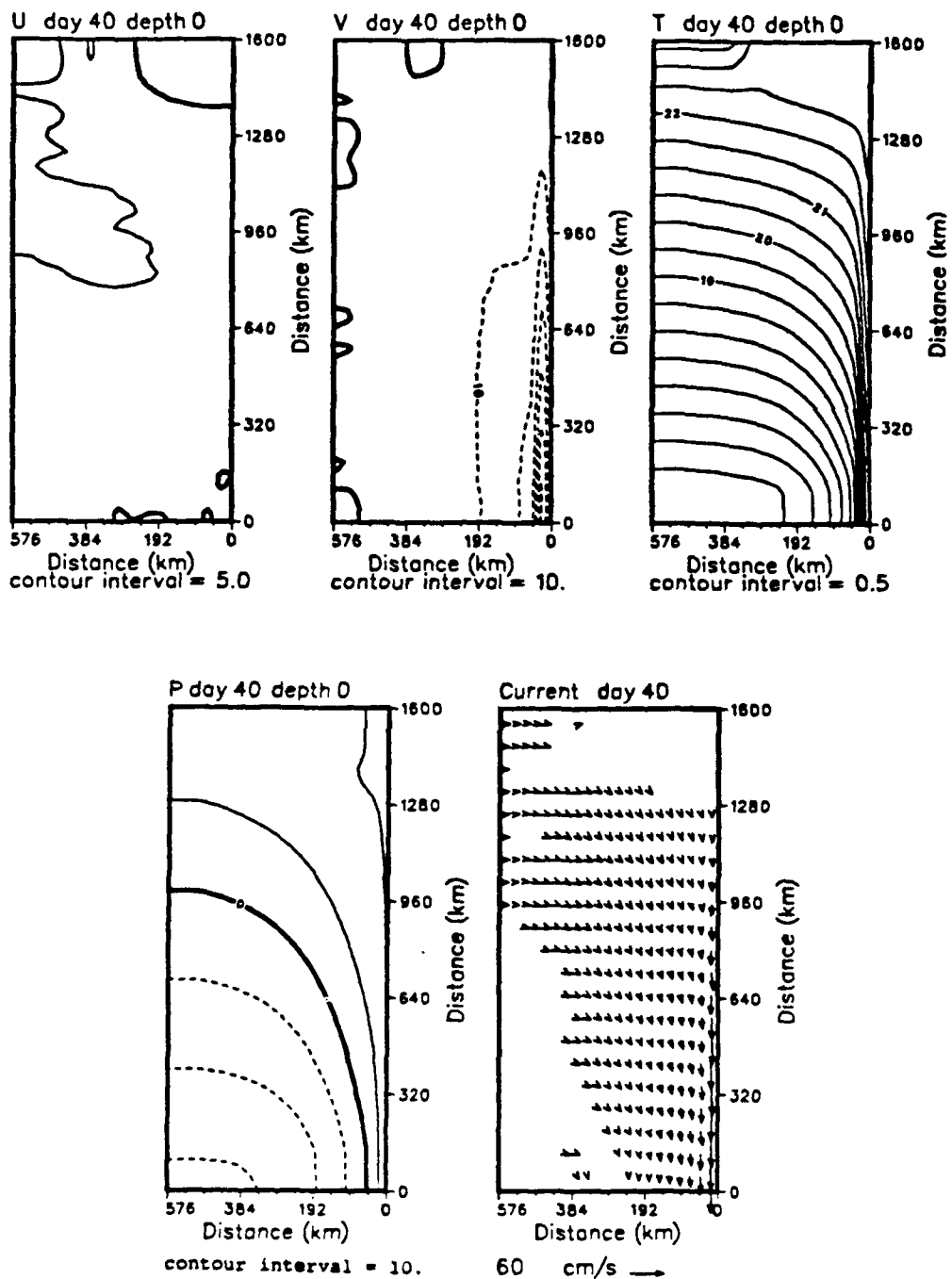


Figure 5.6 Case 2 surface fields, day 40: As for Figure 5.5.

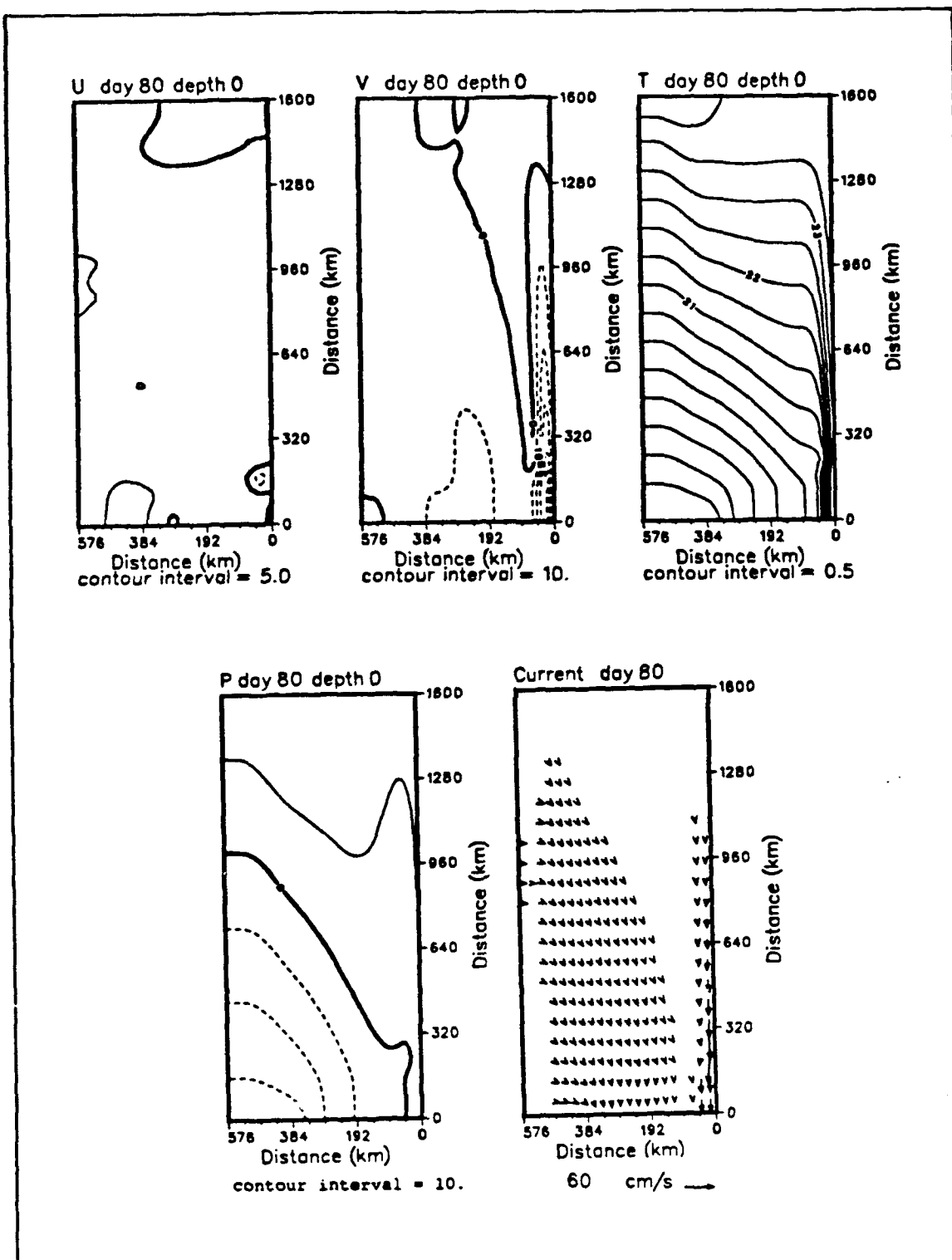


Figure 5.7 Case 1 surface fields, day 80: As for Figure 5.5.

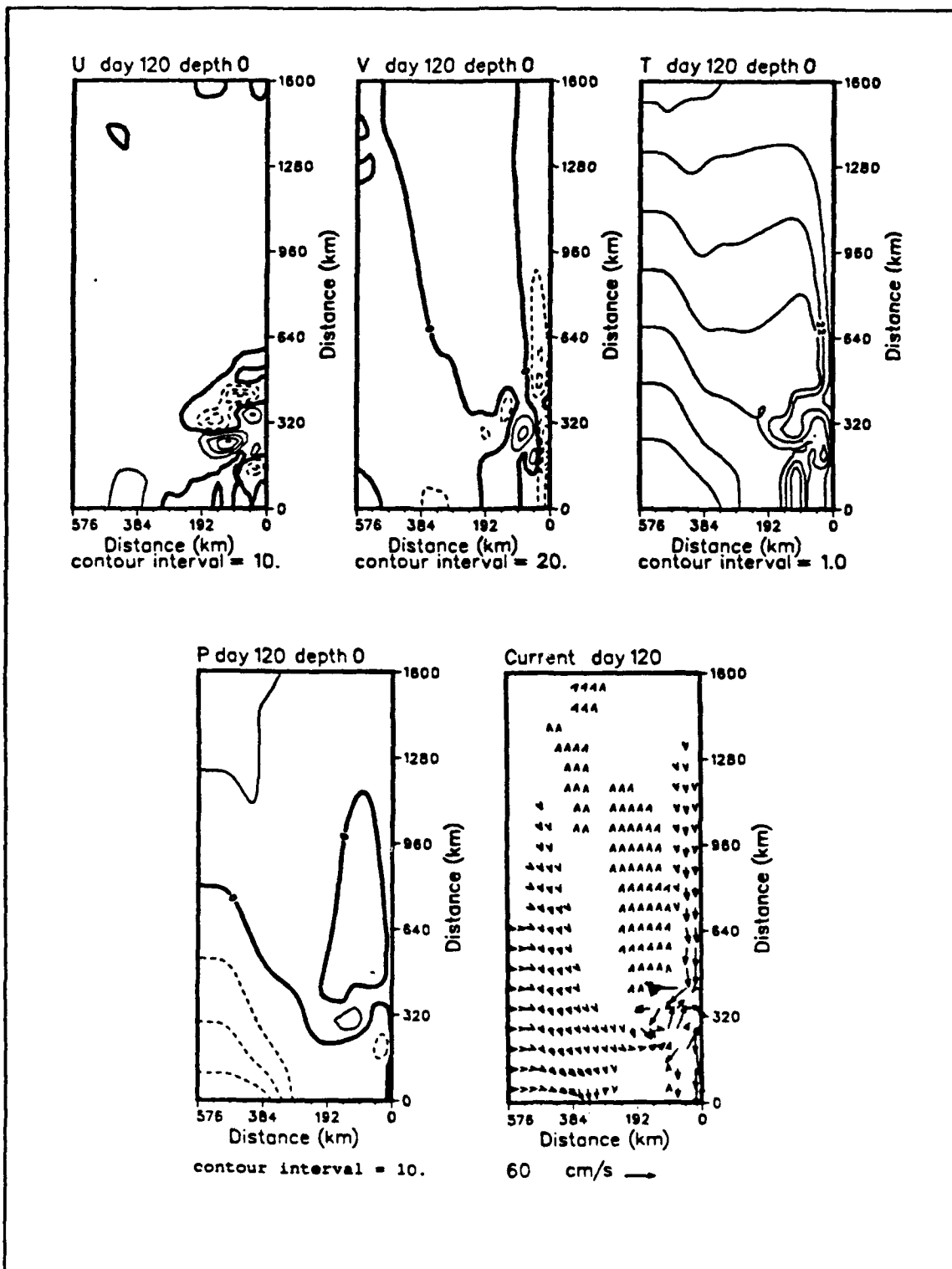


Figure 5.8 Case 1 surface fields, day 120: As for Figure 5.5.

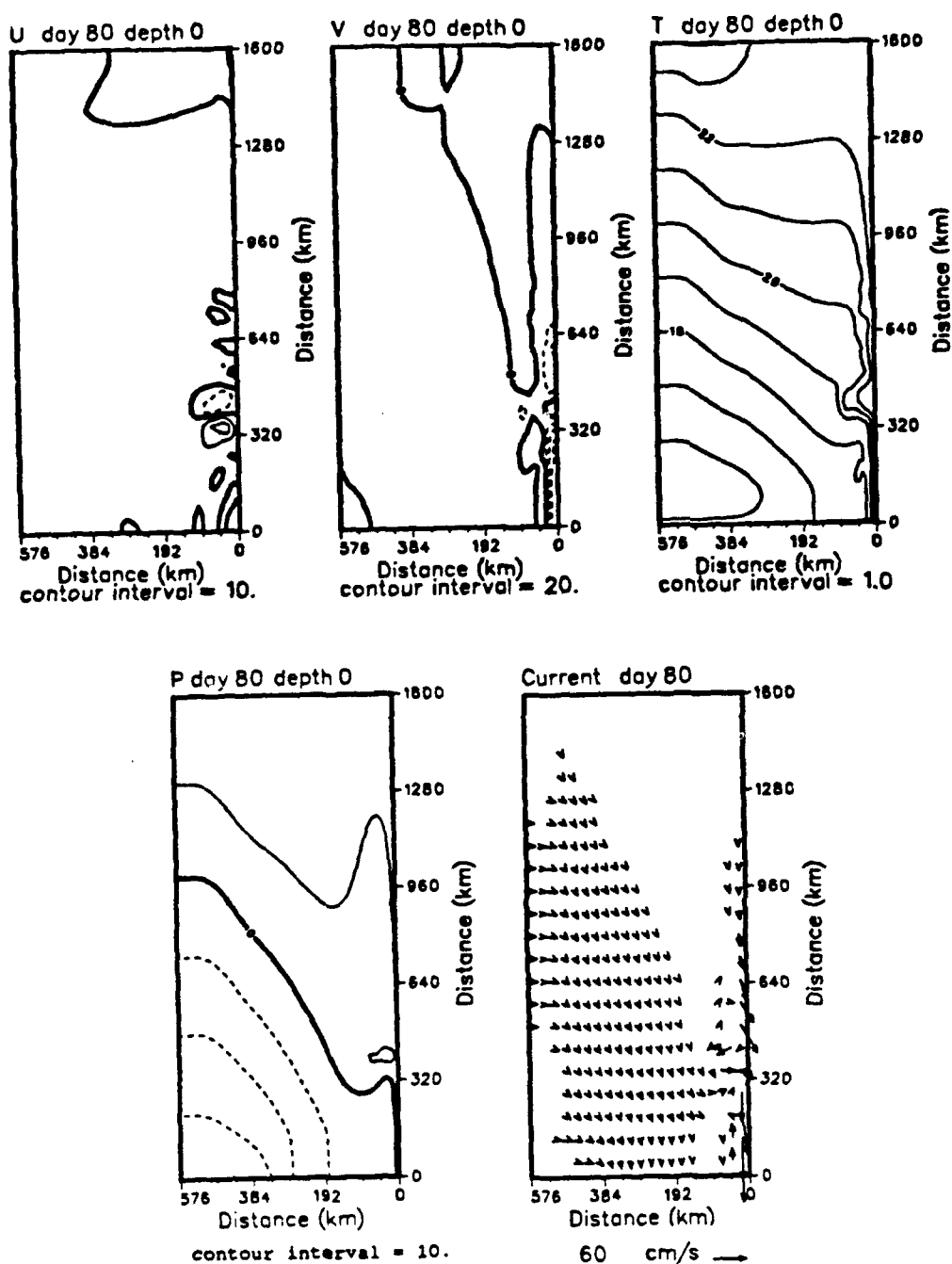


Figure 5.9 Case 2 surface fields, day 80: As for Figure 5.5.

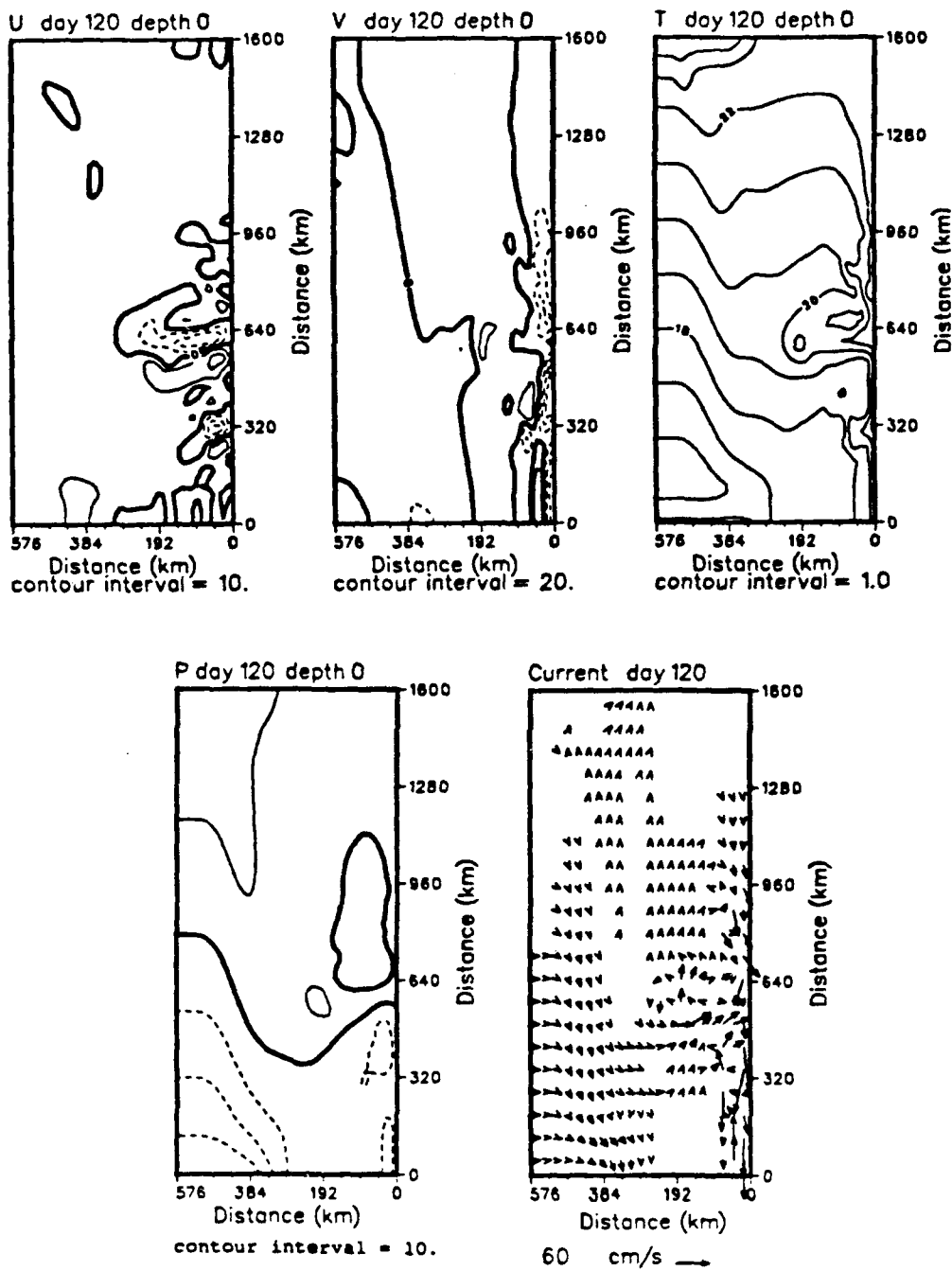


Figure 5.10 Case 2 surface fields, day 120: As for Figure 5.5.

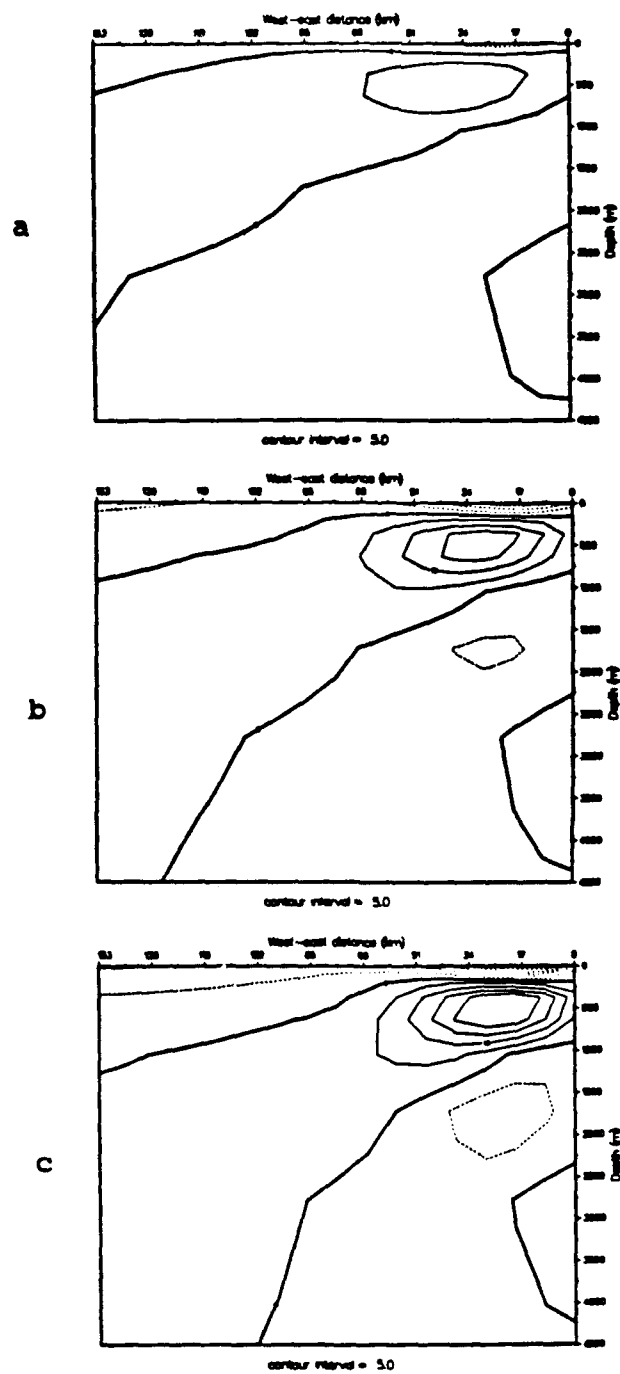


Figure 5.11 Case 1 30-day time-averaged meridional velocity cross-sections centered on day 60: Velocity (cm/s) (negative values denote poleward flow), (a) equatorward ($y = 1125$ km), (b) mid-domain ($y = 800$ km), (c) poleward ($y = 475$ km) regions.

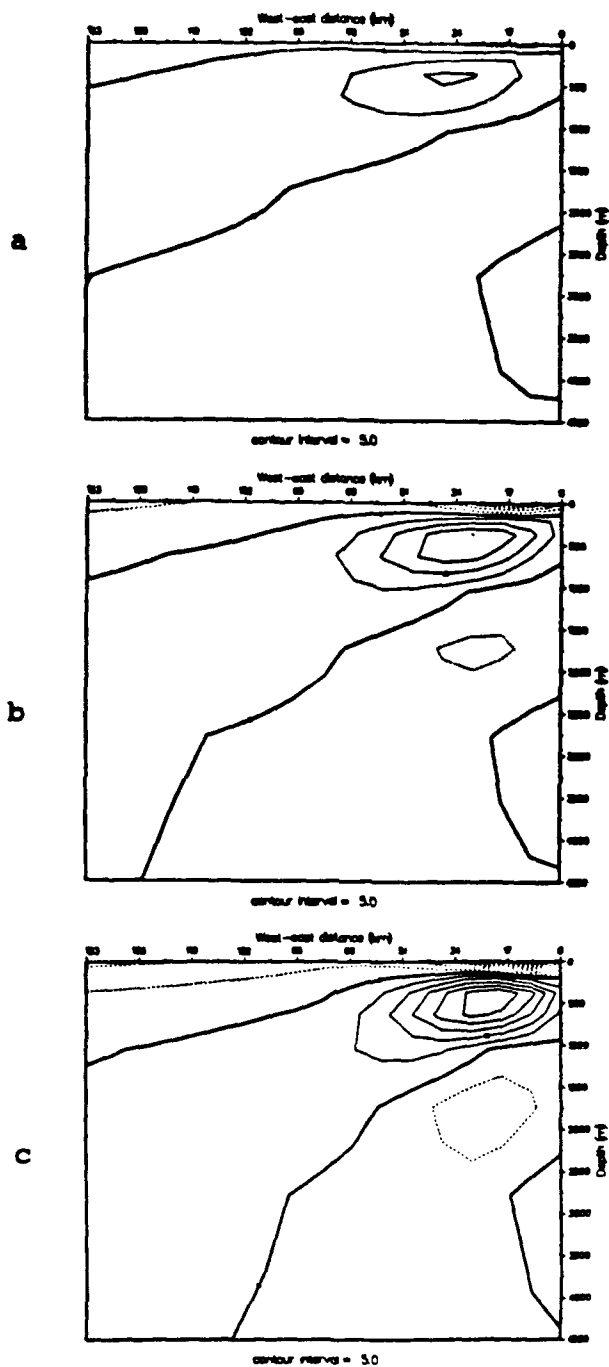


Figure 5.12 Case 2 30-day time-averaged meridional velocity cross-sections centered on day 60: As for Figure 5.11.

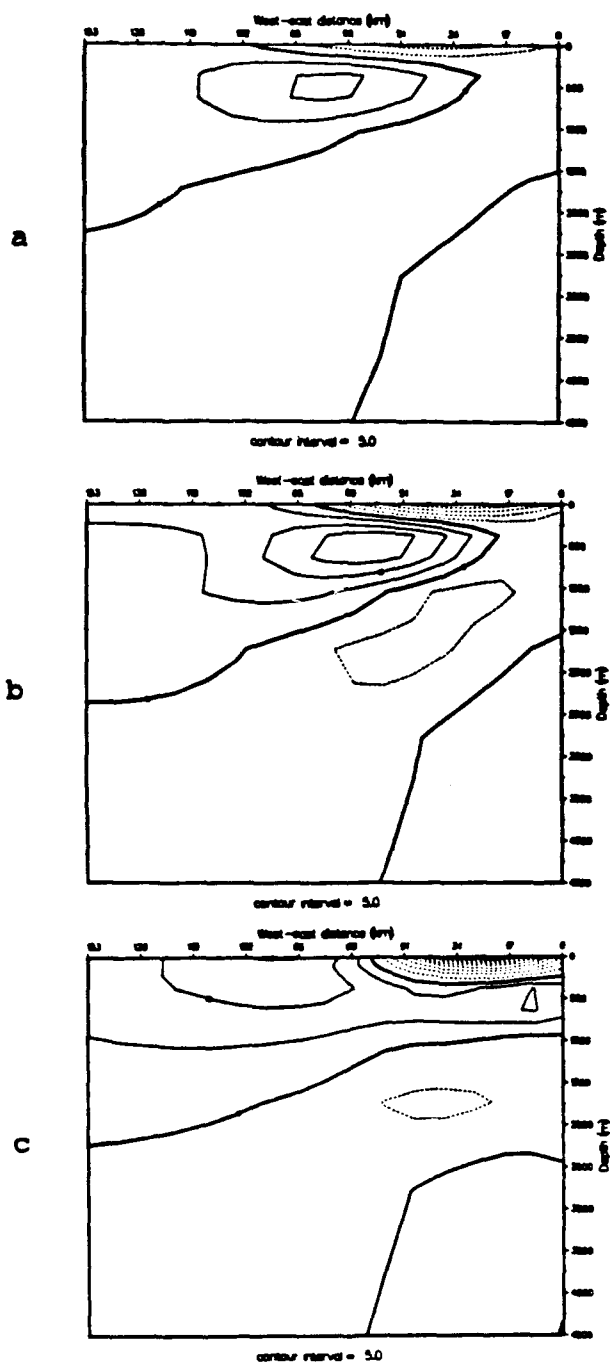


Figure 5.13 Case 1 30-day time-averaged meridional velocity cross-sections centered on day 120: As for Figure 5.11.

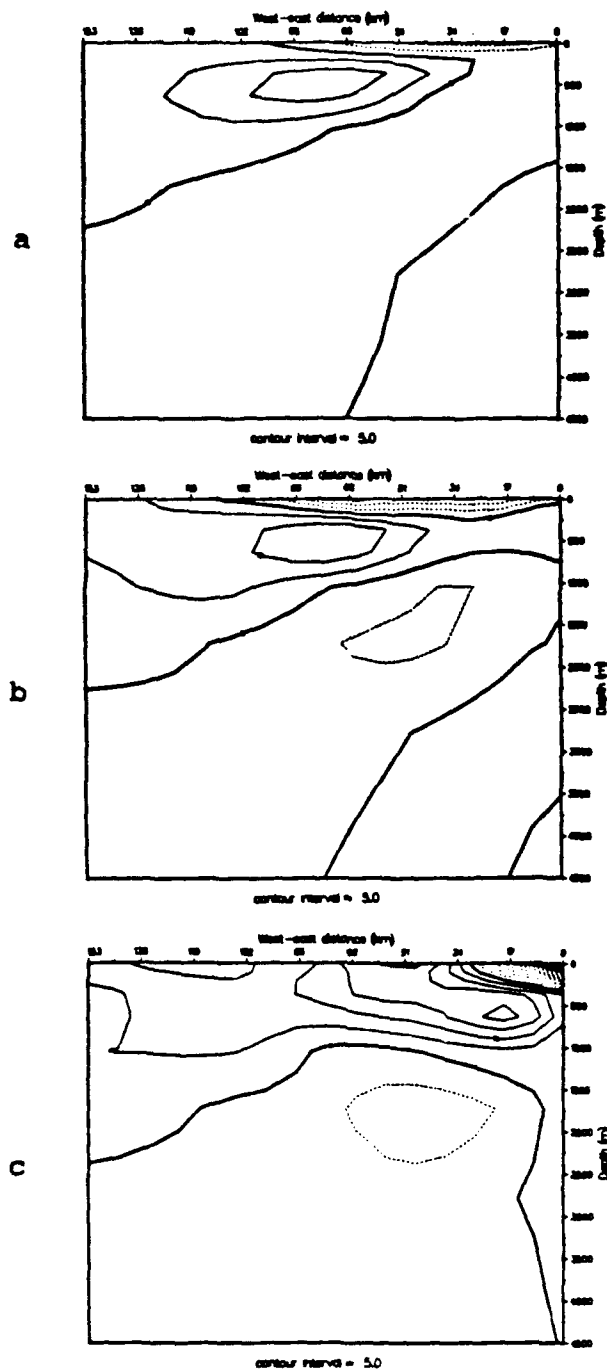


Figure 5.14 Case 2 30-day time-averaged meridional velocity cross-sections centered on day 120: As for Figure 5.11.

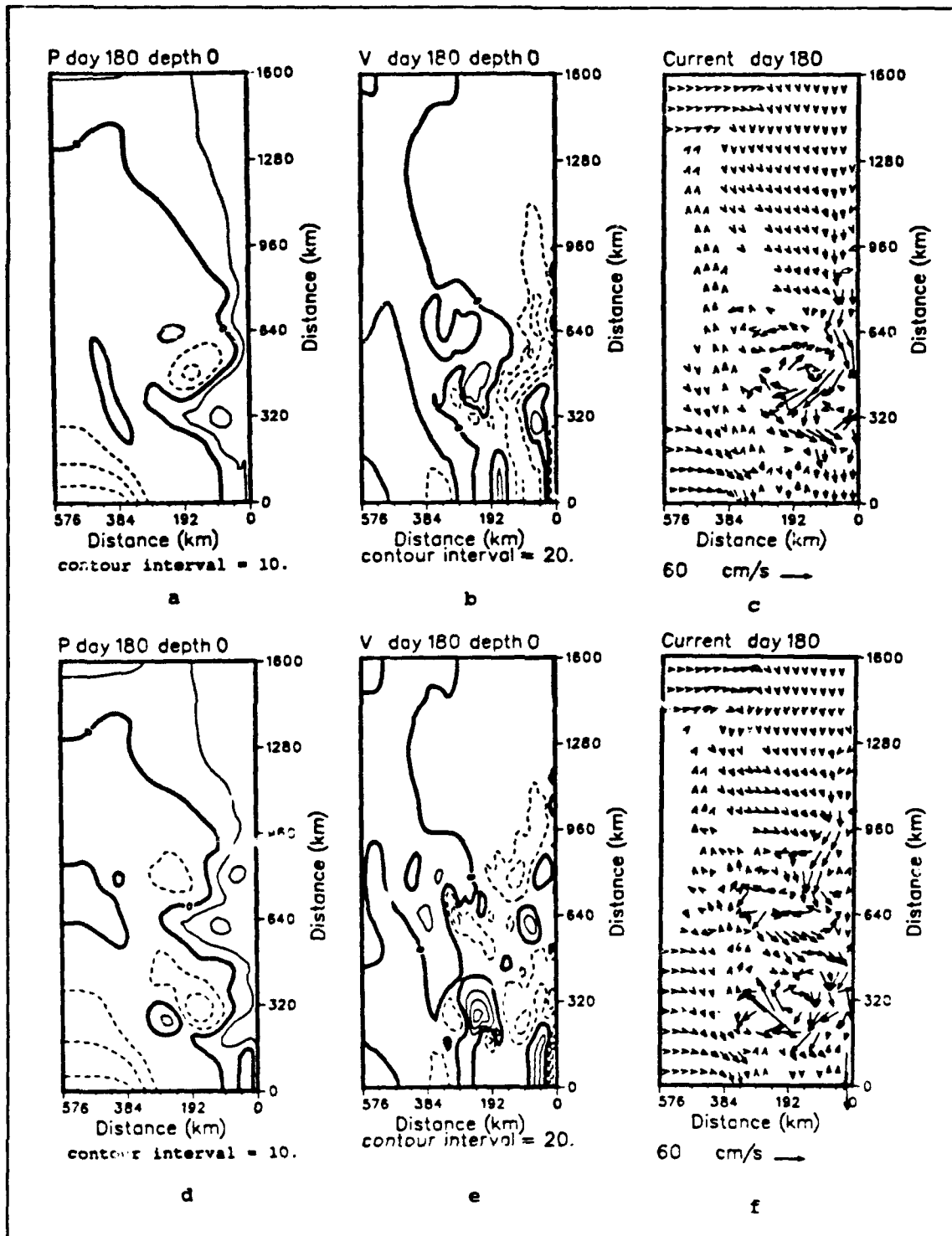


Figure 5.15 Case 2, Case 1 surface pressure, meridional velocity, current vector fields, day 180: Case 2 (a-c), Case 1 (d-f); dashes denote negative values, dynamic height anomaly (cm) ref. 2000 m, velocity (cm/s).

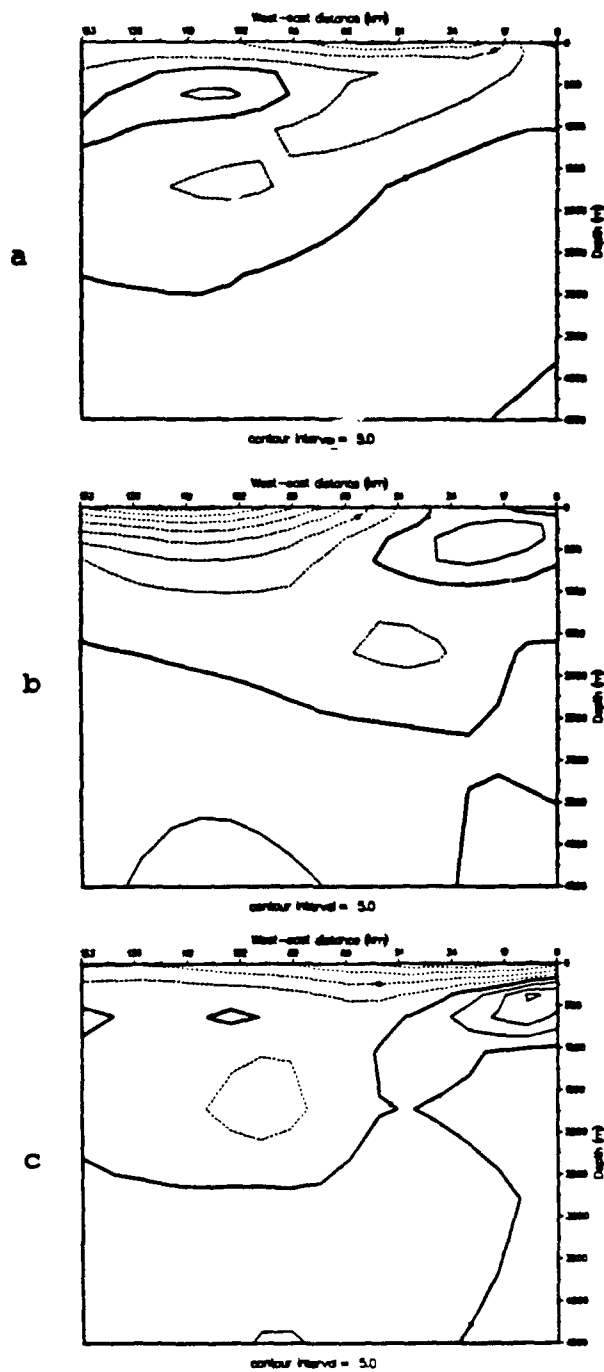


Figure 5.16 Case 2 30-day time-averaged meridional velocity cross-sections centered on day 180: As for Figure 5.11.

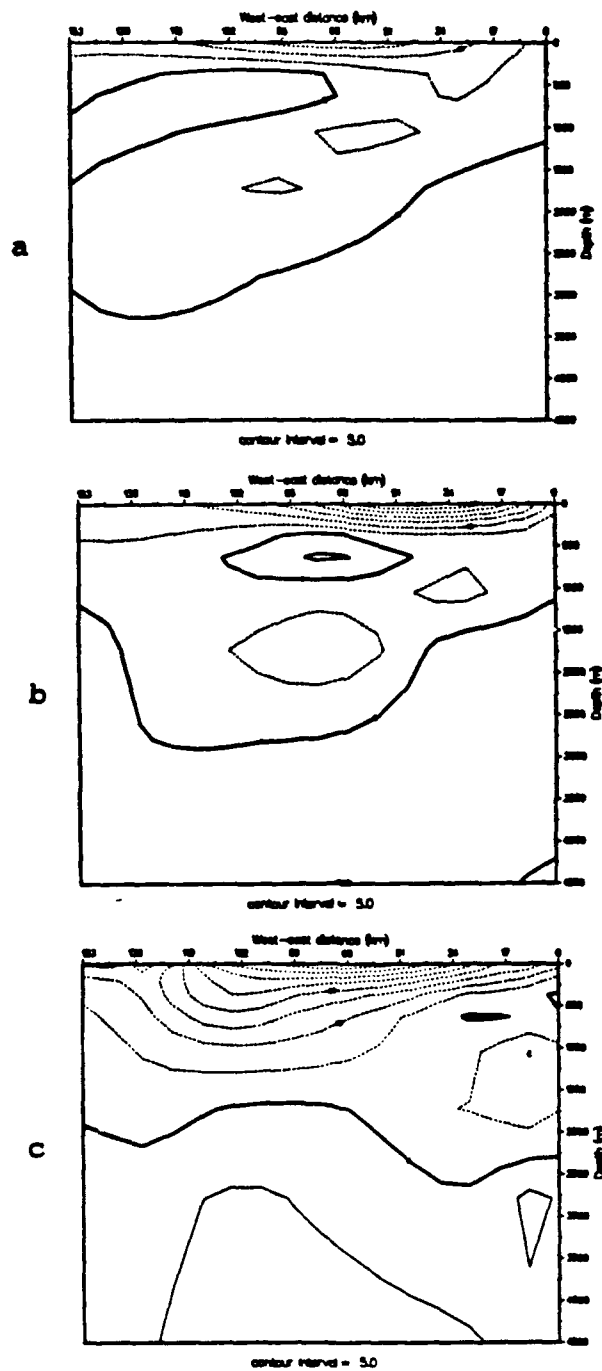


Figure 5.17 Case 1 30-day time-averaged meridional velocity cross-sections centered on day 180: As for Figure 5.11.

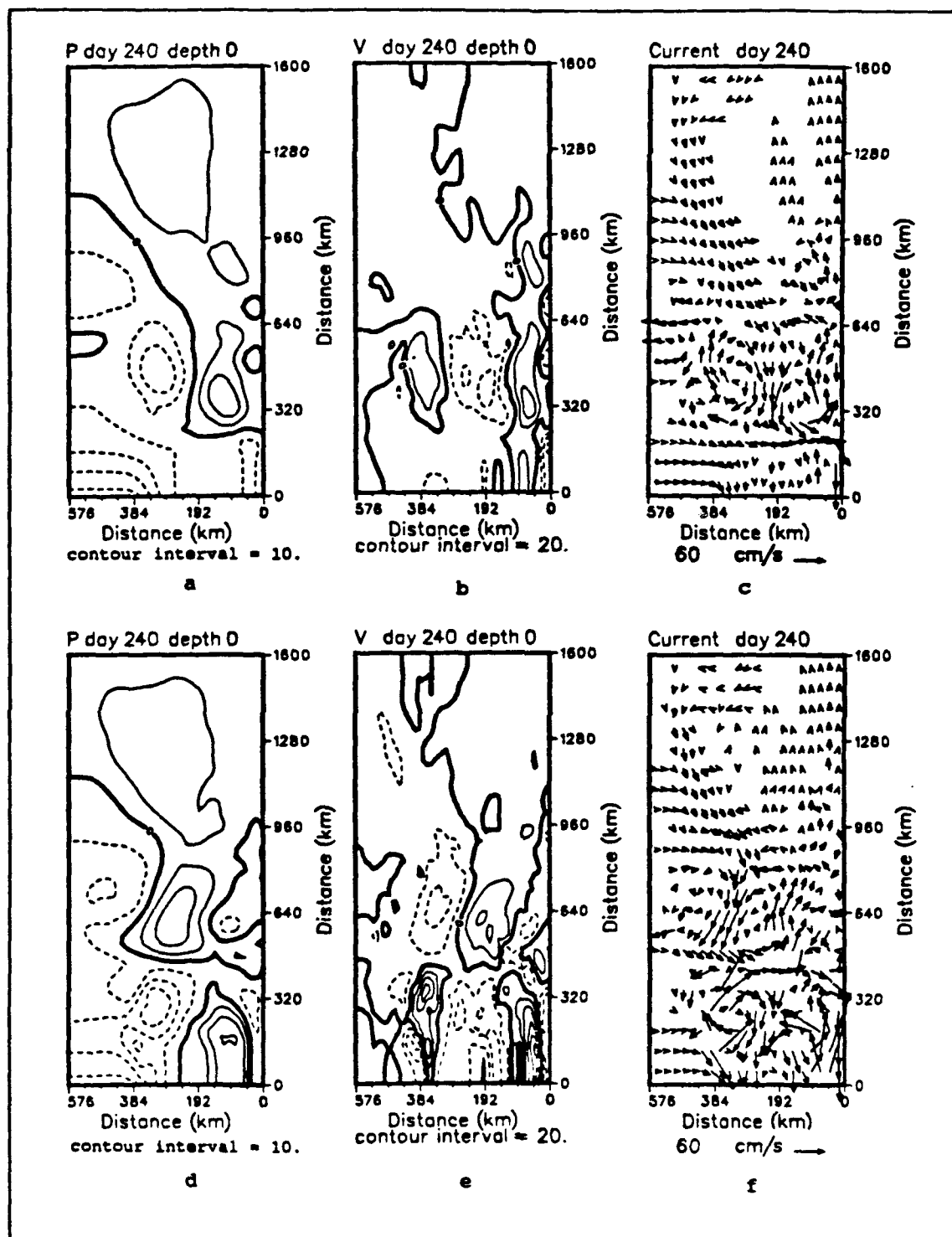


Figure 5.18 Case 1, Case 2 pressure, meridional velocity, current velocity vector fields for the surface, day 240: Case 1 (a-c), Case 2 (d-f), as for Figure 5.15.

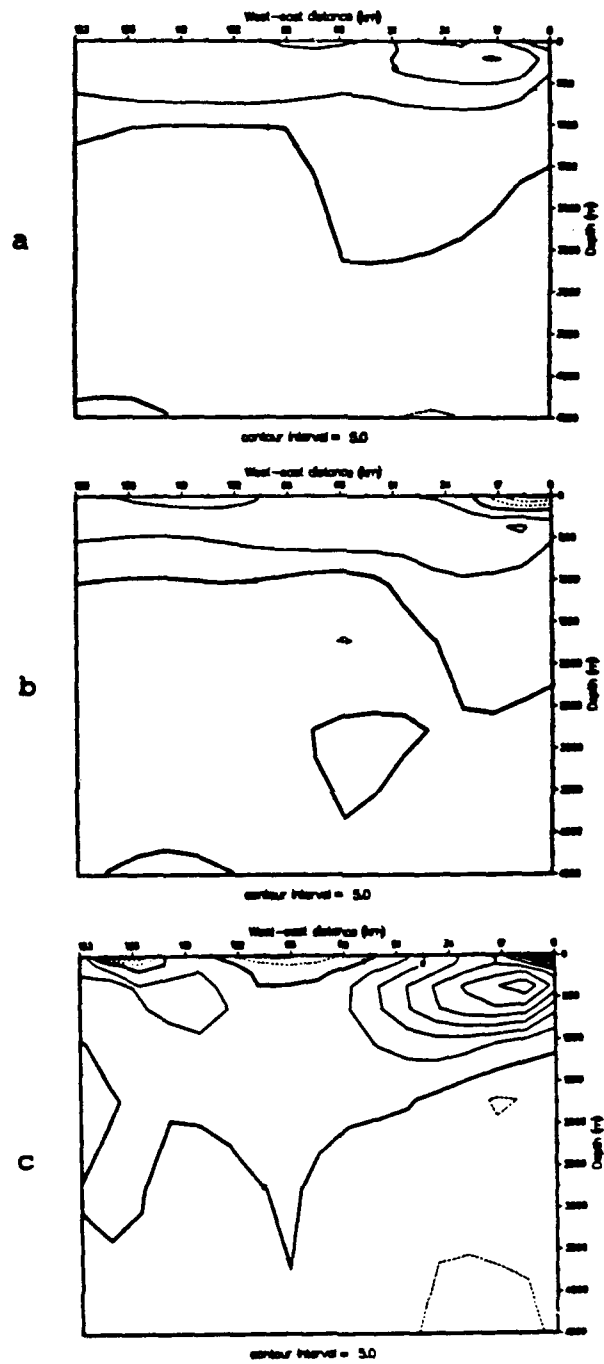


Figure 5.19 Case 2 30-day time-averaged meridional velocity cross-sections centered on day 240: As for Figure 5.11.

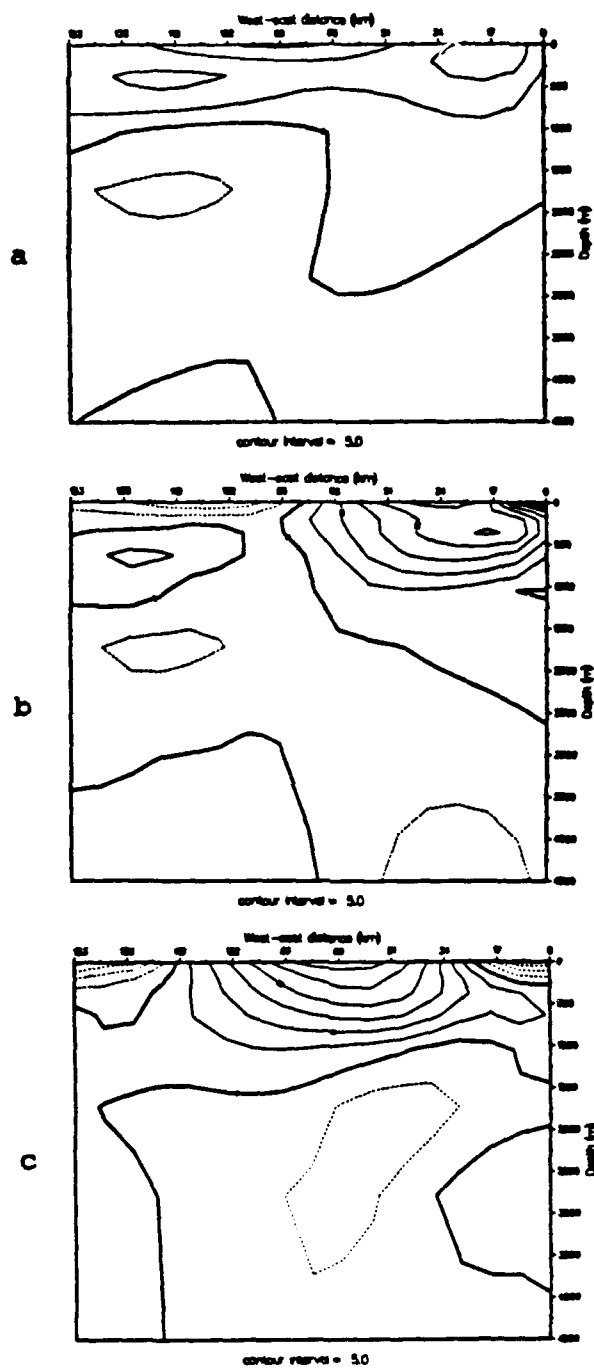


Figure 5.20 Case 1 30-day time-averaged meridional velocity cross-sections centered on day 240: As for Figure 5.11.

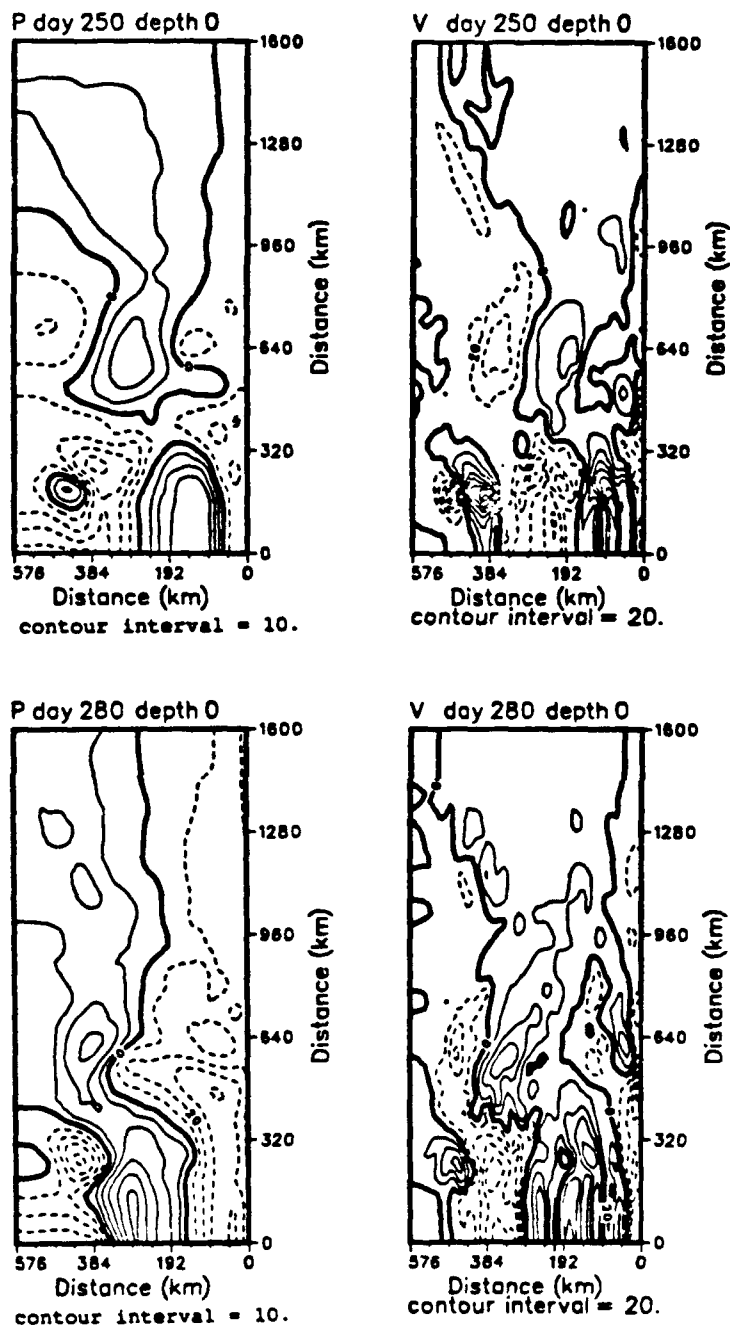


Figure 5.21 Case 2 pressure, meridional velocity fields for the surface at days 250, 280: Pressure (dynamic height anomaly (cm), ref. 2000 m), velocity (cm/s).

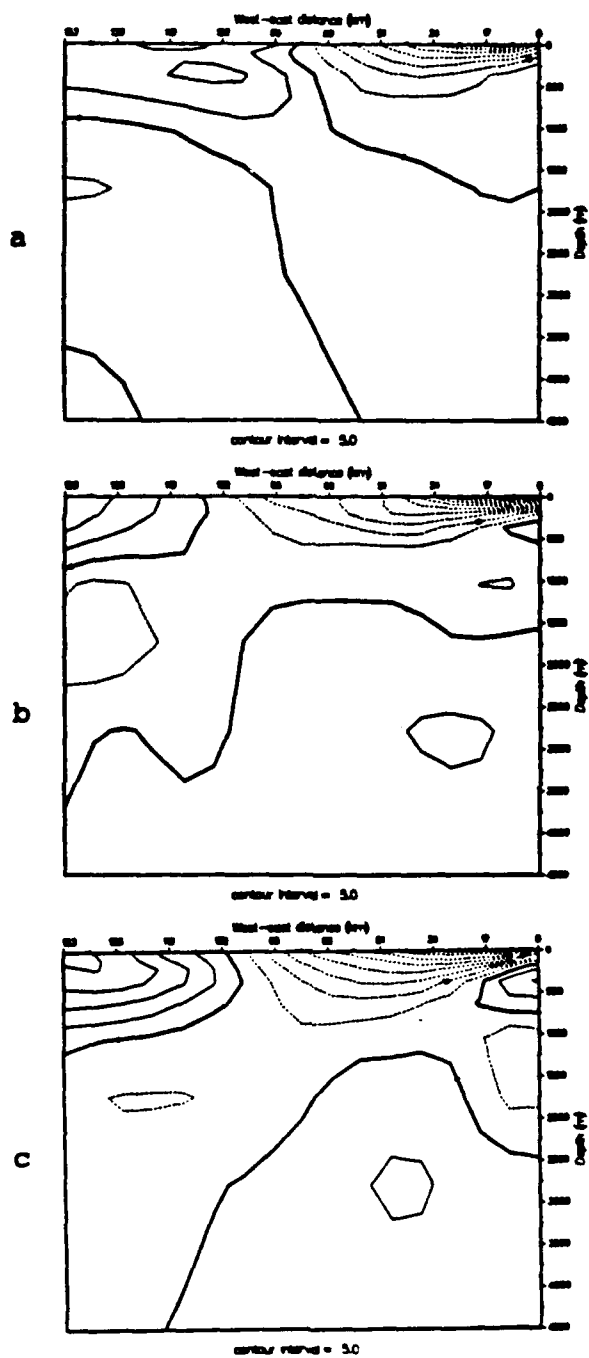


Figure 5.23 Case 1 30-day time-averaged meridional velocity cross-sections centered on day 300: As for Figure 5.11.

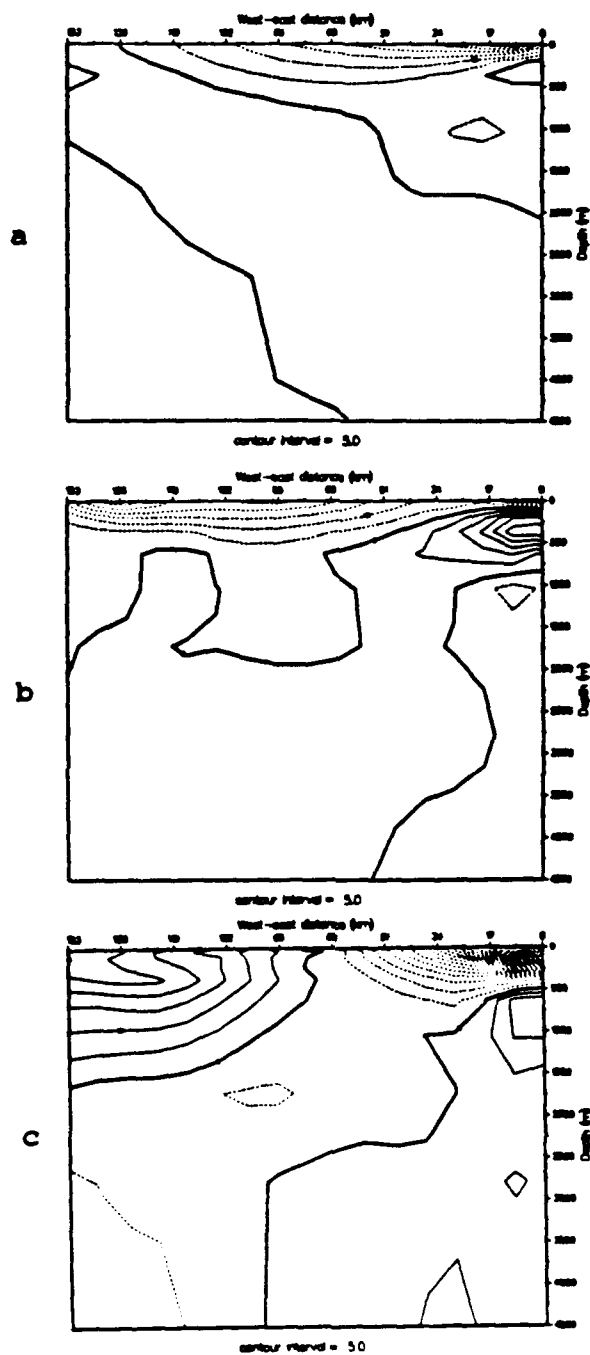


Figure 5.24 Case 2 30-day time-averaged meridional velocity cross-sections centered on day 300: As for Figure 5.11.

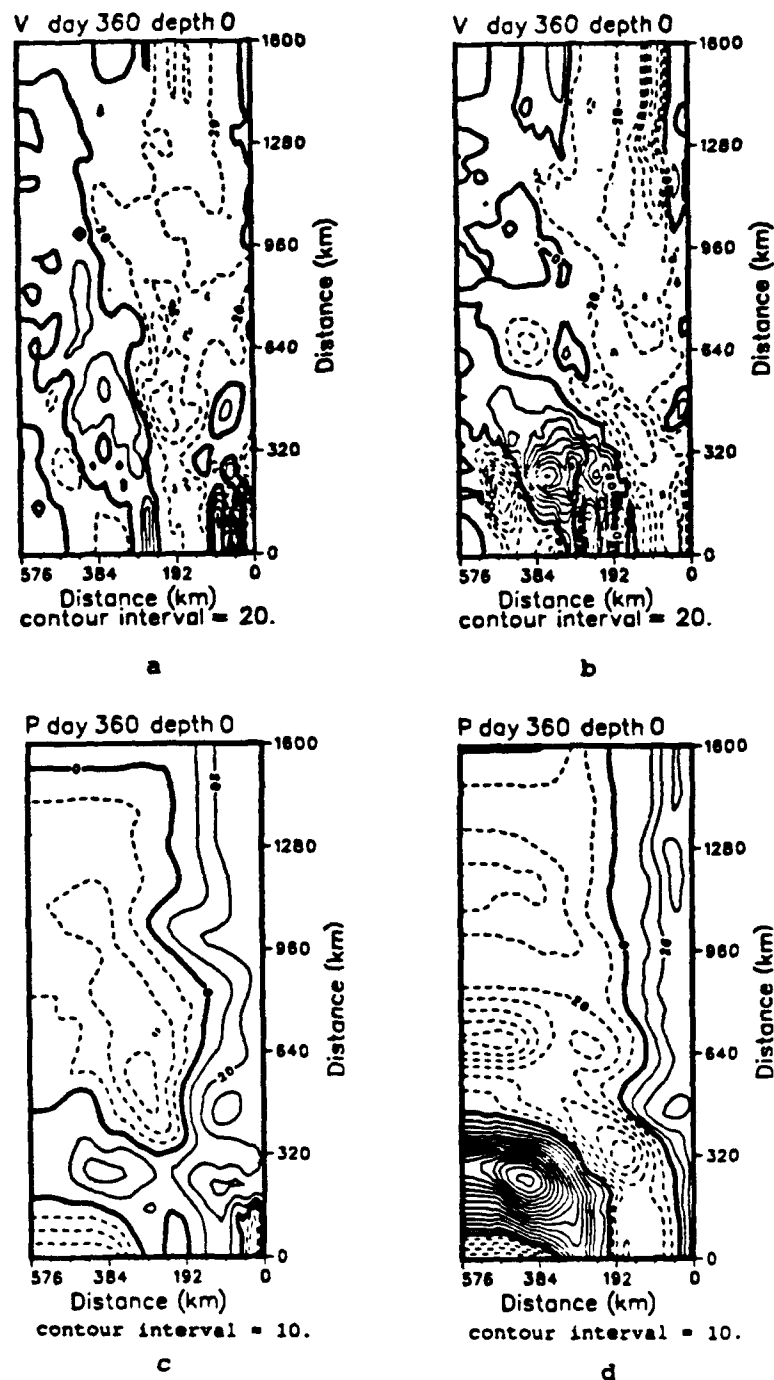


Figure 5.25 Case 1, Case 2 meridional velocity, pressure fields for the surface, day 360: (a, c) Case 1, (b, d) Case 2; dashes denote negative values, velocity (cm/s), dynamic height anomaly (cm), ref. 2000 m.

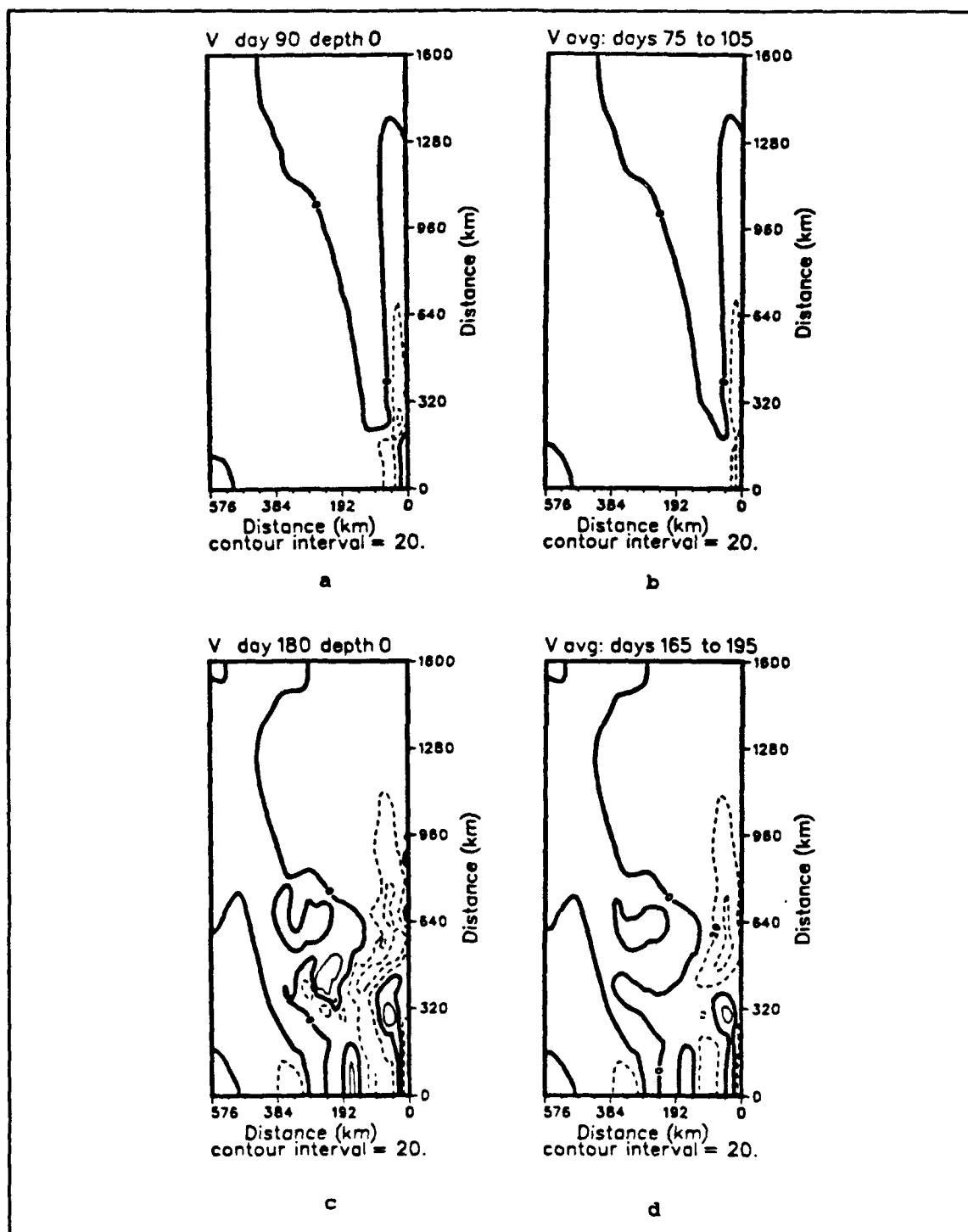
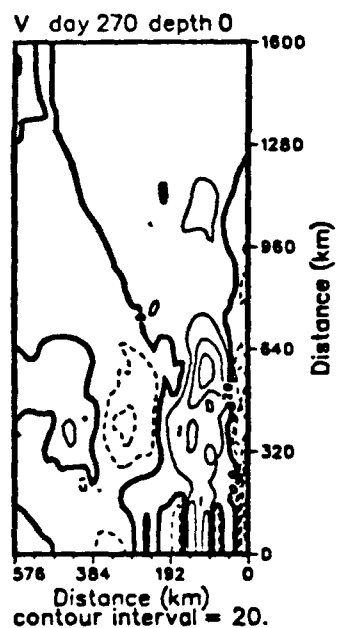
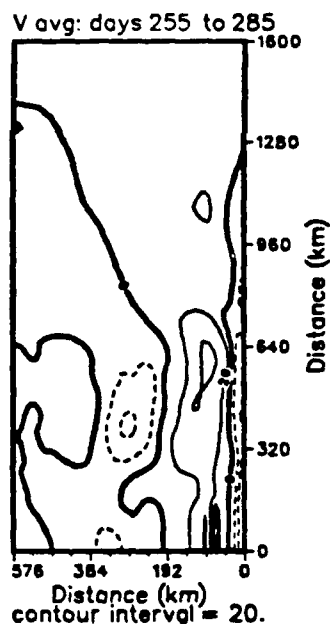


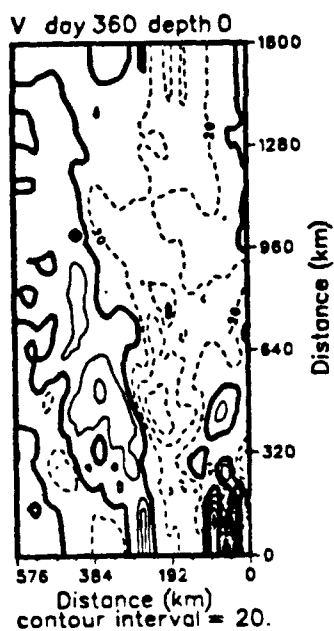
Figure 5.26 Case 1 instantaneous and 30-day time-averaged surface meridional velocity fields: (a, b) austral summer (December), (c, d) austral autumn (March); velocity (cm/s), dashed contours denote poleward flow.



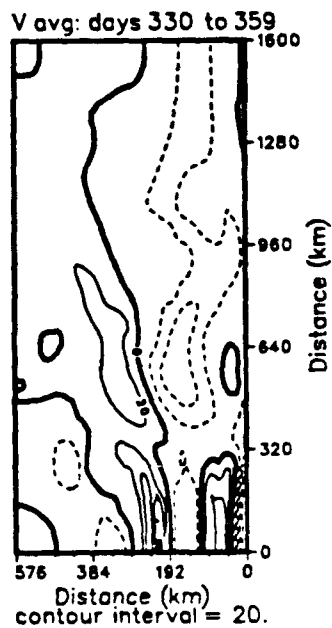
e



f



g



h

Figure 5.26 cont. Case 1 instantaneous and 30-day time-averaged meridional velocity fields: (e, f) austral winter (June), (g, h) austral spring (September); velocity (cm/s).

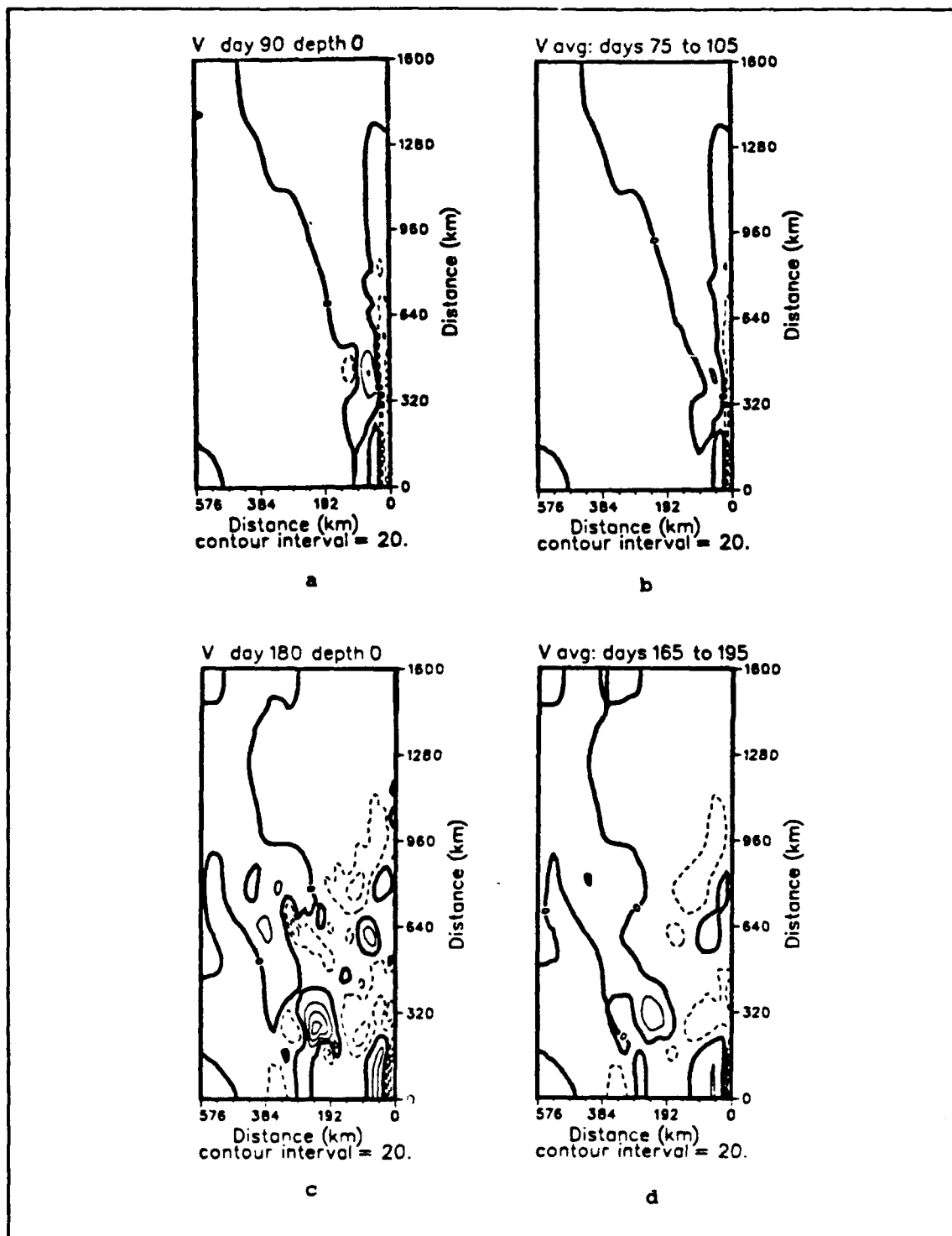


Figure 5.27 Case 2 instantaneous and 30-day time-averaged meridional velocity fields: (a, b) austral summer (December), (c, d) austral autumn; as for Figure 5.26.

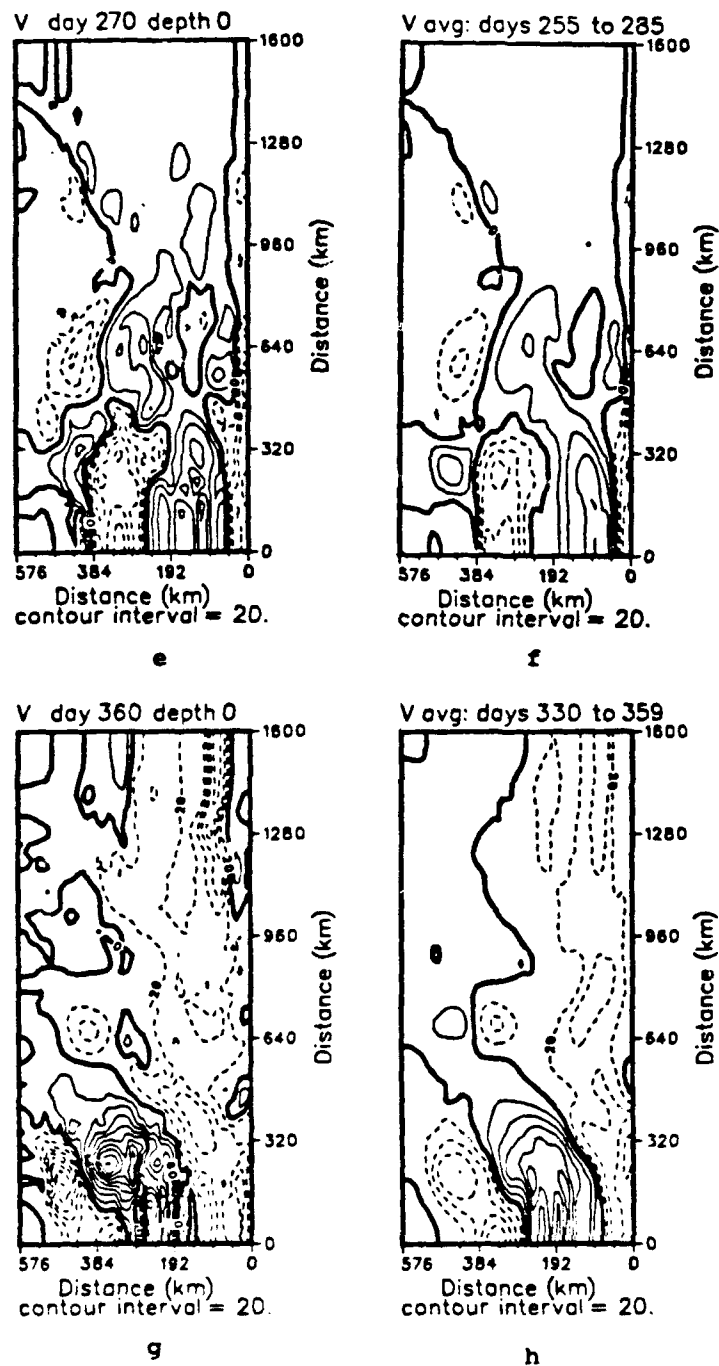


Figure 5.27 cont. Case 2 instantaneous and 30-day time-averaged meridional velocity fields: (e, f) austral winter (June), (g, h) austral spring (September); as for Figure 5.26.

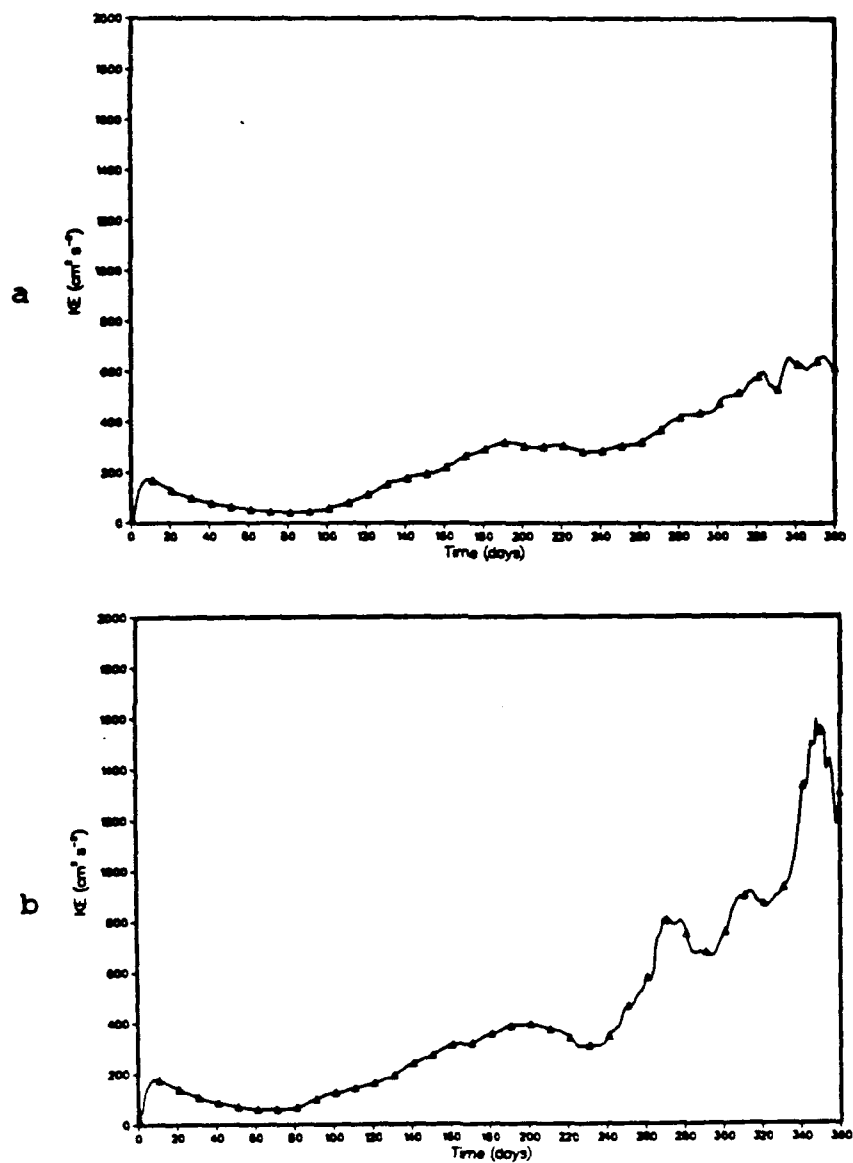


Figure 5.28 Kinetic energy time-series: Kinetic energy computed for a reduced area ($1108 \times 288 \text{ km}$) of the coastal interior of the model domain, (a) Case 1, (b) Case 2.

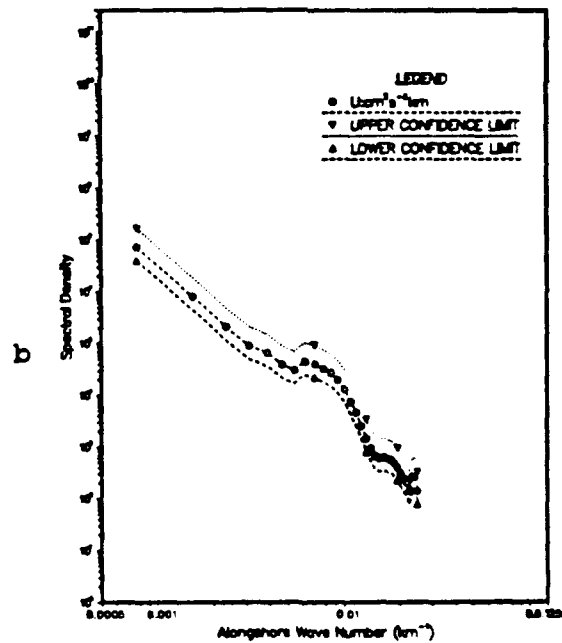
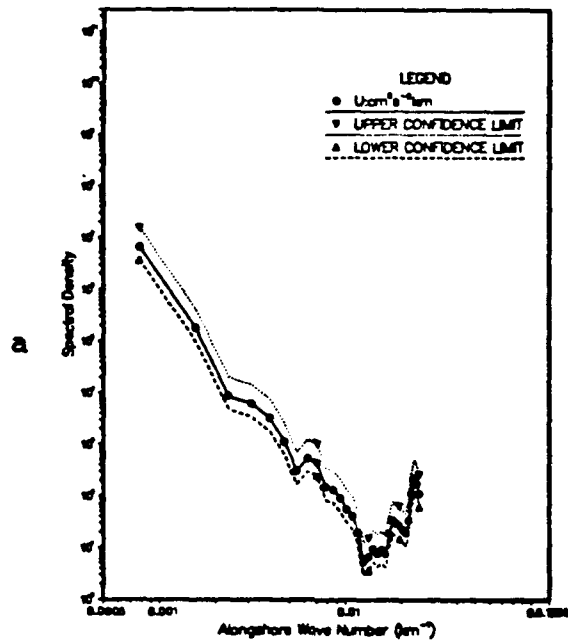


Figure 5.29 Case 1 spectral density, day 60 and day 100: Spectral density (reduced coastal region) versus alongshore wavenumber. The wavenumber is an inverse wavelength. The spectral density scale for all spectral density plots extends from 10^0 (bottom) to 10^{11} (top).

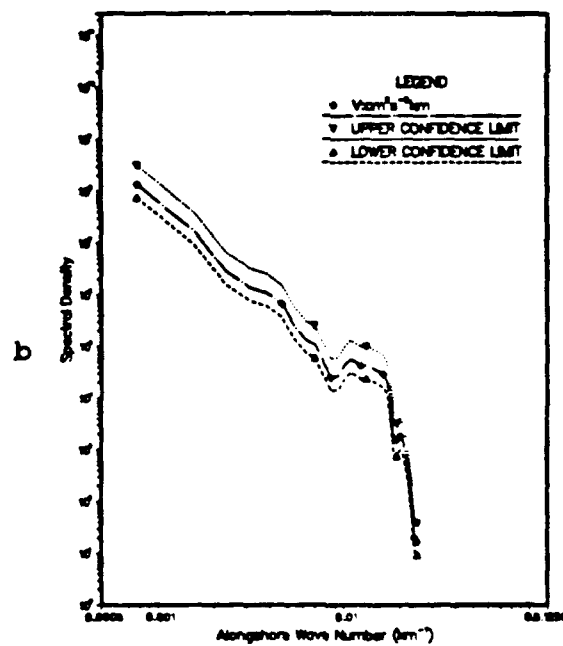
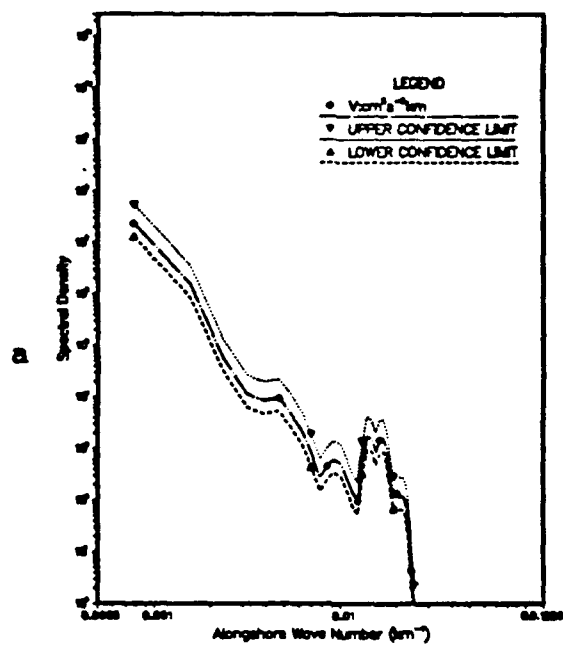


Figure 5.30 Case 2 spectral density at day 60 and day 90: As for Figure 5.29.

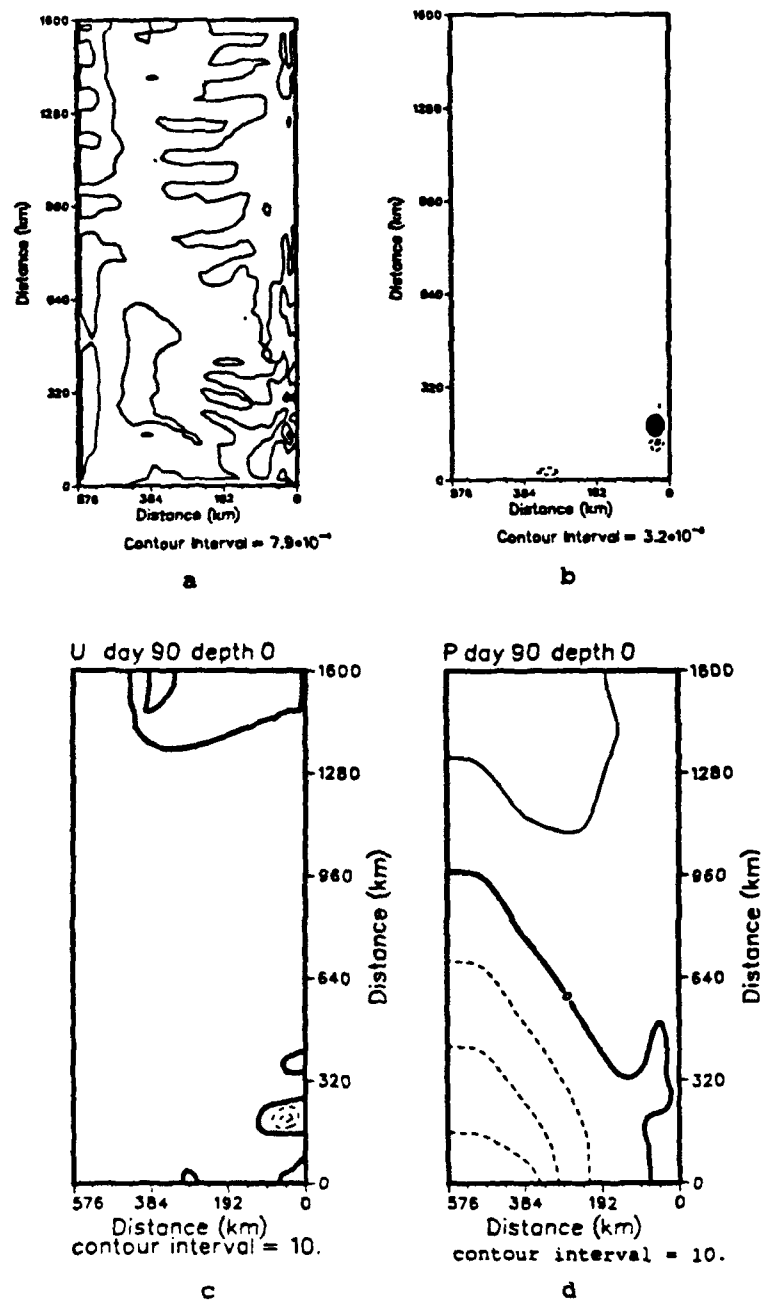


Figure 5.31 Case 1 instability, days 60 - 90: (a) barotropic transfer ($\text{ergs}/(\text{cm}^3 \text{ s})$), (b) baroclinic transfer ($\text{ergs}/(\text{cm}^3 \text{ s})$), (c) zonal velocity (cm/s), pressure (cm ref. 2000 m).

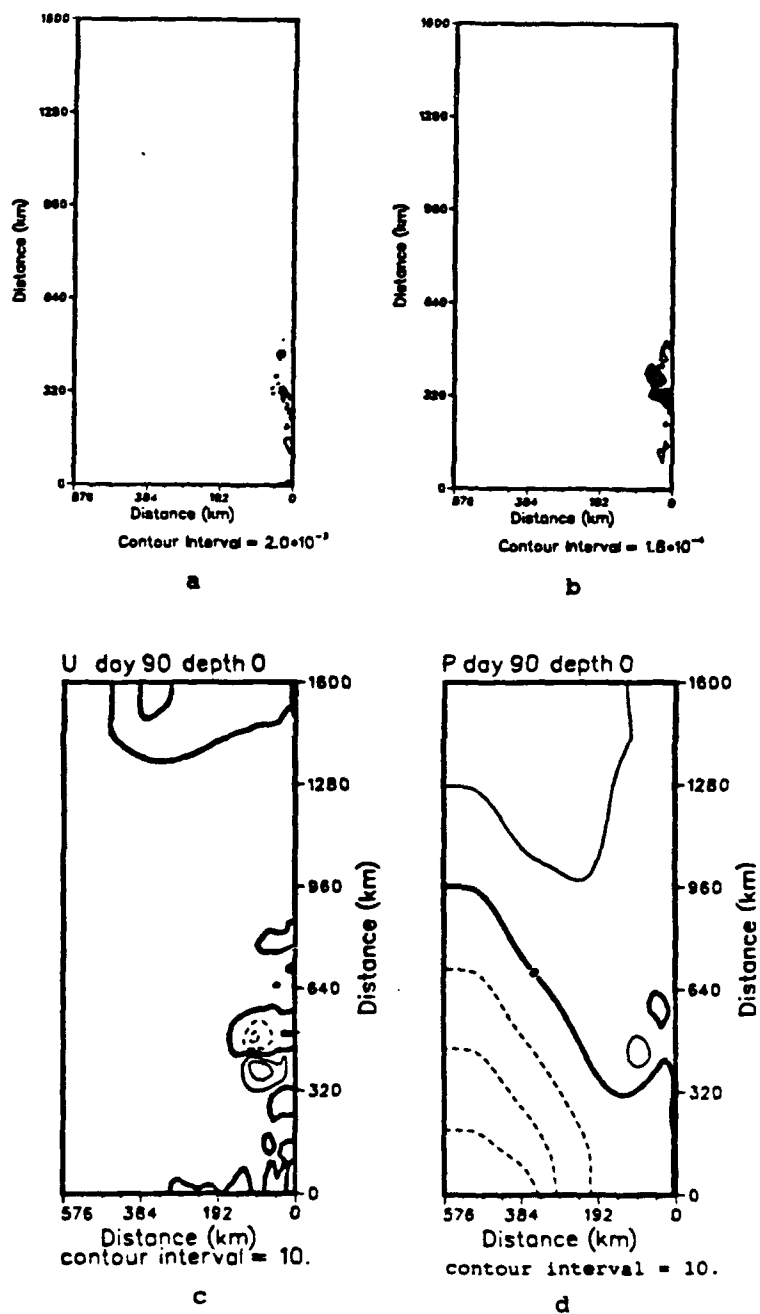
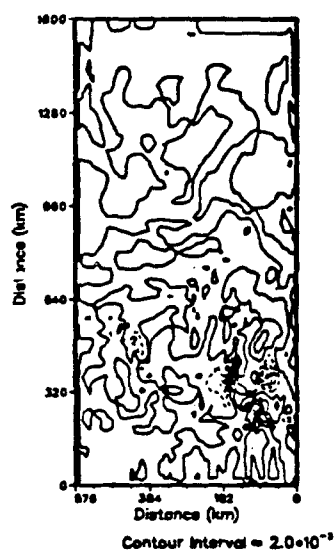
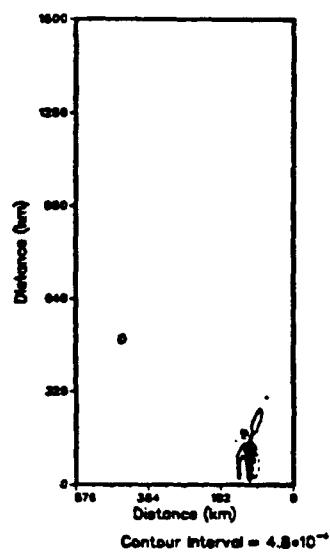


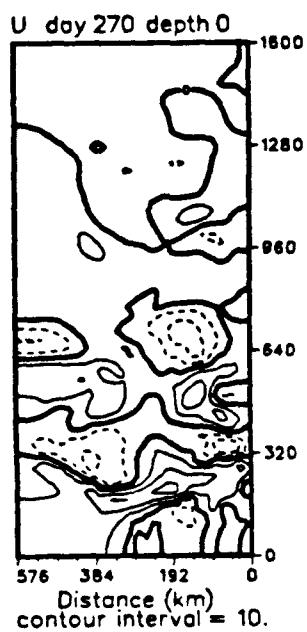
Figure 5.32 Case 2 instability, days 60 - 80: As for Figure 5.31.



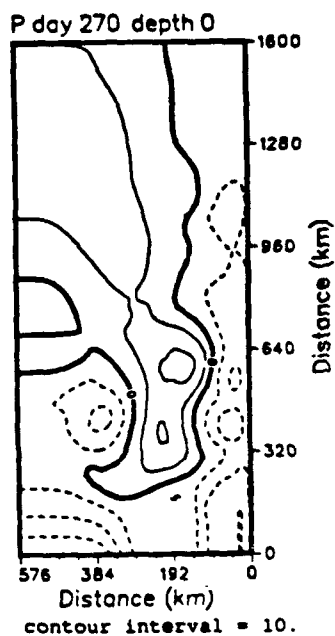
a



b



c



d

Figure 5.33 Case 1 instability, days 230 - 260: As for Figure 5.31.

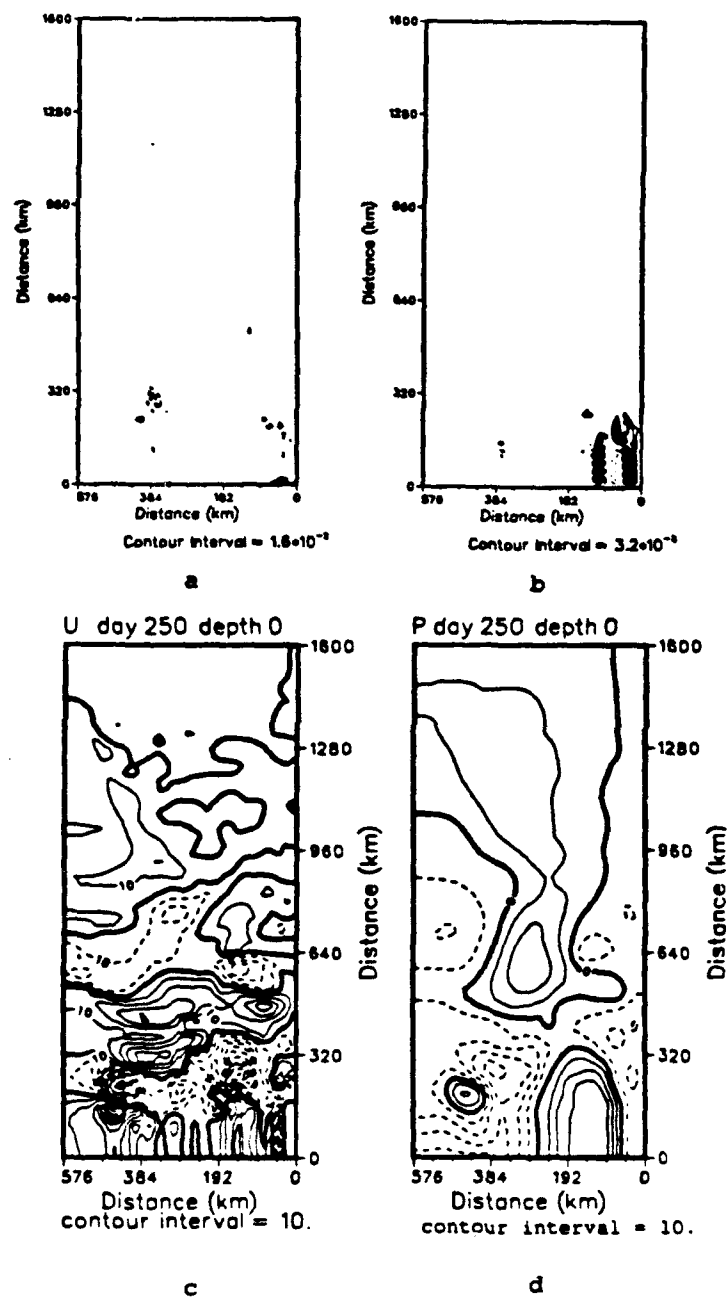


Figure 5.34 Case 2 instability, days 220 - 240: As for Figure 5.31.

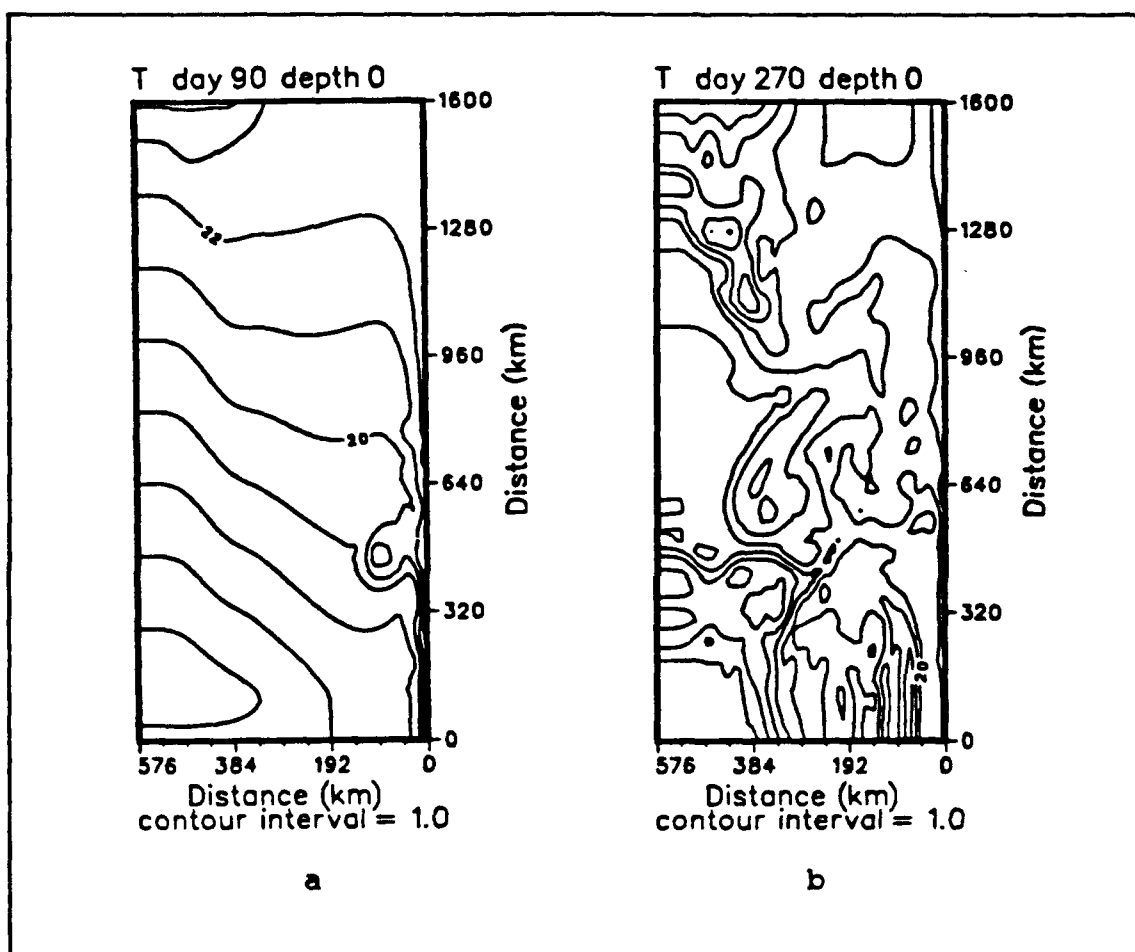


Figure 5.35 Meridional surface thermal advection: (a) Case 2, day 90, (b) Case 2, day 270; temperature ($^{\circ}\text{C}$).

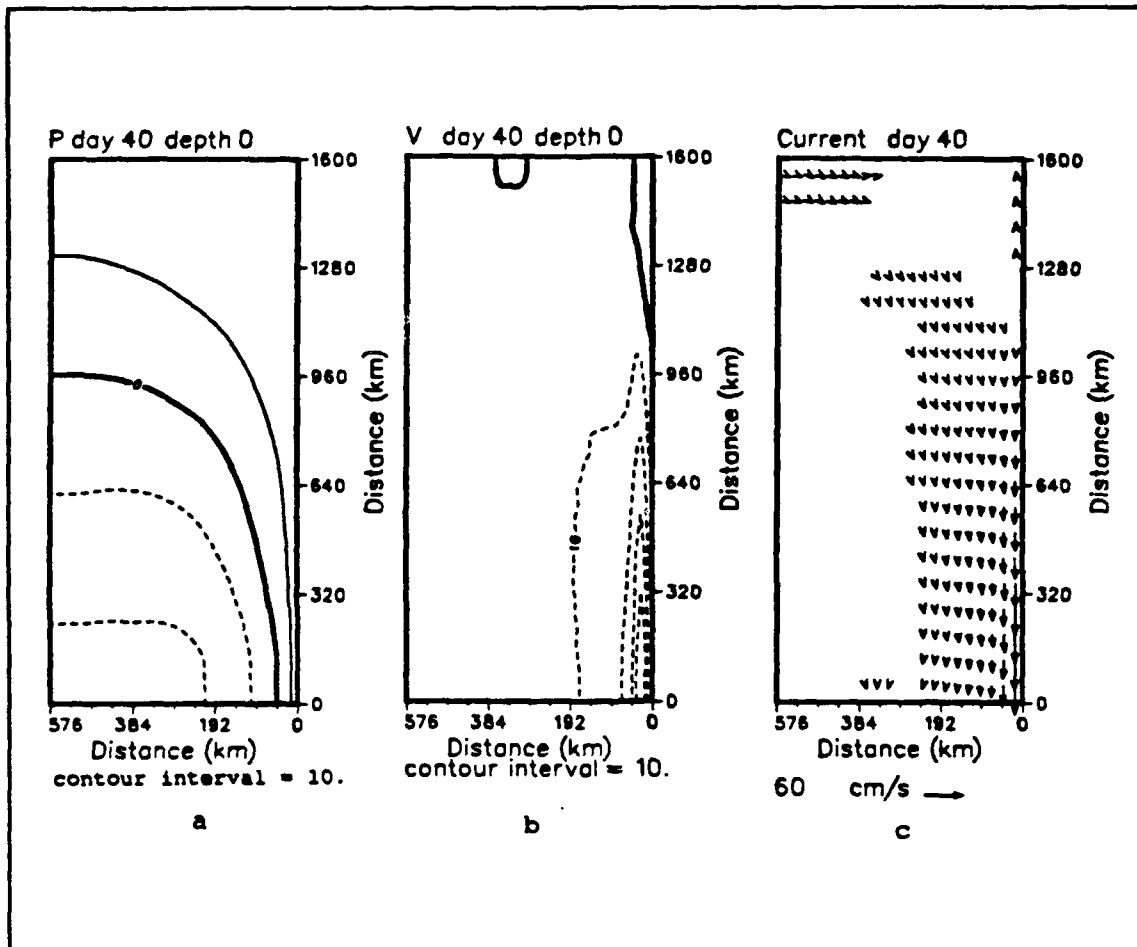


Figure 5.36 Case 3 pressure, meridional velocity, and current vector fields for the surface, day 40: dashes denote negative, (a) dynamic height anomaly (cm), ref. 2000 m, (b) velocity (cm/s), (c) current vector field.

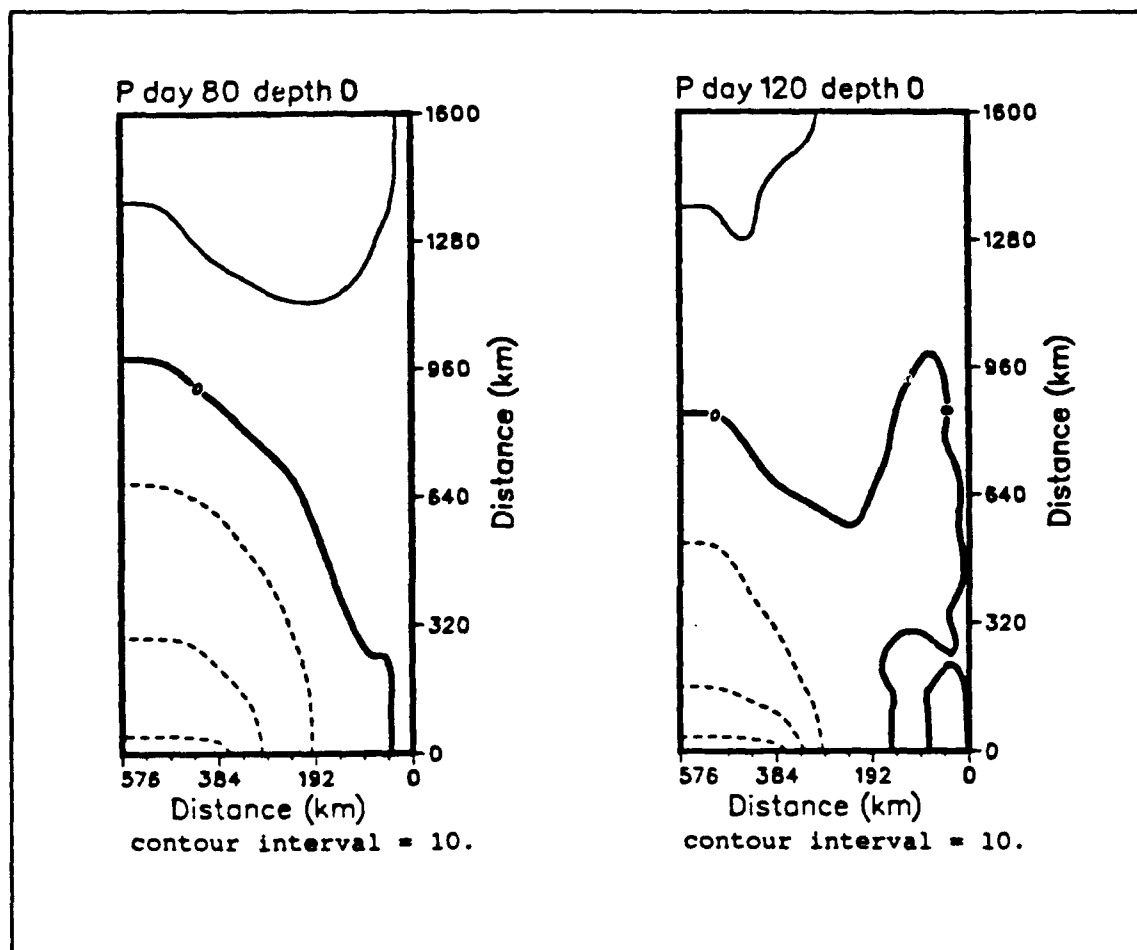


Figure 5.37 Case 3 surface pressure fields, day 80 and day 120: Pressure (dynamic height anomaly (cm), ref. 2000 m), dashed contours denote negative values.

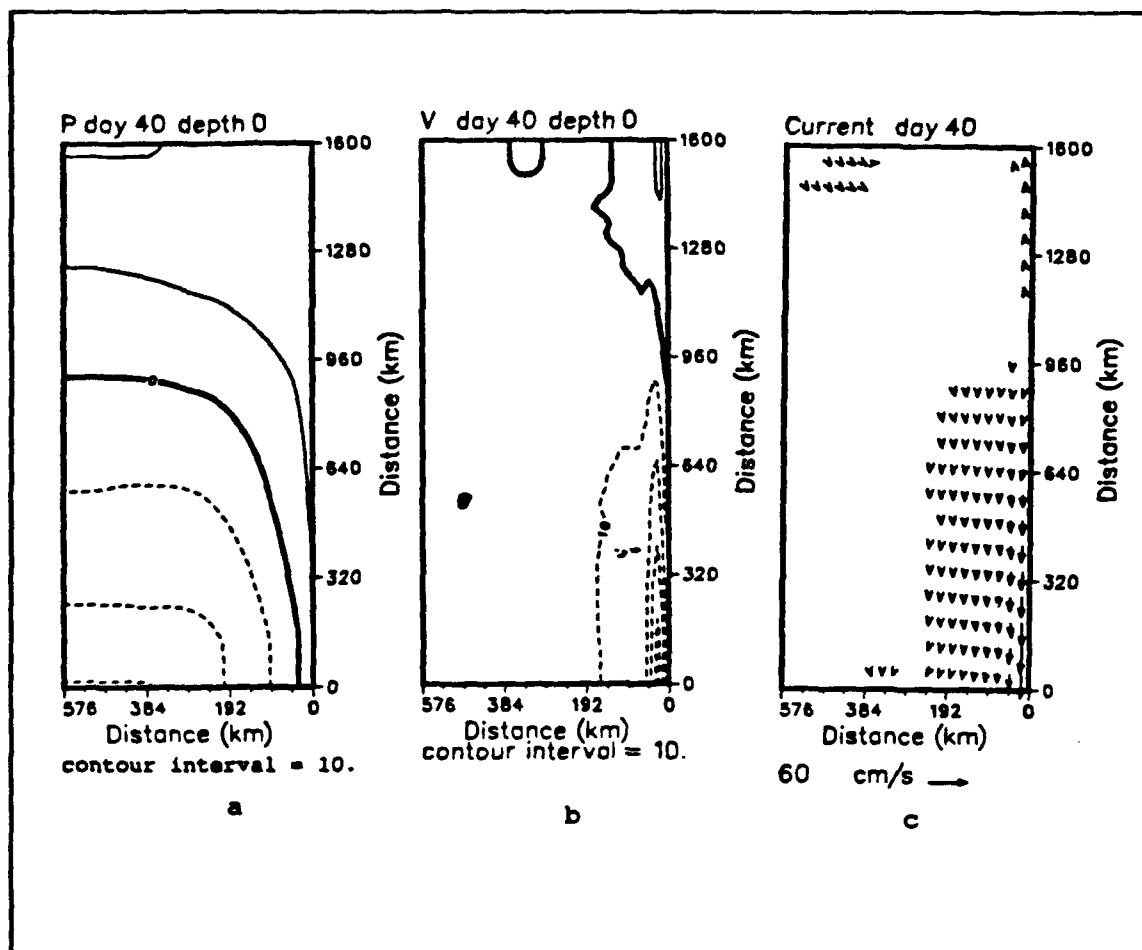


Figure 5.38 Case 4 pressure, meridional velocity, and current vector velocity fields for the surface, day 40: As for Figure 5.36.

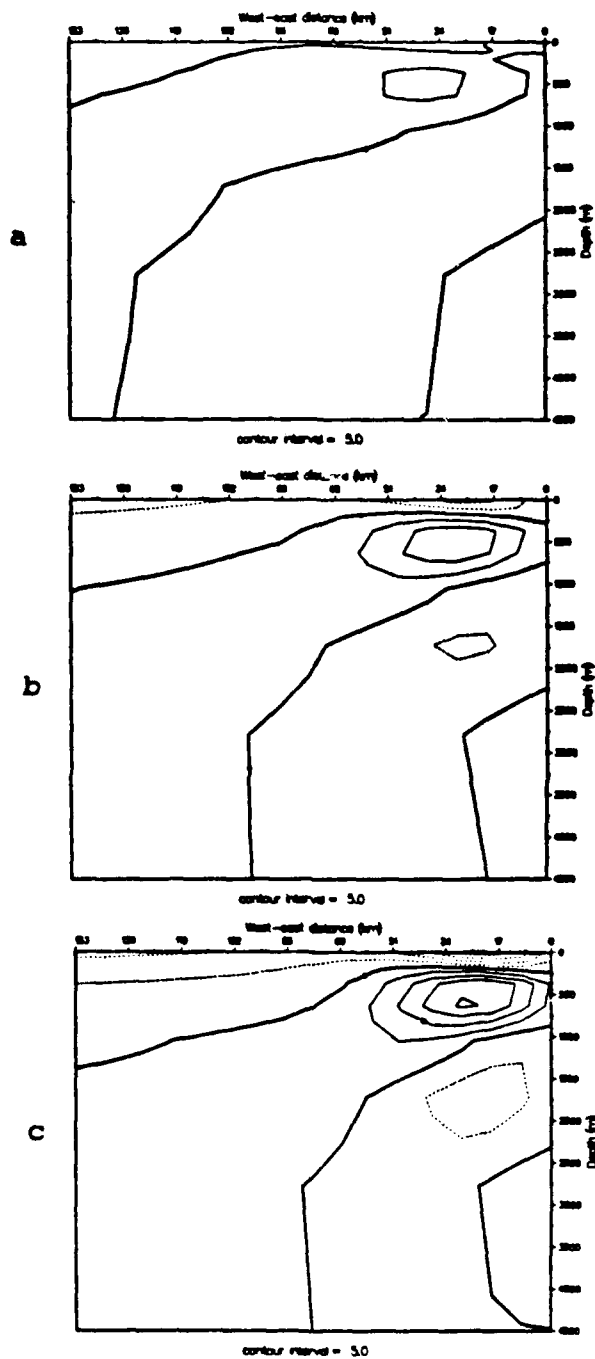


Figure 5.39 Case 3 30-day time-averaged meridional velocity cross-sections centered on day 60: As for Figure 5.11.

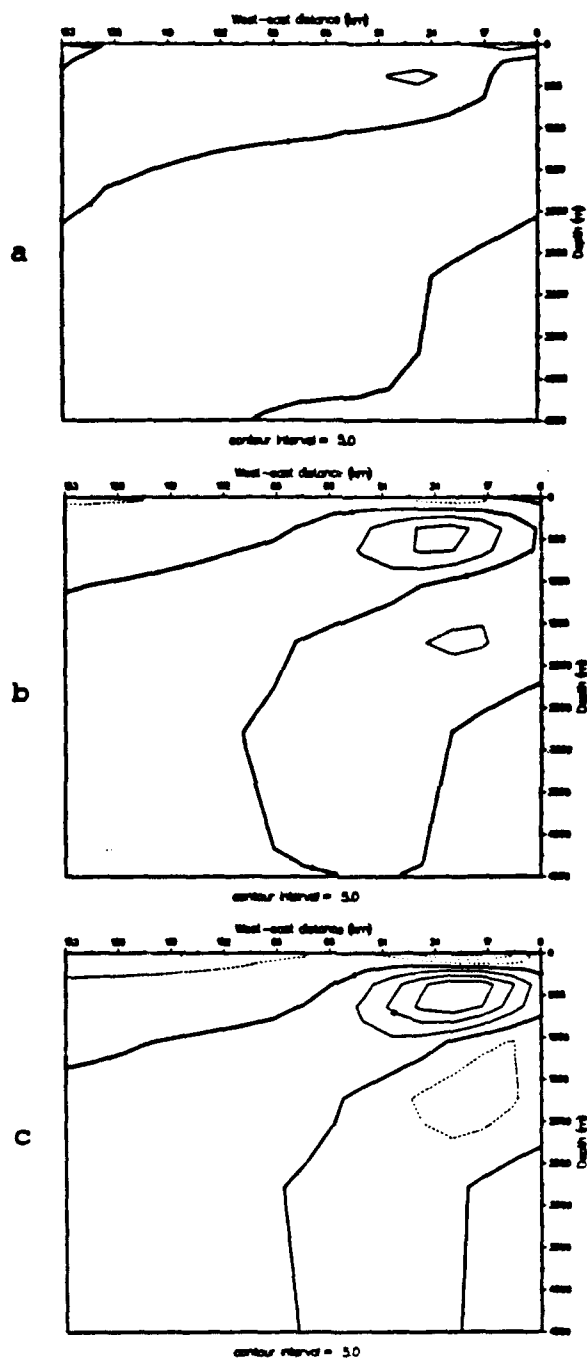


Figure 5.40 Case 4 30-day time-averaged meridional velocity cross-sections centered on day 60: As for Figure 5.11.

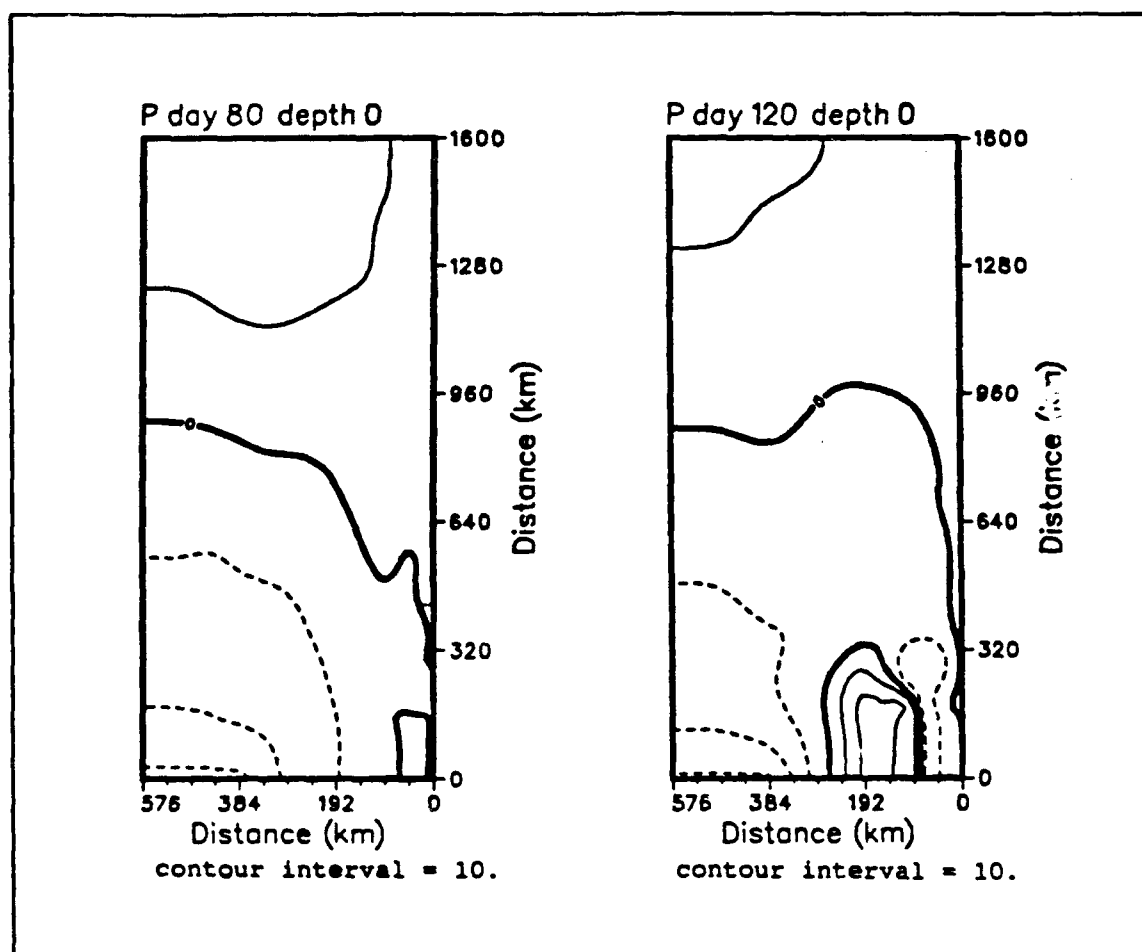


Figure 5.41 Case 4 surface pressure fields, days 80 and 120: As for Figure 5.37.

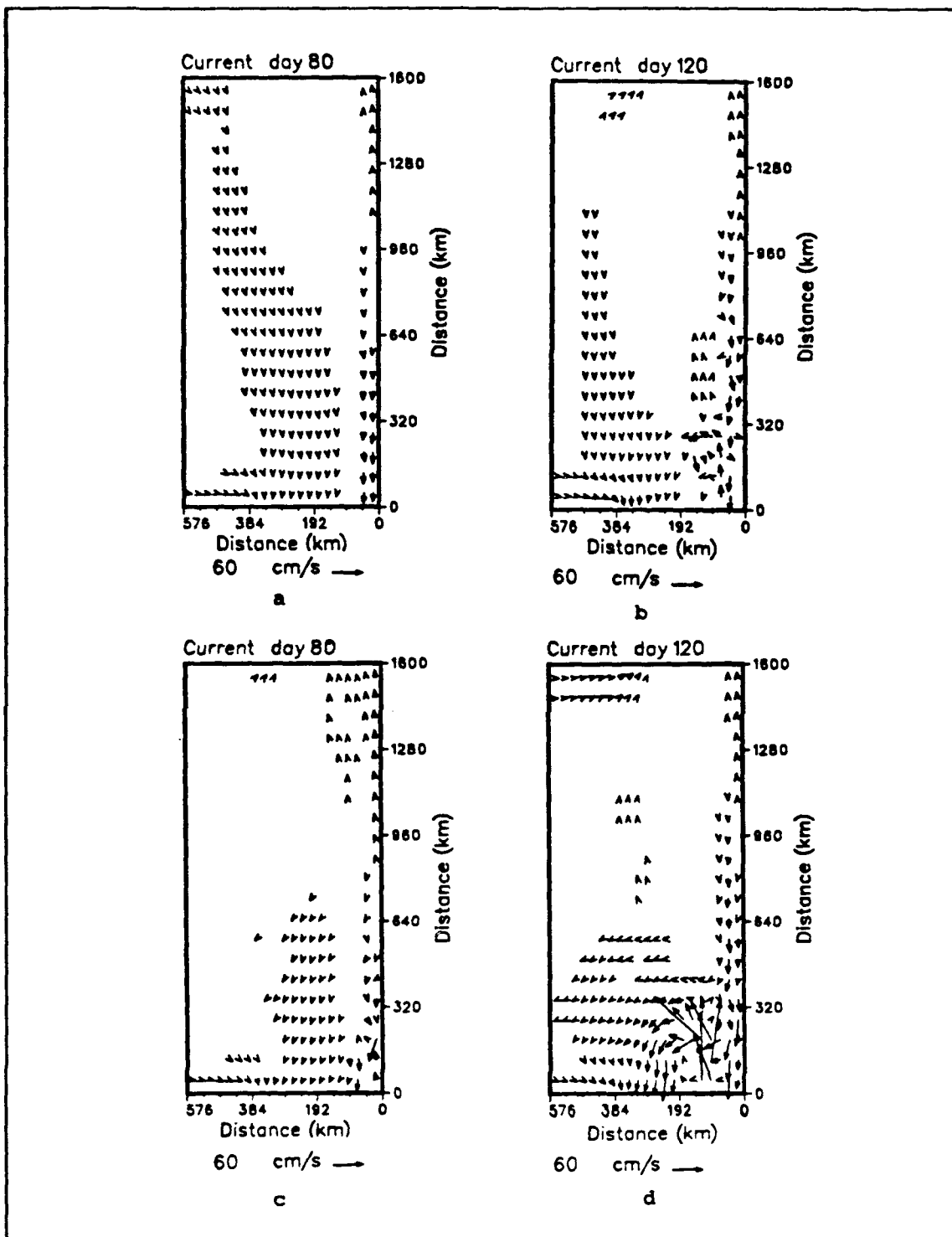


Figure 5.42 Case 3, Case 4 current vector velocity fields for the surface, day 80 and day 120: (a, b) Case 3, (c, d) Case 4.

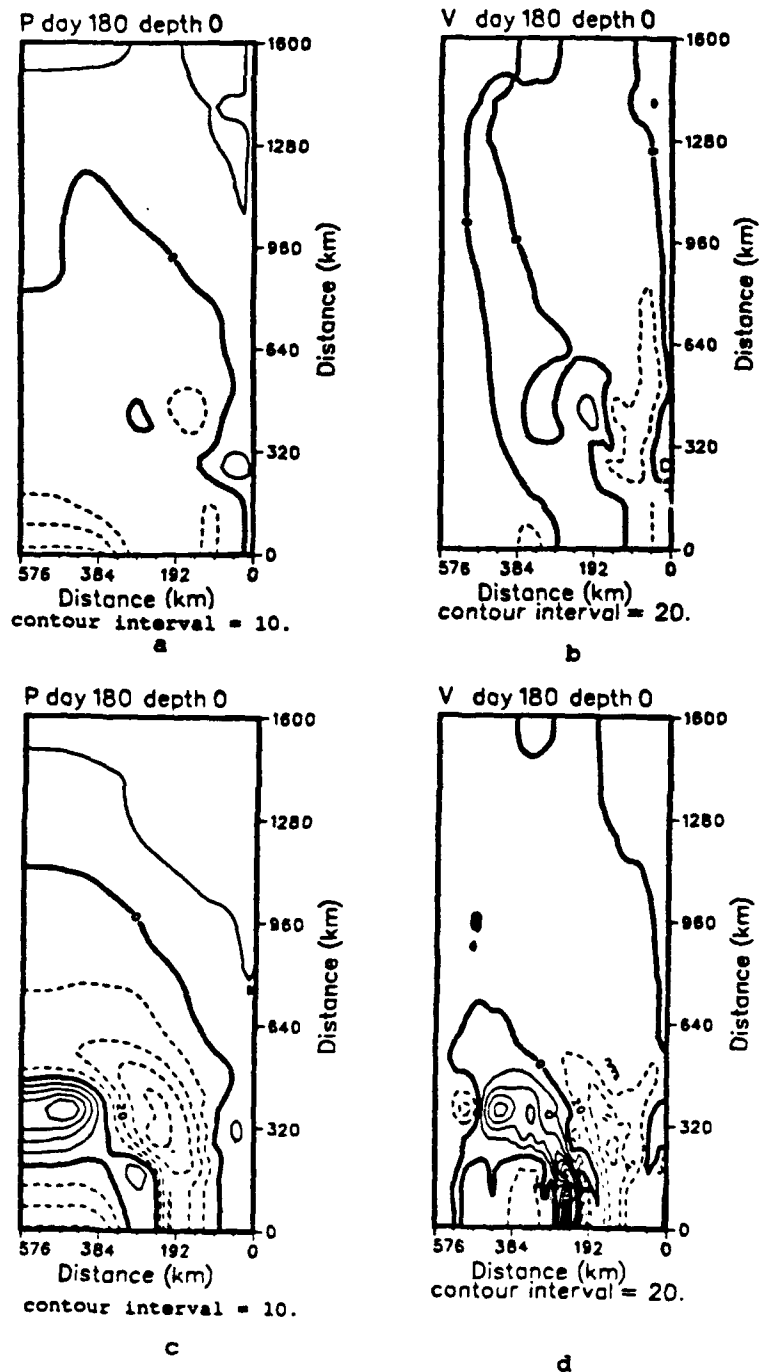


Figure 5.43 Case 3, Case 4 pressure and meridional velocity fields for the surface, day 180: (a, b) Case 3, (c, d) Case 4; dashes denote negative, pressure (dynamic height anomaly (cm), ref. 2000 m), velocity (cm).

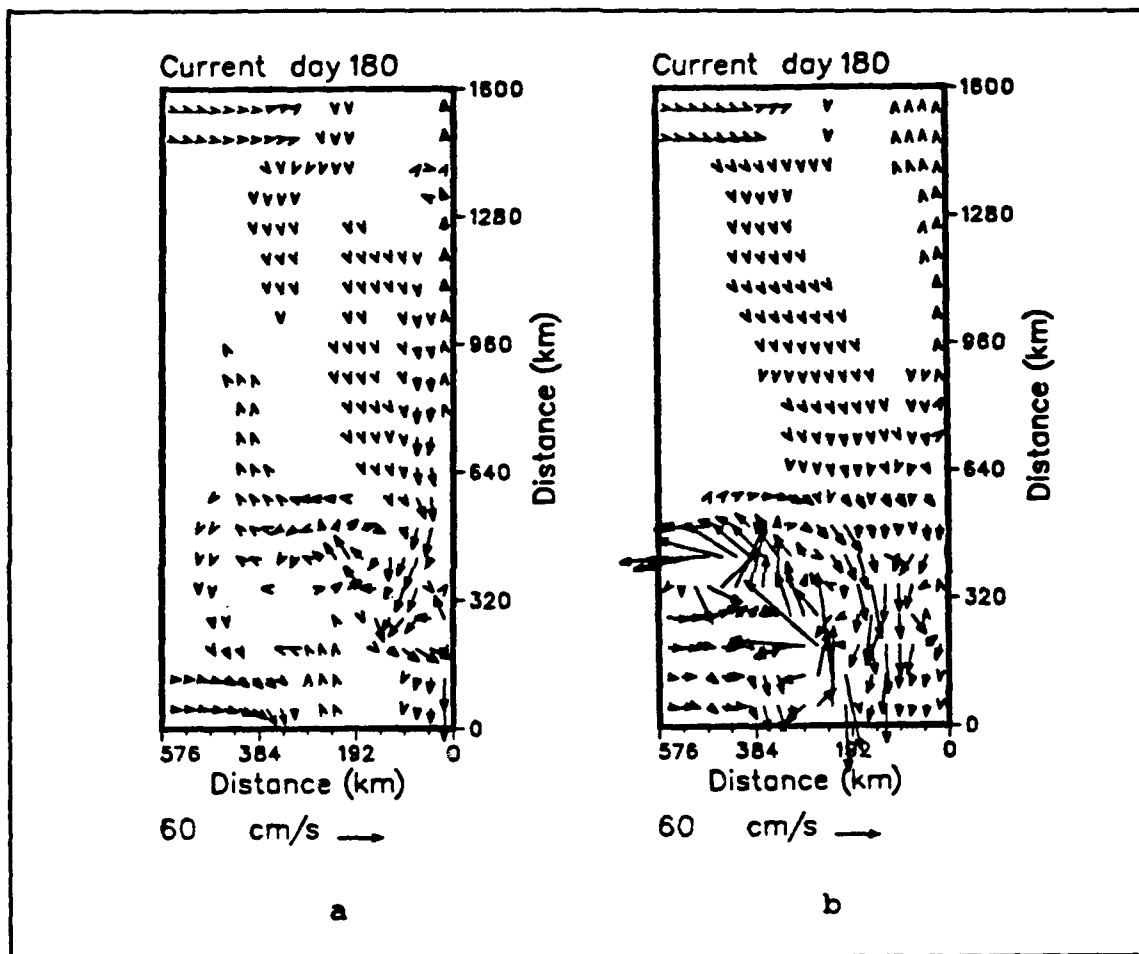


Figure 5.44 Case 3, Case 4 surface current velocity vector fields, day 180: (a) Case 3, (b) Case 4.

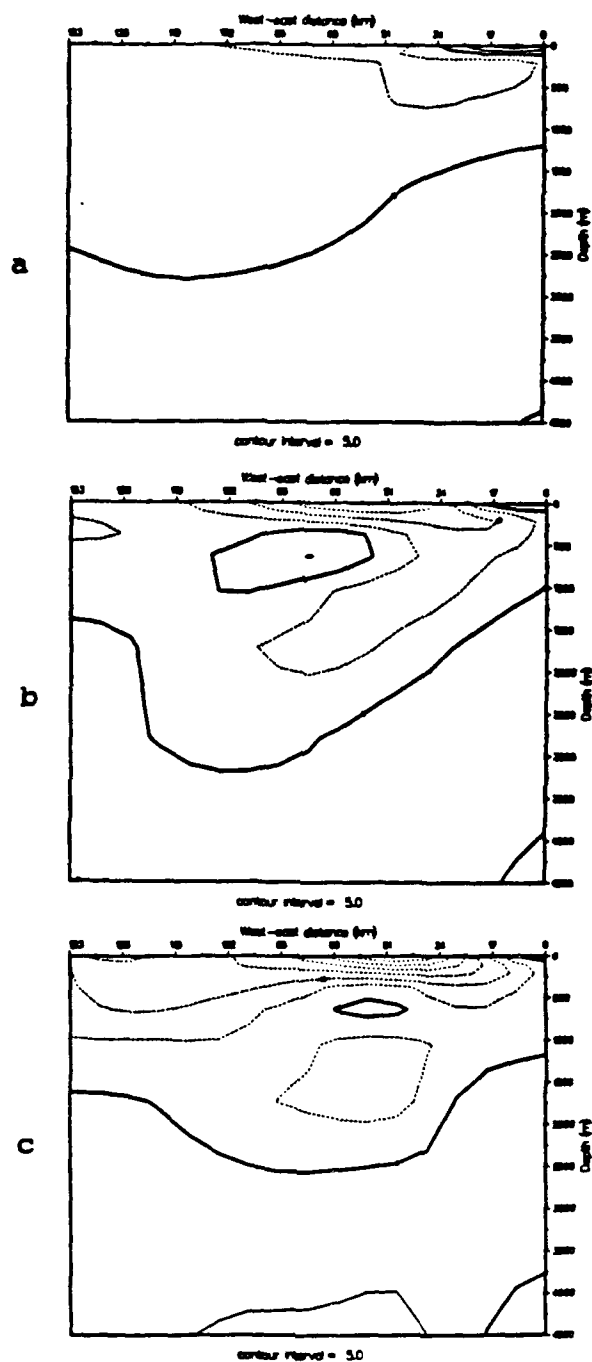


Figure 5.45 Case 3 30-day time-averaged meridional velocity cross-sections centered on day 180: As for Figure 5.11.

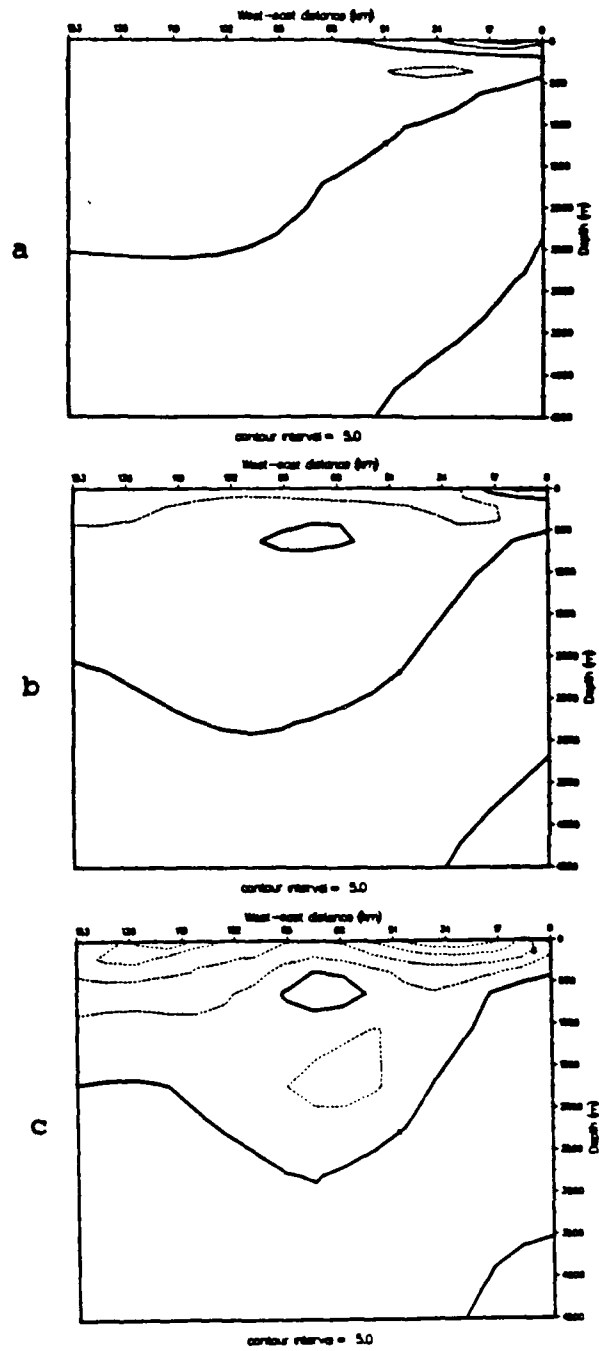


Figure 5.46 Case 4 30-day time-averaged meridional velocity cross-sections centered on day 180: As for Figure 5.11.

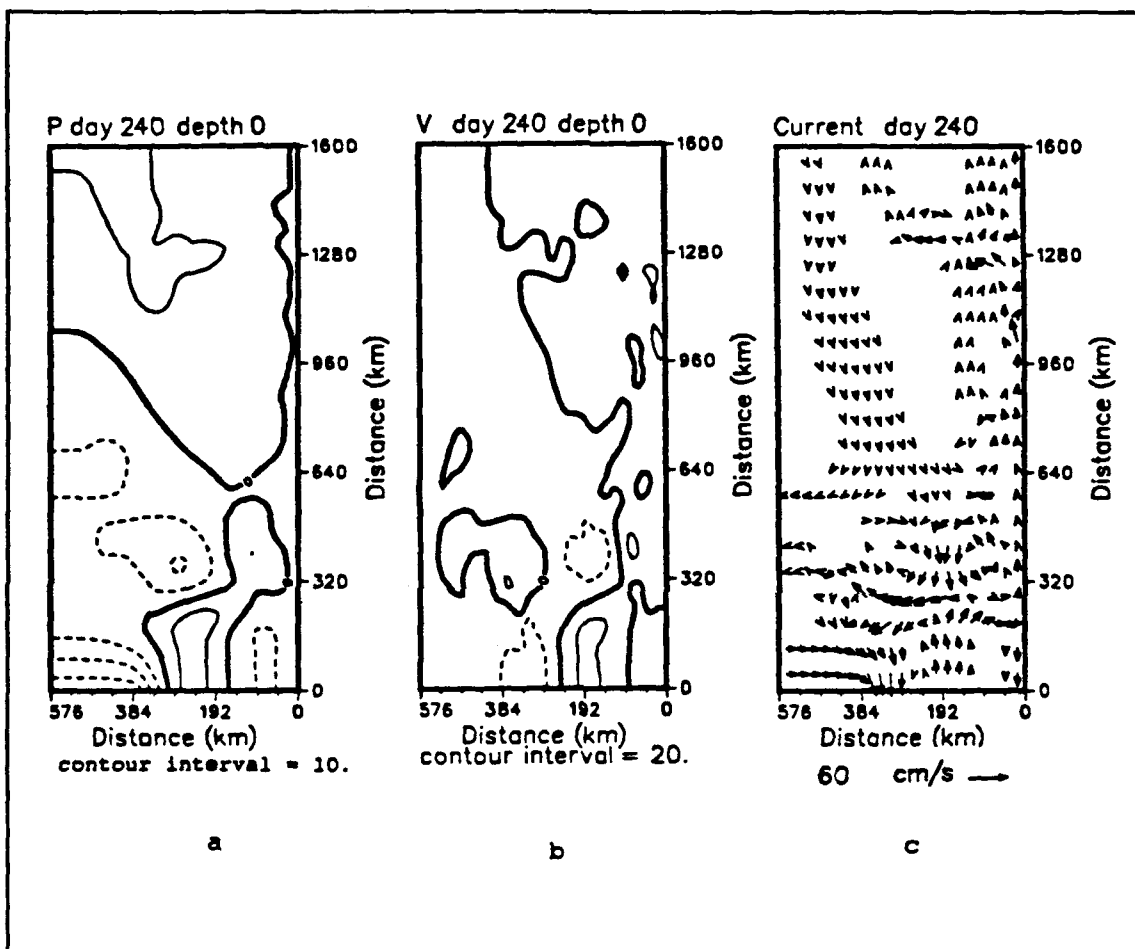


Figure 5.47 Case 3 pressure, meridional velocity, and current vector fields at the surface, day 240: Dashes denote negative, (a) dynamic height anomaly (cm), ref. 2000 m, (b) velocity (cm), (c) velocity vectors.

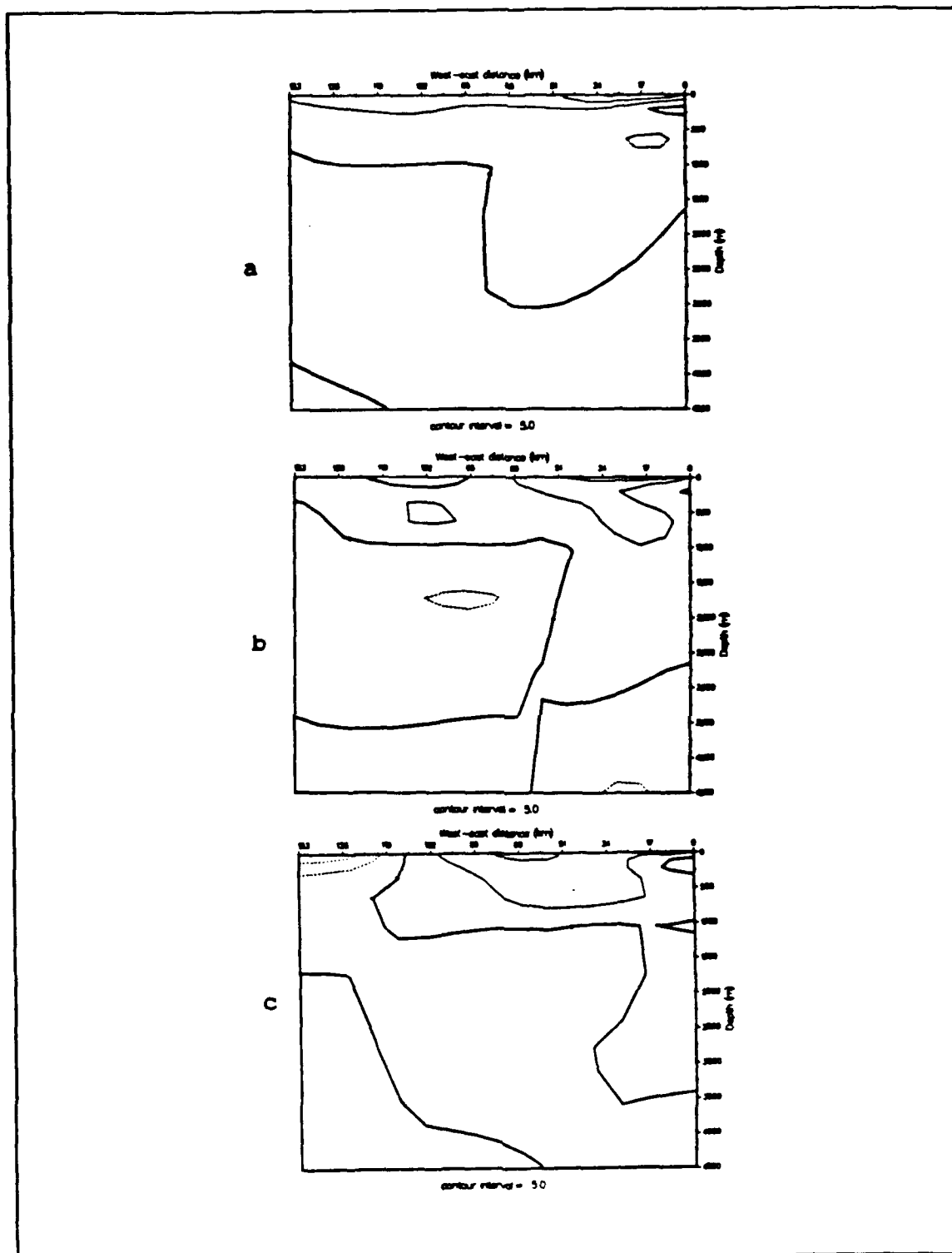


Figure 5.48 Case 3 30-day time-averaged meridional velocity cross-sections centered on day 240: As for Figure 5.11.

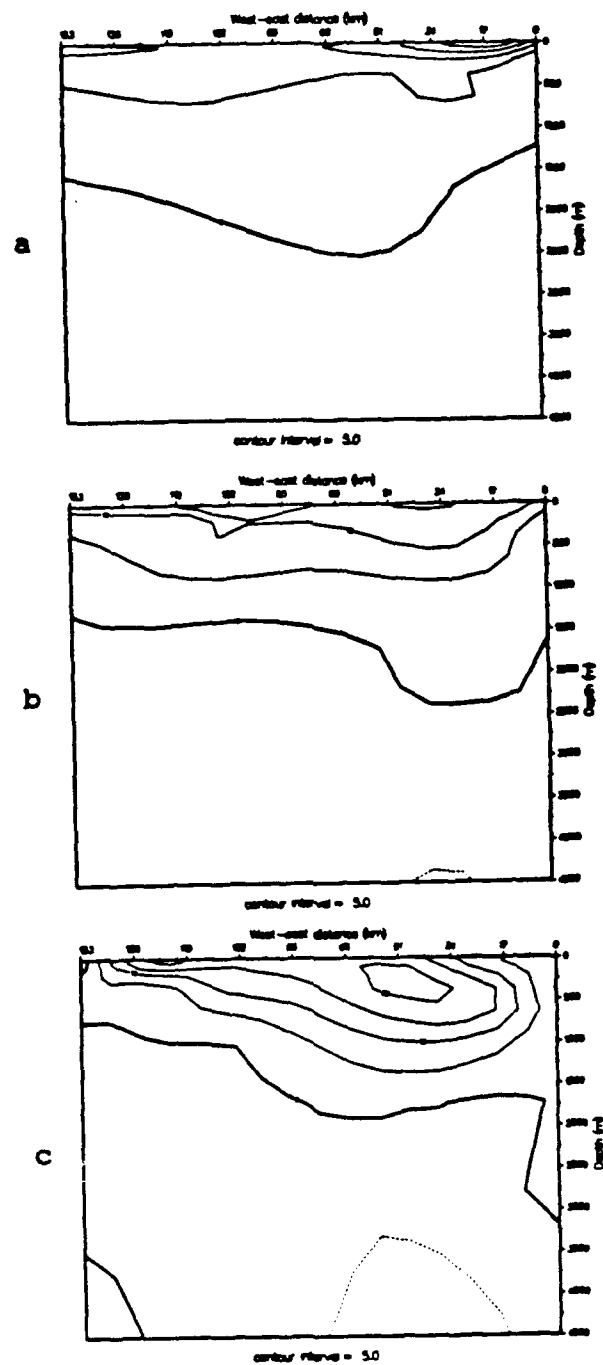


Figure 5.49 Case 4 30-day time-averaged meridional velocity cross-sections centered on day 240: As for Figure 5.11.

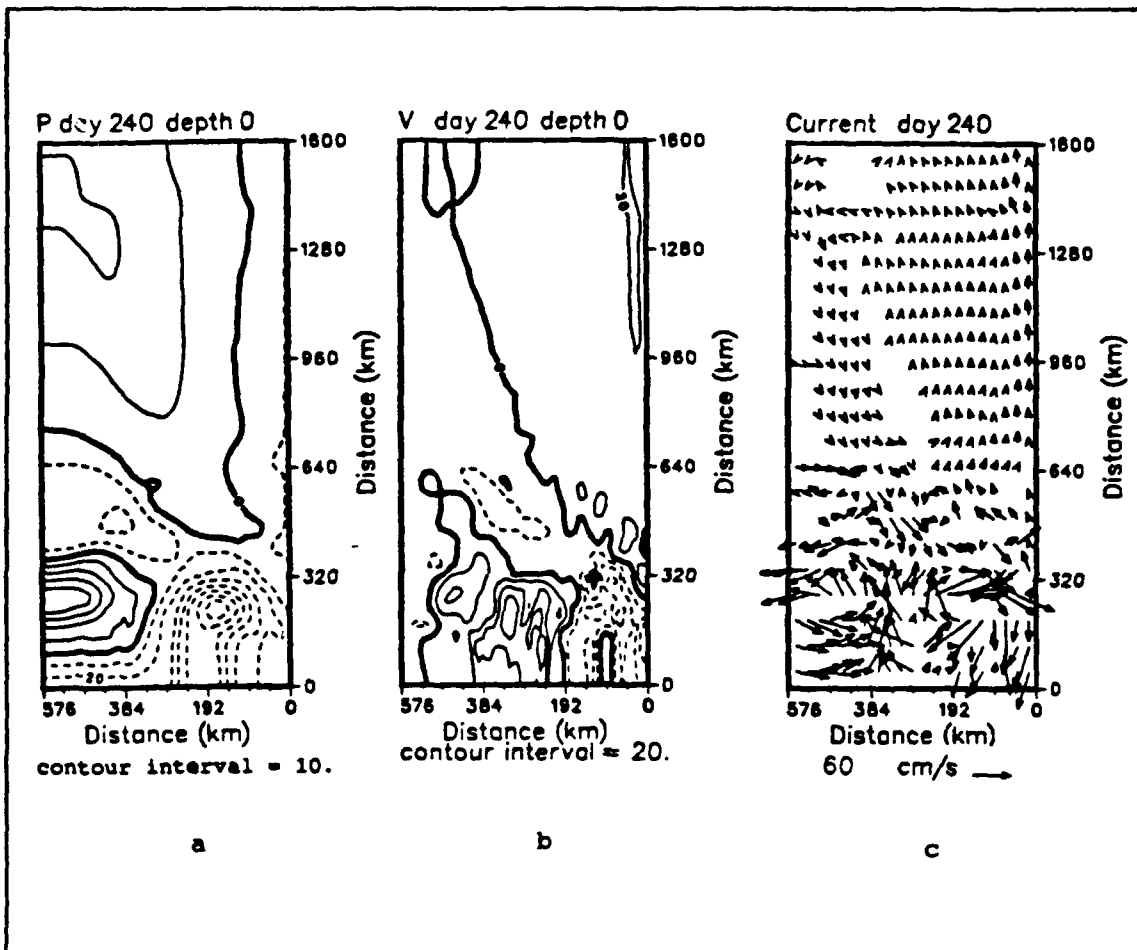


Figure 5.50 Case 4 pressure, meridional velocity, and current velocity vector fields for the surface, day 240: As for Figure 5.47.

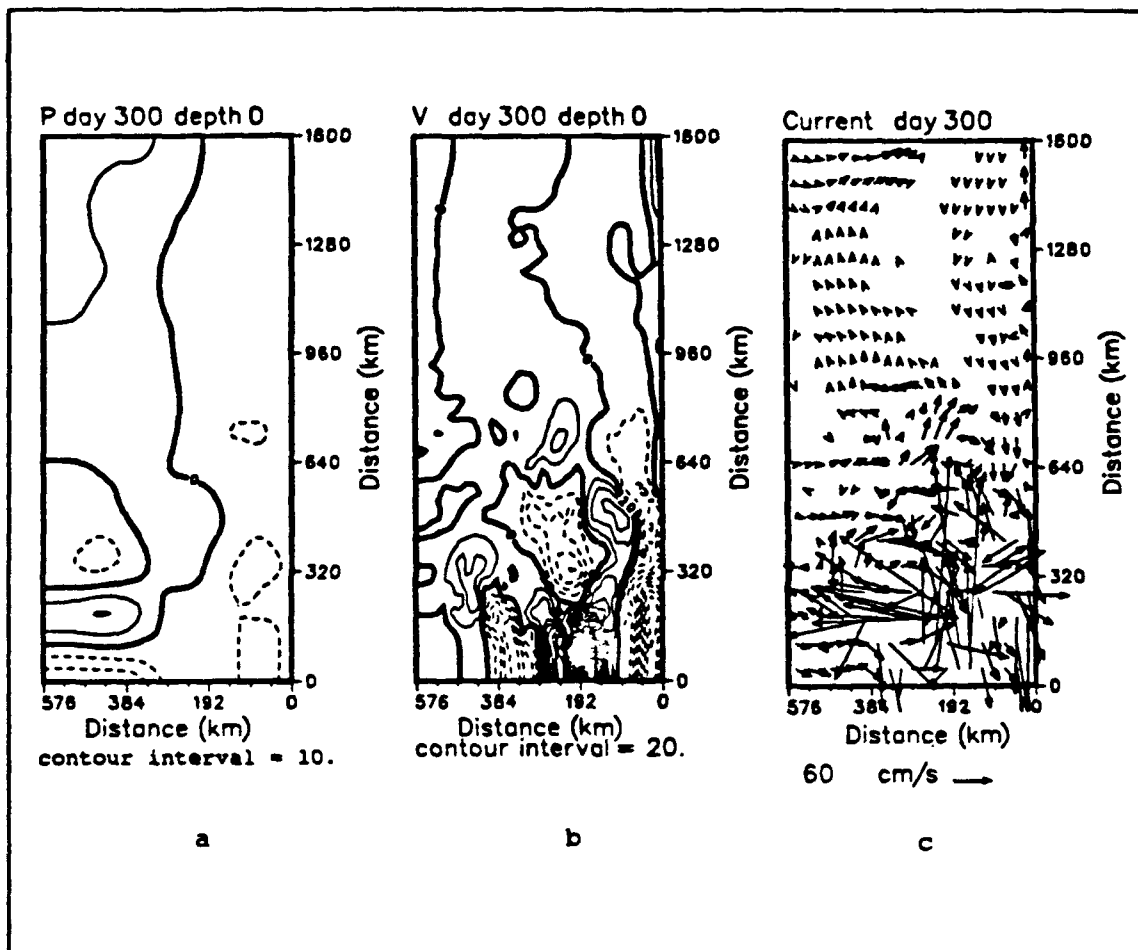


Figure 5.51 Case 4 pressure, meridional velocity, and current velocity vector fields for the surface, day 300: As for Figure 5.47.

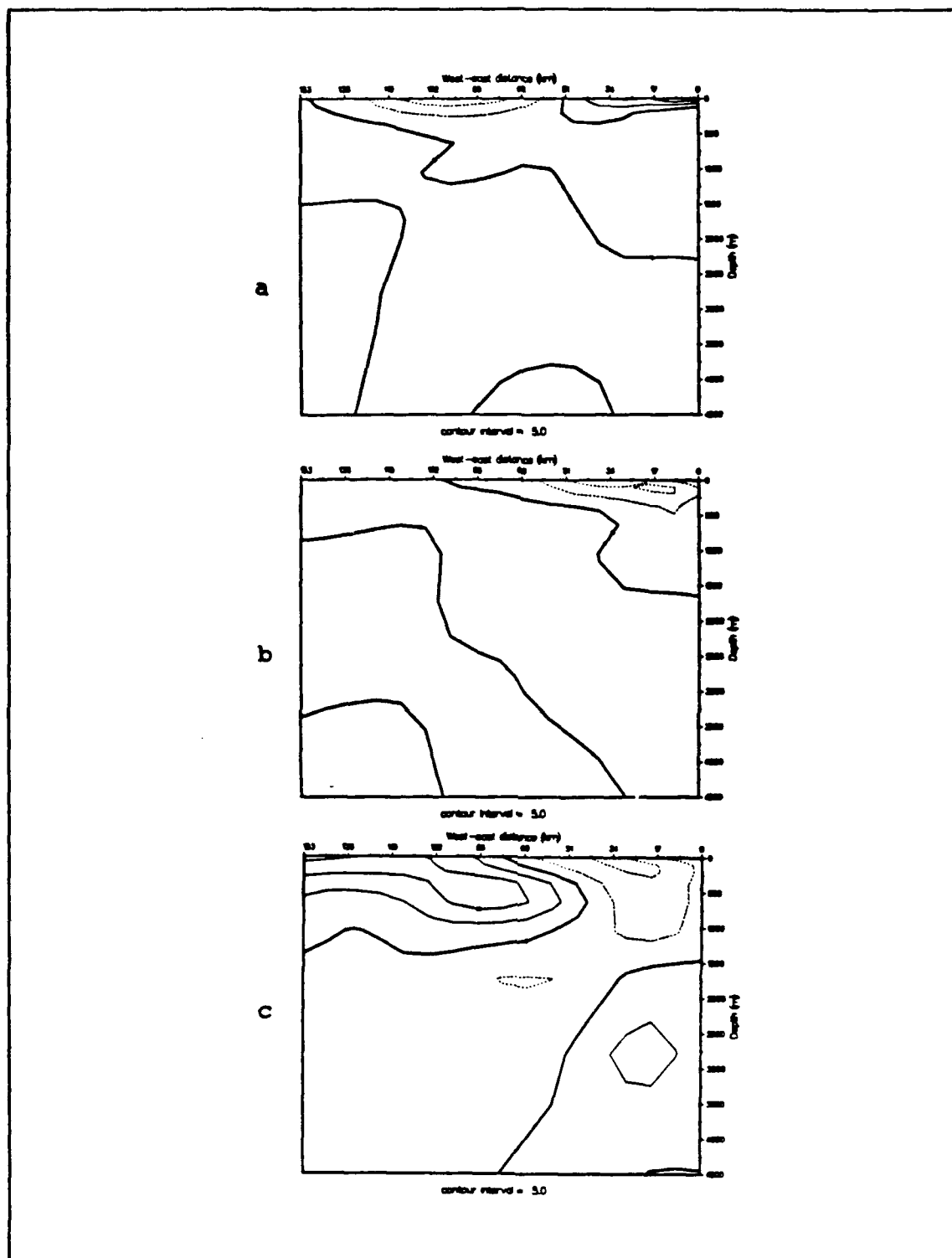


Figure 5.52 Case 3 30-day time-averaged meridional velocity cross-sections centered on day 300: As for Figure 5.11.

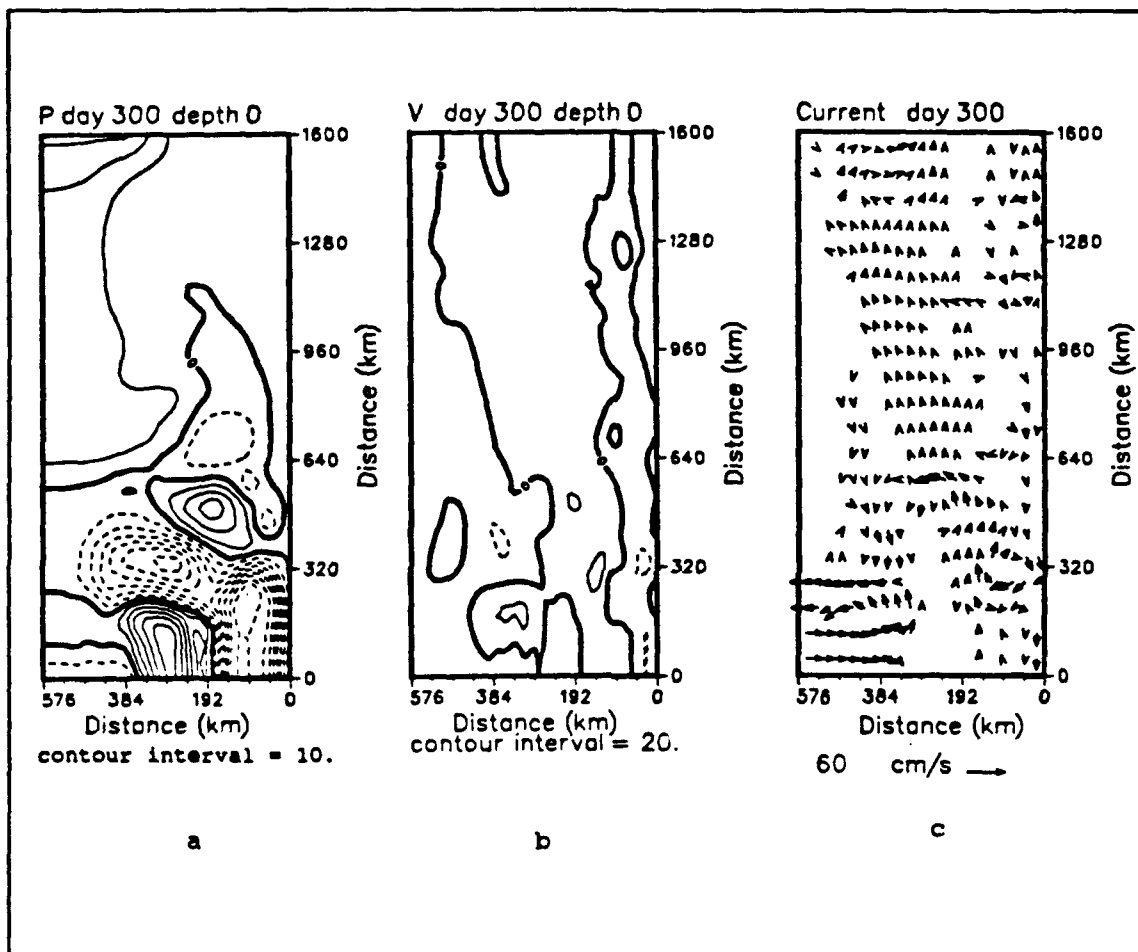


Figure 5.53 Case 3 pressure, meridional velocity, and current velocity vector fields for the surface, day 300: As for Figure 5.47.

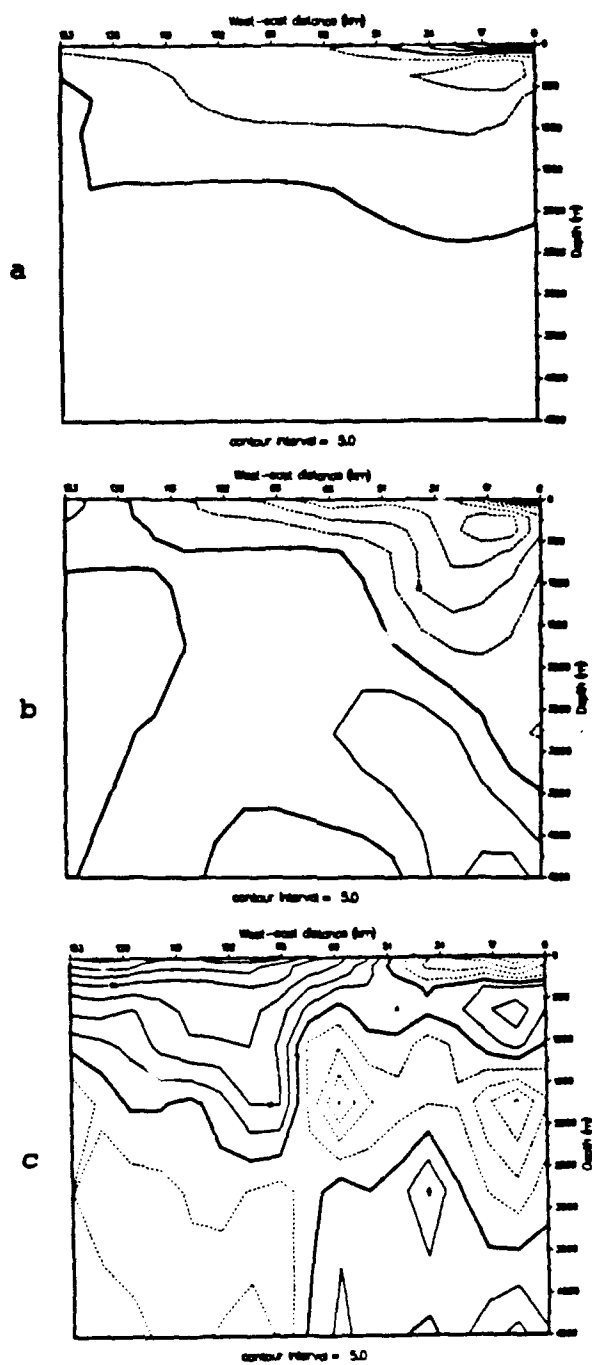


Figure 5.54 Case 4 30-day time-averaged meridional velocity cross-sections centered on day 300: As for Figure 5.11.

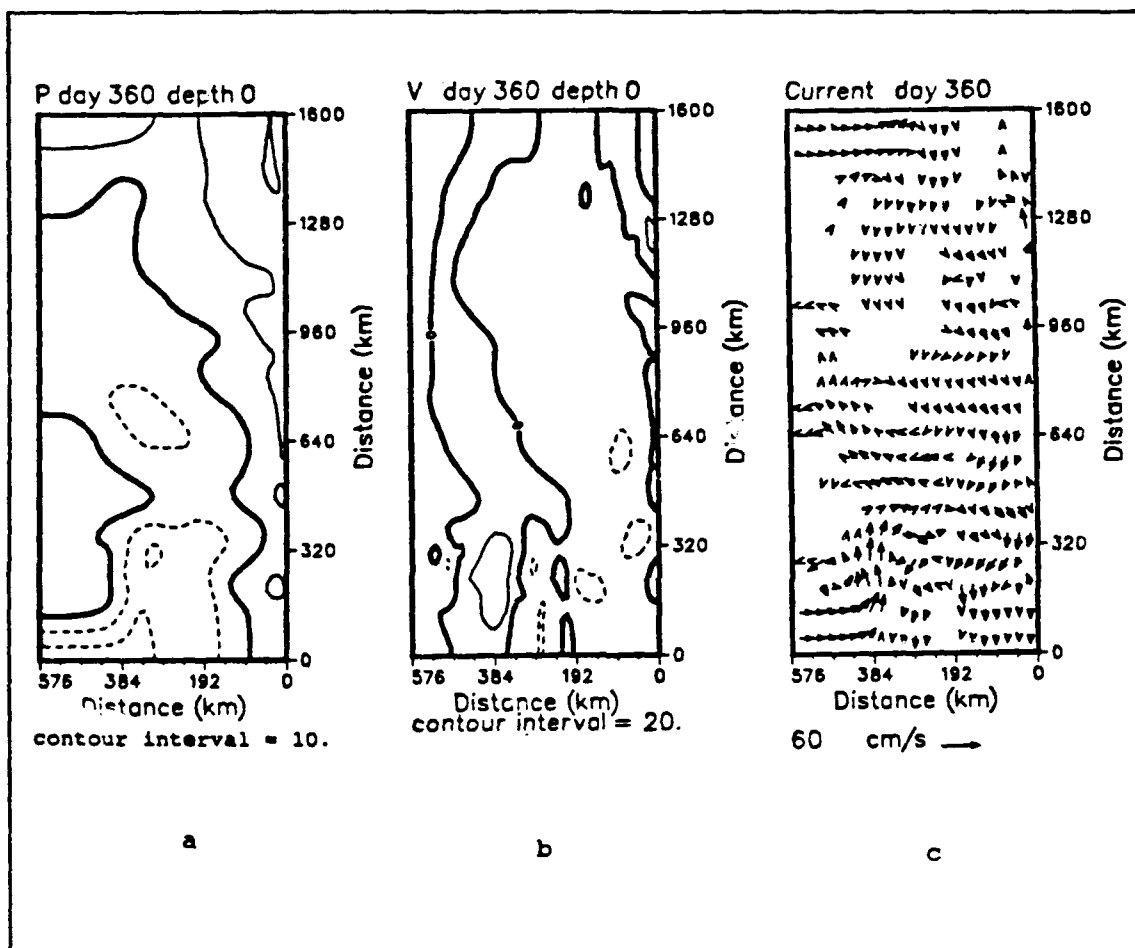


Figure 5.55 Case 3 pressure, meridional velocity, and current velocity vector fields for the surface, Day 360: As for Figure 5.47.

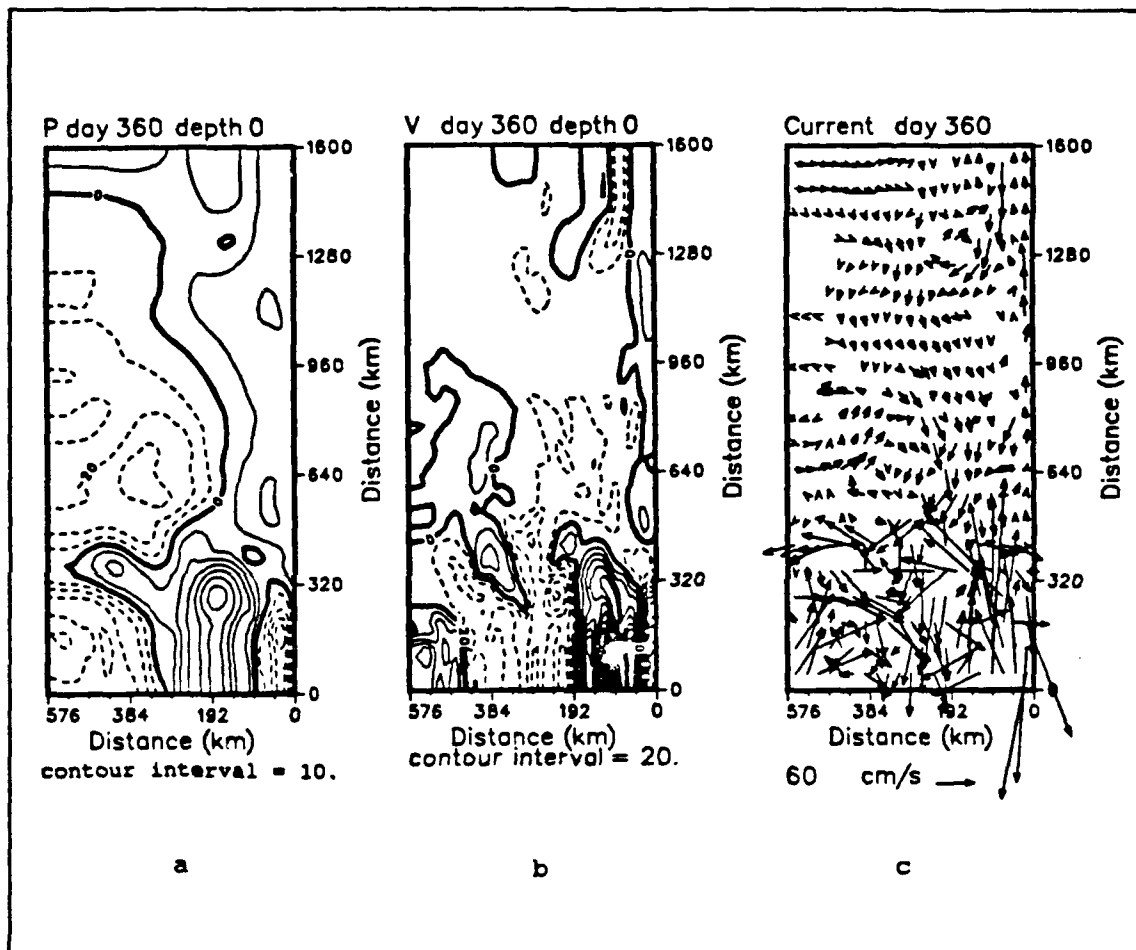


Figure 5.56 Case 4 pressure, meridional velocity, and current velocity vector fields for the surface, day 360: As for Figure 5.47.

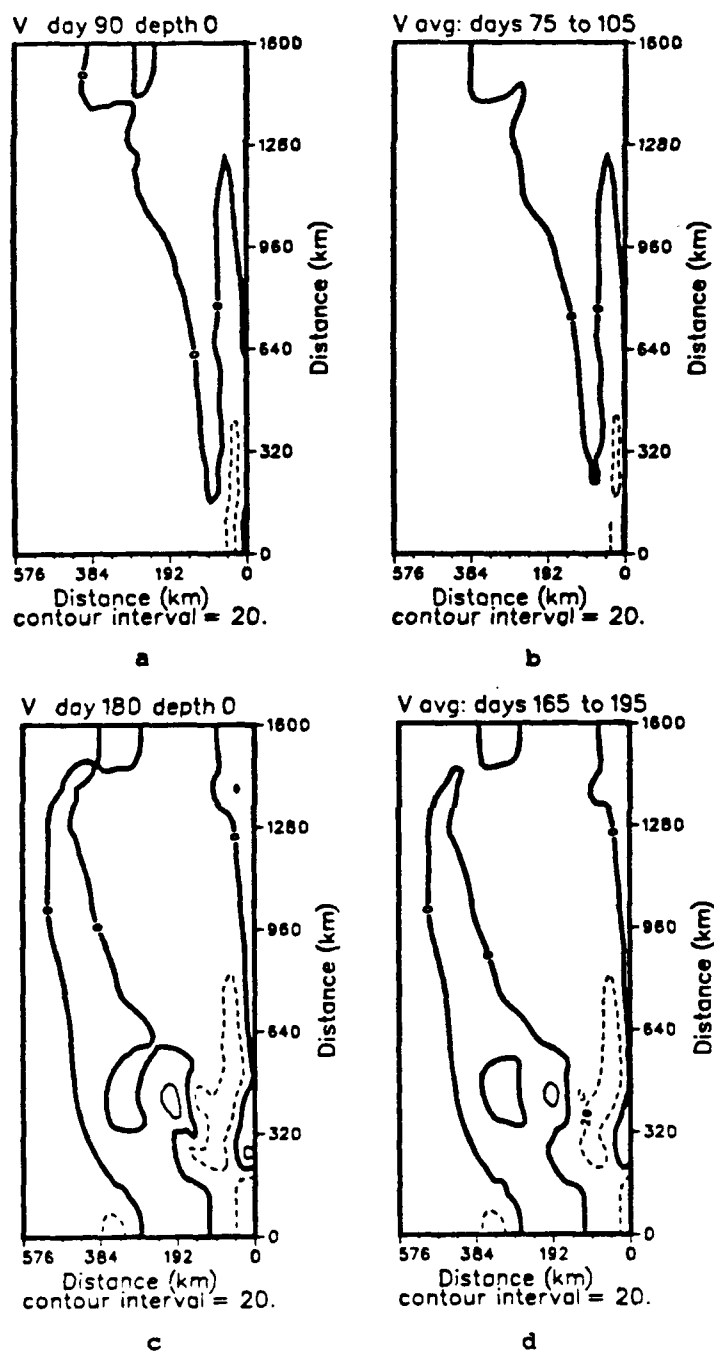


Figure 5.57 Case 3 instantaneous and 30-day time-averaged meridional surface velocity fields: (a, b) austral summer (December), (c, d) austral autumn (March); velocity (cm/s) dashed contours denote poleward flow.

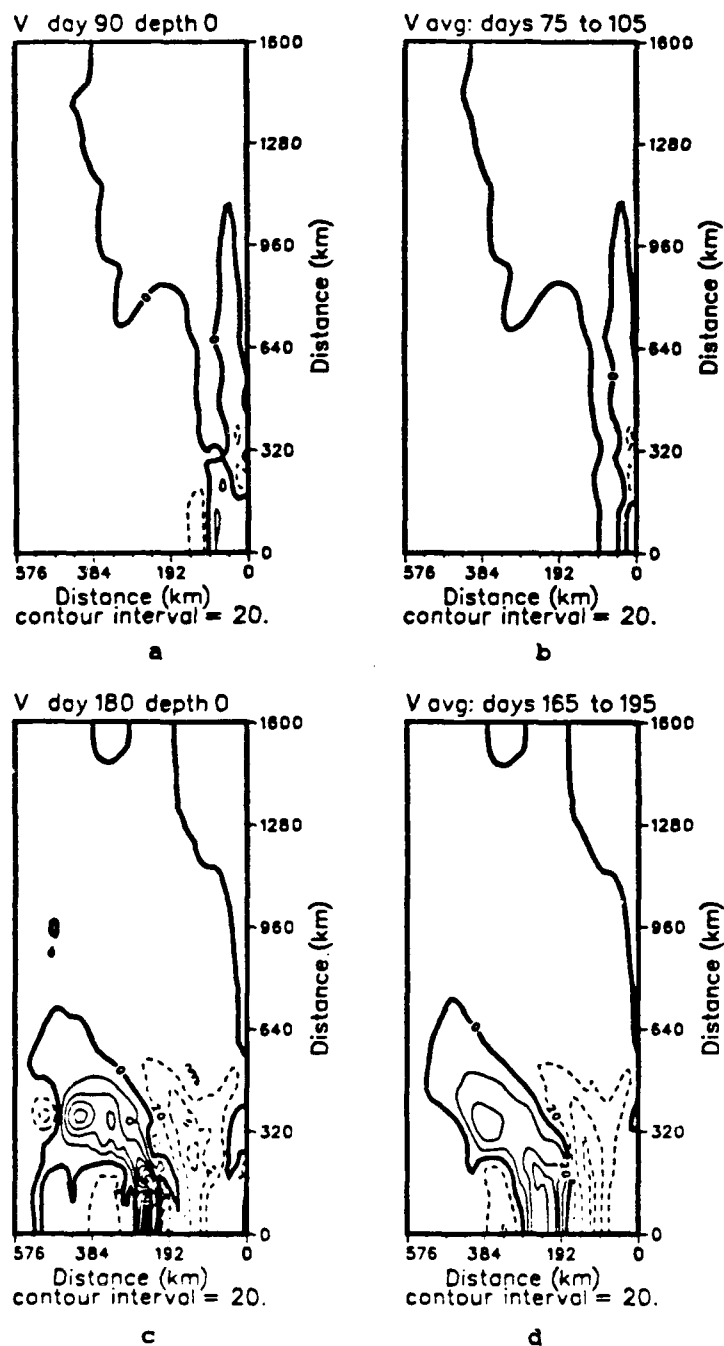


Figure 5.58 Case 4 instantaneous and 30-day time-averaged meridional surface velocity fields: (a, b) austral summer (December), (c, d) austral autumn (March); as for Figure 5.57.

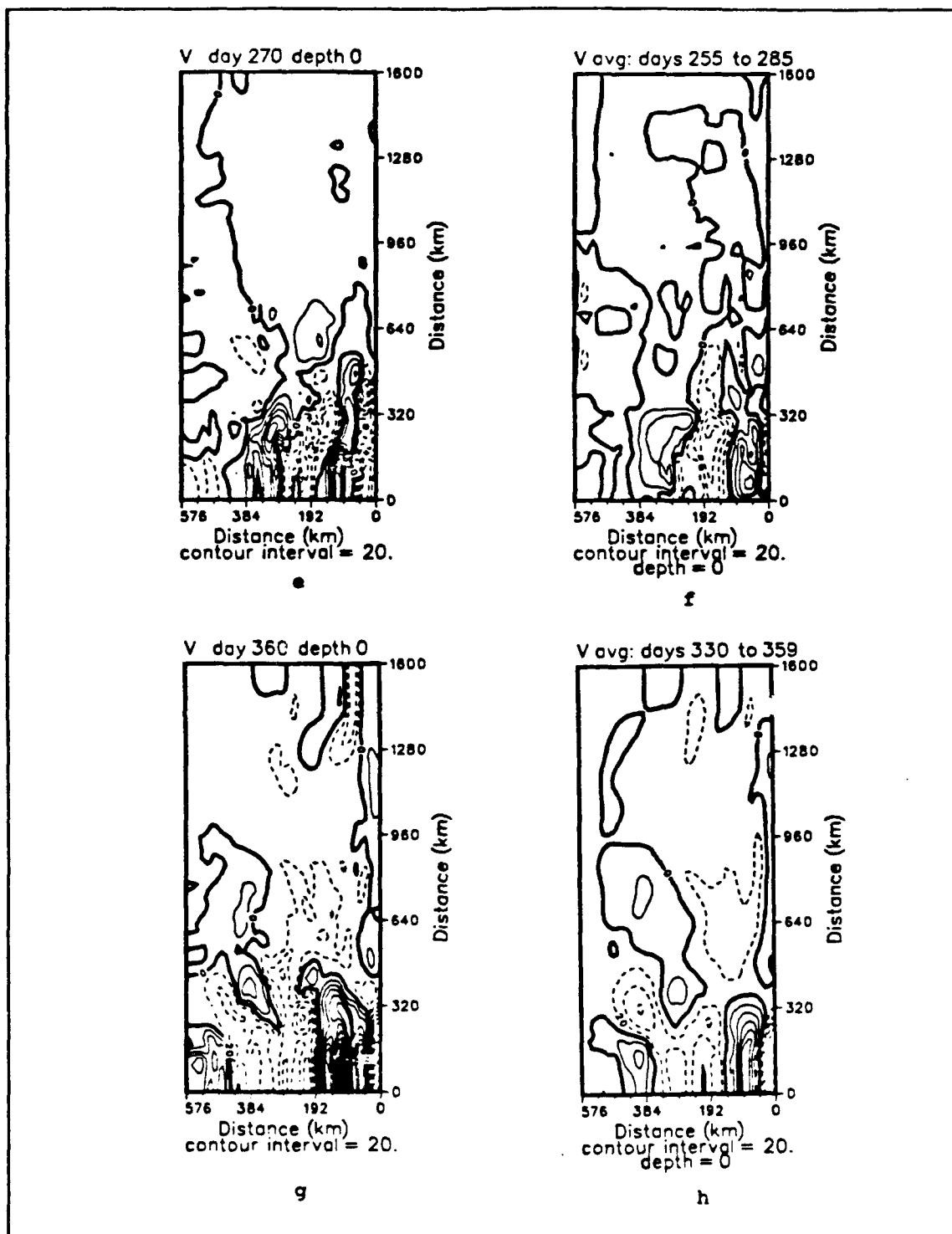


Figure 5.58 cont. Case 4 instantaneous and 30-day time-averaged meridional surface velocity fields: (e, f) austral winter (June), (g, h) austral spring (September).

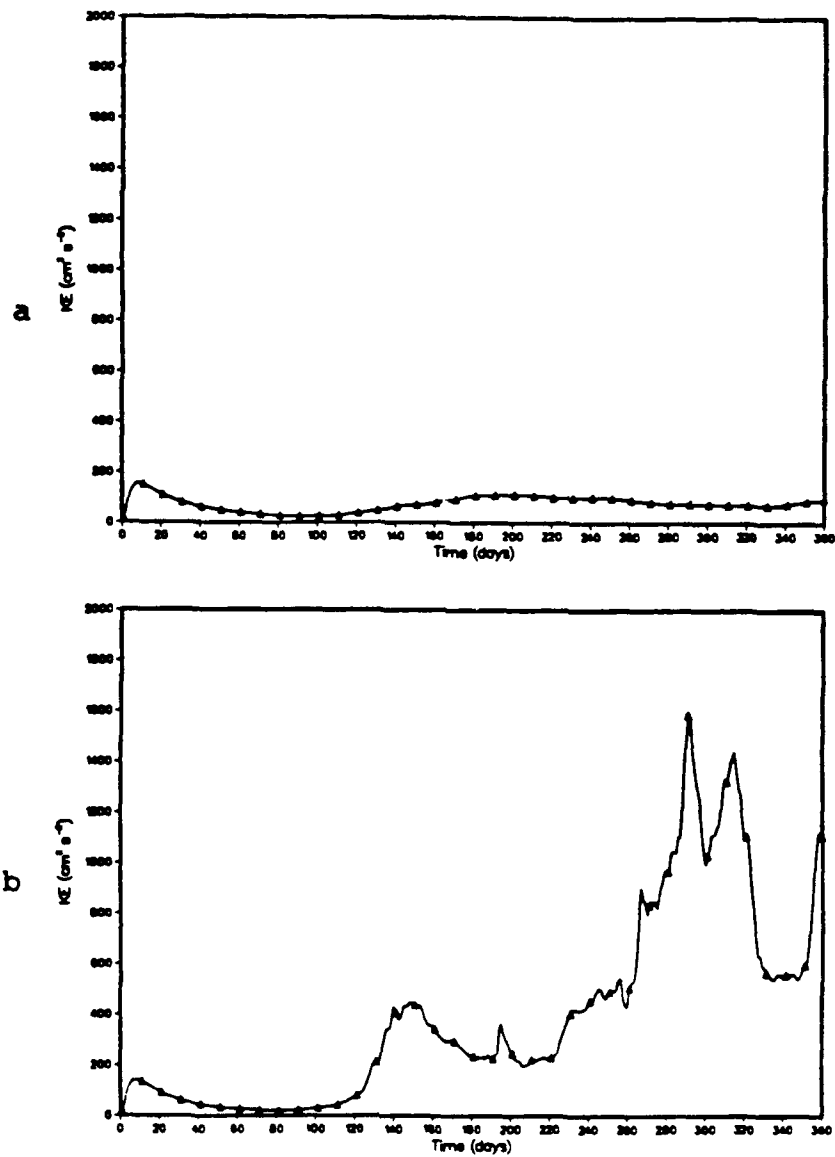


Figure 5.59 Case 3, Case 4 time series of kinetic energy: (a) Case 3, (b) Case 4; as for Figure 5.28.

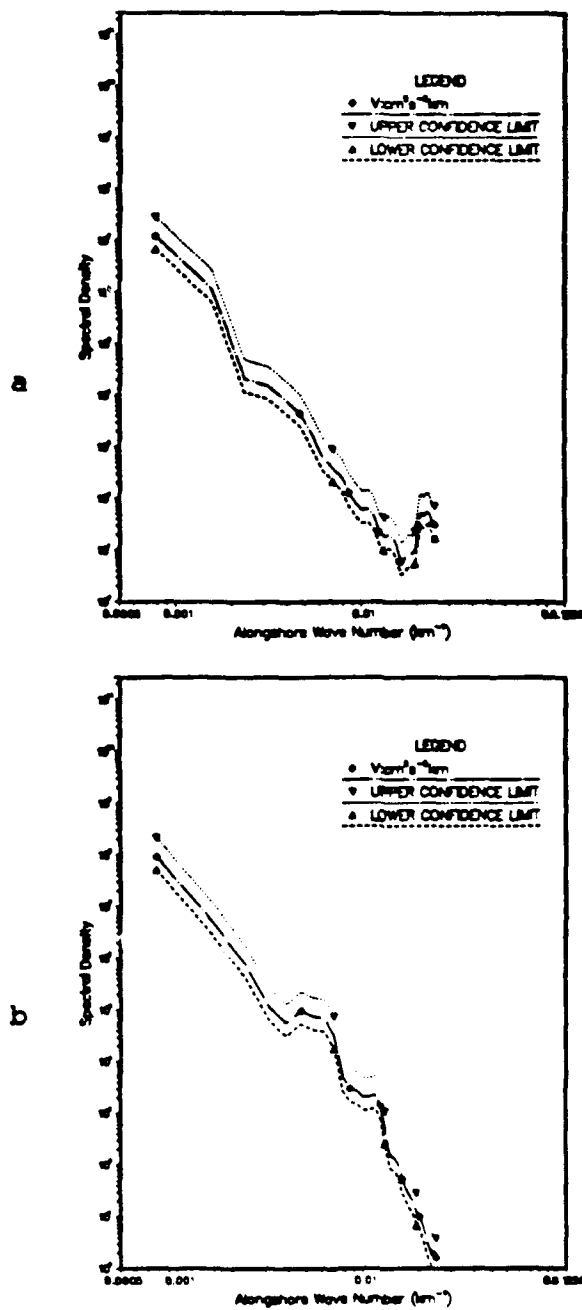


Figure 5.60 Case 3 spectral density, day 80 and day 110: Spectral density (reduced coastal region) versus alongshore wavenumber (inverse wavelength), (a) v at day 80, (b) v at day 110.

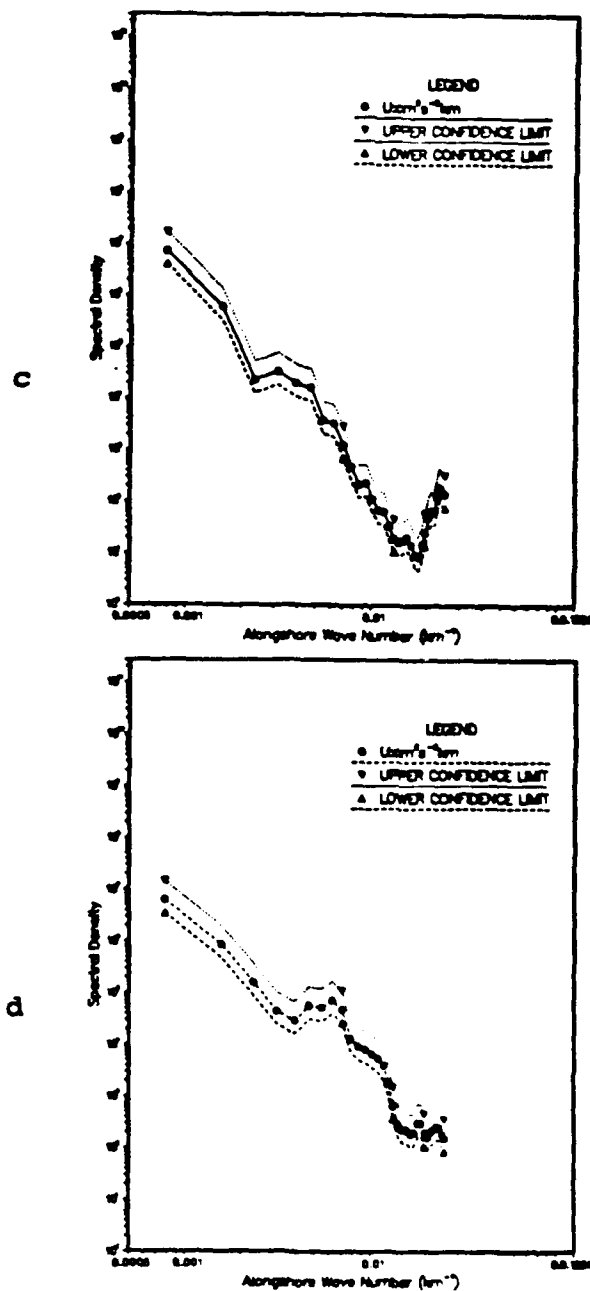


Figure 5.60 cont. Case 3 spectral density, day 80 and day 110: Spectral density (reduced coastal region) versus alongshore wavenumber (inverse wavelength), (c) u at day 80, (d) v at day 110.

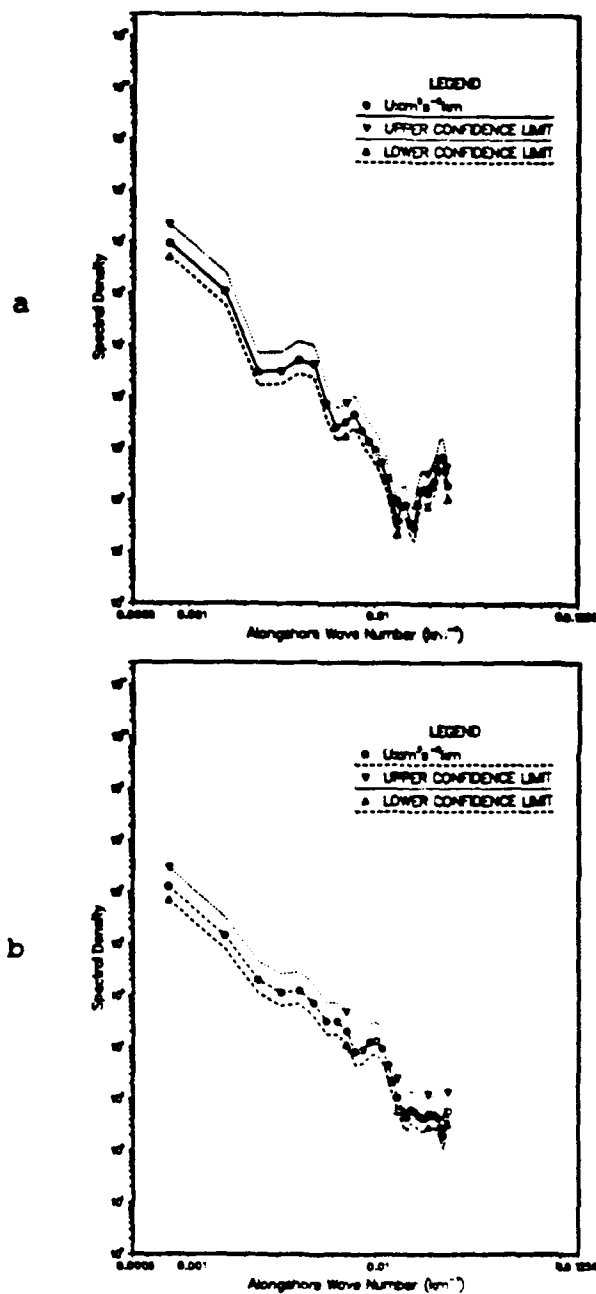


Figure 5.61 Case 4 spectral density, day 70 and day 100: Spectral density (reduced coastal region) versus alongshore wavenumber, (a) day 70, (b) day 100; wavenumber is an inverse wavelength.

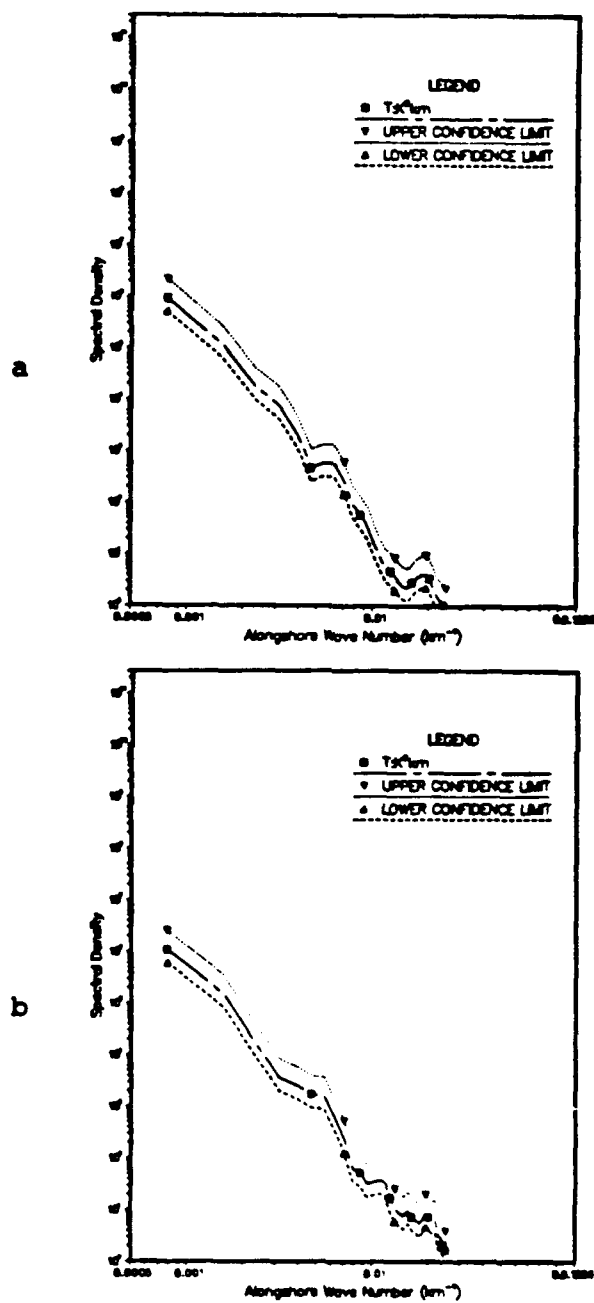


Figure 5.62 Case 3 spectral density, day 170 and day 210: Spectral density (reduced coastal region) versus alongshore wavenumber, (a) day 170, (b) day 210; wavenumber is an inverse wavelength.

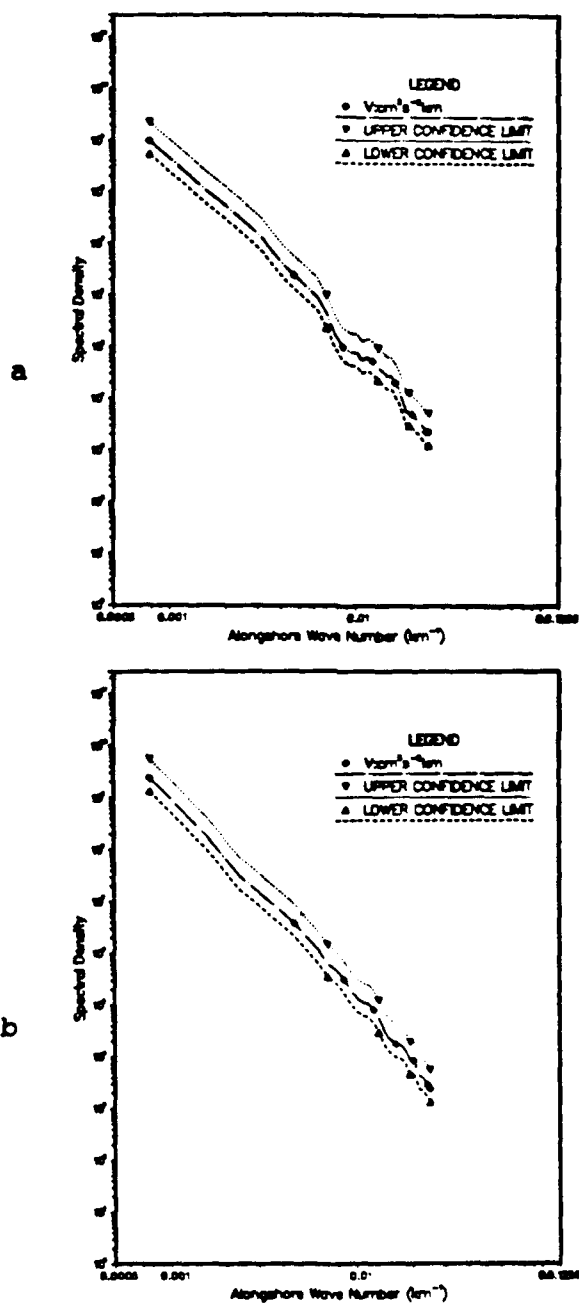


Figure 5.63 Case 4 spectral density, day 200 and day 230: Spectral density (reduced coastal region) versus alongshore wavenumber, (a) day 200, (b) day 230; wavenumber is an inverse wavelength.

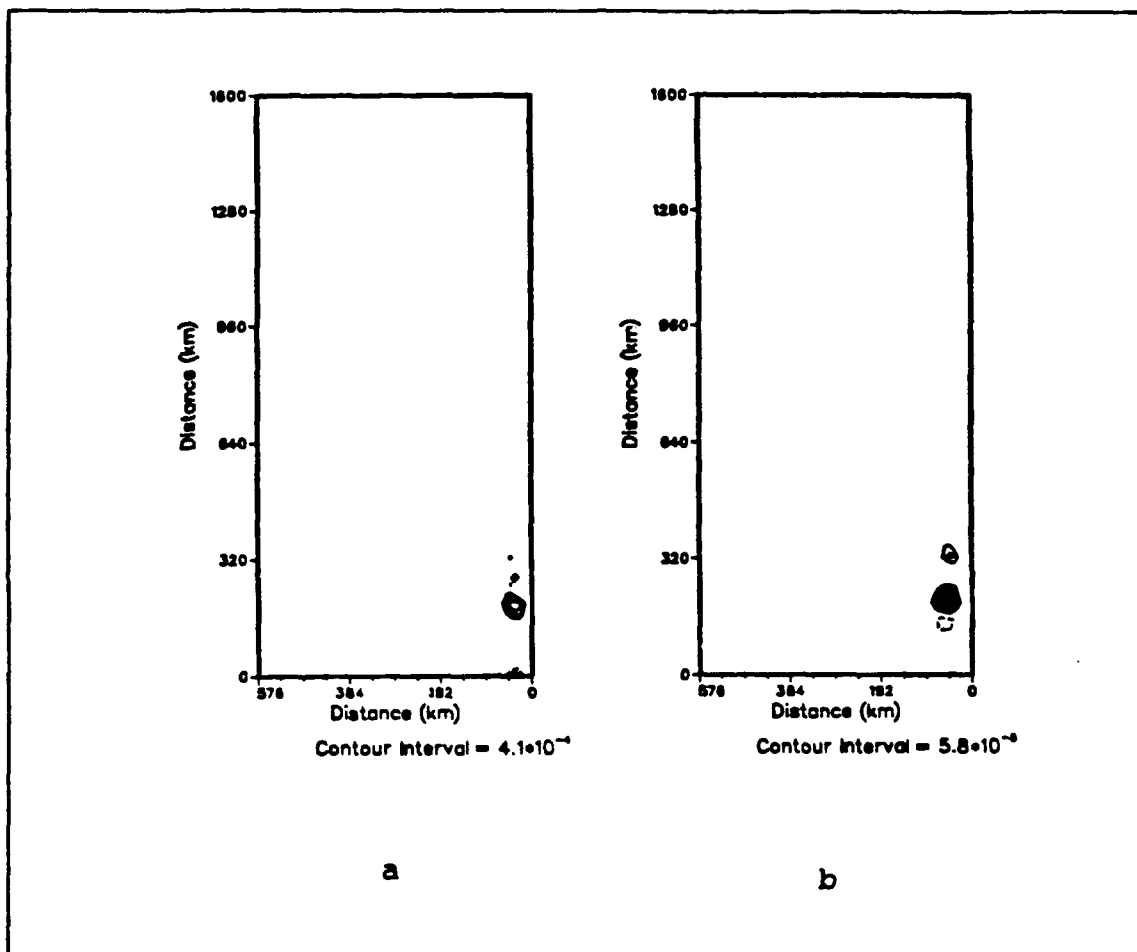
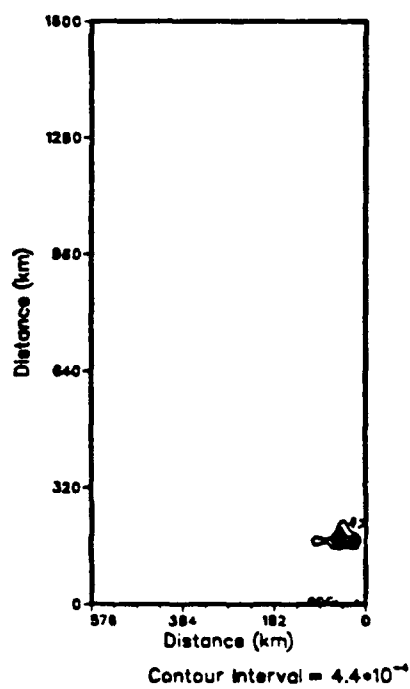
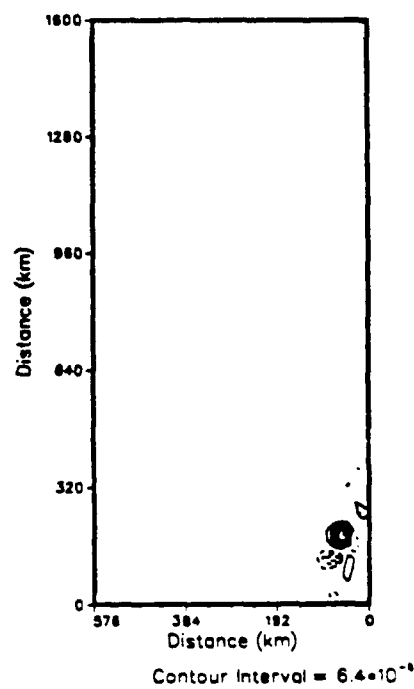


Figure 5.64 Case 3 energy transfer fields, days 80 - 110: (a) barotropic transfer ($\text{ergs}/(\text{cm}^3 \text{ s})$), (b) baroclinic transfer ($\text{ergs}/(\text{cm}^3 \text{ s})$).

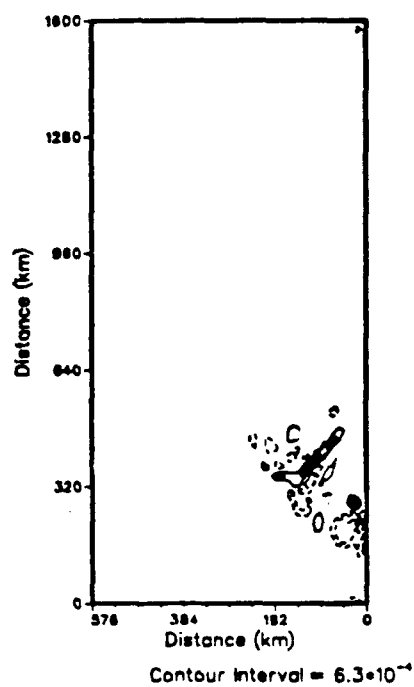


a

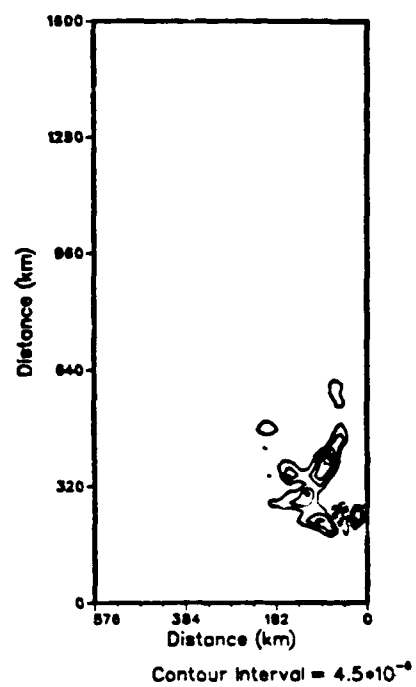


b

Figure 5.65 Case 4 energy transfer fields, days 70 - 90: As for Figure 5.64.

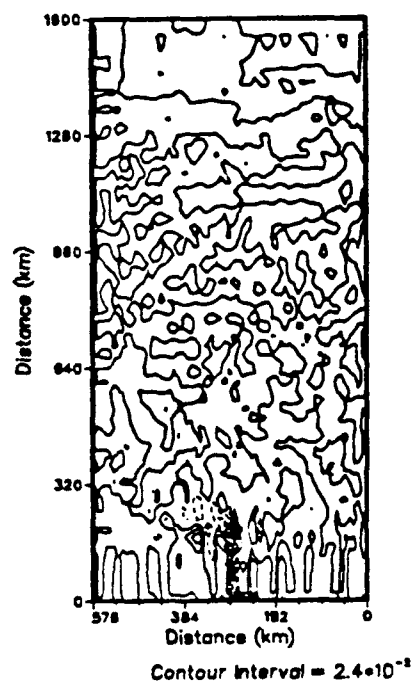


a

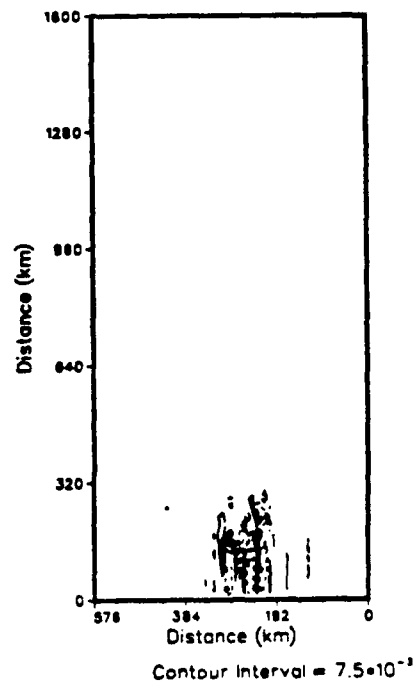


b

Figure 5.66 Case 3 energy transfer fields, days 170 - 200: As for Figure 5.64.



a



b

Figure 5.67 Case 4 energy transfer fields, days 200 - 220: As for Figure 5.64.

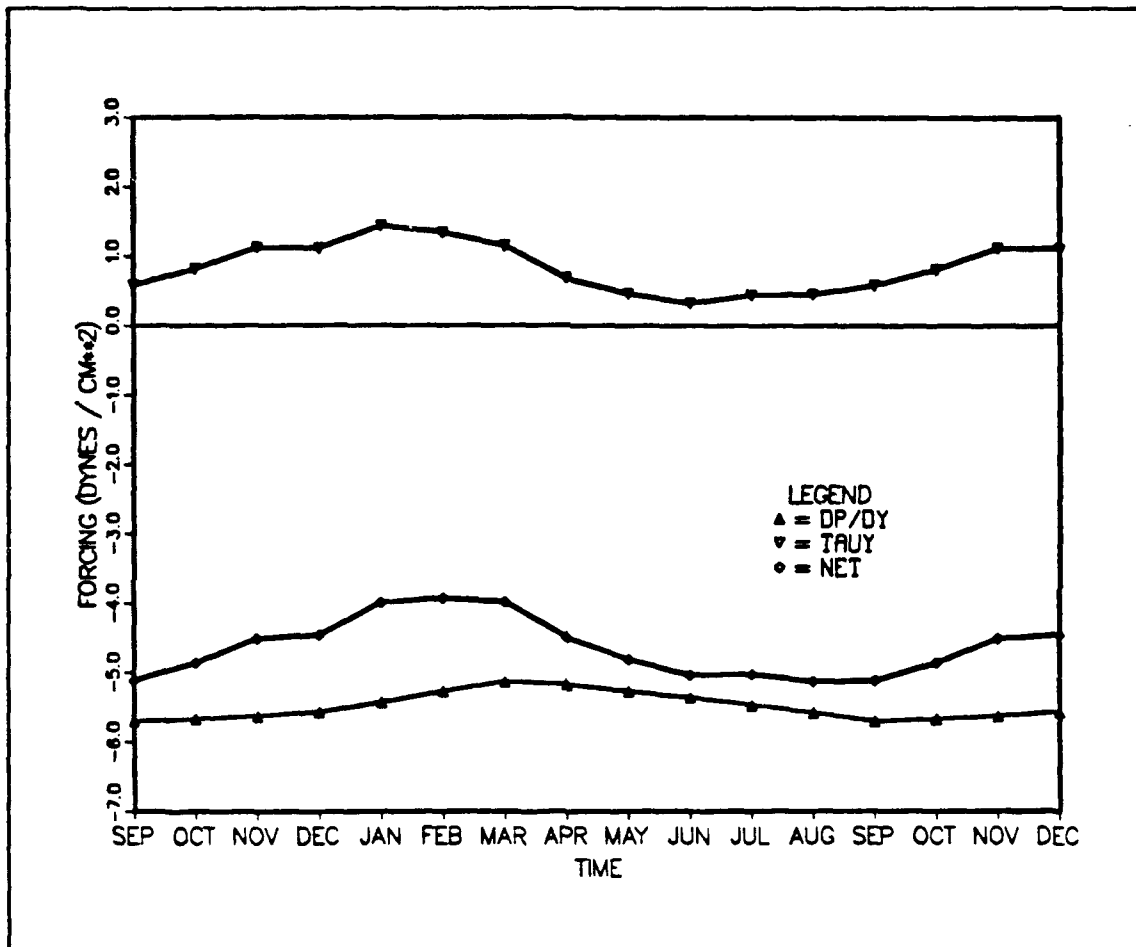


Figure 5.68 Climatological forcing cycles: Onshore geostrophic forcing ($\partial p / \partial y$, ref. 300 m), wind stress (τ_y), net (positive forcing is equatorward) forcing versus month.

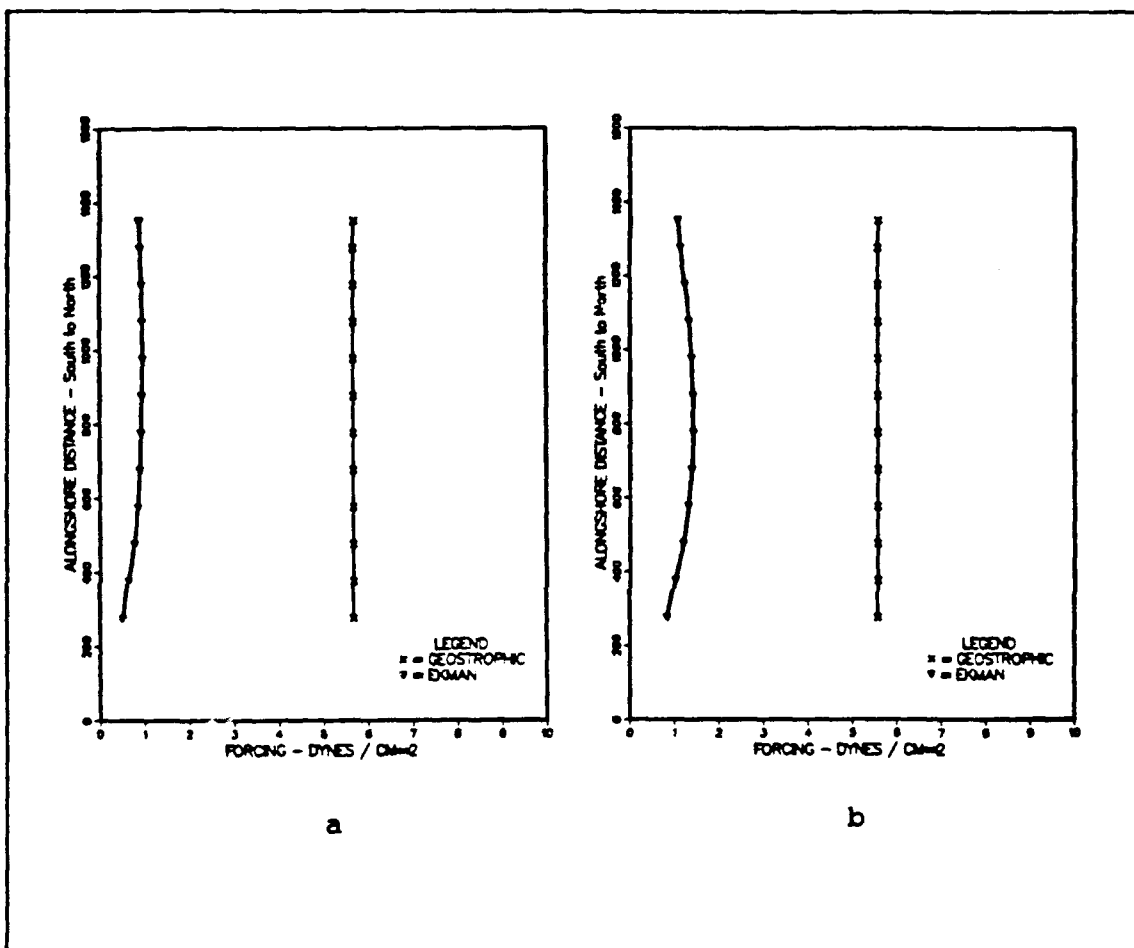


Figure 5.69 Geostrophic versus surface Ekman forcing: (a) October, (b) December; geostrophic (pressure gradient forcing ($\partial p / \partial y$) ref. 300 m), surface Ekman forcing (wind stress (τ_y)).

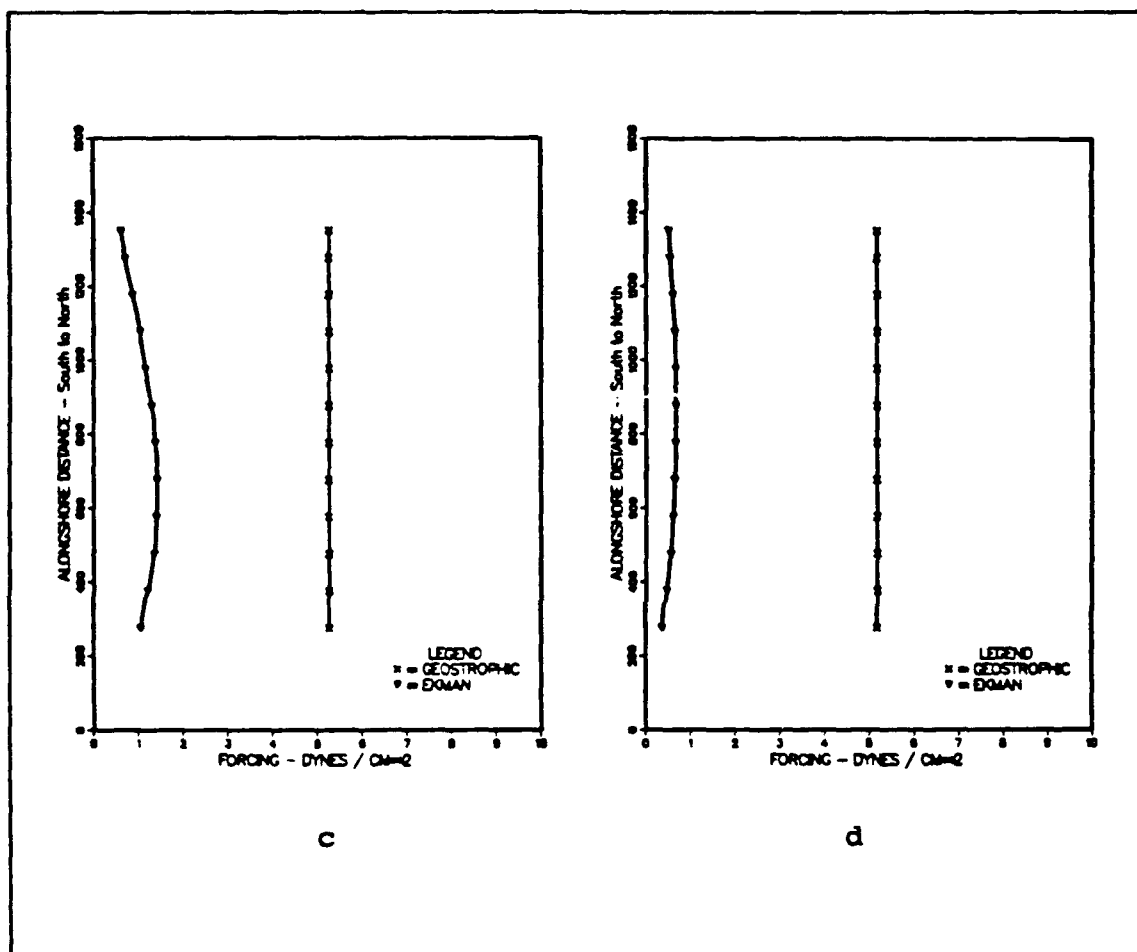
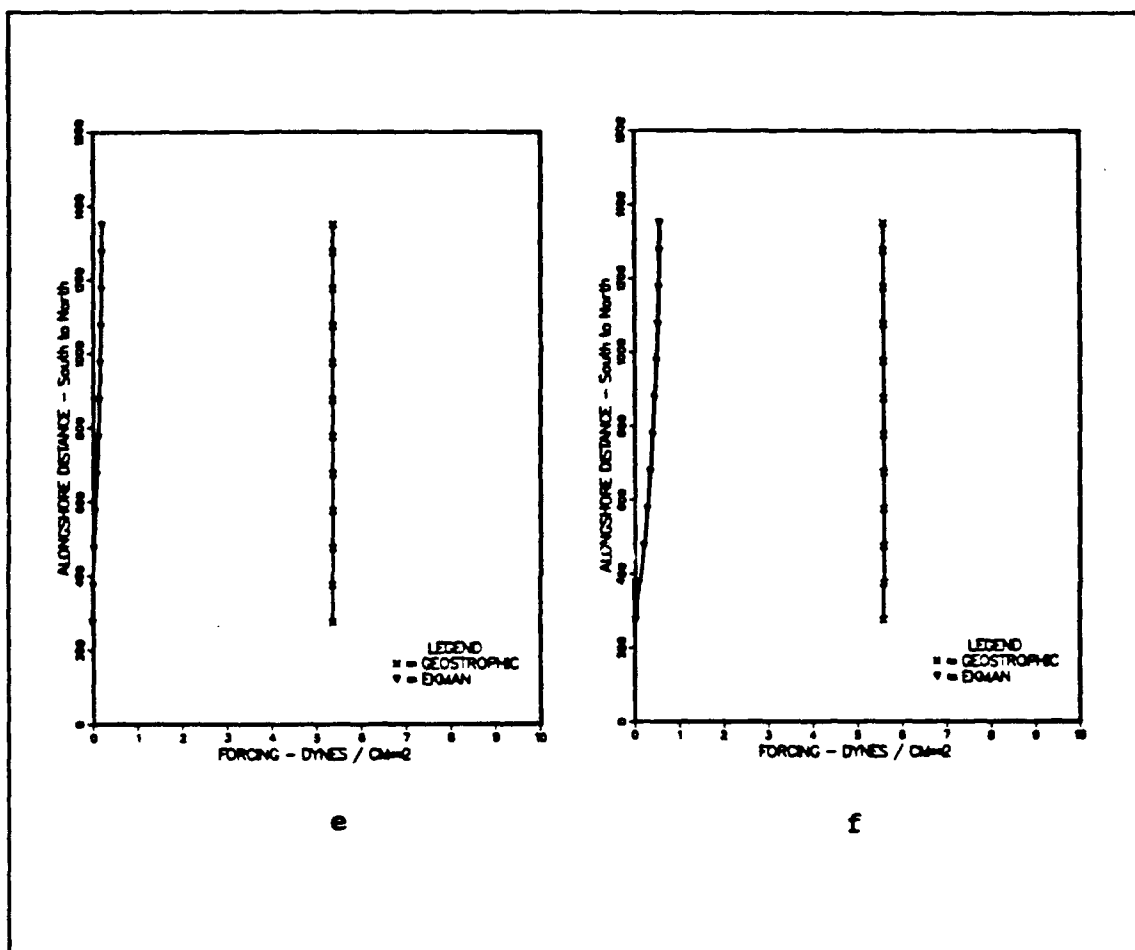


Figure 5.69 cont. Geostrophic versus surface Ekman forcing: (c) February, (d) April; geostrophic (pressure gradient forcing ($\partial p / \partial y$) ref. 300 m), surface Ekman forcing (wind stress (τ_y)).



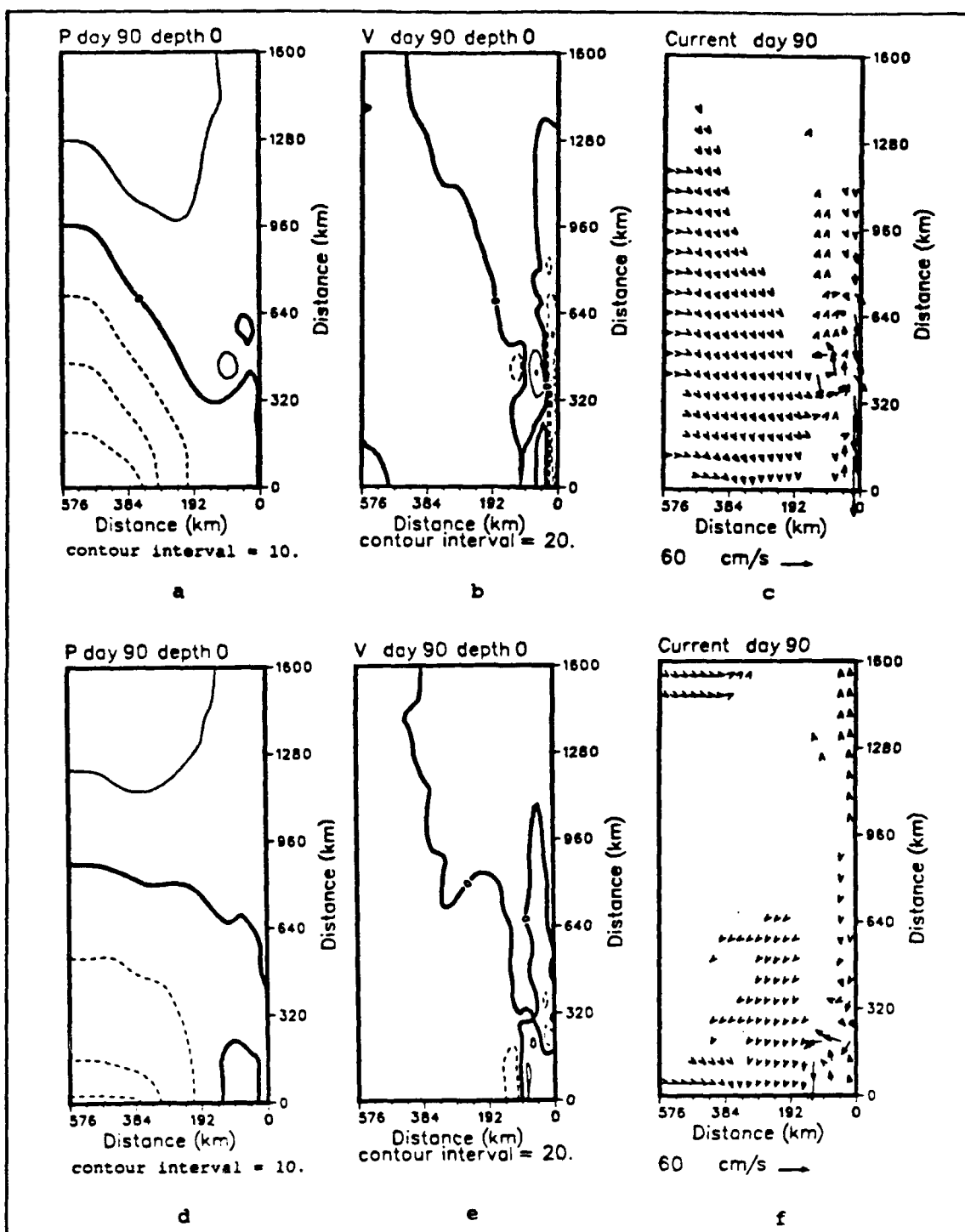


Figure 5.70 Case 2, Case 4 pressure, meridional velocity, current velocity vector fields at the surface, day 90: Dashes denote negative values, (a-c) Case 2, (d-f) Case 4; pressure (cm) ref. 2000 m, velocity (cm/s).

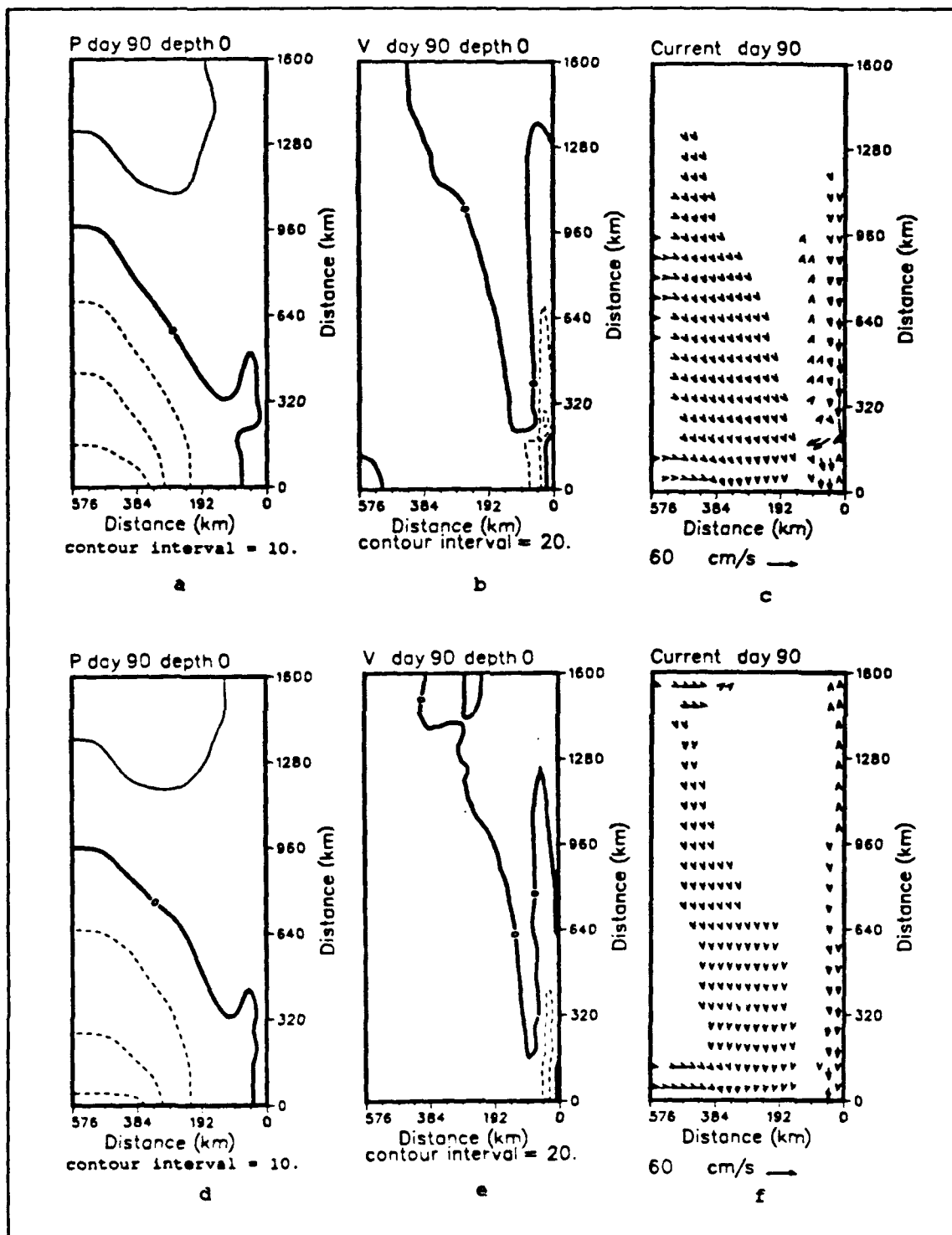


Figure 5.71 Case 1, Case 3 pressure, meridional velocity, current velocity vector fields at the surface, day 90: (a-c) Case 1, (d-f) Case 3; as for Figure 5.70.

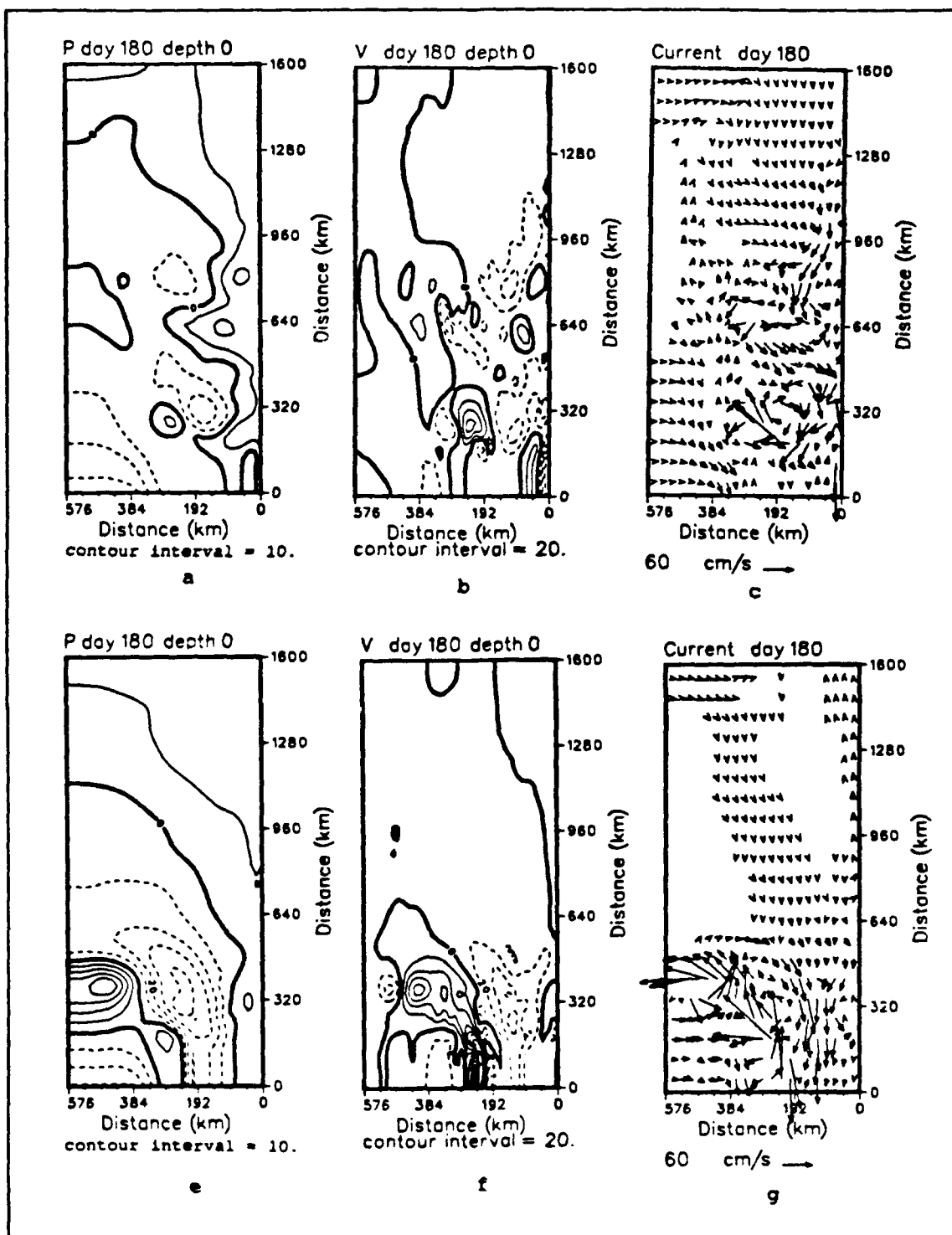


Figure 5.72 Case 2, Case 4 pressure, meridional velocity, current velocity vector fields at the surface, day 180: (a-c) Case 2, (d-f) Case 4; as for Figure 5.70.

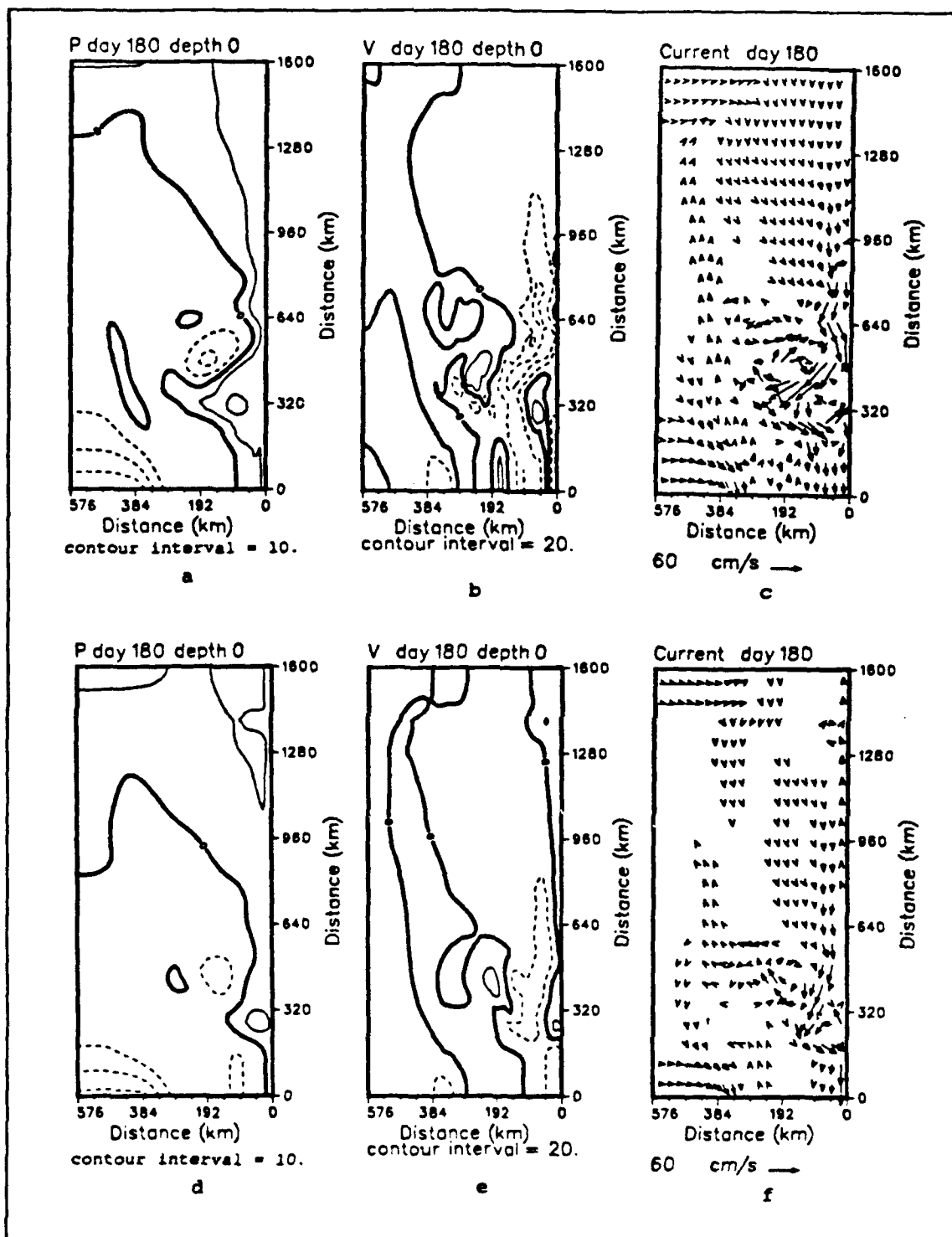


Figure 5.73 Case 1, Case 3 pressure, meridional velocity, current velocity vector fields at the surface, day 180: (a-c) Case 1, (d-f) Case 3; as for Figure 5.70.

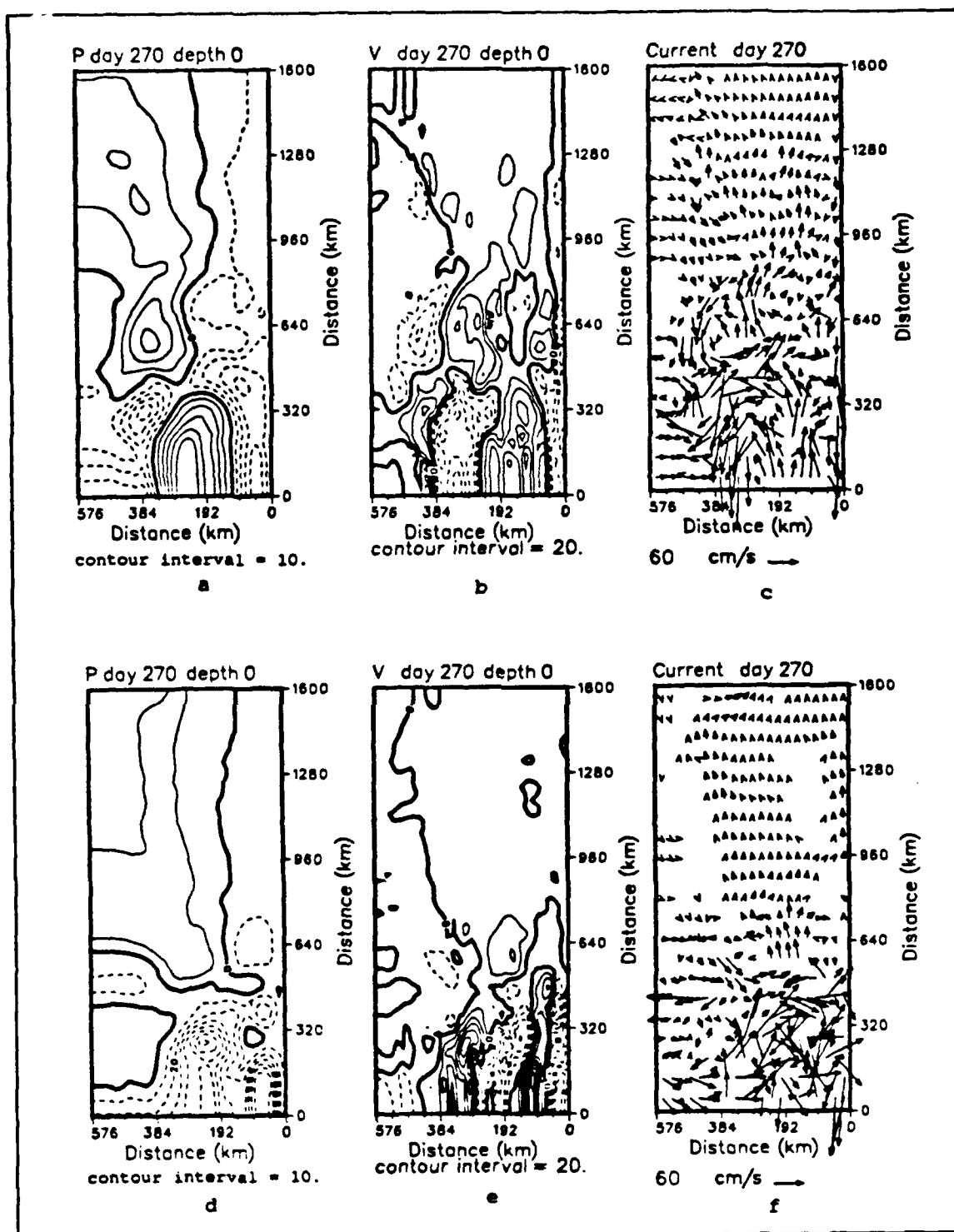


Figure 5.74 Case 2, Case 4 pressure, meridional velocity, current velocity vector fields at the surface, day 270: (a-c) Case 2, (d-f) Case 4; as for Figure 5.70.

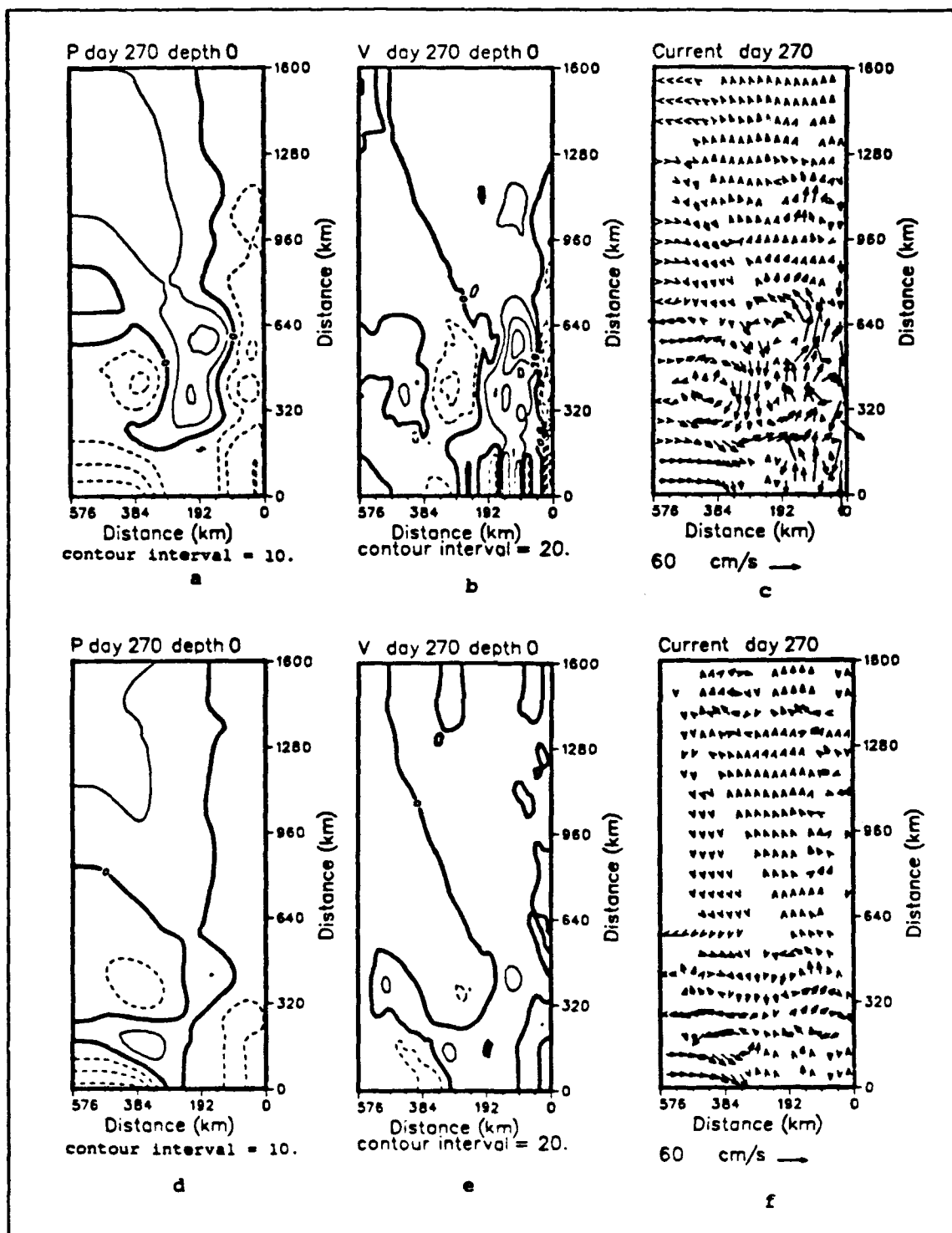


Figure 5.75 Case 1, Case 3 pressure, meridional velocity, current velocity vector fields at the surface, day 270: (a-c) Case 1, (d-f) Case 3; as for Figure 5.70.

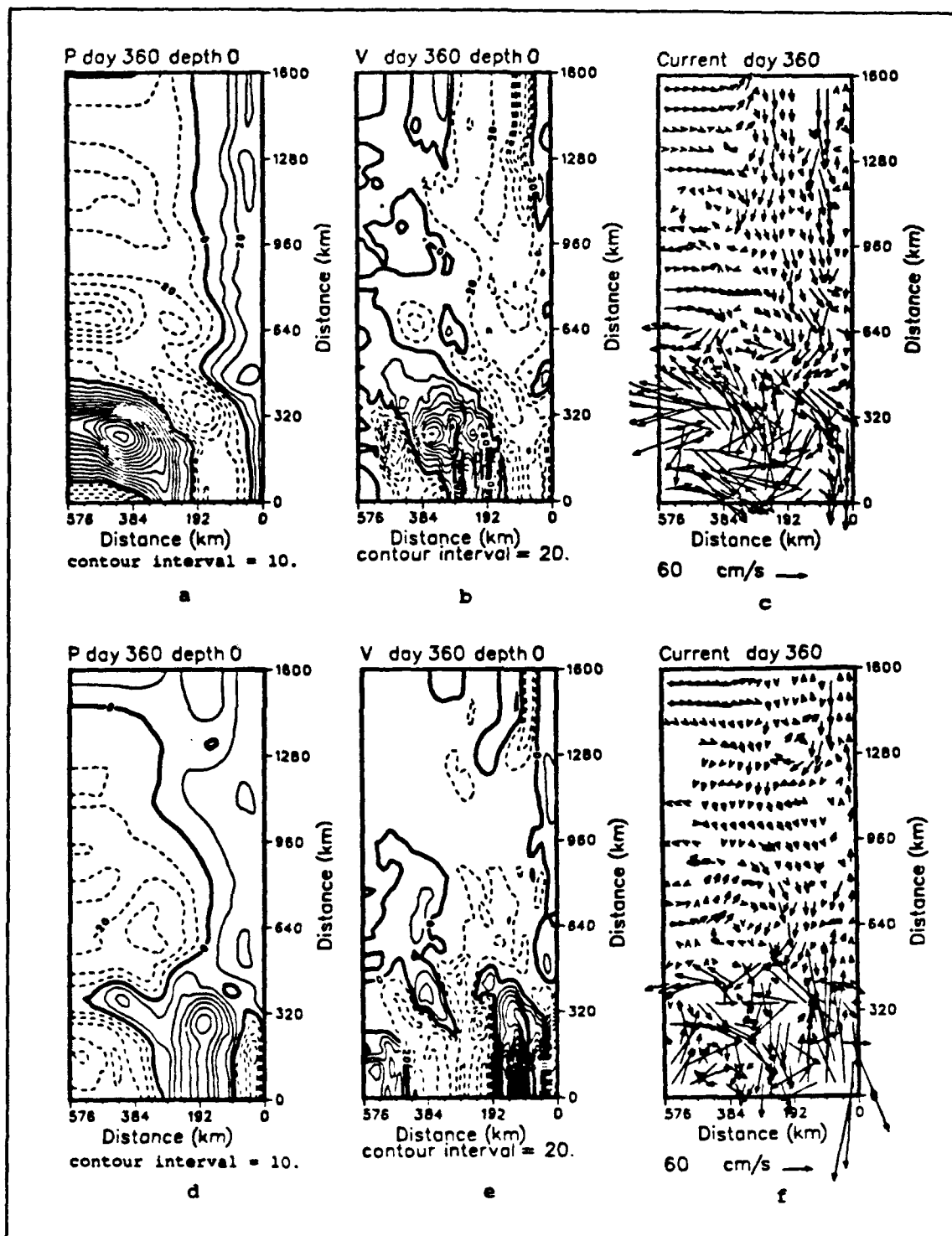


Figure 5.76 Case 2, Case 4 pressure, meridional velocity, current velocity vector fields at the surface, day 360: (a-c) Case 2, (d-f) Case 4; as for Figure 5.70.

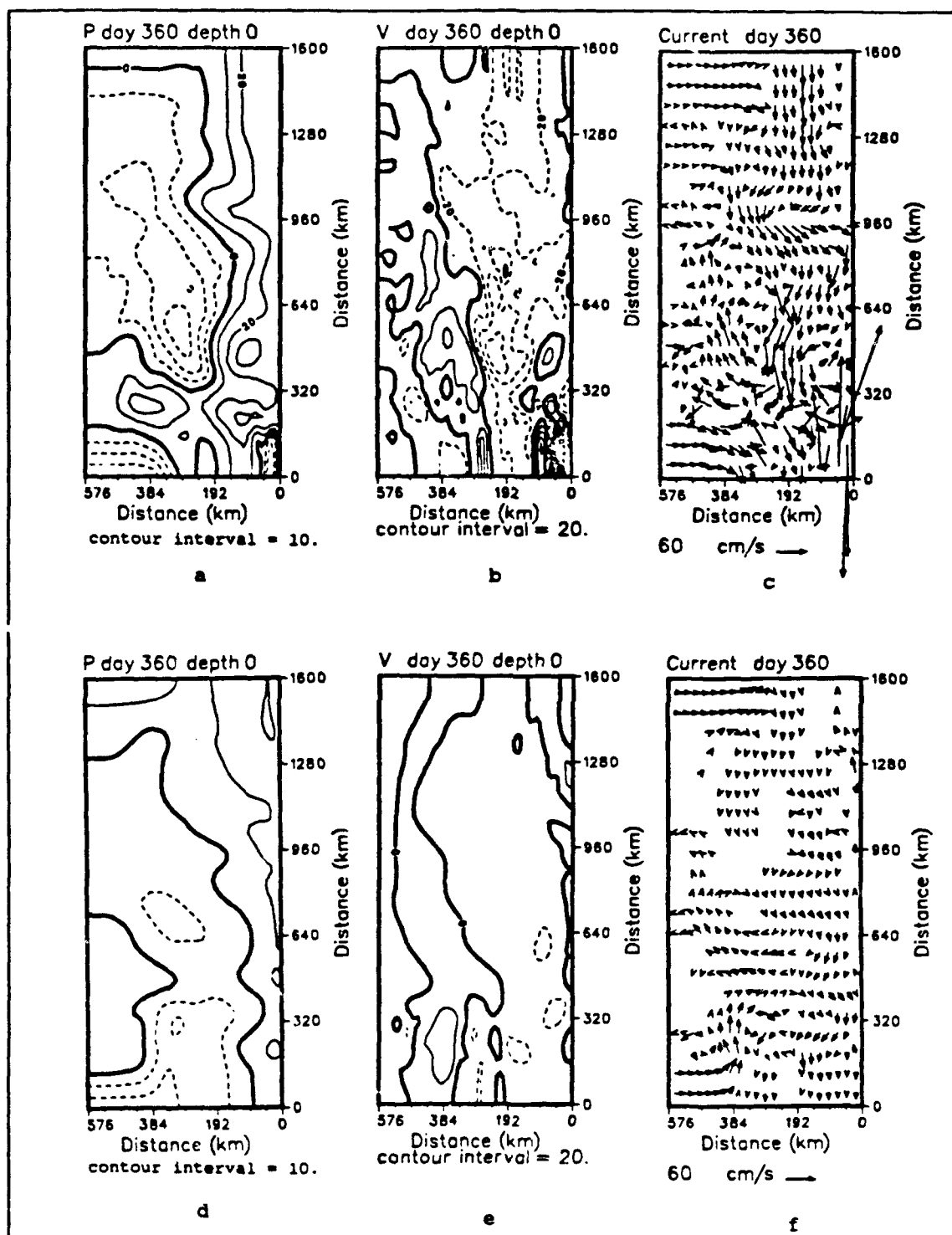


Figure 5.77 Case 1, Case 3 pressure, meridional velocity, current velocity vector fields at the surface, day 360: (a-c) Case 1, (d-f) Case 3; as for Figure 5.70.

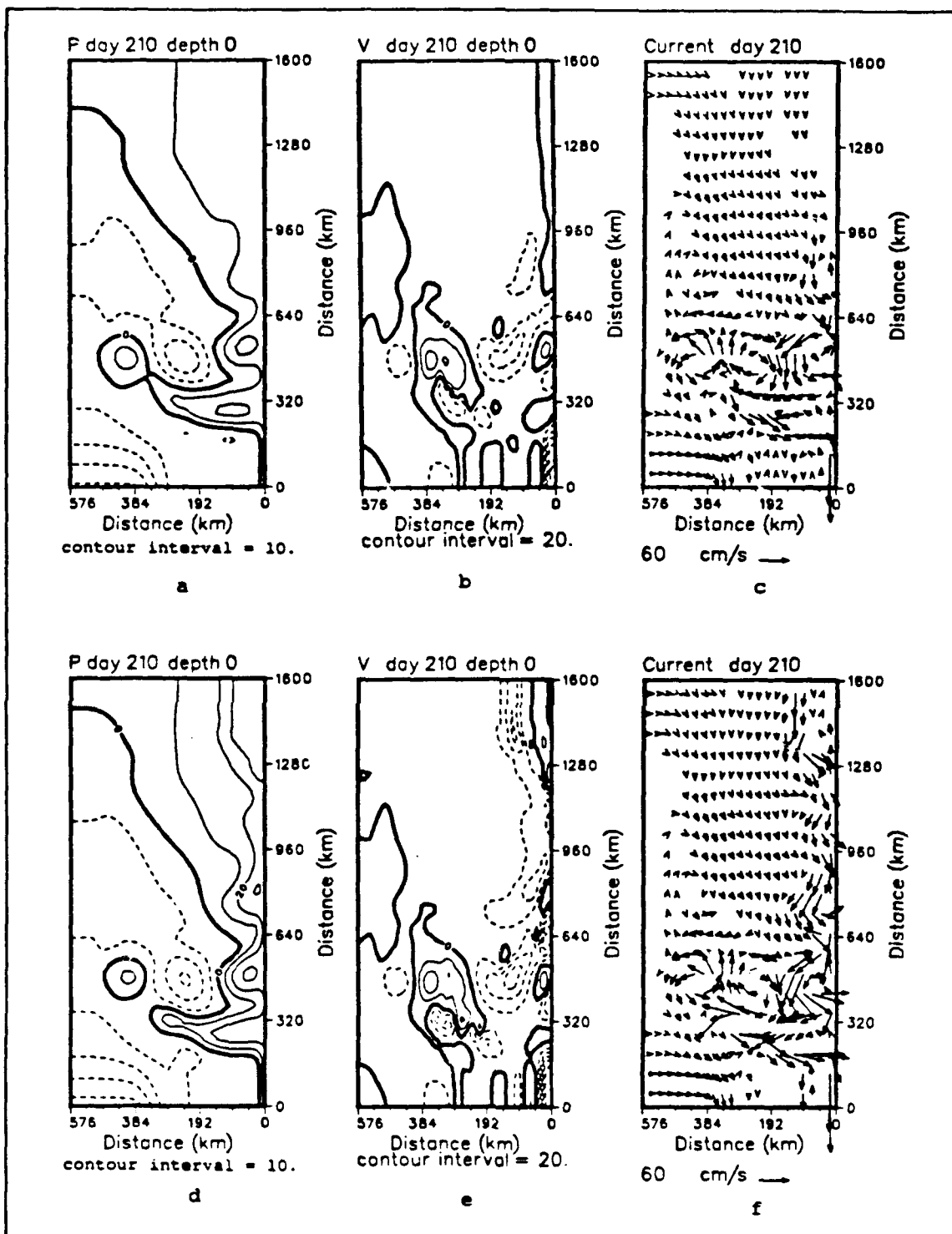


Figure 5.78 Case 1, Case 5 pressure, meridional velocity, current velocity vector fields at the surface, day 210: (a-c) Case 1, (d-f) Case 5; as for Figure 5.70.

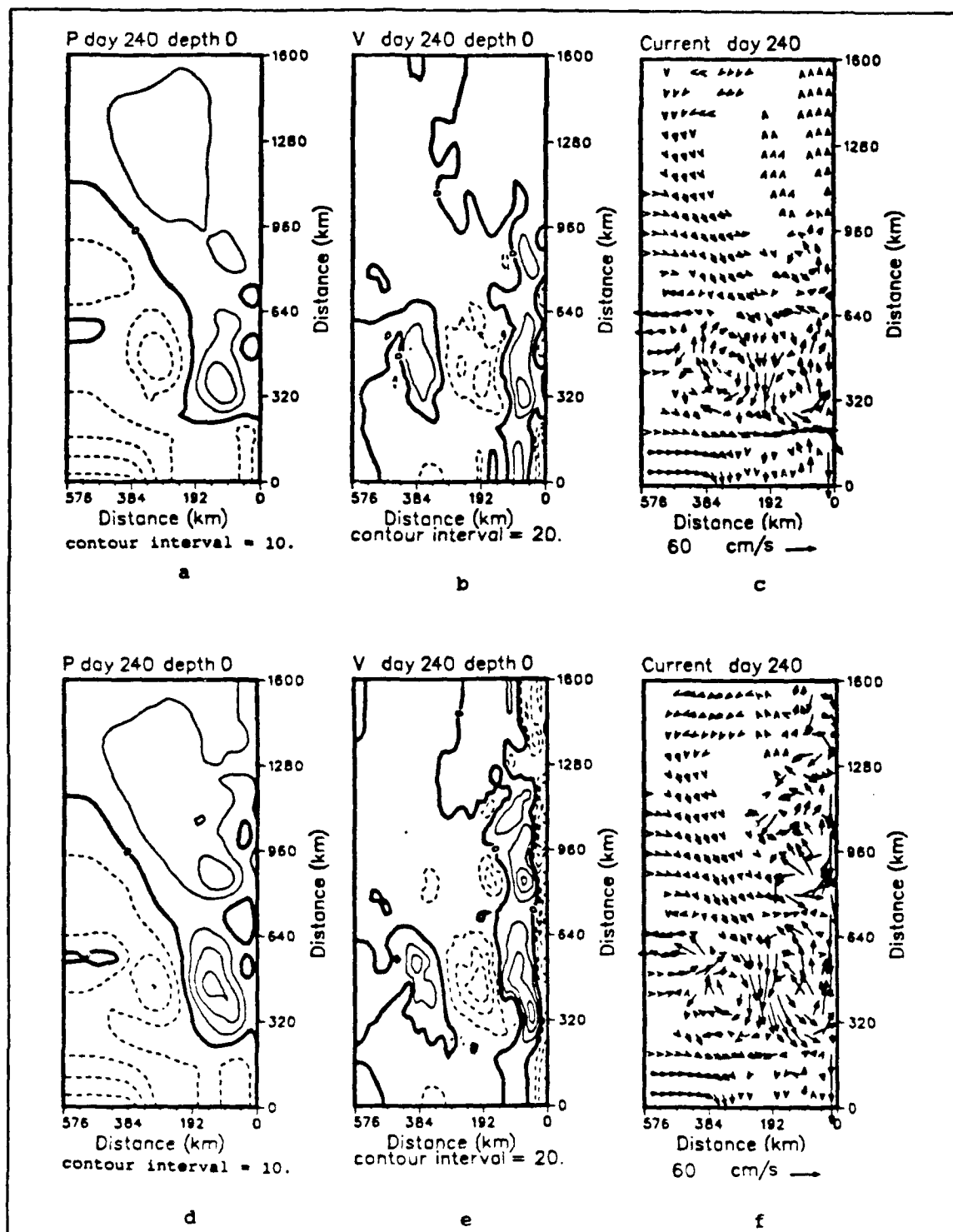


Figure 5.79 Case 1, Case 5 pressure, meridional velocity, current velocity vector fields at the surface, day 240: (a-c) Case 1, (d-f) Case 5; as for Figure 5.70.

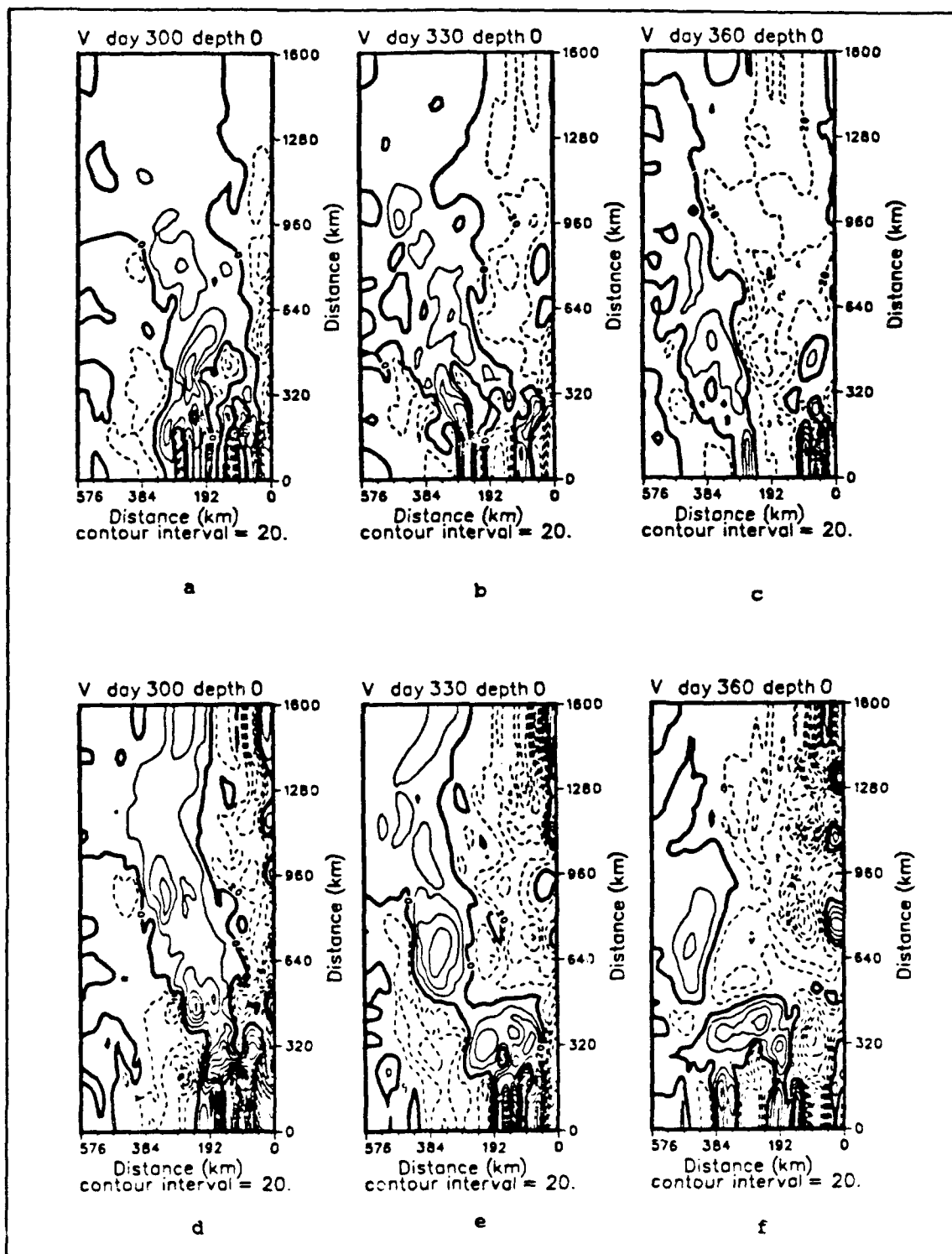


Figure 5.80 Case 1, Case 5 meridional surface velocity, days 300, 330, 360: (a-c) Case 1, (d-f) Case 5; velocity (cm/s), dashes denote poleward flow.

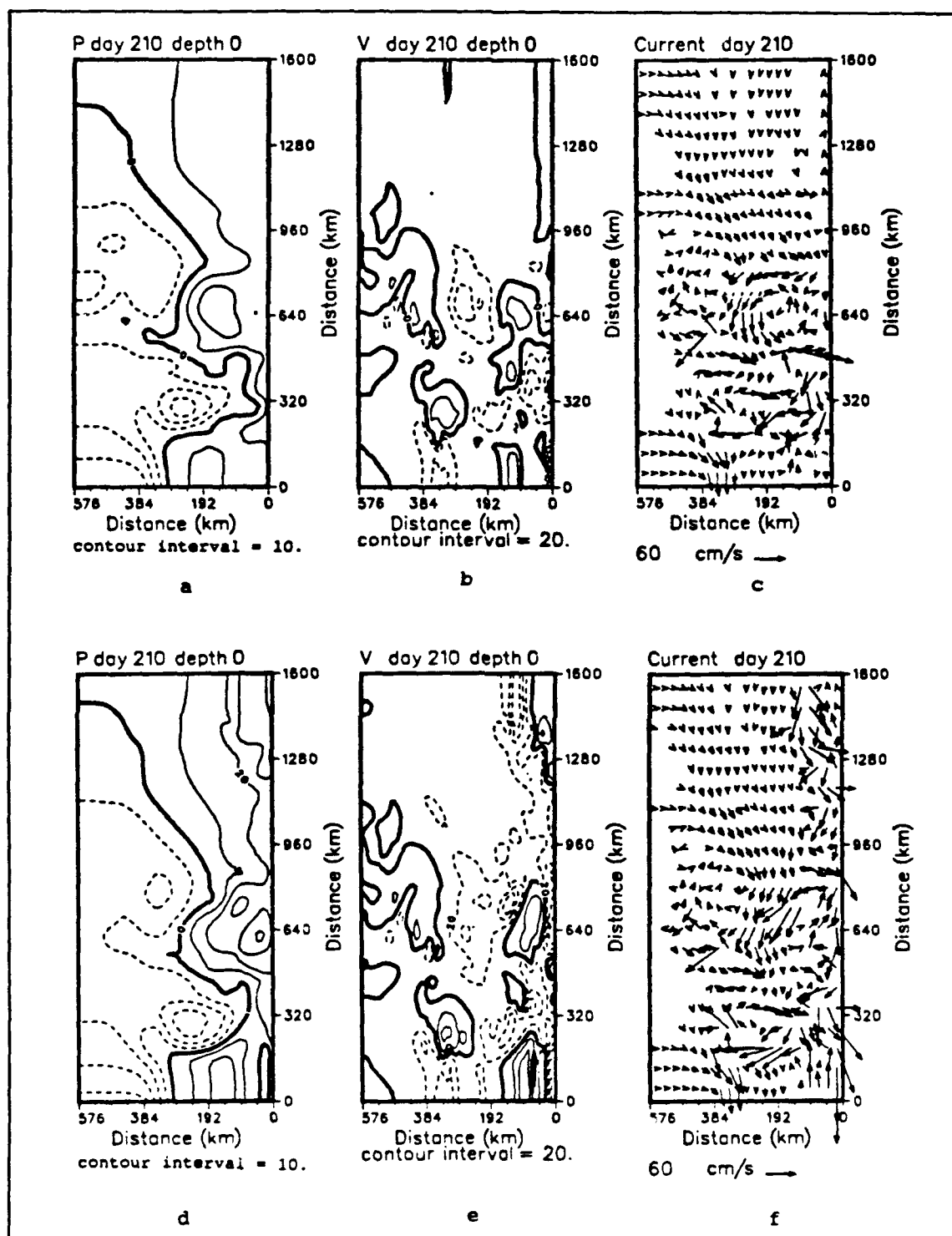


Figure 5.81 Case 2, Case 6 pressure, meridional velocity, current velocity vector fields at the surface, day 210: (a-c) Case 2, (d-f) Case 6; as for Figure 5.70.

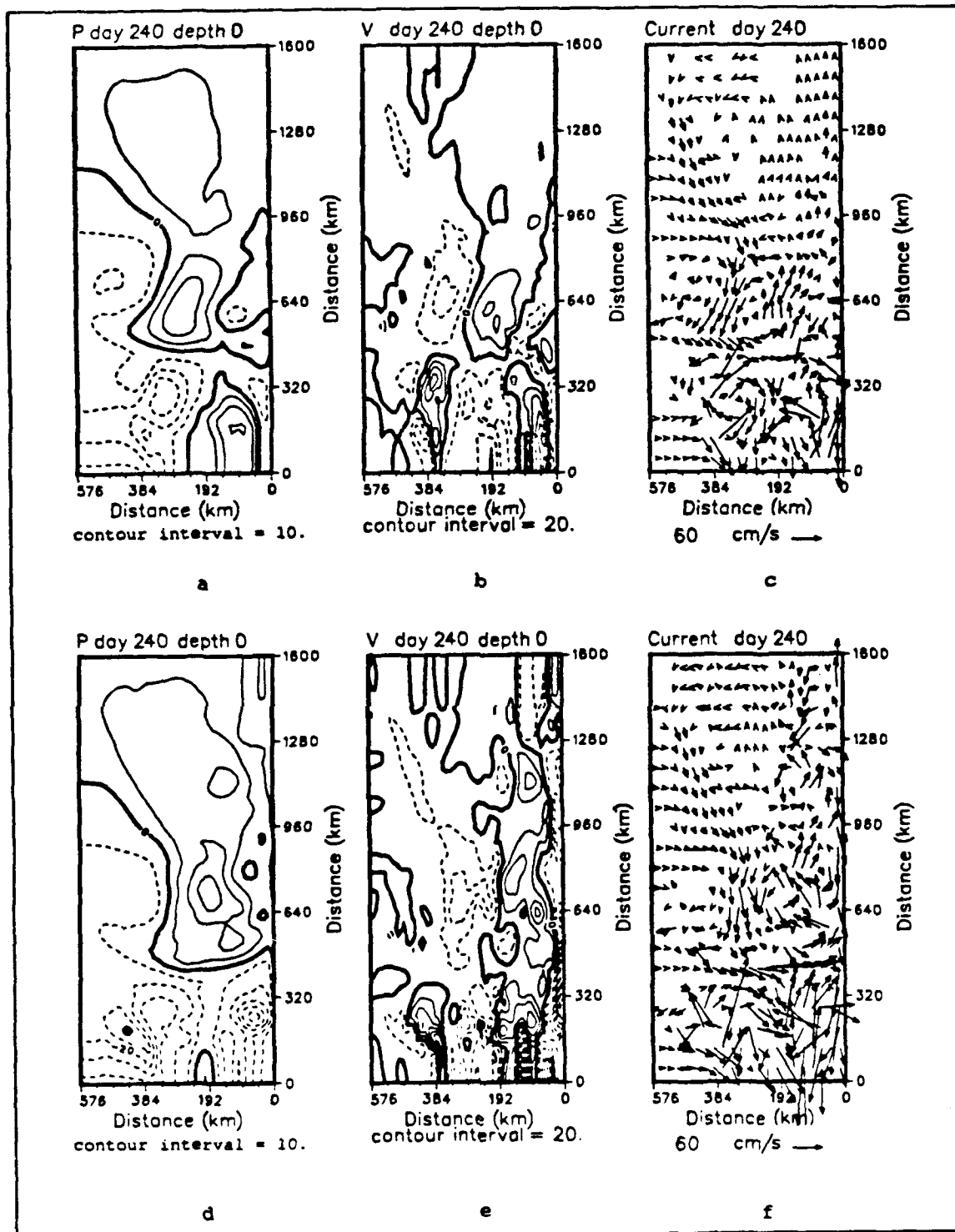


Figure 5.82 Case 2, Case 6 pressure, meridional velocity, current velocity vector fields at the surface, day 240: (a-c) Case 2, (d-f) Case 6; as for Figure 5.70.

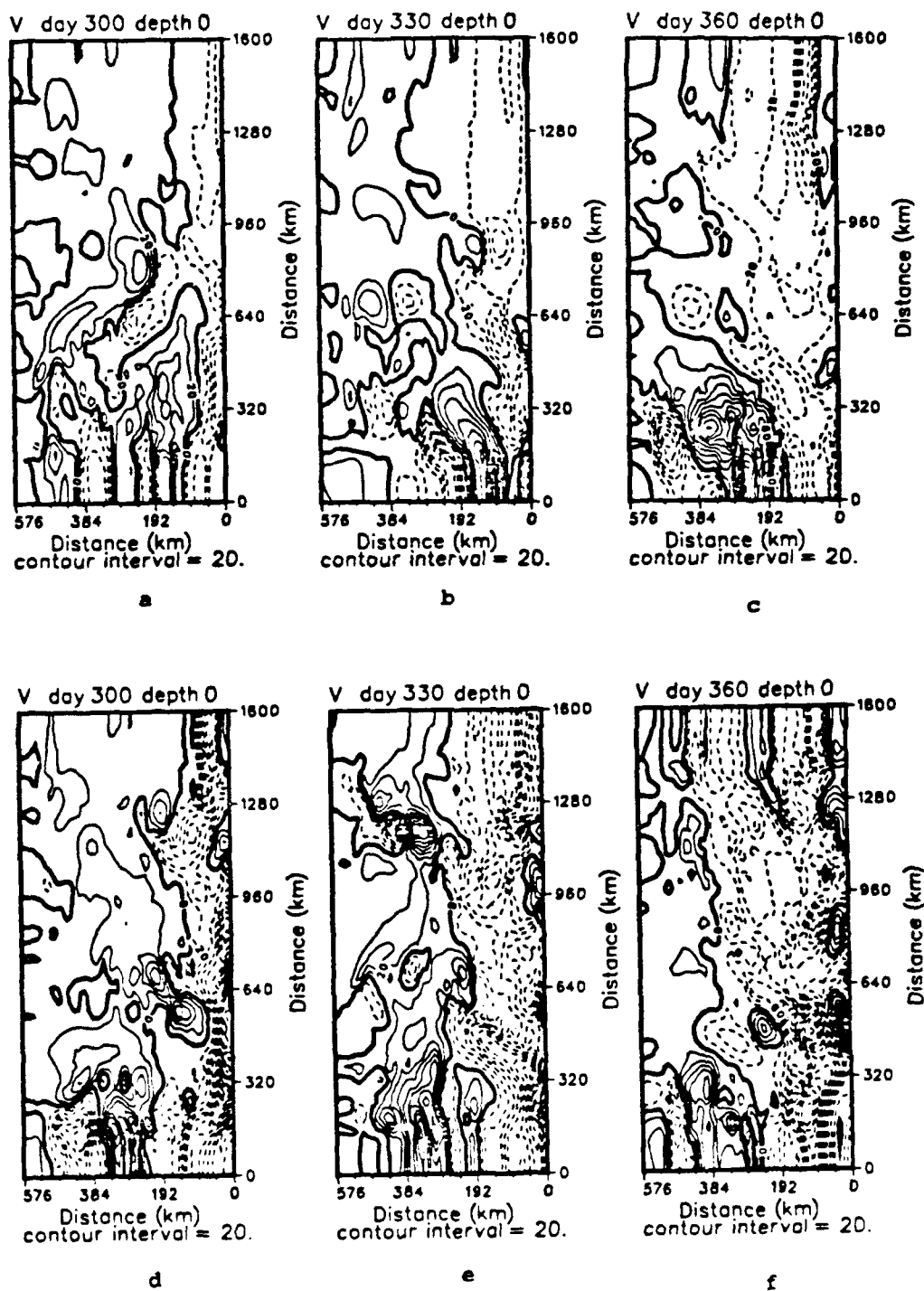


Figure 5.83 Case 2, Case 6 meridional surface velocity, days 300, 330, 360: (a-c) Case 2, (d-f) Case 6; velocity (cm/s), dashes denote poleward flow.

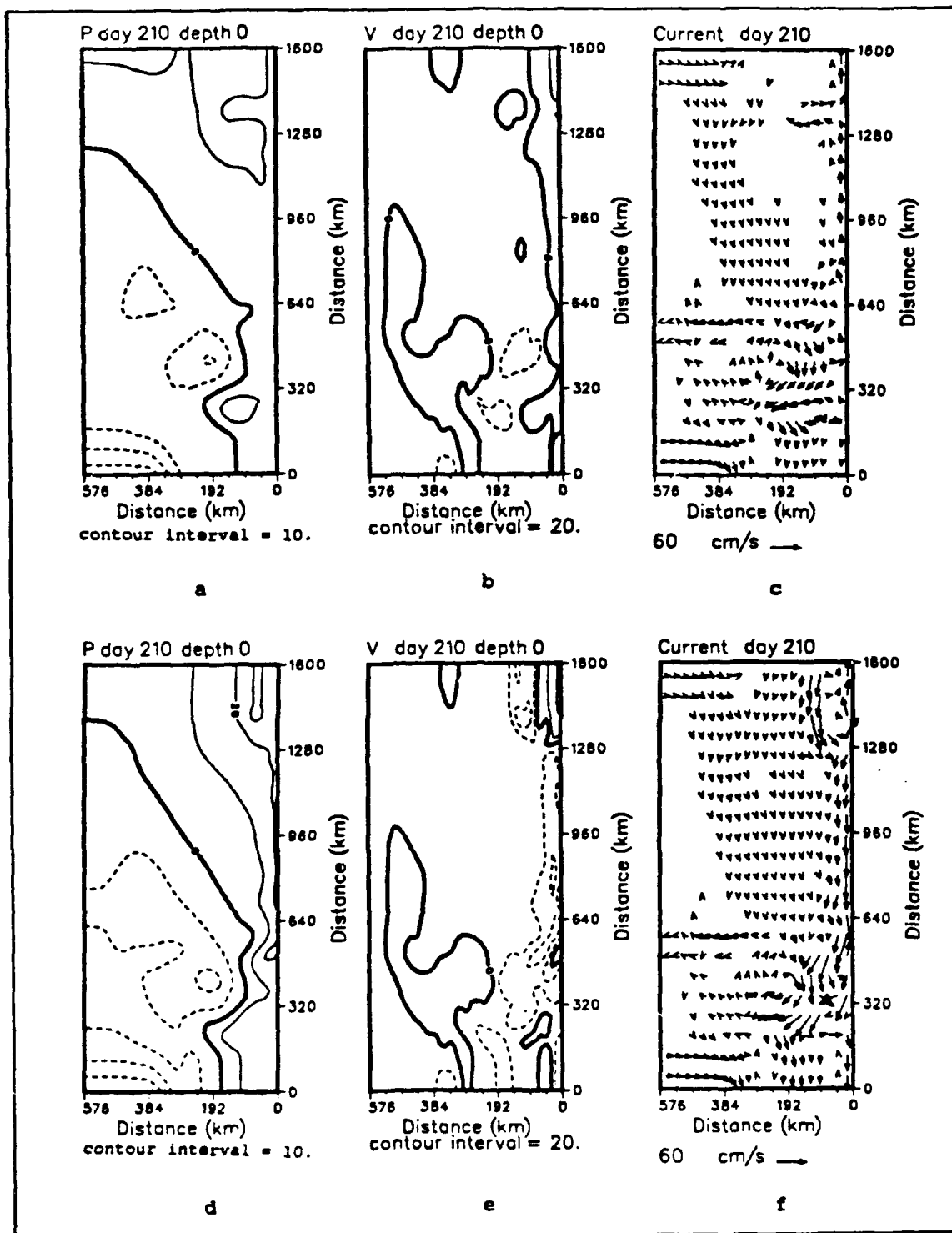


Figure 5.84 Case 3, Case 7 pressure, meridional velocity, current velocity vector fields at the surface, day 210: (a-c) Case 3, (d-f) Case 7; as for Figure 5.70.

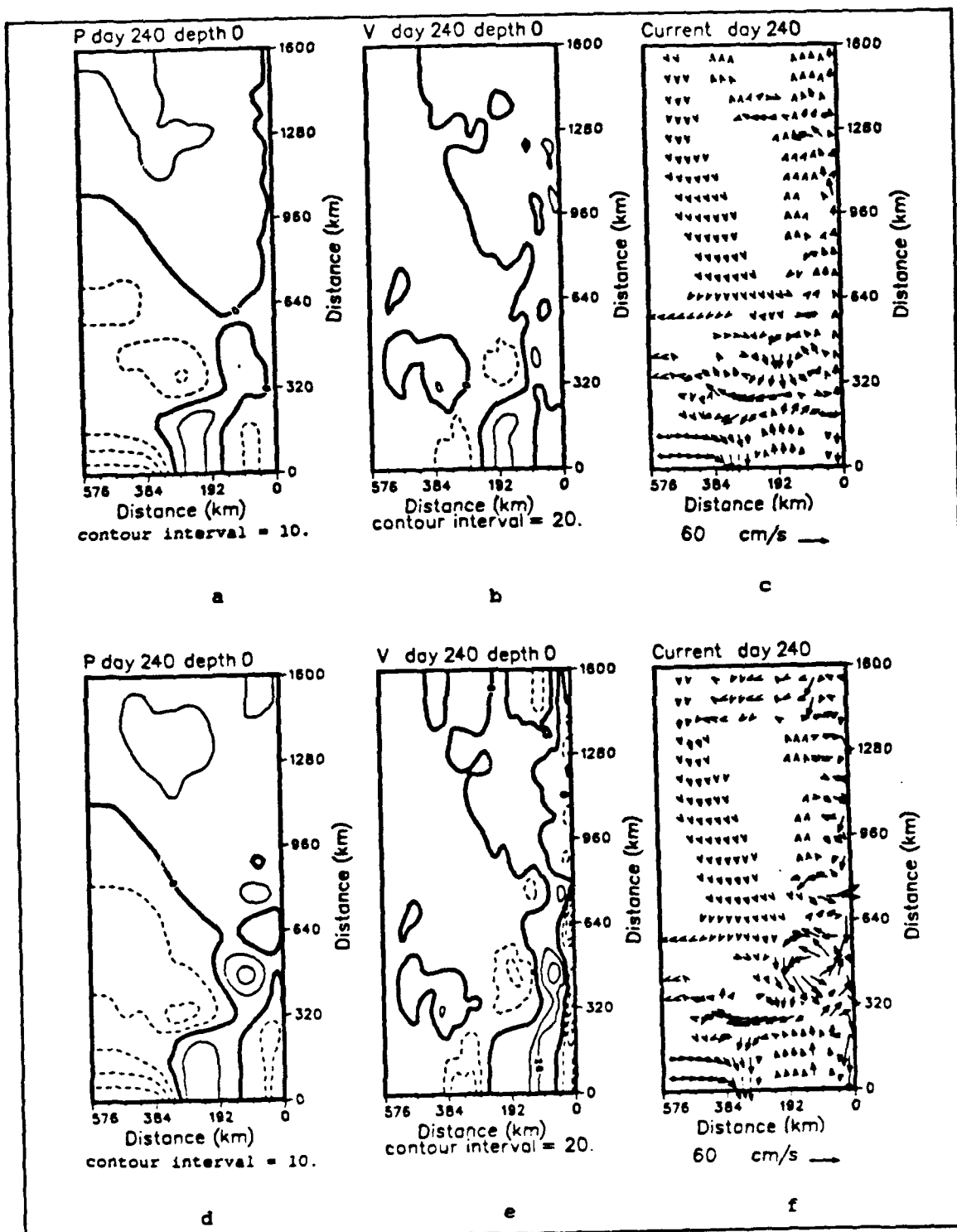


Figure 5.85 Case 3, Case 7 pressure, meridional velocity, current velocity vector fields at the surface, day 240: (a-c) Case 3, (d-f) Case 7; as for Figure 5.70.

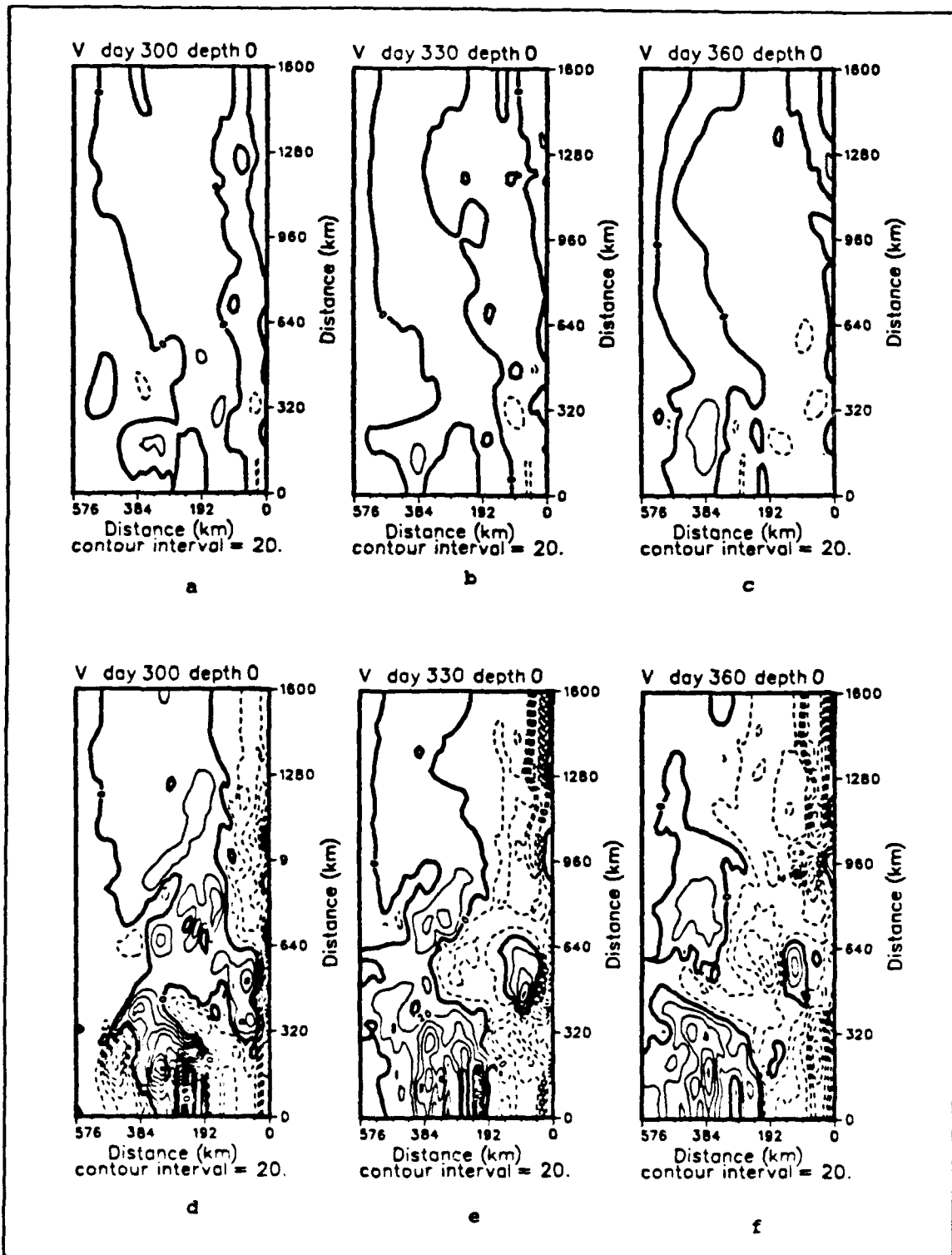


Figure 5.86 Case 3, Case 7 meridional surface velocity, days 300, 330, 360: (a-c) Case 3, (d-f) Case 7; velocity (cm/s), dashes denote poleward flow.

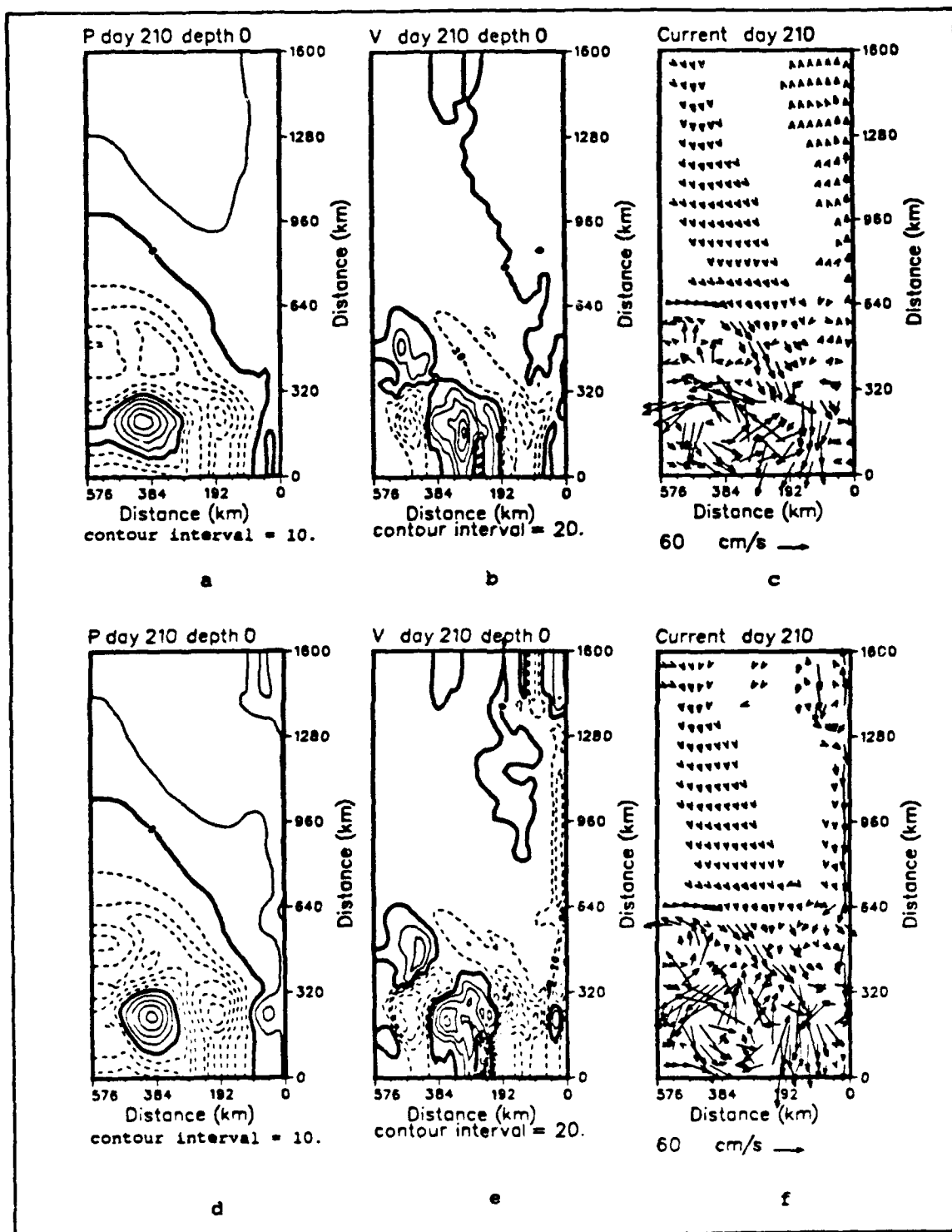


Figure 5.87 Case 4, Case 8 pressure, meridional velocity, current velocity vector fields at the surface, day 210: (a-c) Case 4, (d-f) Case 8; as for Figure 5.70.

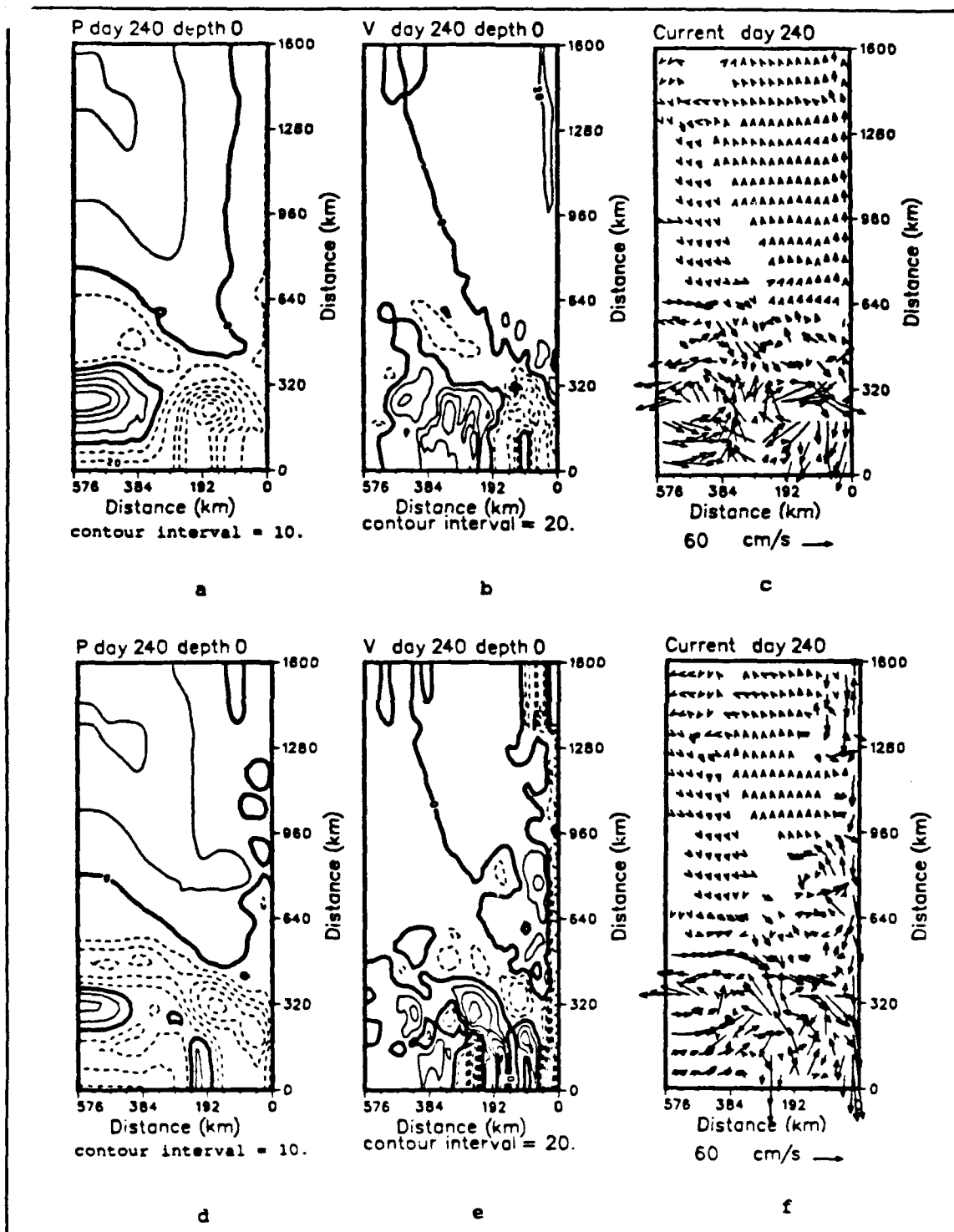


Figure 5.88 Case 4, Case 8 pressure, meridional velocity, current velocity vector fields at the surface, day 240: (a-c) Case 4 (d-f) Case 8; as for Figure 5.70.

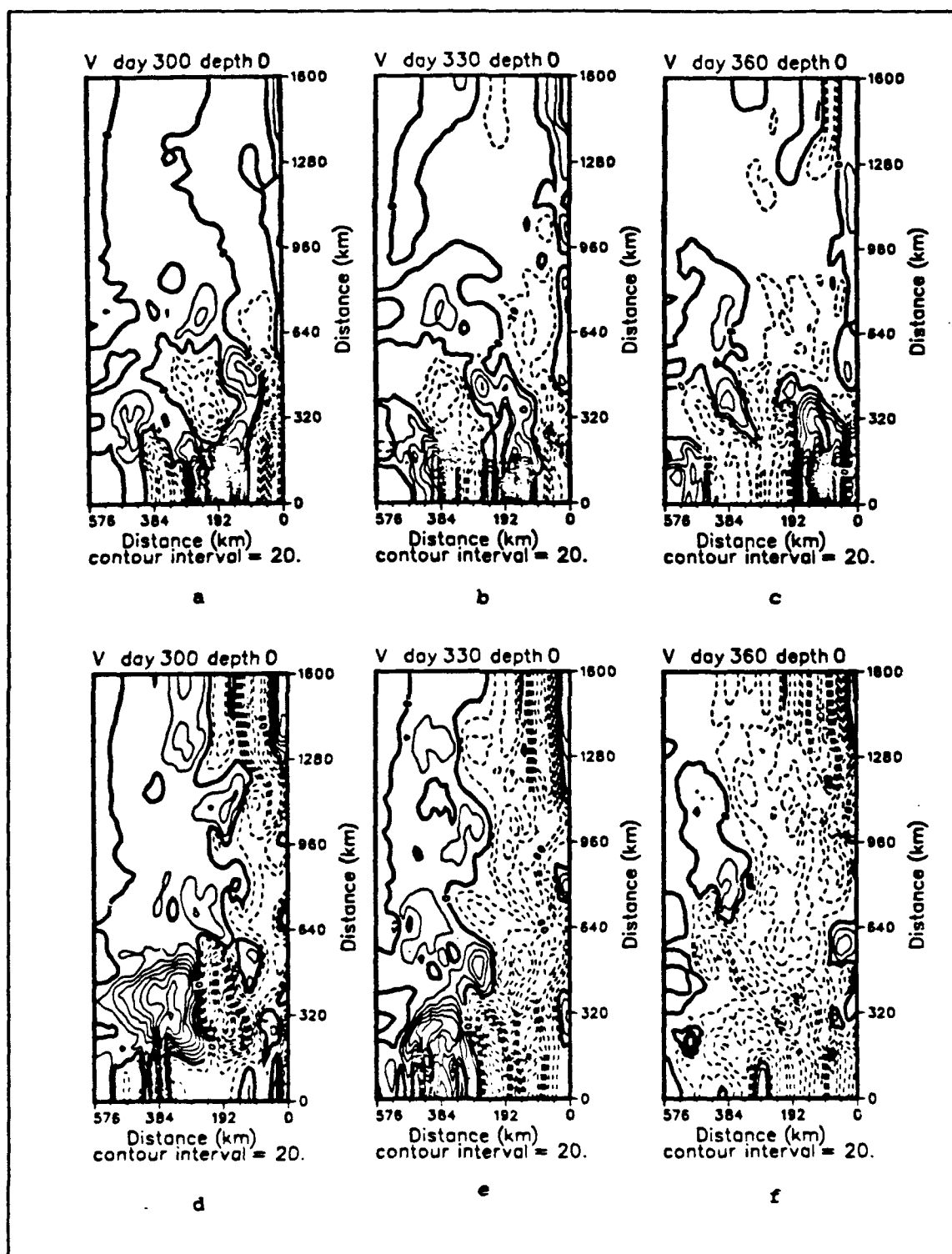


Figure 5.89 Case 4, Case 8 meridional surface velocity, days 300, 330, 360: (a-c) Case 4, (d-f) Case 8; velocity (cm/s), dashes denote poleward flow.

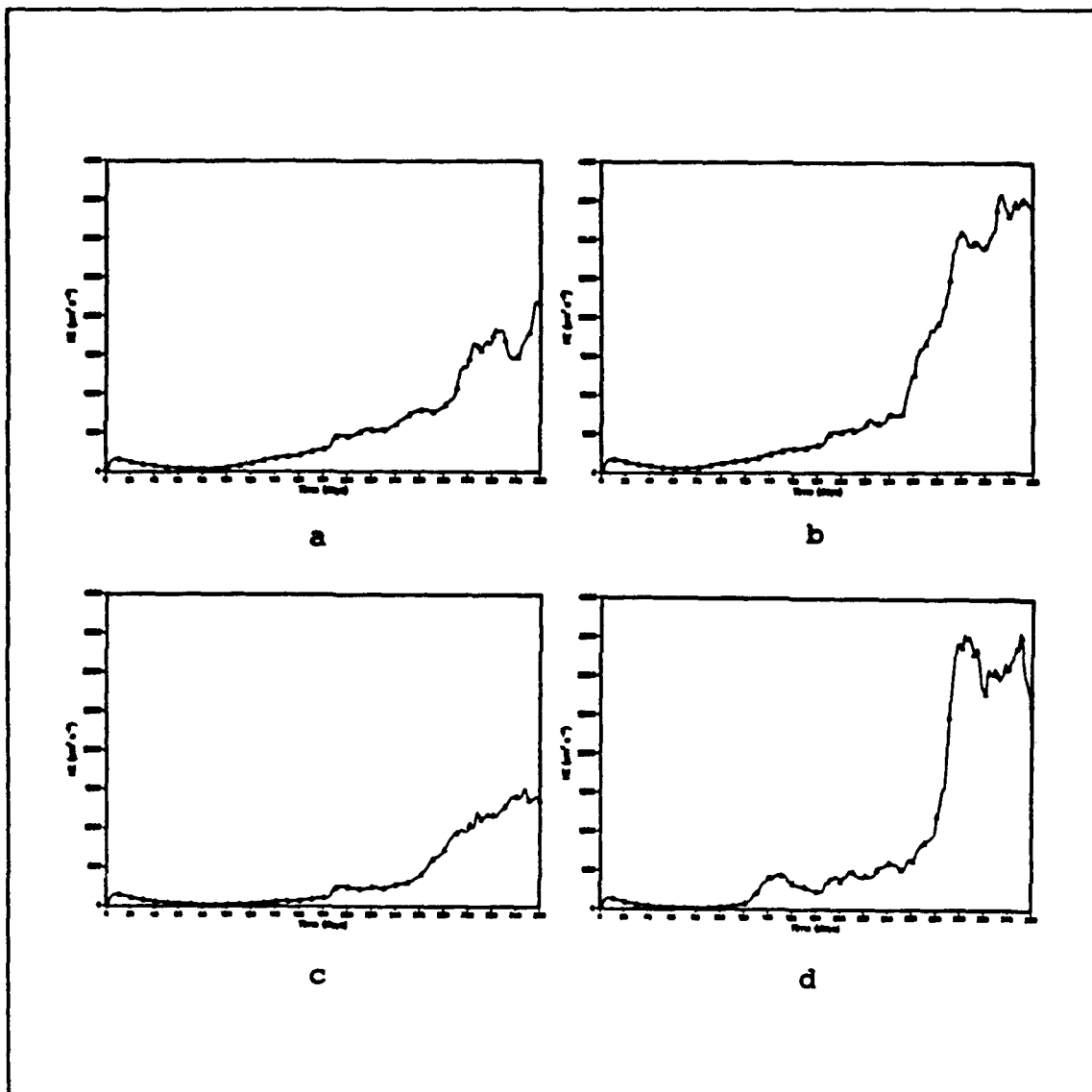


Figure 5.90 Time series of kinetic energy for North West Shelf forcing cases: (a) Case 5, (b) Case 6, (c) Case 7, (d) Case 8; As for Figure 5.28.

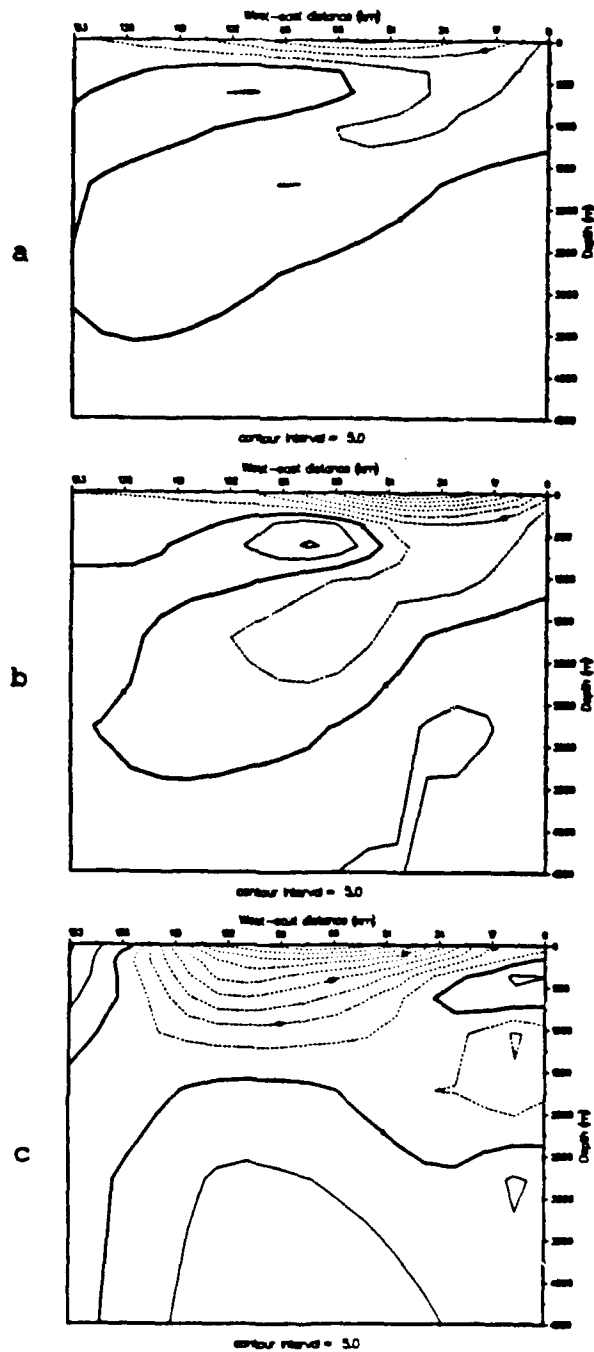


Figure 5.91 Case 5 20-day time-averaged meridional velocity cross-sections centered on day 200: As for Figure 5.11.

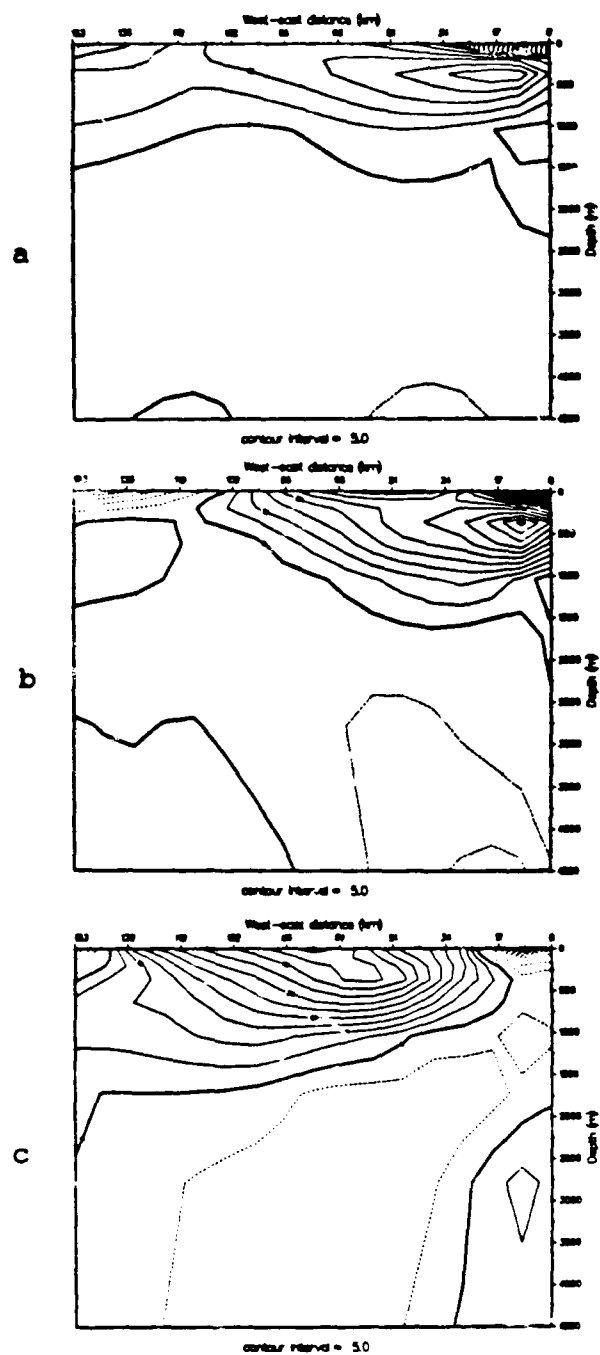


Figure 5.92 Case 5 20-day time-averaged meridional velocity cross-sections centered on day 240: As for Figure 5.11.

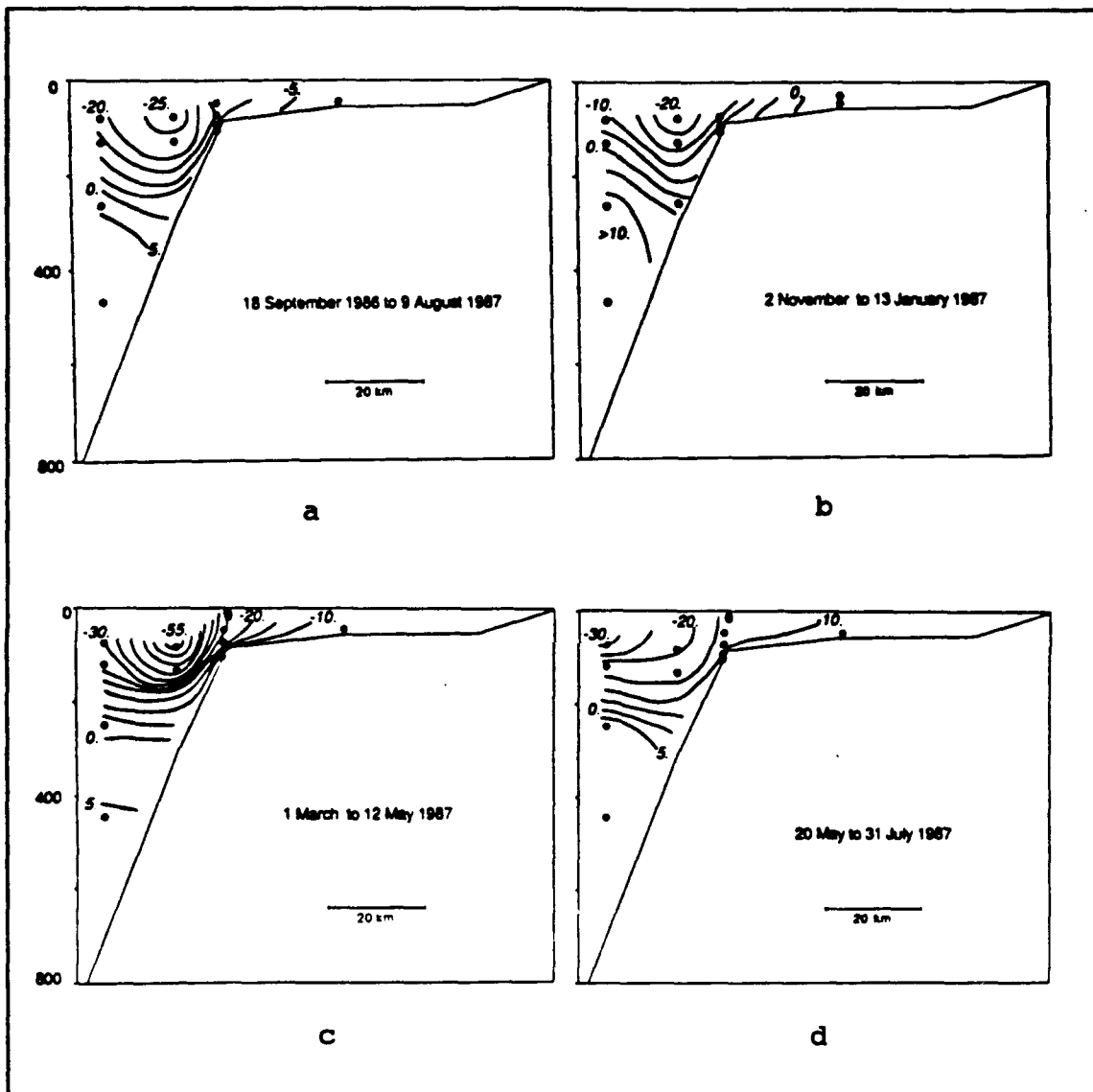


Figure 5.93 LUCIE cross-sections of mean meridional velocity: (a) September-August, (b) November-mid January, (c) March-mid May, (d) mid May-July; velocity (cm/s) (from Smith et al., 1991).

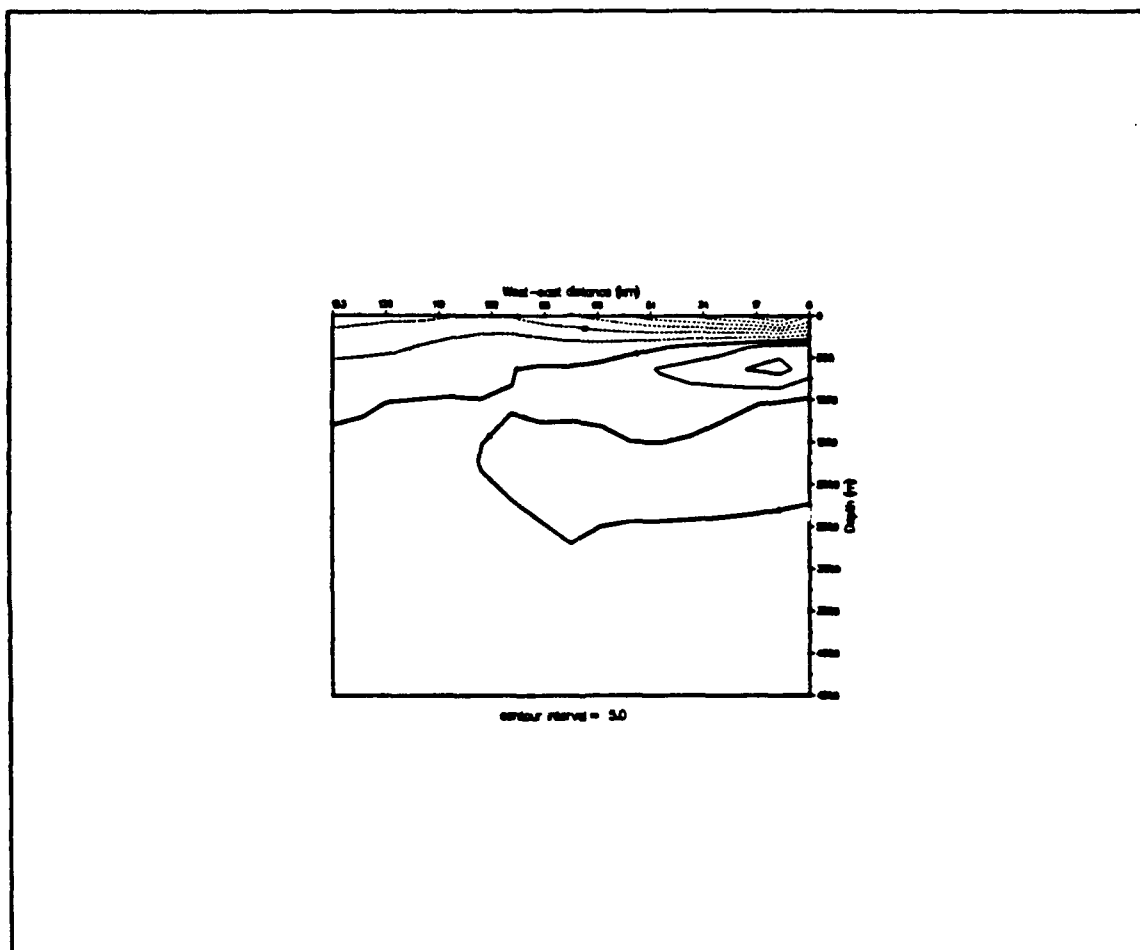


Figure 5.94 Case 8 annual average meridional velocity cross-section: Poleward region of model domain; velocity (cm/s), dashed contours denote poleward flow.

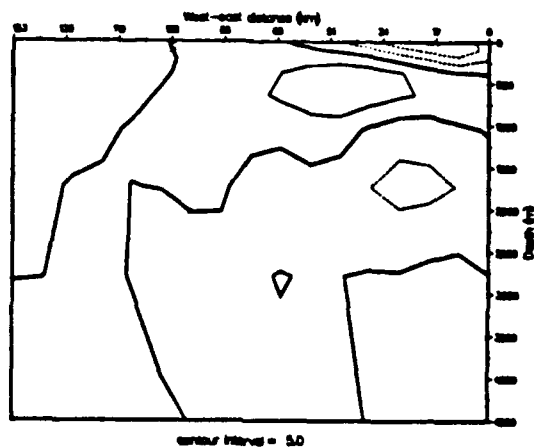


Figure 5.95 Case 4 annual average meridional velocity cross-section: Poleward region of model domain; velocity (cm/s), dashed contours denote poleward flow.

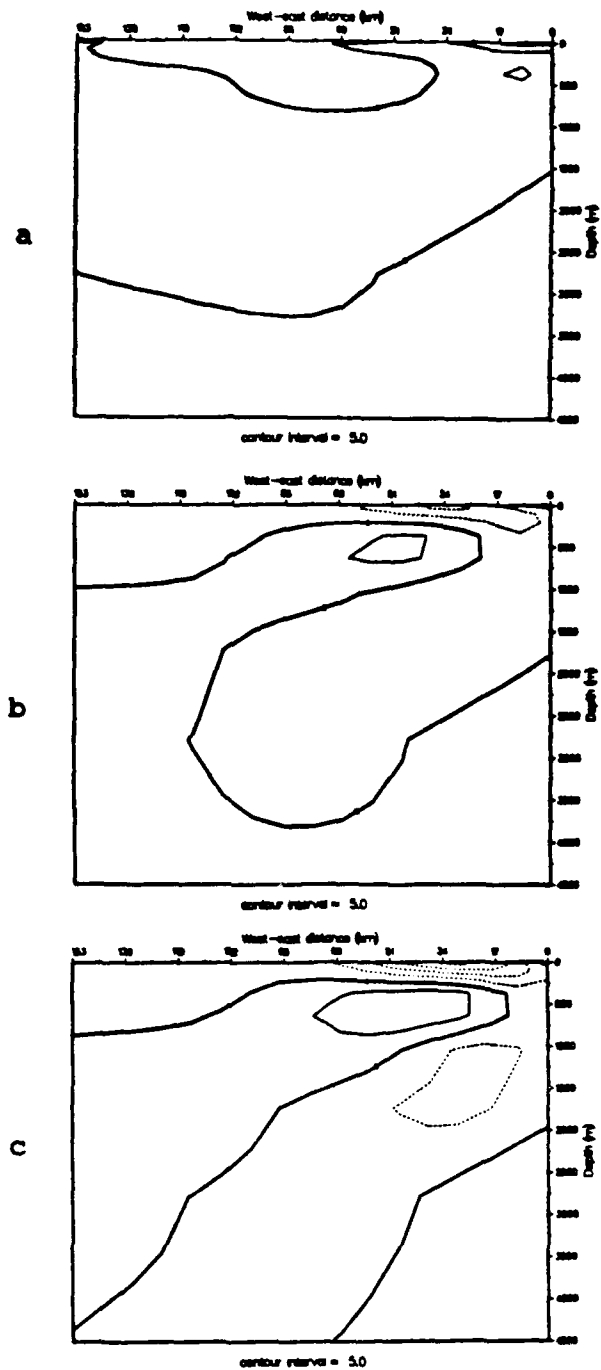


Figure 5.96 Case 8 100-day time-averaged meridional velocity cross-sections centered on day 90: Comparable period to Figure 5.93.b; as for Figure 5.11.

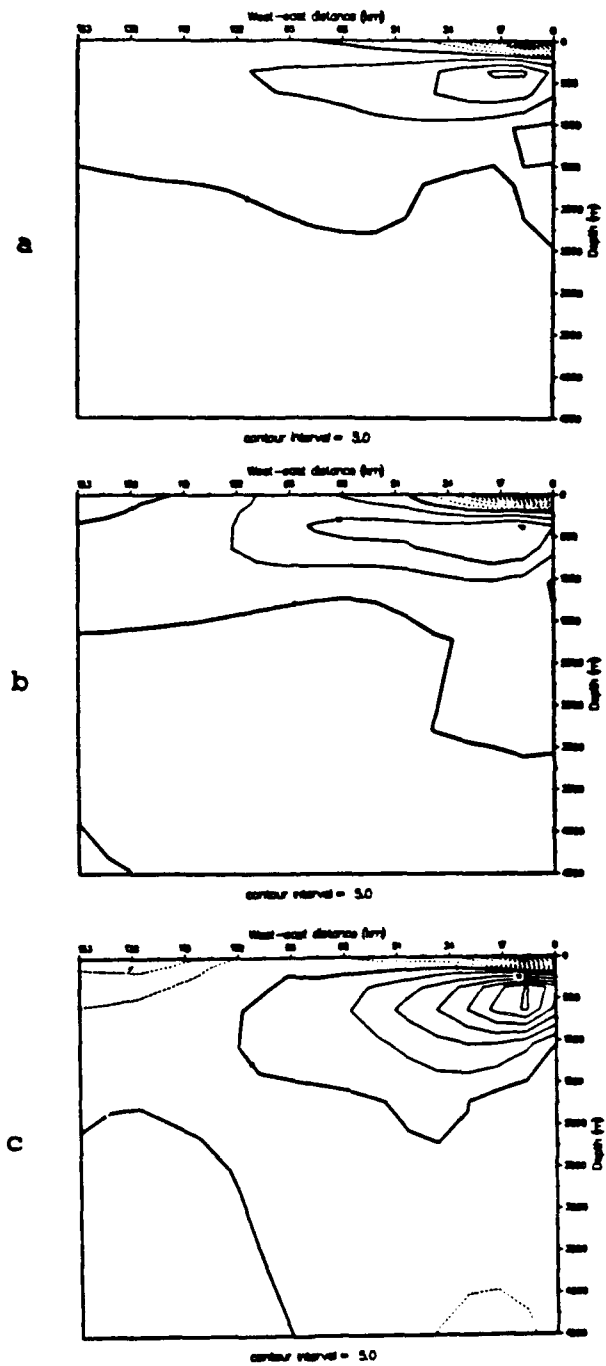


Figure 5.97 Case 8 100-day time-averaged meridional velocity cross-sections centered on day 215: Comparable period to Figure 5.93.c; as for Figure 5.11.

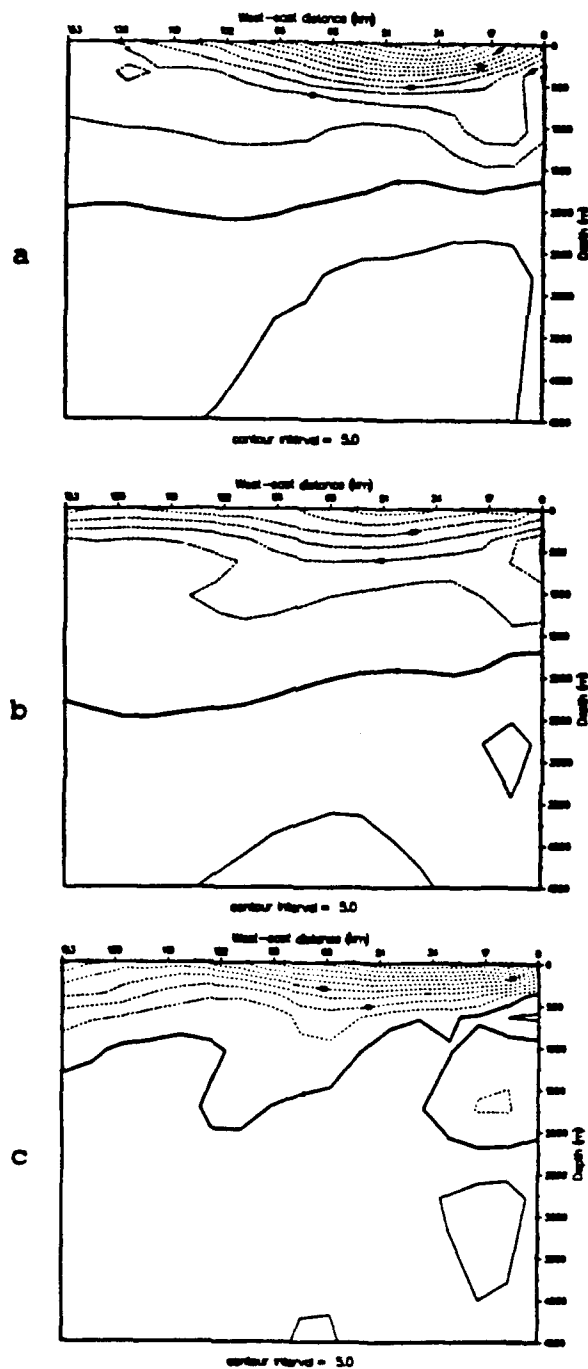


Figure 5.98 Case 8 100-day time-averaged meridional velocity cross-sections centered on day 295: Comparable period to Figure 5.93.d; as for Figure 5.11.

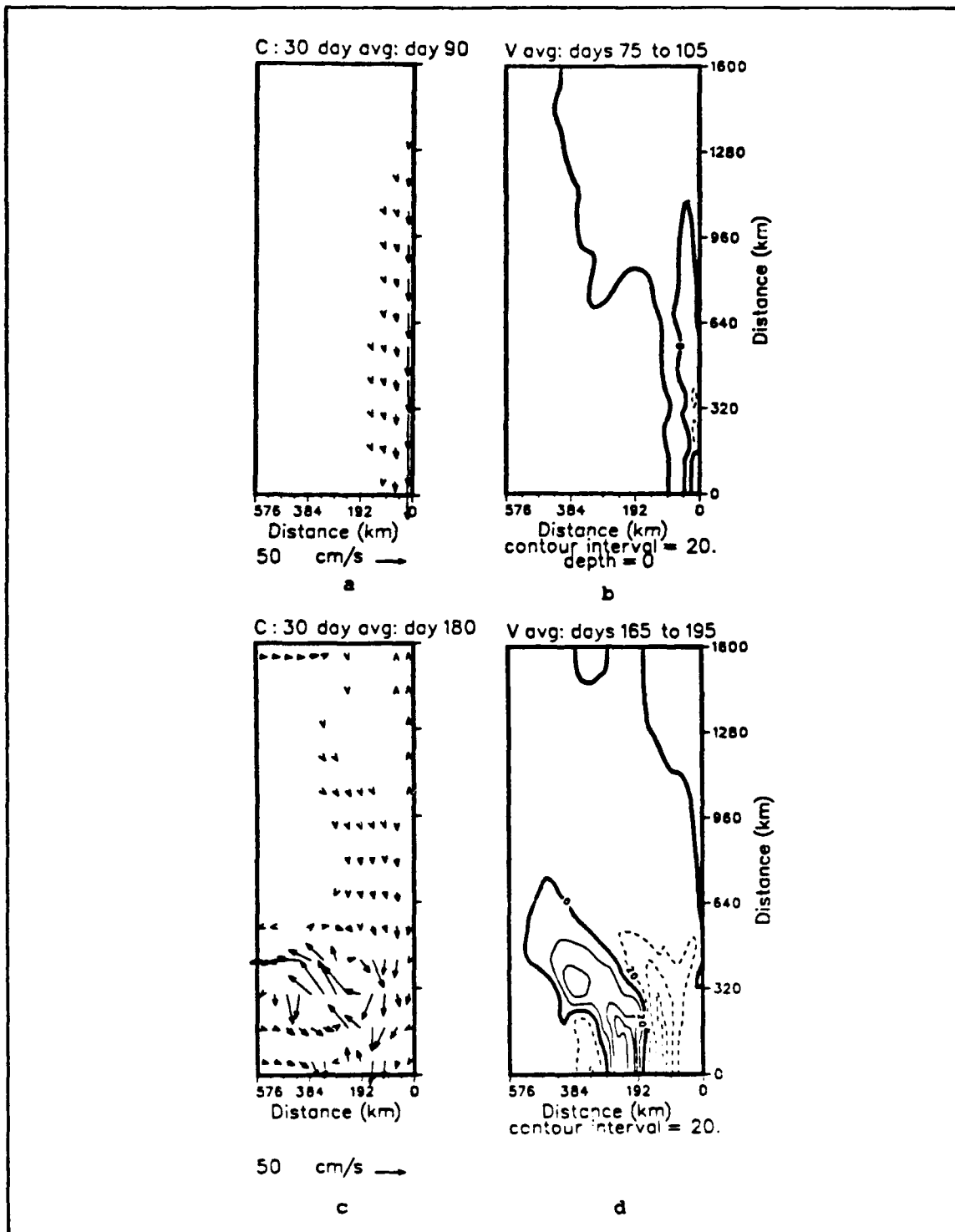


Figure 5.99 Case 8 30-day time-averaged surface velocity vector and meridional velocity fields: Austral (a, b) summer (December), (c, d) autumn (March); velocity (cm/s), dashes denote poleward flow.

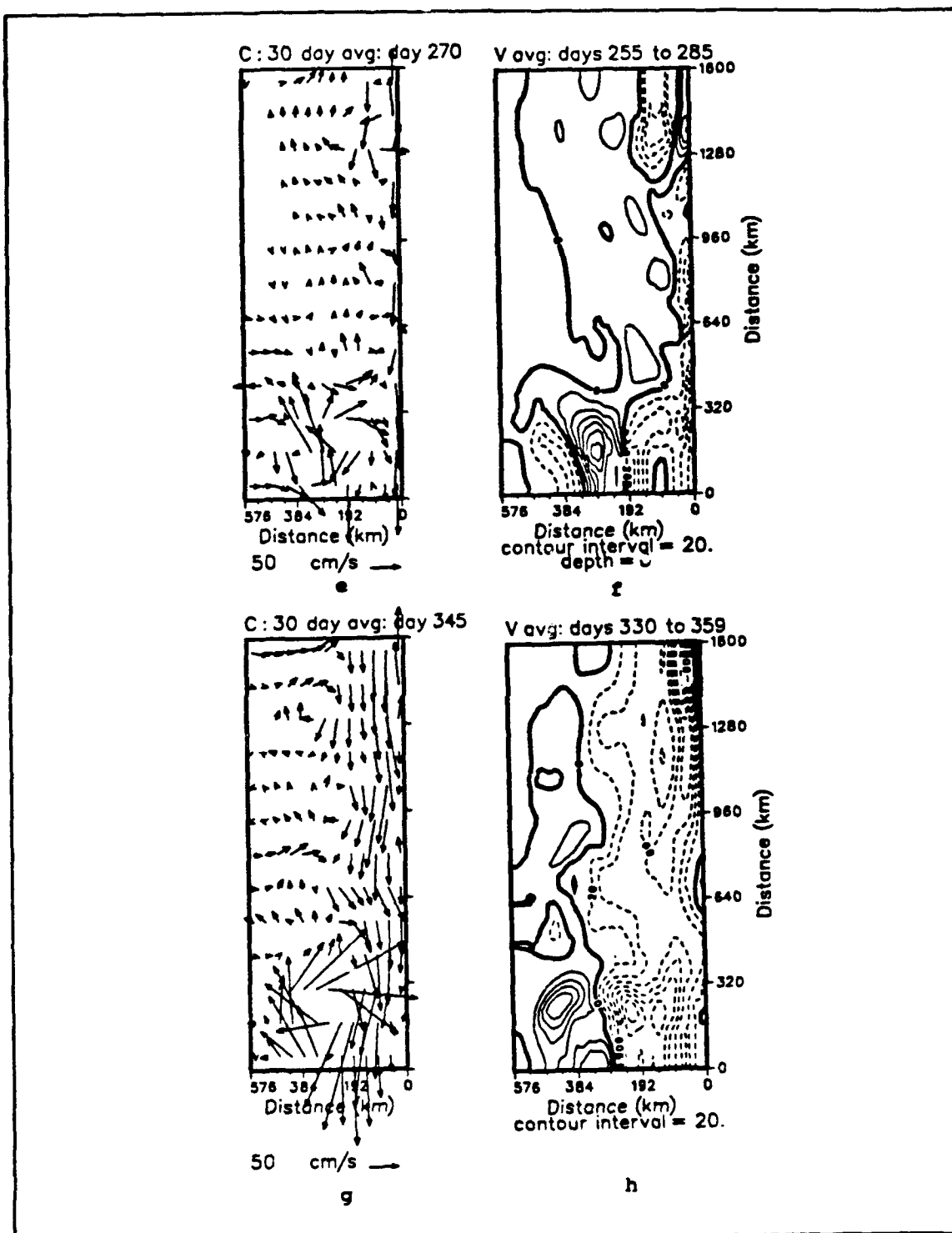


Figure 5.99 cont. Case 8 30-day time-averaged surface velocity vector and meridional velocity fields: Austral (e, f) winter (June), (g, h) spring (September); velocity (cm/s), dashes denote poleward flow.

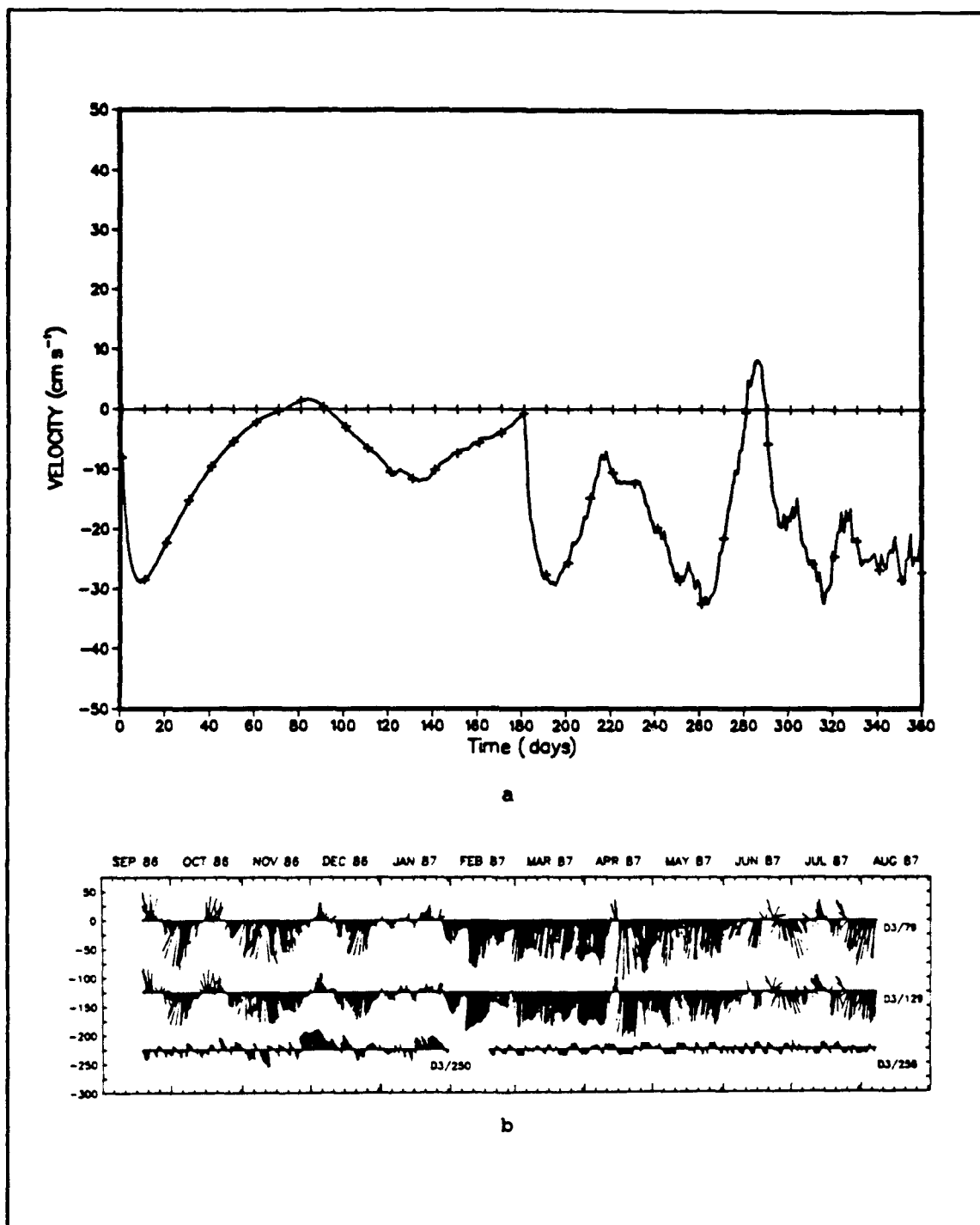


Figure 5.100 Time series of coastal surface flow: (a) Case 8 spatially-averaged meridional flow for a 45 km wide band along the coast, (b) LUCIE current data at Dongara (Smith et al., 1991).

VI. SUMMARY AND RECOMMENDATIONS

A. SUMMARY

This study used a high-resolution primitive equation numerical model to examine the contributions of seasonally varying ocean thermal forcing and seasonally varying wind forcing to the highly seasonal flow of the Leeuwin Current. The unique aspects of this research effort include the continuous thermal forcing of an otherwise open boundary regional ocean model, the application of a climatological seasonal signal to the thermal forcing, the superposition of climatological seasonal wind forcing, and the simulation of the surge-like flow of the North West Shelf waters, including the subsequent interaction with the existing flow field.

Case 1 employed only annual mean ocean thermal forcing. This case acted as a reference case for checking the results of this study versus previous studies. The results were consistent with Batteen and Rutherford (1990), showing that the method for forcing the model was appropriate and sufficient to produce Leeuwin Current type flow. This case also provides insight into the effects of continuous forcing versus evolution from only initial conditions. As anticipated, the flow fields were somewhat stronger than Batteen and Rutherford (1990) and, as a result, instabilities developed sooner in the evolution of the model. The nonlinear feedback mechanism, described by Weaver and Middleton (1989), is evident in this case, so this case serves as a basis for comparison on the relative strength and importance of this phenomenon.

The addition of a climatological seasonal signal to the ocean thermal forcing, Case 2, highlighted the asymmetrical nature of the Leeuwin Current thermal structure. The strongest meridional temperature gradient immediately follows the period of the weakest meridional temperature gradient. This case demonstrated greater dynamic activity, yet the general cycle of events, when compared to Case 1, showed few major differences. The poleward flow along the coast reflected more variability due to baroclinic Rossby wave propagation than due to the changing temperature gradient. The seasonal signal did, however, manifest itself during the austral winter as evidenced by notably stronger flow.

The inclusion of annual mean wind forcing with the annual mean ocean thermal forcing (Case 3) illustrated the necessity for using seasonal forcing (Case 4) when studying the Leeuwin Current system. The flow regime developed in Case 3 was by far the weakest and the least representative with respect to observations. Annual mean forcing for

models of the Leeuwin Current is inadequate because the reinforcing effects of the two principal forcing cycles create a significant seasonal signal in the magnitude of the Leeuwin Current flow. Poleward coastal flow was weak and slow to develop instabilities. The eddies created were weak compared to those generated by the seasonal forcing case.

Seasonal wind forcing superimposed on the seasonal ocean thermal cycle, Case 4, produced weaker flow than in Case 2 and stronger flow, in general, than Case 3. The large change in the wind forcing between February and June did create a significant change in the eastern boundary flow: however, the ocean response did not fully reflect this change until the June through August period. There appears to be a phase lag of a couple months.

The addition of the North West Shelf waters significantly altered the eastern boundary flow. While they are not considered a primary forcing mechanism for the Leeuwin Current, they exerted a powerful influence. In particular, the North West Shelf waters added a baroclinic as well as a barotropic component to the Leeuwin Current flow. This additional baroclinicity builds the cross-shelf pressure gradient, amplifying the poleward geostrophic flow. After the initial poleward surge from March through May, a nonlinear response develops, further amplifying the poleward flow and extending the duration of the strong poleward flow through the austral winter.

The surging signal of North West Shelf waters masks the slower increase in poleward forcing caused by the climatological abatement of winds and the increase in the meridional temperature gradient. The combined effects act to create the strongest Leeuwin Current flow during May/June at the poleward end of the model domain. The steadily increasing ocean thermal forcing combines with the weaker austral winter winds and the decaying influence of the surge of North West Shelf waters to form a steadier and broader poleward flow for the remainder of the austral winter (June through August). Although the model does appear to slightly lag the timing of observed events, this flow evolution is consistent with the observations made during LUCIE (Smith, et al., 1991). The seasonal magnitudes of the model's alongshore velocity are comparable to the LUCIE (Smith, et al., 1991) analyses.

The conclusion extracted from the sequence of events in Case 8 is that the sharp reduction in wind forcing combines with the sharpest increase in ocean thermal forcing to release the North West Shelf water, allowing this water to flow poleward as a surge. The strong baroclinic character of this poleward rush induces a strong nonlinear feedback mechanism that serves to extend the duration of the influence of the North West Shelf

waters on the Leeuwin Current flow. It is the nonlinear feedback that appears to have a greater long-term influence on the poleward flow because it acts to extend the poleward range of influence of the warm tropical waters from the North West Shelf, which, in turn, acts to increase the strength of the poleward flow through geostrophic adjustment to the supplied baroclinicity.

B. RECOMMENDATIONS

Several interesting questions arose from this study concerning the role of the baroclinic Rossby wave propagation in the determination of the flow regime at the eastern boundary. Although the short term effects from the initial conditions appear to disappear after the first 80 model days, a multi-year study could reduce model transients and provide insight on the model's ability to continue representing the seasonality of the Leeuwin Current flow, as well as whether the baroclinic Rossby waves are a function of the seasonal cycle. Altering the starting point in the seasonal cycle may effect the model results, especially, for those cases where baroclinic Rossby wave propagation appears to dominate the flow regime. The release of the North West Shelf waters may be important to study in this context since it appears to temporarily subjugate any influence of baroclinic Rossby waves along the coast. Therefore, sensitivity studies should be conducted on the choice of season for the initial condition and the timing of the release of the North West Shelf waters. Because the NWS forcing appears to dominate over baroclinic Rossby wave propagation, the annual cycle of events, including baroclinic Rossby wave propagation, could be reinitialized each year when the North West Shelf waters are released to flow poleward.

LIST OF REFERENCES

- Adamec, D., R.L. Elsberry, R.W. Garwood, Jr., and R.L. Haney, 1981: An embedded mixed layer-ocean circulation model. *Dyn. Atmos. Oceans*, 5, 69-96.
- Arakawa, A., and V.R. Lamb, 1977: Computational design of the basic dynamical processes of the UCLA general circulation model. *Methods in Computational Physics*, (J. Chang, Ed.), Academic Press, 17, 173-265.
- Batteen, M.L., 1989: Model simulations of a coastal jet and undercurrent in the presence of edies and jets in the California Current System. *Poleward Flows Along Eastern Ocean Boundaries*, S. J. Neshyba, C. N. Mooers, R. L. Smith and R. T. Barber, Eds., Springer-Verlag, 263-279.
- Batteen, M.L., and Y.-J. Han, 1981: On the computational noise of finite-difference schemes used in ocean models. *Tellus*, 33, 387-396.
- Batteen, M.L., R.L. Haney, T.A. Tielking and P.G. Renaud, 1989: A numerical study of wind forcing of eddies and jets in the California Current System. *J. Mar. Res.*, 47, 493-523.
- Batteen, M.L. and M.J. Rutherford, 1990: Modeling studies of eddies in the Leeuwin Current: The role of thermal forcing. *J. Phys. Oceanogr.*, 20, 1484-1520.
- Batteen, M.L., M.J. Rutherford and E.J. Bayler, 1991: A numerical study of wind and thermal forcing effects on the ocean circulation off Western Australia. *J. Phys. Oceanogr.*, submitted.
- Bendat, J.S., and A.G. Piersol, 1986: *Random Data: Analysis and Measurement Procedures*, Second edition, John Wiley and Sons, 566 pp.
- Boland, F.M., J.A. Church, A.M.G. Forbes, J.S. Godfrey, A. Huyer, R.L. Smith and N.J. White, 1988: Current-meter data from the Leeuwin Current Interdisciplinary Experiment. *CSIRO Marine Laboratories, Report 198*, 31 pp.
- Church, J.A., G.R. Cresswell , and J.S. Godfrey, 1989: The Leeuwin Current. *Poleward Flows along Eastern Ocean Boundaries*, S. Neshyba, C.N.K. Mooers, R.I. Smith, and R.T. Barber, Eds., Springer-Verlag, 230-252.
- Camerlengo, A.L. and J.J. O'Brien, 1980: Open boundary conditions in rotating fluids. *J. Comput. Physics*, 35, 12-35.
- Cresswell, G.R., and T. J. Golding, 1980: Observations of a south-flowing current in the southeastern Indian Ocean. *Deep-Sea Res.*, 27A, 449-466.

- Gentilli, J., 1972: Thermal anomalies in the Eastern Indian Ocean. *Nature (London) Physical Sciences*, 238, 93-95.
- Godfrey, J.S., and K.R. Ridgway, 1985: The large-scale environment of the poleward-flowing Leeuwin Current, Western Australia: Longshore steric height gradients, wind stresses and geostrophic flow. *J. Phys. Oceanogr.*, 15, 481-495.
- Hamon, B.V., 1965: Geostrophic currents in the south-eastern Indian Ocean. *Aust. J. Mar. Freshwat. Res.* 16, 255-271.
- Hamon, B.V., 1972: Geopotential topographies and currents off West Australia, 1965-69. *CSIRO Division of Fisheries and Oceanography, Technical Paper No. 32*, 11 pp.
- Han, Y.-J., 1975: Numerical simulation of mesoscale eddies. Ph.D. thesis, University of California, Los Angeles, 154 pp.
- Haney, R.L., 1974: A numerical study of the response of an idealized ocean to large-scale surface heat and momentum flux. *J. Phys. Oceanogr.*, 4, 145-167.
- Haney, R.L., W.S. Shriver and K.H. Bunt, 1978: A dynamical-numerical study of the formation and evolution of large-scale ocean anomalies. *J. Phys. Oceanogr.*, 8, 952-969.
- Haney, R.L., 1985: Midlatitude sea surface temperature anomalies: A numerical hindcast. *J. Phys. Oceanogr.*, 15, 787-799.
- Holland, W.R., 1978: The role of mesoscale eddies in the general circulation of the ocean-numerical experiments using a wind-driven quasi-geostrophic model. *J. Phys. Oceanogr.*, 8, 363-392.
- Holland, W.R., and M.L. Batteen, 1986: The parameterization of subgrid scale heat diffusion in eddy-resolved ocean circulation model. *J. Phys. Oceanogr.*, 16, 200-206.
- Kamenkovich, V.M., M.N. Koshlyakov and A.S. Monin, 1986: *Synoptic Eddies in the Ocean*. D. Riedel, 433 pp.
- Kundu, P.K., and J.P. McCreary, 1986: On the dynamics of the throughflow from the Pacific into the Indian Ocean. *J. Phys. Oceanogr.*, 16, 2191-2198.
- Levitus, S., 1982: *Climatological Atlas of the World Ocean*. NOAA Professional Paper 13. US Department of Commerce: National Oceanic and Atmospheric Administration. 173 pp.
- List, R. J., 1951: *Smithsonian Meteorological Tables*, 6th Ed., 527 pp.
- Lopes da Costa, C.N., 1989: A numerical study of wind forcing in the eastern boundary current system off Portugal. M.S. thesis, Naval Postgraduate School, 114pp.
- McCreary, J.P., Jr., 1981: A linear stratified ocean model of the coastal undercurrent. *Phil. Trans. Roy. Soc., London*, A302, 385-413.

- McCreary, J.P., Jr., S.R. Shetye and P.K. Kundu, 1986: Thermohaline forcing of eastern boundary currents: With application to the circulation off the west coast of Australia. *J. Mar. Res.*, **44**, 71-92.
- McCreary, J.P., Jr., P.K. Kundu and S.-Y. Chao, 1987: On the dynamics of the California Current System. *J. Mar. Res.*, **45**, 1-32.
- Olivier, D.A., 1987: Numerical simulations of the California Current: Filament formation as related to baroclinic instability. M.S. thesis, Naval Postgraduate School, 69 pp.
- Paulson, C.A. and J.J. Simpson, 1977: Irradiance measurements in the upper ocean. *J. Phys. Oceanogr.*, **7**, 952-956.
- Pearce, A.F. and G.R. Cresswell, 1985: Ocean circulation off Western Australia and the Leeuwin Current. *CSIRO Information Service, Sheet No. 16-3*, 4 pp.
- Phillips, N.A., 1966: The equations of motion for a shallow rotating atmosphere and the traditional approximations, *J. Atmos. Sci.*, **23**, 626, 1966.
- Phillips, O.M., 1969: The dynamics of the upper ocean, Cambridge University Press, 216 pp.
- Rochford, D.J., 1962: Hydrology of the Indian Ocean. Part II: the surface waters of the south-east Indian Ocean and Arafura Sea in the spring and summer. *Austr. J. Mar. Freshwater Res.*, **13**, 226-251.
- Rochford, D.J., 1969: Seasonal variations in the Indian Ocean along 110° E. Part I: Hydrological structure of the upper 500 m. *Austr. J. Mar. Freshwater Res.*, **20**, 1-50.
- Semtner, A.J., and Y. Mintz, 1977: Numerical simulation of the Gulf Stream and mid-ocean eddies. *J. Phys. Oceanogr.*, **7**, 208-230.
- Smith, R.L., A. Huyer and J.S. Godfrey, 1991: The Leeuwin Current off Western Australia, 1986-1987. *J. Phys. Oceanogr.*, **21**, 323-345.
- Thompson, R.O.R.Y., 1987: Continental-shelf-scale model of the Leeuwin Current. *J. Mar. Res.*, **45**, 813-827.
- Trenberth, K.E., W.G. Large and J.G. Olson, 1989a: The effective drag coefficient for evaluating wind stress over the oceans. *J. Climate.*, **1507-1516**.
- Trenberth, K.E., J.G. Olson, and W.G. Large, 1989b: A global ocean wind stress climatology based on ECMWF analyses. *NCAR Tech. Note NCAR/TN-338+STR*, 93 pp.
- Trenberth, K.E., W.G. Large and J.G. Olson, 1990: The mean annual cycle in global ocean wind stress. *J. Phys. Oceanogr.*, **20**, 1742-1760.
- USSR Ministry of Defense, 1979: World Ocean Atlas, Vol. 2: Atlantic and Indian Oceans. (S.G. Gorshkov, Ed.) Pergamon Press. 351 pp.

- Weatherly, G.L., 1972: A study of the bottom boundary layer of the Florida Current. *J. Phys. Oceanogr.*, 2, 54-72.
- Weaver, A.J., and J.H. Middleton, 1988: An analytic model for the Leeuwin Current off Western Australia, School of Mathematics, *Appl. Math. Preprint*, No. AM 88/31, University of New South Wales.
- Weaver, A.J., and J.H. Middleton, 1989: On the dynamics of the Leeuwin Current. *J. Phys. Oceanogr.*, 19, 626-648.
- Weaver, A.J., and J.H. Middleton, 1990: An analytic model for the Leeuwin Current off Western Australia. *Cont. Shelf Res.*, 10, 105-122.

INITIAL DISTRIBUTION LIST

	No. Copies
1. Defense Technical Information Center Cameron Station Alexandria, VA 22304-6145	2
2. Library, Code 0142 Naval Postgraduate School Monterey, CA 93943-5002	2
3. Chairman (Code OC/Co) Department of Oceanography Naval Postgraduate School Monterey, CA 93943-5000	1
4. Chairman (Code ME/Hy) Department of Meteorology Naval Postgraduate School Monterey, CA 93943-5000	1
5. Dr. Mary L. Batteen, (Code OC/Bv) Department of Oceanography Naval Postgraduate School Monterey, CA 93943-5000	2
6. Commander Naval Oceanography Command Stennis Space Center MS 39529-5000	1
7. Commanding Officer Fleet Numerical Oceanography Center Monterey, CA 93943-5005	1
8. Office of Naval Research (Code 420) 800 N. Quincy Street Arlington, VA 22217	1
9. Director of Research Administration (Code 012) Naval Postgraduate School Monterey, CA 93943-5000	1
10. Dr. Thomas Spence National Science Foundation 1800 G Street N. W. Washington, DC 20550	1
11. LCDR Eric J. Bayler, USN 263 Copco Lane San Jose, CA 95123	2